Simple process-led algorithms for simulating habitats (SPLASH v.2.0): ~~calibration-free~~ robust calculations of water and energy fluxes

David Sandoval[1], Iain Colin Prentice[1,2,3], and Rodolfo L.B. Nóbrega[4]

[1]Georgina Mace Centre for the Living Planet, Department of Life Sciences, Imperial College London, Ascot, UK
[2]Department of Biological Sciences, Macquarie University, North Ryde, NSW, Australia
[3]Department of Earth System Science, Institute for Global Change Studies, Tsinghua University, Beijing, China
[4]School of Geographical Sciences, University of Bristol, Bristol

Correspondence: David Sandoval (d.sandoval17@imperial.ac.uk)

Abstract.

The current representation of key processes in Land Surface Models (LSM) for estimating water and energy balances still relies heavily on empirical equations that require calibration oriented to site-specific characteristics. When multiple parameters are used, different combinations of parameter values can produce equally acceptable results, leading to a risk of obtaining "right answers for wrong reasons", compromising the reproducibility of the simulations and limiting the ecological interpretability of the results. To address this problem and reduce the need for free parameters, here we present novel formulations based on first-principles to calculate key components of water and energy balances, extending the already parsimonious SPLASH model v.1.0 (Davis et al. 2017, GMD). We found analytical solutions for many processes, enabling us to increase spatial resolution and include the terrain effects directly in the calculations without unreasonably inflating computational demands. This calibration-free model estimates quantities such as net radiation, evapotranspiration, condensation, soil water content, surface runoff, subsurface lateral flow and snow-water equivalent. These quantities are derived from readily meteorological data such as near-surface air temperature, precipitation and solar radiation, and soil physical properties. Whenever empirical formulations were required, e.g. pedotransfer functions and albedo-snow cover relationships, we selected and optimized the best-performing equations through a combination of remote sensing and globally distributed terrestrial observational datasets. Simulations at global scales at different resolutions were run to evaluate spatial patterns, while simulations with point-based observations were run to evaluate seasonal patterns using data from hundreds of stations and comparisons with the VIC-3L model, demonstrating improved performance based on statistical tests and observational comparisons. In summary, our model offers a more robust, reproducible, and ecologically interpretable solution compared to more complex LSMs.

Copyright statement.

1

1 Introduction

Robust representations of water and energy fluxes provide essential foundations for the analysis of interactions and feedbacks within soil, atmosphere and vegetation continuum in complex Land Surface Models (LSMs) (Wang et al., 2014; Prentice et al., 2015). These fluxes are greatly shaped by complex topography, which determines the amount of solar energy received at the surface; and by gradients of atmospheric pressure, temperature and moisture, soil development and gravitational potential en-

ergy, which together control vegetation dynamics and the emergent spatial patterns of ecosystem composition and structure (Tromp-van Meerveld and McDonnell, 2006; Körner, 1999; Sarmiento, 1986). Current models represent the complexity of topographic effects in various simplified ways, for example through discretization of the spatial continuum into hydrological response units (Grayson and Blöschl, 2000; Rodell et al., 2004), or predefined biomes (Liang et al., 1996) or stochastic representation of terrain and land cover at subgrid scales (Lawrence et al., 2019; Liang and Xie, 2001). Or, alternatively, models

designed for large-scale applications may simply disregard terrain effects (Davis et al., 2017). This approach has arisen because models typically divide the soil-vegetation-atmosphere column into layers, or small storages, resulting in a large computational demand. So, to run models at higher resolution would increase the required computing power exponentially (Clark et al., 2017).

Although the higher precision of numerical schemes increases the accuracy of the models, the representation of some core hydrological processes still relies on empirical equations that require site-specific calibration (Clark et al., 2017). One outcome

of this process is that different combinations of parameter values can produce equally acceptable results, implying a risk of obtaining "right answers for wrong reasons" (Grayson and Blöschl, 2000; Prentice et al., 2015), compromising the reproducibility of simulations, and limiting the ecological interpretability of the results obtained.

The use of optimization algorithms for multiple parameters in ever more complex models may not necessarily improve matters and, indeed, may hide the inadequacy of concepts such as "field capacity" and "permanent wilting point" when repre-

senting one of the most important ecological quantities, the soil water availability to plants. Although these constructs make sense conceptually, they can be misleading. For example, field capacity is described as the remaining water in the soil after drainage has ceased (Kramer and Boyer, 1995; Veihmeyer and Hendrickson, 1931). Still, its value is found in laboratory tests using small soil cores, and it is arbitrarily assumed to be equivalent to the water left after applying 33 kPa of suction (or 10 kPa in sandy soils). The permanent wilting point by definition depends on the plant as well as soil properties. Nonetheless, it

is assumed by convention to be equivalent to the water left after applying 1.5 MPa of suction (M. B. Kirkham, 2005). Such values are upscaled globally using pedotransfer functions (PFTs), assuming they represent conditions found in nature, but their validity is virtually impossible to test using current LSMs.

The SPLASH model (Davis et al., 2017), is a highly parsimonious, multi-purpose set of algorithms mainly designed for eco-hydrological and bioclimatic analysis: see e.g. Harrison et al. (2010); Gallego-Sala and Prentice (2012); Ukkola et al. (2015).

Even though the original SPLASH assumes a flat cell, neglecting terrain influence on the fluxes, it includes explicit effects of elevation on biophysical quantities with minimum meteorological inputs. At its core, it conceptualizes the daily cycles of water and energy fluxes, and it solves their respective budgets using analytical integrals at a daily timestep (Cramer and Prentice,

1988; Davis et al., 2017). We propose new formulations to extend the original SPLASH using theory and concepts based on first principles, thus minimizing the need for free parameters while allowing the representation of processes in complex terrain.

55 To improve the calculations of the energy fluxes we adapted SPLASH v1.0 mathematical framework to use shortwave radiation as input instead of cloudiness as a proxy for it. Furthermore, we included terrain (slope and aspect) effects on the analytical integrals of the daily energy fluxes and updated the empirical functions used to estimate net longwave radiation.

Since one of the main applications of SPLASH is to infer the water limitation on photosynthesis (Wang et al., 2014; Stocker et al., 2018), we no longer consider the available plant water capacity as a constant value and added the calculation of subsurface

60 flows. Here, we enhanced SPLASH with an analytical solution for the Green-Ampt equation to calculate daily infiltration, including corrections for slope effects; and analytical solutions for lateral flow, water viscosity effects on hydraulic conductivity, and Dunne and/or Hortonian runoff generation. To upgrade the "bucket model" used in the estimation of soil water content in SPLASH we have included soil hydrophysical properties estimated by PTFs and proposed a theoretical field capacity found by equilibrating gravity with capillarity force. This new version of SPLASH also includes an analytical solution to estimate soil

65 moisture at any depth; and a simple snowpack module, which accounts for snowfall occurrence, snow mass balance and effects on albedo. Processes that still require empirical formulations in the model (i.e., snowfall occurrence, snow-albedo feedback, and the effect of soil physical properties on the water retention curve) were optimized using "big data" from remote sensing and in situ measurements.

Some simplifications were adopted in order to allow analytical solutions, based on the prevalence of shallow soils and

70 impervious bedrock in mountain regions around the world:

1. The drop of the saturated hydraulic conductivity with depth is neglected.

2. Soil moisture redistribution through the soil profile (down to 2 m) takes no longer than one day.

3. Water fluxes in the soil column are in a steady state.

4. The shape of the moisture profile follows Hilberts et al. (2005) and Fan et al. (2007).

75 5. The snow temperature is 0°C, so implicitly the energy required to raise the snow temperature is neglected.

The proposed analytical solutions greatly reduce the computational demand compared to numerical schemes, enabling the model to perform calculations using global high-resolution datasets at daily or monthly timesteps, and to provide emergent spatial patterns of key model outputs such as net radiation, snowpack size, lateral flow, surface runoff, condensation, evapo-transpiration and soil water content.

80 The inputs of the model are precipitation, solar radiation and air temperature. To derive terrain information (slope, aspect and upslope contributing area) the algorithm requires a digital elevation model (DEM) when the grid functionality is used, but, if used with site-specific data (i.e. station data), these variables should be computed beforehand. To estimate some soil hydrophysical properties, the algorithm also requires soil texture, organic matter content and thickness.

2   Methods: Model description

2.1   Energy fluxes

2.1.1   Surface solar radiation

Starting from the original formulation for extraterrestrial solar radiation flux I_0 ($W\,m^{-2}$) from SPLASH (Davis et al., 2017), which is defined as:

$$I_0 = I_{SC}\,d_r\,cos\,\theta_z \tag{1}$$

Where, I_{SC} is the solar constant ($W\,m^{-2}$), d_r ($unitless$) is the distance factor, and $cos\theta_z$ is inclination factor. The effects of the slope inclination and orientation on the surface solar radiation were included by using a more complex formulation of $cos\,\theta_z$, parameterized after Allen et al. (2006) as follows:

$$
\begin{aligned}
cos(\theta_z) = {}& sin(\delta)\,sin(\phi)\,cos(s) \\
& - sin(\delta)\,cos(\phi)\,sin(s)\,cos(\gamma) \\
& + cos(\delta)\,cos(\phi)\,cos(s)\,cos(h) \\
& + cos(\delta)\,sin(\phi)\,sin(s)\,cos(\gamma)\,cos(h) \\
& + cos(\delta)\,sin(\gamma)\,sin(s)\,sin(h)
\end{aligned}
\tag{2}
$$

Where, $\delta(\text{rad})$ is the declination angle between earth's equator and the sun at solar noon, and describes the seasonal changes at different latitude $\phi(\text{rad})$, the hour angle $h(\text{rad})$ describes the sun's position above the horizon, $s(\text{rad})$ is the slope inclination and $\gamma(\text{rad})$ is the slope orientation, or aspect, being $\gamma = 0$ for slopes oriented due south with its values increasing clockwise.

The hour angle when the solar radiation flux reaches the horizon or sunset hour [1] h_s was found by replacing Eq. (2) in Eq. (1), setting $I_o = 0$, and solving for h, thus:

$$h_s = arccos\left(-\frac{sin(\delta)\,sin(\phi)\,cos(s)\,-\,sin(\delta)\,cos(\phi)\,sin(s)\,cos(\gamma)\,+\,cos(\delta)\,sin(\gamma)\,sin(s)\,sin(h_s)}{cos(\delta)\,cos(\phi)\,cos(s)\,+\,cos(\delta)\,sin(\phi)\,sin(s)\,cos(\gamma)}\right) \tag{3}$$

Furthermore, to simplify the notation, Eq. (3) can be rewritten as:

$$h_s = arccos\left(-\frac{r_u}{r_v}\right) \tag{4}$$

Where, $r_u = sin(\delta)sin(\phi)cos(s) - sin(\delta)cos(\phi)sin(s)cos(\gamma) + cos(\delta)sin(\gamma)sin(s)sin(h_s)$ and $r_v = cos(\delta)cos(\phi)cos(s) + cos(\delta)\,sin(\phi)\,sin(s)\,cos(\gamma)$, respectively. To account for the occurrences of polar days (i.e., no sunset) or polar nights (i.e., no sunrise), h_s is set to π when $r_u/r_v \geq 1$, and to zero when $r_u/r_v \leq -1$ respectively. Here, to approximate the value of $sin(h_s)$, the analytical solution proposed by Allen et al. (2006) is used as follows:

$$sin(h_s) = \frac{ac + b\sqrt{b^2 + c^2 - a^2}}{b^2 + c2} \tag{5}$$

---

[1] ~~If we evaluate Eq. (3) for flat surfaces ($s = 0$), it becomes $h_s = arccos\left(-\frac{sin(\delta)\,sin(\phi)}{cos(\delta)\,cos(\phi)}\right)$, which is the original SPLASH equation described by Davis et al. (2017)~~

Where,

$$a = sin(\delta)\,cos(\phi)\,sin(s)\,cos(\gamma) - sin(\delta)\,sin(\phi)\,cos(s) \tag{6a}$$

$$b = cos(\delta)\,cos(\phi)\,cos(s) + cos(\delta)\,sin(\phi)\,sin(s)\,cos(\gamma) \tag{6b}$$

110 $\quad c = cos(\delta)\,sin(\gamma)\,sin(s) \tag{6c}$

~~Therefore, the~~

Note that if we evaluate Eq. (3) for flat surfaces $(s = 0)$, it becomes $h_s = arccos\left(-\frac{sin(\delta)\,sin(\phi)}{cos(\delta)\,cos(\phi)}\right)$, which is the original SPLASH equation described by Davis et al. (2017).

The daily accumulated incoming radiation $(MJ\,m^{-2}\,d^{-1})$ is calculated as twice the integral of the Eq. (1), with $cos(\theta_z(h))$
115 $\quad$ ranging from solar noon $(h = 0)$ to sunset $(h = h_s)$, times the atmosphere's transmittance τ $(unitless)$.

$$H = 2\int_0^{h_s} \tau I_0 = 2\int_0^{h_s} \tau I_{SC}\,d_r\,cos\theta_z dh = \frac{86400}{\pi}\,\tau\,I_{SC}\,d_r\,(r_u h_s + r_v\,sin(h_s)) \tag{7}$$

To exploit datasets of daily average incoming shortwave radiation SW $(W\,m^{-2})$ and deprecate the empirical parameters in the previous model version which uses the classic Ångstrom–Prescott formula and cloudiness data, we set, $H = SW(W\,m^{-2}) *$ $86400(s\,d^{-1})$ in Eq. (7). Then multiplying both sides of Eq. (7) by $(1 - \beta_{SW})$, we solve for $\tau\,I_{SC}\,d_r\,(1 - \beta_{SW})$ to match the
120 $\quad$ original formulation of the variable r_w $(W\,m^{-2})$ as follows:

$$r_w = \tau\,I_{SC}\,d_r\,(1 - \beta_{SW}) = \frac{SW\,\pi(1 - \beta_{SW})}{r_u h_s + r_v\,sin(h_s)} \tag{8}$$

Where β_{SW} is the albedo and the other variables previously defined.

2.1.2 Net surface radiation

The net radiation flux at the surface, I_N $(W\,m^{-2})$, is defined as the difference between the net shortwave radiation flux, I_{SW}
125 $\quad$ $(W\,m^-2)$ and the net long-wave radiation flux, I_{LW} $(W\,m^{-2})$,

$$I_N = I_{SW} - I_{LW} \tag{9}$$

Where, I_{SW} is computed simply as the fraction of the incoming shortwave radiation flux not reflected by the albedo, β_{SW} $(unitless)$:

$$I_{SW} = SW(1 - \beta_{SW}) \tag{10}$$

130 $\quad$ I_{LW} is computed in a similar fashion as the original SPLASH, by merging empirical formulations for clear and cloudy skies, both fitted using Eddy covariance data from the whole FLUXNET database, thus, replacing the old empirical formulations from (Monteith and Unsworth, 1990) and (Linacre, 1968) used in the first version.

$$I_{LW} = (k_4 + (1.0 - k_3)\,S_f)\,(k_1 + k_2\,T_{air}); \tag{11}$$

Where k_{1-4} are empirical coefficients, T_{air} ($°C$) is the daily mean near-surface air temperature and S_f (*unitless*) is the sunshine fraction, derived from a general form of the Ångstrom–Prescott equation, with parameters fitted from global databases according to Suehrcke et al. (2013):

$$s_f = \left(\frac{\tau - \tau_o\, k_5}{\tau_o\,(1 - k_5)} \right)^{(1/k_6)} \tag{12}$$

Where k_{5-6} are empirical coefficients, τ is the atmosphere's transmittance, calculated as the ratio between TOA solar radiation and surface SW data, and τ_o is the clear sky atmospheric transmittance, computed following (Allen, 1996). Values for the coefficients are provided in the Table (1).

Table 1. Constants and Standard Values

Variable	Value	Units	Description	Reference
I_{SC}	1360.8	$W\,m^{-2}$	solar constant Eq. (1)	(Kopp and Lean, 2011)
β_o	0.17	–	shortwave background albedo Eq. (25)	(Federer, 1968)
β_o^{snw}	0.85	-	new fallen snow albedo Eq. (26)	(Wang and Zeng, 2010; Barry, 1996)
k_1	91.86	($°C$)	empirical constant Eq. (11)	(This study)
k_2	1.95	–	empirical constant Eq. (11)	(This study)
k_3	0.20	–	empirical constant Eq. (11)	(Linacre, 1968)
k_4	0.088	–	empirical constant Eq. (11)	(This study)
k_5	0.1898	–	empirical constant Eq. (12)	(Suehrcke et al., 2013)
k_6	0.7410	–	empirical constant Eq. (12)	(Suehrcke et al., 2013)
k_7	-0.5827	–	empirical constant Eq. (19)	(This study)
k_8	1.319	–	empirical constant Eq. (19)	(This study)
k_9	4.18×10^{-4}	–	empirical constant Eq. (19)	(This study)
k_{10}	1.140×10^{-2}	–	empirical constant Eq. (19)	(This study)
k_{11}	0.443	–	empirical constant Eq. (26)	(This study)
k_{12}	0.895	–	empirical constant Eq. (26)	(This study)
L_f	334000	$J\,kg^{-1}$	Latent heat of fusion Eq. (32)	(Monteith and Unsworth, 1990)
g	9.81	$m\,s^{-2}$	gravitational acceleration Eq. (19)	(Monteith and Unsworth, 1990)
SWE_n^c	140	mm	Minimum snow water equivalent for full snow cover Eq. (27)	(This study)

The daily accumulated net radiation, H_N ($MJ\,m^{-2}d^{-1}$), is calculated as net positive H_N^+ (daytime approximately), and net negative H_N^- (night-time approximately), the threshold between H_N^+ and H_N^- is the hour angle when I_{SW} equals I_{LW}, (h_n)

(Fig.1). It is found by setting $I_N = 0$ in Eq. (9) as follows:

$$h_n = arccos\left(\frac{I_{LW} - r_w\, r_u}{r_w\, r_v}\right) \tag{13}$$

For cases where the net radiation is always positive $((I_{LW} - r_w r_u)/(r_w r_v) \geq -1)$ hn is limited to π, while for the opposite cases, where the net radiation is always negative $((I_{LW} - r_w r_u)/(r_w r_v) \geq 1)$, hn is limited to zero.
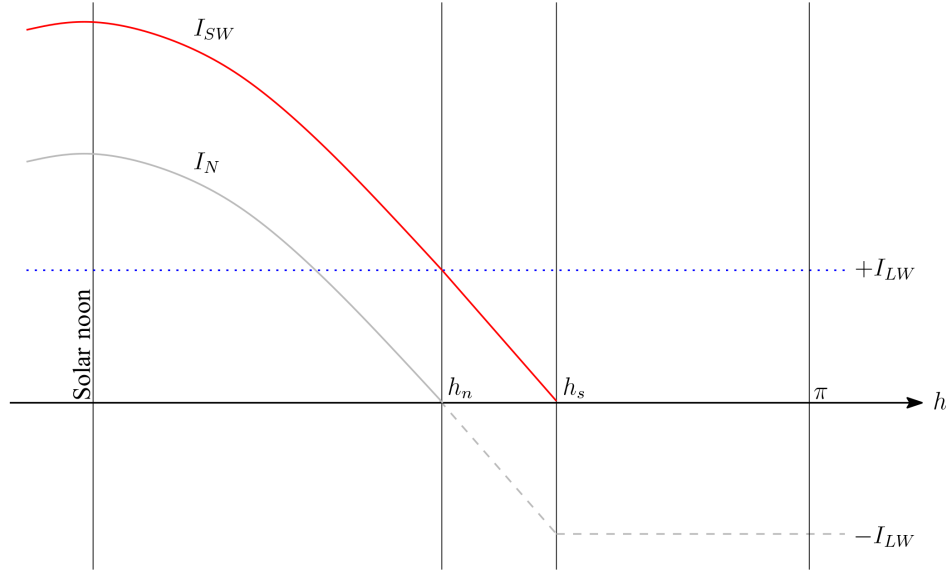

Figure 1. Conceptualization of the net radiation flux between solar noon (i.e., $h = 0$) and solar midnight (i.e., $h = \pi$) after Davis et al. (2017).

Therefore, as described by Davis et al. (2017), H_N^+ is defined as twice the integral of I_N from solar noon to the flux crossover hour angle h_n (Eq.14), while H_N^- is calculated as twice the integral of I_N between h_n and solar midnight ($h = \pi$) (Eq.15),

$$H_N^+ = 2\int_{h=0}^{h_n} I_N = \frac{86400}{\pi}\left((r_w r_u - I_{LW})h_n + r_w r_v sin(h_n)\right) \tag{14}$$

$$H_N^- = 2\left(\int_{h_n}^{h_s} I_N - \int_{h_s}^{\pi} I_{LW}\right) = \frac{86400}{\pi}\left[r_w r_v(sin(h_s) - sin(h_n)) + r_w r_u(h_s - h_n) - I_{LW}(\pi - h_n)\right] \tag{15}$$

2.2 Water fluxes and storages

2.2.1 Snowfall

The freezing temperature of the water, 0.0 °C is the usual threshold to categorize rainfall as snowfall in several models (Pomeroy and Brun, 2001), however, other atmospheric variables like cloudiness, atmospheric pressure and relative humidity are defining

define the snowfall formation (Jennings et al., 2018), therefore changing this temperature threshold in a narrow range across locations (Kienzle, 2008). Here, to get the rainfall/snowfall proportion it is usual to find, among different methods in the literature, linear approximations based on air temperature (Harder and Pomeroy, 2014; Marks et al., 1999; Rene Orth and Seneviratne, 2015), or simply the 100% of the precipitation falling below 0.0 °C assigned as snowfall (Bergström, 1995; Dirmeyer et al., 2006) which might lead to miscalculations in some regions like the Alps, where up to 80% of its annual precipitation might be in the form of snowfall (Barry, 2008).

Therefore, in the current version of the model a sigmoid curve is used to describe the rain-snow proportion (f_{rain}) following Kienzle (2008), who fit empirical equations using 64 years of measurements of rainfall/snowfall proportions from 113 Canadian stations as follows:

$$f_{rain} = 5 \left(\frac{T_{air} - T_{tm}}{1.4 T_{rm}} \right)^3 + 6.76 \left(\frac{T_{air} - T_{tm}}{1.4 T_{rm}} \right)^2 + 3.19 \left(\frac{T_{air} - T_{tm}}{1.4 T_{rm}} \right) + 0.5 \tag{16}$$

Where, T_{tm} (C) is the monthly temperature threshold for the 50% of rain-snow occurrence, and T_{rm} ($°C$) is the monthly range of temperatures for snowfall occurrence, both calculated according to:

$$T_{tm} = T_t + T_t \sin \left(\frac{m_i + 2}{1.91} \right) \tag{17}$$

$$T_{rm} = T_r \left(0.55 + \sin(m_i + 4) \right) * 0.6 \tag{18}$$

Where, m_i is a monthly index (from 1 to 12), T_r ($°C$) is the annual range of temperatures for snowfall occurrence, found in 13°C as first approximation by Kienzle (2008). And T_t ($°C$) is the annual threshold for snowfall formation, defined for each year as the annual maximum air temperature when the probability of snowfall occurrence $p(snow)$ is equals or exceeds 0.5.

$p(snow)$ was estimated using a binary logistic regression, following the method and datasets provided by Jennings et al. (2018), but reducing the number of explanatory variables to air temperature T_{air} ($°C$), elevation z ($m.a.s.l$) and latitude ϕ ($°$) as follows (Appendix A4.3):

$$p(snow) = \frac{1}{1 + e^{(k_7 + k_8 \, T_{air} + k_9 \, z + k_{10} \, \phi)}} \tag{19}$$

Where, k_7, k_8, k_9 and k_{10} are coefficients (Table 1). Then, the snowfall is calculated by,

$$Sf = P_n \left(1 - f_{rain} \right) \tag{20}$$

2.2.2 Snowmelt

Snowmelt Sm ($mm \, d^{-1}$) was calculated using a simple relationship between available energy and the size of the snowpack SWE (mm) (snow water equivalent) as follows:

$$Sm = \min \left(SWE, \frac{H_N^+}{\rho_w L_f} * 1000 \right) \tag{21}$$

Where SWE is the size of the snowpack expressed as snow water equivalent (mm), H_N^+ ($MJ\,m^{-2}d^{-1}$) is the daytime accumulated net radiation, ρ_w ($kg\,m^{-3}$) is the water density at 0°C, L_f ($J\,kg^{-1}$) is the latent heat of fusion, and 1000 is the factor to convert m^3 to $litres$. Following Barry (2008), we assumed direct-sublimation as negligible, however, if there is residual energy after the melting ~~occur~~ occurs, we directed that energy to evaporate Sm, flux hereafter denoted simply as "sublimation" (E^{swe}), which reduces the amount of Sm reaching the soil or producing runoff.

$$E^{swe} = \min\left(S_m, \frac{H_A^+}{E_{con}} * 1000\right) \tag{22}$$

Where H_A^+ ($MJ\,m^{-2}d^{-1}$) is the daytime available energy, (daytime accumulated net radiation – energy used in melting), E_{con} ($m^3 J^{-1}$) is the energy to water equivalent conversion factor (Davis et al., 2017) and 1000 is the factor to convert m^3 to $litres$. Thus, the water from snowmelt reaching the soil is:

$$Sm_e = Sm - E^{swe} \tag{23}$$

2.2.3 Snowpack

The size of the snowpack, expressed as snow water equivalent SWE (mm) is computed as a simple balance using the previous-day SWE, inputs and outputs as follows:

$$SWE_n = SWE_{n-1} + Sf - Sm \tag{24}$$

The effect of the snow on the albedo was formulated as a simple ~~weighted-average~~ weighted average using the snow cover fraction, following Wang and Zeng (2010); Roesch and Roeckner (2006); Niu and Yang (2007),

$$\beta_{sw} = \beta_o * (1.0 - f_{snw}) + (f_{snw} * \beta_{snw}) \tag{25}$$

Where β_o the is background albedo (Federer, 1968), β_{snw} is the snow albedo, calculated according to the age of the snow, following the widely used formulation from the Corps of Engineers (1956)

$$\beta_{snw} = (\beta_o^{snw} - k_{11}) + k_{11}\,e^{-k_{12}\,n_d} \tag{26}$$

Here β_o^{snw} is the albedo of the ~~new fallen~~ new-fallen snow, n_d is the number of days since a snowfall event greater than 3mm (Chen et al., 2014), and $k_{11,12}$ empirical constants. The snow cover fraction (f_{snw}) from Eq.(25) was estimated using a simple hyperbolic function following Dickinson et al. (1986) and Barry (1996).

$$f_{snw} = \frac{SWE_n}{SWE_c + SWE_n} \tag{27}$$

Where SWE_c is the snow water equivalent where f_{snw} starts to saturate.

The optimized parameters of eq. 26 and eq. 27 using remote sensing and ground observations are listed in ~~the Table~~ table 1.

2.2.4 Infiltration

The infiltration flux rate i ($mm\,h^{-1}$), was conceptualized as a two stages process, which can happen independently or one after another according to the magnitudes of the incoming flux r ($mm\,h^{-1}$) (rain/snowmelt), and the infiltration capacity of the soil (Fig. 2).
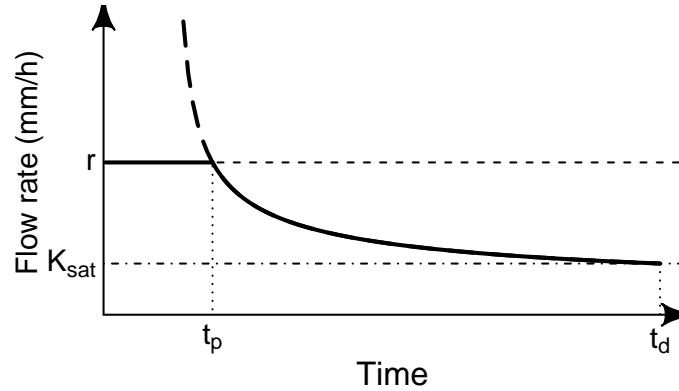

Figure 2. Conceptualization of the infiltration process with a constant rainfall r (modified from Tindall et al. (1999)). Here, K_{sat} is the saturated hydraulic conductivity, t_p and t_d stand for ponding and duration times respectively.

The first stage, usual when the soil is dry, describes an infiltration rate lower than the infiltration capacity, thus, it is limited by the rainfall/snowmelt rate , and lasts until the water flux starts to pond at t_p (Vereecken et al., 2019; Assouline, 2013). A second stage describes the system once the water starts to pond on the surface, here the infiltration rate is limited by the infiltration capacity, which in turn ~~is decreasing~~ decreases inversely to the water content of the soil, reaching its minimum value (equivalent to K_{sat}) at saturation following the Green-Ampt formulation, as described by Assouline (2013); Tindall et al. (1999).

$$i_{t+1} = \frac{dI}{dt} = K_{sat}\left(\frac{\psi_f(\theta_{sat} - \theta_t)}{I(t)} + 1\right) \tag{28}$$

Where K_{sat} ($mm\,h^{-1}$) is the saturated hydraulic conductivity, $\theta_{t,sat}$ ($m^3 m^{-3}$) are the volumetric soil water content at the time t and at saturation sat respectively, $I(t)$ is the cumulative infiltration at the time t, and ψ_f (mm) is the capillary head at the wetting front, which according to Tindall et al. (1999) is calculated as:

$$\psi_f = \frac{2+3\lambda}{1+3\lambda}\frac{\psi_b}{2} \tag{29}$$

Being λ the pore-size distribution index ($unitless$), and ψ_b (mm) the air-entry pressure, both shaping parameters of the soil-water retention curve proposed by Brooks and Corey (1964) (referred as BC model hereafter).

Therefore, the ponding time t_p can be found by setting Eq.(28) equals to r, which yields:

$$t_p = \frac{K_{sat}\psi_f(\theta_{sat} - \theta_t)}{r(r - K_{sat})} \tag{30}$$

Moreover, to account for the slope (s) effects on t_p, the factor $\frac{1}{cos^2(s)}$, is used to reduce t_p, following the analysis of Morbidelli
230   et al. (2018), thus, the cumulative infiltration is defined as follows:

$$I = rt_p + \int_{t_p}^{t_d} i\, dt = r\frac{t_p}{cos^2(s)} + K_{sat}\left(t_d - \frac{t_p}{cos^2(s)}\right) - \psi_f\, \Delta\theta\, ln\left(1 - \frac{r\frac{t_p}{cos^2(s)}}{\psi_f\, \Delta\theta}\right); r > K_{sat} \tag{31a}$$

$$I = rt_d; r \leq K_{sat} \tag{31b}$$

Where t_d is the duration of the precipitation event, and $\Delta\theta$ is the difference between θ_{sat} and the previous θ at the near soil
surface, which is calculated using an analytical solution of the Brooks and Corey (1964) model with the previous-day moisture
235   and the depth of the profile (See section 2.7).

The set of equations presented above still requires rainfall intensity and the event's duration to perform the calculations,
however, the "minimum inter-event time", which is used to define a precipitation event, is not consistent in the literature, and
varies according to the author, location and application, ranging from 15 min to 24 hours (Dunkerley, 2008; Molina-Sanchis
et al., 2016), making it difficult to define a criteria for global applications. Therefore, as a simplification, an average daily
240   rainfall duration was proposed instead, similar conceptually to the design storm, which is used in calculations for infrastructure
design (Smith and Parlange, 1978). In this way, to find the average daily rainfall duration, the daily number of hours with
precipitation and the daily precipitation amount were extracted from the Global Satellite Mapping of Precipitation (GsMap
v6.0) dataset during the 2000-2014 period (Mega et al., 2014; Yamamoto and Shige, 2015) using the Google Earth Engine
platform (GEE), and the most frequent value was chosen ($6hrs$).

245   The parameters λ and ψ_b, which shape the BC model, and K_{sat} were estimated using pedotransfer functions detailed in
Saxton and Rawls (2006) which use soil texture and soil organic matter (SOM) as inputs.

To account for the effects of temperature and atmospheric pressure on the water viscosity and hence on K_{sat} (Fig. 3), we
used the formula described by Hillel (1998):

$$K_{sat} = k_i \frac{\rho g}{\eta} \tag{32}$$

250   Where, k_i (m^2) is the soil's intrinsic permeability, ρ $(kg\, m^{-3})$ is the water density, g $(m\, s^{-2})$ gravitational acceleration and η
$(Pa\, s)$ is the dynamic viscosity. Thus, we simply used K_{sat} from the pedotransfer functions, assuming $\frac{\rho}{\eta}$ at standard conditions
to find k_i, which was later replaced in Eq. 32 using actual environmental conditions.
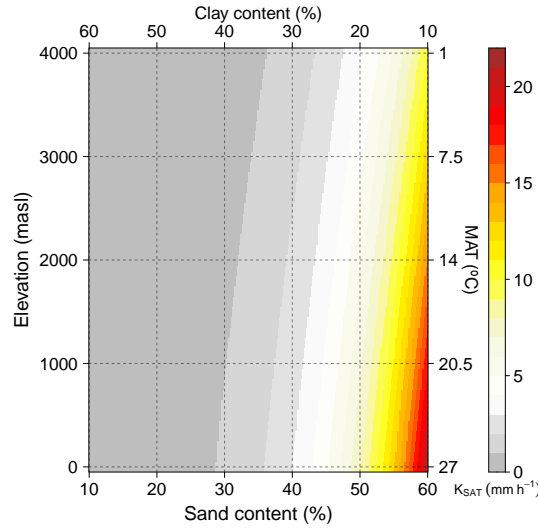
Figure 3. Effects of elevation (atmospheric pressure and temperature) on the saturated hydraulic conductivity, using a hypothetical soil with 10% SOM, 30% Silt, and varying Sand and Clay

2.2.5 Surface Runoff

The runoff formulation considers the different generation mechanisms: the saturation excess overland runoff RO_D $(mm\,d^{-1})$ (Dunne runoff), which is produced after the soil became saturated and is frequent in humid climates or riparian areas (Vereecken et al., 2019), and, the infiltration excess overland runoff RO_H $(mm\,d^{-1})$ (Hortonian runoff), which is produced when the precipitation rate exceeds the infiltration capacity, more frequent in semi-arid climates (Grayson and Blöschl, 2000; Vereecken et al., 2019).

$$RO_D = max(0, W_n - W_{sat}) \tag{33a}$$
$$RO_H = r - I \tag{33b}$$

Where, r $(mm\,d^{-1})$ is water input (rainfall + snowmelt), I $(mm\,d^{-1})$ is the infiltration, $W_{n,sat}$ (mm) are the actual and soil water content at saturation respectively.

Therefore, the daily total RO is simply defined as:

$$RO = RO_D + RO_H \tag{34}$$

2.2.6 Lateral flow

The lateral flow in one cell was defined at steady state as:

$$q_{in} = q_{out} \tag{35}$$

12

Where q_{in} $(mm\,d^{-1})$ is the water draining into the cell from the upslope contributing area and q_{out} $(mm\,d^{-1})$ is the water draining out from the cell.

270   The lateral outgoing flow q_{out} $(mm\,d^{-1})$ was conceptualized using some of the TOPMODEL's ideas (Beven and Kirby, 1979) on the profile transmissivity (soil hydraulic conductivity K integrated over the soil column), and the hydraulic gradient defined by local topography $tan(s)$ as follows:

$$q_{out} = \frac{w}{A_i} \int_0^{z_s} K(\theta, z)\, dz \, \tan(s) \tag{36}$$

Where w is the width of the profile's cross-section and A_i is the area of the cell, used here to convert the volumetric flow
275   through the cross-section to equivalent water column units over the cell.

     In order to solve the transmittance, the soil moisture distribution through the profile was conceptualized following Hilberts et al. (2005) and Fan et al. (2007) (Fig. 4) with hydrostatic equilibrium at the water table (Remson and Randolph, 1962). Here, the soil moisture redistribution after infiltration was assumed to last shorter than one day within the first 2 m. of soil depth, implying a permanent shape of the moisture profile.

280   Similarly to Fan et al. (2007), due to the lack of information on how K_{sat} is decreasing with depth, the model assumes K_{sat} constant through the first 2 meters of depth extending the original 1.5 m. proposed by Fan et al. (2007).
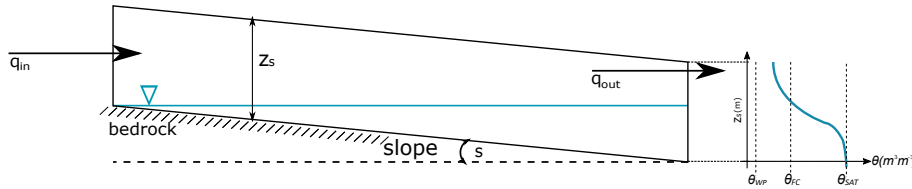

Figure 4. Conceptualization of the soil moisture profile in a shallow soil column, after Hilberts et al. (2005) and Fan et al. (2007). We assumed a cell with low spatial resolution and next to a stream.

     Therefore, we defined the transmissivity of the profile as the sum of the transmissivities in the unsaturated and saturated parts of the profile as follows:

$$T = \int_0^z K(\theta, z)\, dz = T_{uns} + T_{sat} = \int_0^{z_{wtd}} K(\theta, z)\, dz + \int_{z_{wtd}}^z K(\theta, z)\, dz \tag{37}$$

285 Thus, to approximate the distribution of $\theta(z)$ through the unsaturated part of the soil column, the BC model was used with the total soil-water potential (matric+gravitational) after Hino et al. (1988); Beldring et al. (1999).

$$\theta(z) = \theta_r + (\theta_{sat} - \theta_r)\left(\frac{\psi_m + \psi_g(z)}{\psi_b}\right)^{-\lambda} \tag{38}$$

Where, θ_r $(m^3 m^{-3})$ is the residual soil water content, ψ_m (mm) is the soil-matric potential and $\psi_g(z)$ (mm) the gravitational potential.

The hydraulic conductivity, $K(\theta)$ $(mm\,h^{-1})$, was defined according to Brooks and Corey (1964) as follows:

$$K(\theta) = K_{sat} \left(\frac{\theta}{\theta_{sat}} \right)^{\left(3+\frac{2}{\lambda}\right)} \tag{39}$$

Therefore, replacing Eq.(26) in Eq. (27), and solving the integral analytically for the unsaturated part, the transmissivity is defined as:

$$T_{uns} = \int_0^{z_{wtd}} K(\theta, z)\, dz = \frac{K_{sat}\psi_b}{3\lambda+1} \left[\left(\frac{\psi_b}{\psi_m} \right)^{3\lambda+1} - \left(\frac{\psi_b}{\psi_m + z_{wtd}} \right)^{3\lambda+1} \right] \tag{40}$$

Where z_{wtd} (m) is the depth to the water table, found when $\psi_m + \psi_g = \psi_b$.

While the transmissivity in the saturated part of the profile T_{sat} is calculated as

$$T_{sat} = \int_{z_{wtd}}^z K(\theta, z)\, dz = K_{sat}(z - z_{wtd}) \tag{41}$$

The lateral incoming flux q_{in} was formulated using a simple linear reservoir model (Buytaert et al., 2004; Yang et al., 2018; Vogel and Kroll, 1996), with a decaying volumetric flux as a function of time.

$$Q_f = Q_o\, K_b{}^t \tag{42}$$

Where Q_f is the final flux after the time t and Q_o $(m^3\,d^{-1})$ is the initial volumetric flow soon after the precipitation event. If we set the cease of drainage at field capacity we get:

$$\lim_{t \to \infty} Q_o K_b{}^t = Q_{fc} \tag{43}$$

Where Q_{fc} $(m^3\,d^{-1})$ is the volumetric flow after the time t (d), and K_b is the recession constant $(unitless)$, which was found using the drainable porosity, see Appendix (A). Therefore, the total volume result of a daily $(1d)$ recharge $(R > 0)$ over the upslope area (Fig. 5), theoretically, can be approximated by:

$$A_u\, R\,(1d) = \int_{t_0}^t Q_o K_b{}^t dt \tag{44}$$

Where A_u is the upslope area (m^2), ~~and~~ R is the recharge $(mm\,d^{-1})$, defined as infiltration minus evapotranspiration $R = I - E^a$ and t_0 is the time at Q_o.
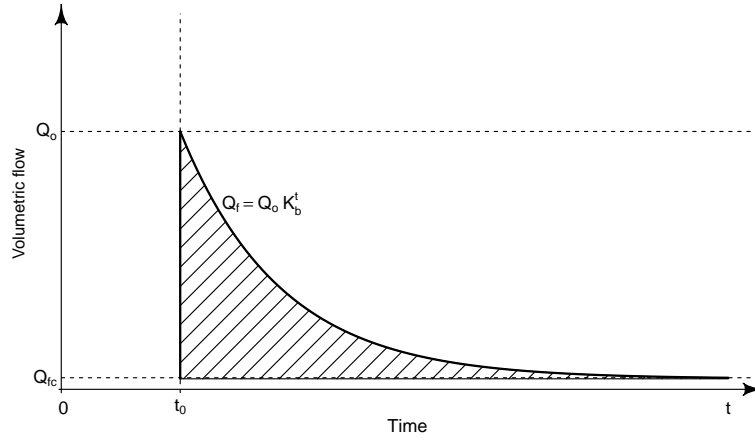
Figure 5. Conceptualization of the recharge from the upslope after one precipitation at t_0, using a simple linear reservoir model. The shaded area represents the Eq.(44).

310   Therefore, if we find t from both, Eq.(43) and Eq.(44), we can set:

$$\frac{1}{\ln(K_b)} \ln\left(\frac{Q_{fc}}{Q_o}\right) = \frac{1}{\ln(K_b)} \ln\left(\frac{A_u R \ln(K_b)}{Q_o} + 1\right) \tag{45}$$

Which, solving for Q_o yields:

$$Q_o = Q_{fc} - A_u R \ln(K_b) \tag{46}$$

Where Q_{fc} can be found by setting θ to field capacity in Eqs.(38 and 40). Thus,

315    $$q_{in} = \begin{cases} \frac{Q_{fc} - A_u R \ln(K_b)}{Ai}; & \text{if } R > 0 \wedge \theta > \theta_{fc} \\ \frac{Q_{in\,n-1} K_b^{\Delta t}}{A_i}; & \text{if } R \leq 0 \wedge \theta > \theta_{fc} \\ 0; & \text{if } \theta \leq \theta_{fc} \end{cases} \tag{47}$$

2.2.7 Evapotranspiration

The actual evapotranspiration, E_n^a ($mm\,d^{-1}$) is computed following the original formulation Davis et al. (2017) with modifications to account for the reduction in available energy, which is diverted to snow melting and sublimation, if any. It starts by defining the actual instantaneous evapotranspiration E^a ($mm\,h^{-1}$) as the minimum between supply S_W ($mm\,h^{-1}$) and

320   demand D_p ($mm\,h^{-1}$) rates (Federer, 1982)

$$E^a = min(S_W, D_p) \tag{48}$$

15

Then, the daily integration of this flux is computed using an analogous form to the daily energy fluxes calculation (Fig. 6), as follows,

$$E_n^a = 2 \int_{h=0}^{h_n} E^a = 2 \left(\int_{h=0}^{h_i} S_W + \int_{h_i}^{h_n} D_p \right) \tag{49}$$

Where $h(\mathrm{rad})$ is the hour angle and h_i is the cross-over angle when the supply is equal to the demand.
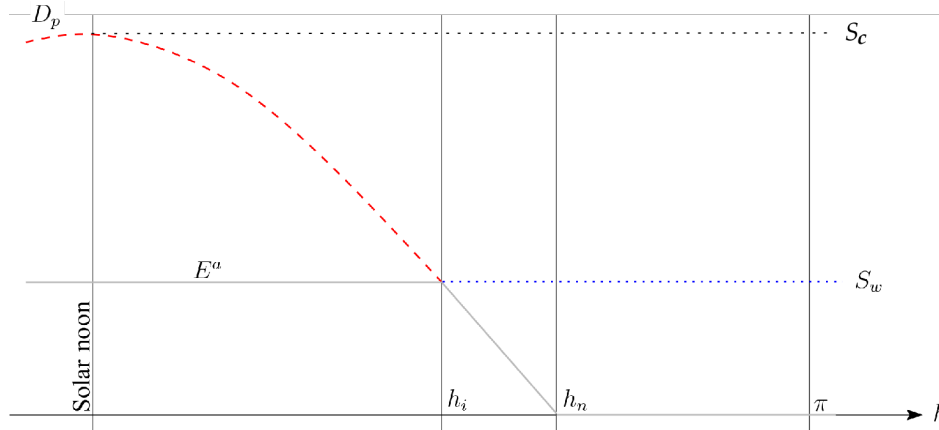

Figure 6. Conceptualization of the actual instantaneous evapotranspiration flux between solar noon (i.e., $h = 0$) and solar midnight (i.e., $h = \pi$), modified from Davis et al. (2017). The evaporative demand D_p (red dashed line) is maximum at solar noon, equivalent to the maximum supply rate Sc. The actual supply rate S_W is constant throughout the day, an depends on soil moisture limitations.

The evaporative demand D_p is defined following the Priestley and Taylor (1972) formulation for potential evapotranspiration:

$$D_p = 3.6 \times 10^6 \, E_{con} \, I_N \tag{50}$$

Where $I_N (W\,m^{-2})$ is the instantaneous net radiation, and $E_{con}(m^3\,J^{-1})$ is the energy-to-water conversion factor, defined following the Priestley-Taylor theory (hereafter PT), with adjustments proposed by Yang and Roderick (2019), which, reproduce the feedback between the surface temperature and E^a, hence their effect on I_N, thus, replacing the need of a Priestley-Taylor α_{PT} coefficient:

$$E_{con} = \frac{s}{L_v \, \rho_w (s + 0.24\gamma)} \tag{51}$$

Where $L_v (J\,kg^{-1})$ is the latent heat of vaporization, $\rho_w (kg\,m^{-3})$ is the water density, $s(Pa\,K^{-1})$ is the slope of the temperature-pressure curve, and $\gamma (Pa\,K^{-1})$ the psychrometric constant, and 0.24 is the constant defined by Yang and Roderick (2019). Equations for temperature and pressure dependencies to calculate ρ_w and γ were used, while only temperature-dependant equations were used for s and L_v (Davis et al., 2017).

16

The stress factor controlling the evaporative supply rate S_W was conceptualized as a piece-wise linear function, where we assumed the stress follows the depletion of the water content in the plant available water region (Fig. 7).
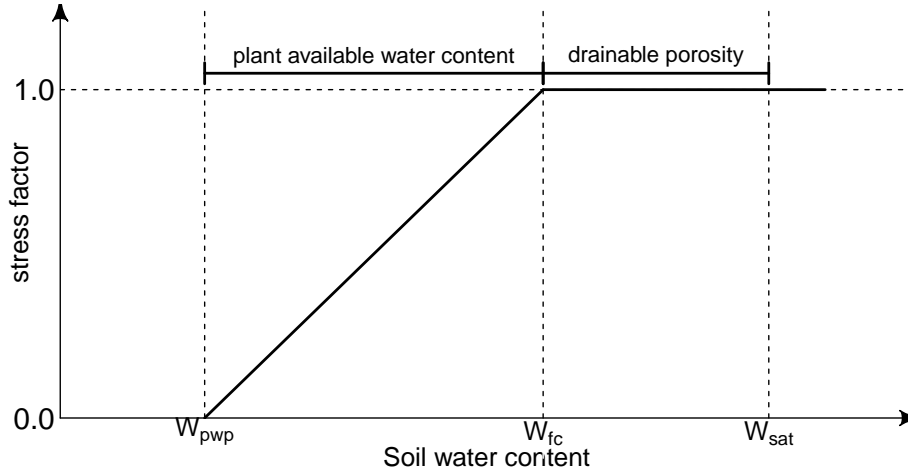

Figure 7. Conceptualization of the stress factor controlling the evaporative supply rate S_W

340   Therefore, S_W is defined as:

$$S_W = \begin{cases} S_c \frac{W_{n-1} - W_{pwp}}{W_{fc} - W_{pwp}}; & \text{if } W_{pwp} \leq W_n < W_{fc} \\ S_c & \text{if } W_n \geq W_{fc} \end{cases} \tag{52}$$

Where, S_c $(mm\,h^{-1})$ is the maximum evaporative supply rate, and W_{n-1} the previous day soil water content.

Here, Davis et al. (2017) adopts S_c as a constant, following Federer (1982), however, the same Federer (1982) points out that this value should change according to morphological traits of the vegetation (i.e. root density and depth).

345   Therefore, since $E^a = min(S_W, D_p)$, and, under well watered conditions $S_W = S_c$, hence, S_c with a value higher than the maximum D_p (at solar noon) won't affect the resultant E^a.

Thus, to estimate S_c, so it applies for non-vegetated areas as well, the supply rate is approximated as the maximum rate of evaporation as follows,

$$Sc = D_{pMAX} = r_x\left((r_w(r_u + r_v)) - I_{LW}\right) \tag{53}$$

350   Where, to simplify the notation, $r_x (mm\,m^2\,W^{-1}\,h^{-1})$ is equal to $3.6 \times 10^6\,E_{con}$.

The upper limit of the Eq.(52) is the water content at field capacity W_{fc} (mm), which was defined as the amount of water held after the drainage ceased (Kramer and Boyer, 1995). This was calculated by setting the total water potential to equilibrium, following Remson and Randolph (1962):

$$\psi_m + \psi_g = 0 \tag{54}$$

17

Where, the matric potential ψ_m was calculated following Saxton and Rawls (2006):

$$\psi_m = A(\theta)^{-B} \tag{55}$$

with,

$$A = e^{\ln(33) + B\ln(\theta_{33})} \tag{56a}$$

$$\theta = W_n/(1000z) \tag{56b}$$

$$B = \frac{1}{\lambda} = \frac{\ln(1500) - \ln(33)}{\ln(\theta_{33} - \ln(\theta_{1500})} \tag{56c}$$

Where, θ_{33} is the volumetric water content at 33 kPa, (usually assumed to be field capacity), θ_{1500} is the volumetric water content at 1500 kPa and z (m) is the depth of the soil profile. Then, using the minimum between 2 m. and the depth to the bedrock as a reference plane, the gravitational potential is defined as:

$$\psi_g = \rho_w \, g \, W_n \tag{57}$$

Therefore, W_{fc} can be found by solving the replacing Eqs. (55 to 57) in Eq. (54) and ~~soving~~ solving for W_n (See Appendix A for intermediate steps):

$$W_{fc} = 1000z \left(\frac{1000 \, A}{\rho_w \, g \, z} \right)^{\frac{1}{1+B}} \tag{58}$$

The lower limit of the Eq. (52) is ~~assumed to be the~~ defined as water content at permanent wilting point [1] W_{pwp} (mm), which was computed as:

$$W_{pwp} = \theta_{1500} * 1000z \tag{59}$$

In order to adopt the best option to compute soil hydro-physical properties (θ_{33}, θ_{1500}, θ_{sat} and K_{sat}) and hence the thresholds proposed, a set of the most widely used PTFs in LSMs were evaluated (Van Looy et al., 2017) were tested with a global dataset of soil physical properties which was compiled from different sources. The models, ranging in complexity, from the most simple mathematical formulations are described in Table 2.

---

[1] ~~Even though the wilting point is an approximation, defined as the water extracted applying 1500kPa of pressure, it also depends on plant physiology, so its value, as a lower boundary, might be not entirely true, especially for dry ecosystems.~~

Table 2. Evaluated pedotransfer functions and their use in Land Surface Models

PTF	LSM/Product	PTF formulation approach[*]	N samples used for training	Inputs
Cosby et al. (1984)	NASA CATCHMENT LSM, CLM 4.5, JULES, Noah-MP/VIC	MLR	1448	Sand (%), clay (%)
Balland et al. (2008)	–	NLR	13088	Sand (%), clay (%), SOM (%), bd ($g\,cm^{-3}$)
Saxton and Rawls (2006)	ESA CCI SM v03.2	MLR	5320	Sand (%), clay (%), SOM (%)
Tóth et al. (2015)	Soil Hydraulic Database of Europe (ESDAC)	RT/LR	2356-5530	Sand (%), clay (%), SOM (%), bd ($g\,cm^{-3}$)
Rosetta 3 (Zhang and Schaap, 2017)	Noah-MP	ANN	2134	Sand (%), clay (%), SOM (%), bd ($g\,cm^{-3}$)

[*]MLR, Multiple linear regression; ANN, Artificial neural networks; RT, regression trees; LR, Linear regression; NLR, non-linear regression.

Thus, finally Eq.(49) is solved analytically as:

$$E_n^a = \frac{24}{\pi}\left(S_W h_i + r_x r_v r_w(\sin h_n - \sin h_i) + (r_x r_u r_w - r_x I_{LW})\,(h_n - h_i)\right) \tag{60}$$

Where, the intersection hour angle h_i is found by setting Eq.(50) equal to Eq. (52) and and solving for h:

$$h_i = \arccos\left(\frac{S_W}{r_x r_v r_w} + \frac{I_{LW}}{r_v r_w} - \frac{r_u}{r_v}\right) \tag{61}$$

2.2.8 Condensation

The daily dew formed by condensation $C_n(mm\,d^{-1})$ is assumed to represent 10% of the water equivalent (Eq.52) of the negative net radiation H_n^- (Eq.15) (Jones, 2013). The remnant energy is assumed to be lost as convective heat. Thus,

$$C_n = 100\,E_{con}\,H_n^- \tag{62}$$

2.2.9 Soil water content

Once calculated inputs and outputs, the total soil water content W_n (mm) can now be calculated using a simple balance expression, with the previous day soil water content W_{n-1} as follows:

$$W_n = W_{n-1} + I + q_{in} - q_{out} - RO_H - E_n^a \tag{63}$$

Furthermore, to calculate the water content $SWC\,(mm)$ accumulated to any depth (z') for further comparison with the observations, if we assume the same moisture profile from Eq. (26), it can be defined as:

$$SWC = \int_0^{z'} \theta(z)dz = \theta_r z + \left. \frac{(\psi_m + \psi_z)(\theta_r - \theta_{sat})\left(\frac{\psi_b}{\psi_m+\psi_z}\right)^\lambda}{\lambda - 1} \right|_0^{z'} \tag{64}$$

2.3 Initial conditions

The SPLASH algorithm assumed steady-state condition as the initial state for the simulations, which is reached by looping $ntimes$ the first year of data until the water balance is preserved:

$$\sum \left(f_{rain}P_n + C_n + Sm_n + q_n^{in} \right) = \sum \left(E_n^a + q_n^{out} + RO \right) \tag{65}$$

3 Methods: ~~Calibration~~ Simulation protocol and ~~validation data~~Performance evaluation

3.1 Point-scale simulations

Point-scale simulations with the SPLASH model were run at individual sites (Figs. 8 and 10) with their entire daily time series of meteorological measurements. Due to different variables measured by the different networks of monitoring, the performance evaluation with the pooled data was done separately per network. The statistics used for the evaluation were the coefficient of determination (R^2), the root mean squared error (RMSE), bias, and the slope of the regression observations simulations. To evaluate the seasonal patterns of fluxes/storages, all the results were aggregated as daily means and grouped by climate zone using the Köppen–Geiger climate classification system (Beck et al., 2018). Only direct measurements were used for the performance evaluations, while some indirect observations were estimated, using the variation with previous-day observations, to visualize seasonal patterns of some fluxes (e.g. Sf and Sm_e). To complement the analysis and interpretation of the results, simulations with the 3-layer variable infiltration capacity model (VIC-3L) (Liang et al., 1996; Liang and Xie, 2001) were performed using the same inputs and in the same way as SPLASH, without local calibration.

Vegetation properties, soil parameters and initial soil moisture, all required by VIC-3L were extracted at the site locations from Schaperow and Li (2020). Extra forcing data required by the VIC-3L, like wind speed and vapour pressure, not measured at the SNOTEL sites, was extracted from the daily, high-resolution GRIDMET (Abatzoglou, 2013) and DAYMET (Thornton et al., 2020) datasets respectively. Since some quantities computed by SPLASH are not standard outputs of the VIC-3L model (e.g. H_N^+ and C_n), some calculations were applied to obtain comparable outputs (Appendix A3.1). To compare seasonal patterns of soil moisture a relative moisture content was calculated with the observations and results from SPLASH, in the same way as the VIC output:

$$\Theta = \frac{W_n - W_{pwp}}{W_{sat} - W_{pwp}} \tag{66}$$

Where W_{sat} is the water content (mm) at saturation. W_n and W_{pwp} are as defined in Section (2.2.7).

3.2 Spatially distributed simulations

Spatially distributed simulations were performed to visualize major spatial patterns of the fluxes/storages, test the computational performance of the model at different resolutions, and evaluate how the global parameters and assumptions of the model hold.

Global simulations were run at a resolution of 5 km, regional simulations (e.g., North America) at a resolution of 1 km, and micro catchments at a resolution of 90 m.

Since the model lacks a routing algorithm, to test the runoff/lateral flow simulations against streamflow observations, yearly aggregated quantities were used.

Spatially distributed simulations of runoff across the US were obtained from Kao et al. (2022). These simulations, conducted independently, employed VIC calibrated with historical hydrological data and were exclusively used for evaluating streamflow against SPLASH simulations run with identical inputs (i.e. DAYMET (Thornton et al., 2018)).

4 Methods: Fitting/Optimization of empirical functions

Parameters from the selected equations (pedotransfer functions) were optimized using the Nash-Sutcliffe (NSE) coefficient, which relates the variance of the residuals with the variance of the data, as the objective function (Nash and Sutcliffe, 1970; Gupta and Kling . Here, an NSE closer to 1.0 expresses ideal estimates. The probabilistic model for snowfall occurrence was fitted using a binomial family Generalized Linear Model (GLM), while the albedo-related functions were fitted using nonlinear least-squares.

To assess the accuracy of the snowfall probability estimation, the Receiver Operating Characteristic (ROC) curve was used, which plots the true positive rate (specificity) against the false positive rate (sensitivity), using a probability of 0.5 as a threshold. Here the area under the curve (AUC) closer to 1.0 expresses a better overall prediction (Fawcett, 2006).

5 Methods: Input data

5.1 Eddy covariance towers

Data from the whole FLUXNET database (Pastorello et al., 2020), comprising 212 stations distributed around the world (Fig. 8) was used to update the empirical functions to compute net longwave radiation, superseding the equations formulated by (Monteith and Unsworth, 1990) and (Linacre, 1968) used in the first version of SPLASH.
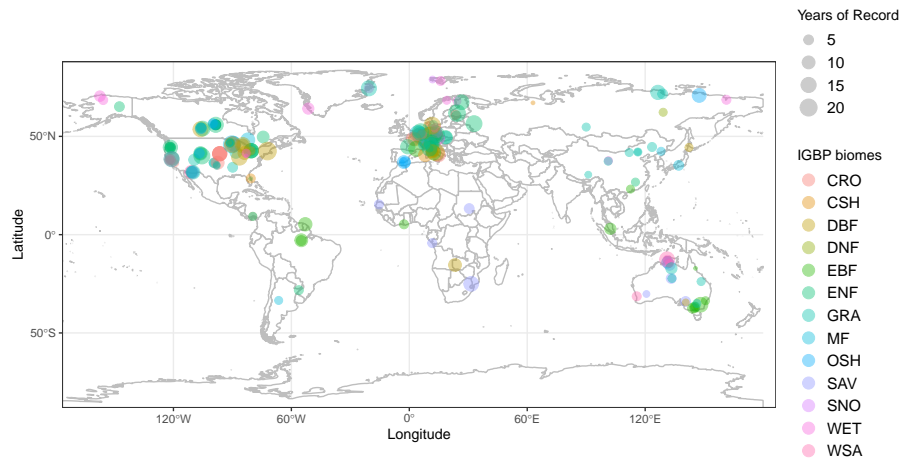
Figure 8. FLUXNET stations used for the I_{LW} parameter calibration.

All the data was aggregated to daily means, while the originally reported latent heat flux was transformed to its equivalent in water flux density ($mm\,d^{-1}$) by using the heat of vaporization corrected for field conditions.

440   To test the validity of the theorized daily cycles and crossover angles, positive values of net radiation were subsetted and aggregated daily, which in theory should be equivalent to Eq.(14). A simple threshold for measured albedo of 0.3 was used to identify snow presence, then, latent heat measurements when snow was present were excluded from the estimations of daily evapotranspiration and condensation, trying to prevent the latent heat used in melting/refreeze/sublimation introduce error in the evaluations.

445   **5.2   Meteorological/hydrometric stations**

To ~~calibrate~~ find the parameters used in the snowcover/albedo functions, 315 stations reporting snow water equivalent or snow-depth from the SNOwpack TELemetry (SNOTEL) network (Serreze et al., 1999), managed by the U.S. Natural Resources Conservation (NCAR) service were used together with remote sensing data (Fig. 9), most of these stations also report solar radiation, precipitation, air temperature and volumetric soil moisture at different depths.

22
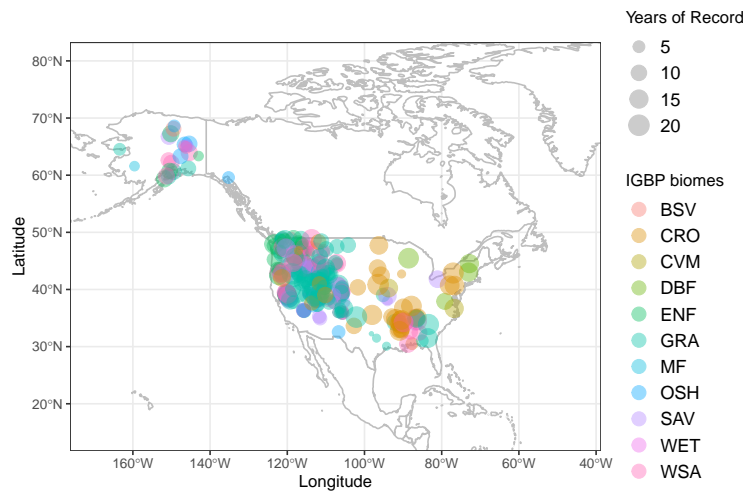
Figure 9. SNOTEL stations used for albedo/snow-cover analysis.

450   To evaluate the model, we subset sites on mountains regions with joint measurements of snow, soil physical properties (i.e. texture, bulk density and SOM), and soil moisture deeper than $30cm$, resulting in 127 sites (Table A4). Data from the DAYMET database (Thornton et al., 2018) was used whenever the solar radiation was not reported (Fig. 10).
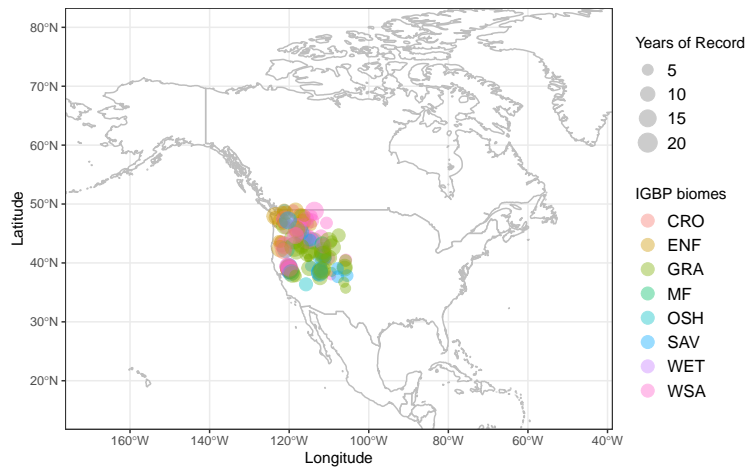
Figure 10. SNOTEL soil moisture and SWE validation sites.

To fit the binary logistic regression used to estimate the probability of snowfall occurrence $p(snow)$, the dataset described by Jennings et al. (2018) was used. Which comprises 11924 stations distributed over the northern hemisphere, adding a total of 17810805 binary observations of snowfall (Fig. 11)
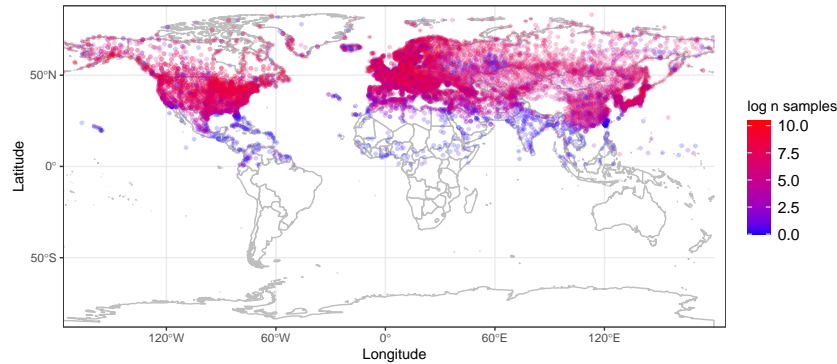
Figure 11. Stations providing snowfall observations from the Jennings et al. (2018) dataset

To test the model capabilities predicting streamflow, with its improvements accounting for slope, small watersheds with areas between 5 and 2000 km^2 located in the mountain regions of Canada and the USA were selected from the global GSIM database (Do et al., 2018) due to the quality of the available forcing data over these regions. The GSIM database provides curated streamflow data from multiple sources and geographic watershed boundaries (Fig. 12). Only watersheds with natural cover higher than 90% and streamflow data covering at least 10 years since 1980 were subset (Table A5), resulting in 15963 station-years. Here, the separation surface runoff/ baseflow was done following the method described by Ladson et al. (2013).
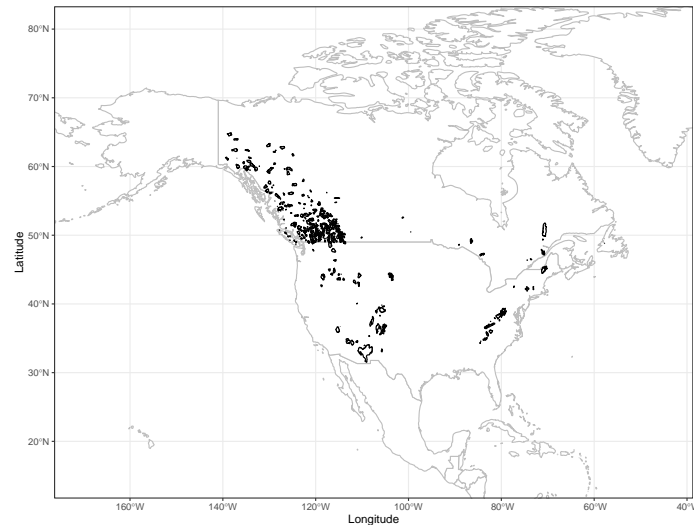
Figure 12. GSIM watersheds for streamflow validation.

24

To evaluate the spatial patterns produced by the model with ~~long term~~ long-term data, hydro-meteorological and soil moisture measurements from the Rietholzbach Research Catchment were used. These datasets are publicly available ~~,~~ and described by Seneviratne et al. (2012); Hirschi et al. (2017). While, to test the model in regions ~~were~~ where the rainfall/runoff response is mainly dominated by subsurface flow (Crespo et al., 2011; Correa et al., 2020), hydro-meteorological data from the tropical Andes, compiled by Ochoa-Tocachi et al. (2018) was used.

5.3 Soil physical properties and Terrain

To calibrate the pedotransfer functions which compute field capacity (θ_{33}) and wilting point (θ_{1500}) a dataset containing data on water retention, texture, organic matter content (SOM), and bulk density was compiled from the U.S Natural Resources Conservation services through the 'soilDB' R-Package (Skovlin and Roecker, 2018), and the 'Wosis' databases (Batjes et al., 2020). Both databases have global coverage and resulted in a total of 68567 usable samples [1] (at least one of the response variables (θ_{fc} or θ_{wp}) and all the predictors) out of 324380 (Fig. 13).

(a) Probability density (b) Soil organic matter
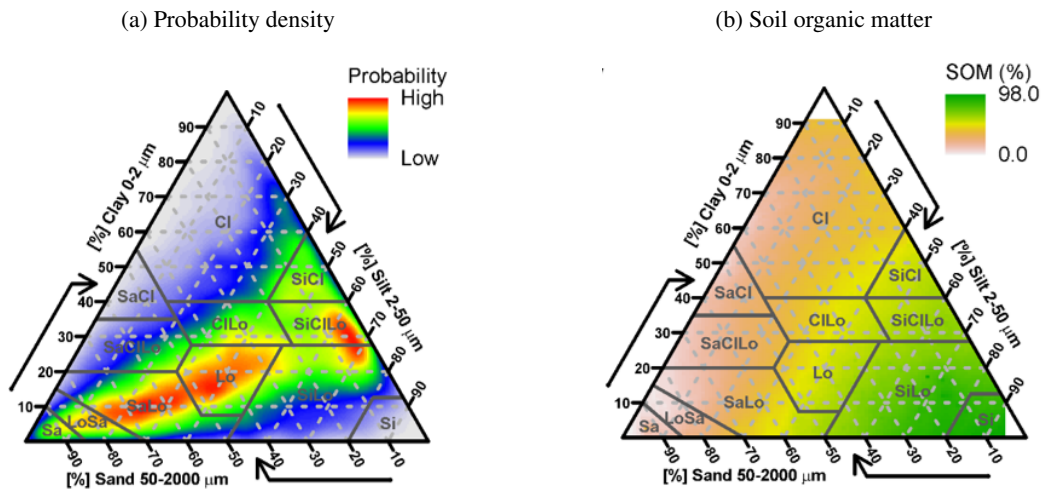
Figure 13. θ_{fc} and θ_{wp} measurements used to calibrate the pedotransfer functions. (a) Probability density of the soil samples according their textural classes. (b) Average soil organic matter content of the samples per textural class.

While, to optimize the functions to estimate soil moisture at saturation (θ_{sat}) and saturated hydraulic conductivity (K_{sat}) data was gathered from the HYBRAS (Ottoni et al., 2018), the SWIG (Rahmati et al., 2018), the UNSODA (Leij et al., 1996) and the Florida University (IFAS, 2007) datasets, for a total of 9346 usable samples out of 15160 (Fig. 14).

---

[1] ~~At least one of the response variables (θ_{fc} or θ_{wp}) and all the predictors~~

(a) Probability density   (b) Soil organic matter
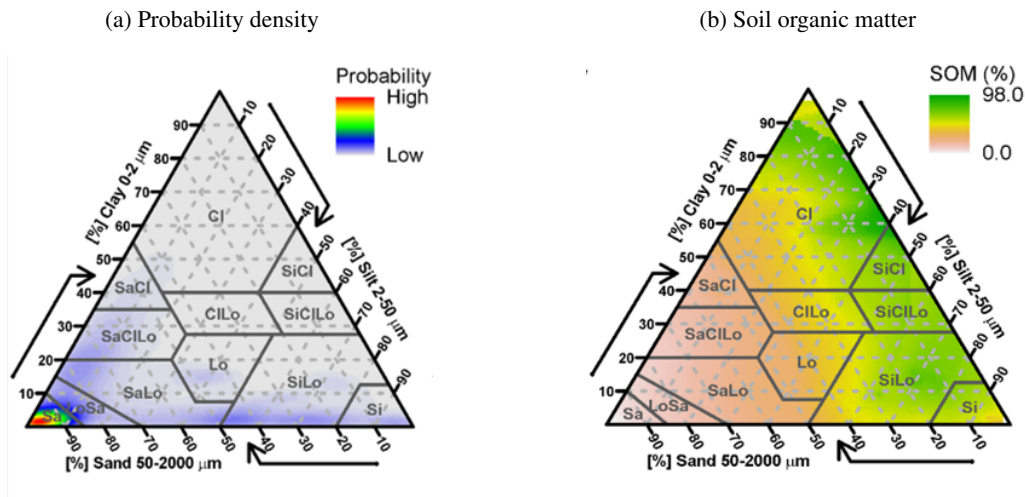
Figure 14. $Ksat$ and θ_{sat} measurements used to calibrate the pedotransfer functions. (a) Probability density of the samples according to their textural classes. (b) Average soil organic matter content of the samples per textural class.

To test the model in the EC sites, soil physical properties ~~abovementioned~~ above-mentioned were retrieved from the Soil-Grids.org dataset (Hengl et al., 2017), while the 'soilDB' R-Package (Skovlin and Roecker, 2018) was used to retrieve soil data at SNOTEL sites.

Slope, slope orientation (aspect), and upslope area were computed using the TauDEM software (Tarboton, 2016) ~~at the~~ ~~Imperial College high performance computing facility (HPC),~~ from the global SRTM digital elevation model resampled to 250m (Jarvis et al., 2008).

5.4 Remote sensing

To calibrate the functions ~~which~~ that calculate the snow cover fraction, and the snow cover effect on the albedo, data from the MODIS MOD10A1 500m-daily product (Hall et al., 2016) was compared against 15 years (2001-2015) of daily data from the 315 SNOTEL stations described previously in this section (Fig. 9).

Information on the biome classification, used to interpret the data, was gathered from the simple typology defined by the International Geosphere-Biosphere Programme (IGBP), available as a MODIS product (MOD12Q1) (Friedl et al., 2019).

To assess the spatial patterns of evapotranspiration in selected small watersheds, the SEBAL algorithm (Bastiaanssen et al., 1998a, b), implemented in Google Earth Engine (GEE) by Laipelt et al. (2021), was used with Landsat 5 atmospherically corrected surface reflectances from 1994-2007 and Landsat 8 from 2014.

To propose a reasonable assumption for the duration of a precipitation event, the global hourly precipitation GsMAP dataset was used. This dataset has 0.1° of resolution and was built using retrievals from NASA's satellite constellation, including infrared, microwave and radar sensors (20 sensors), merged and corrected with NOAA's ground stations (Mega et al., 2014;

Yamamoto and Shige, 2015). Since the ~~gauges~~ gauge count is also available within the dataset, only pixels with 3 or more gauges were used to extract and analyse the hourly data using GEE ~~(Fig. ??)~~.

~~Average number of gauges/pixel used to adjust the RS observations.~~

5.5 Spatially distributed forcing

For the global simulations at 5km of resolution, monthly precipitation data from Beck et al. (2019) was resampled and subset to 2010-2016, air temperature was obtained from the Terraclim dataset (Abatzoglou et al., 2018), together with the solar radiation produced by Ryu et al. (2018), which uses MODIS atmospheric and albedo retrievals as some of the inputs.

For regional simulations (e.g north America), 1km-resolution, temperature and precipitation from CHELSA (Karger et al., 2017) were used, while the solar radiation from Ryu et al. (2018) was downscaled using the theoretical effects of terrain described in Section (2.1.1). Elevation datasets at 1km and 5km resolution used in the respective runs were obtained from Amatulli et al. (2018). While the soil data was resampled from the global 250m SoilGrids dataset (Hengl et al., 2017) (sand, clay, organic matter, coarse fraction, and bulk density). The soil depth/thickness was averaged between SoilGrids and the Pelletier et al. (2016) datasets.

6 ~~Methods: Simulation protocol and Performance evaluation~~

~~The SPLASH model was run at the individual sites located on mountain ecosystems (Figs. **??** and 10) with their entire daily time-series of meteorological measurements. Due to the different variables measured by the different networks of monitoring, the performance evaluation, with the pooled data, was done separately by networks. The statistics used for the evaluation were the determination coefficient (R^2), the root mean squared error (RMSE), bias and the slope of the regression observations simulations. To evaluate the seasonal patterns of fluxes/storages, all the results were aggregated as daily means and grouped by climate zone using the Köppen–Geiger climate classification system (Beck et al., 2018). Only direct measurements were used for the performance evaluations, while some indirect observations were estimated, using the variation with previous-day observations, to visualize seasonal patterns of some fluxes (e.g. Sf and Sm_e). To complement the analysis and interpretation of the results, simulations with the 3-layer variable infiltration capacity model (VIC-3L) (Liang et al., 1996; Liang and Xie, 2001) were run using the same inputs and included alongside the results from SPLASH. The vegetation and soil parameters required by the VIC-3L simulations were extracted at the site locations from Schaperow and Li (2020). Extra forcing data required by the VIC-3L, like wind speed and vapour pressure, not measured at the SNOTEL sites, was extracted from the daily, high-resolution GRIDMET (Abatzoglou, 2013) and DAYMET (Thornton et al., 2020) datasets respectively. Since some quantities computed by SPLASH are not standard outputs of the VIC-3L model (e.g. H_N^+ and C_n), some calculations were applied to obtain comparable outputs (Appendix A3.1). To compare seasonal patterns of soil moisture a relative moisture content was calculated with the observations and results from SPLASH, in the same way as the~~

525 $$\Theta = \frac{W_n - W_{pwp}}{W_{sat} - W_{pwp}}$$

6 Results

6.1 Fitting/optimization results

6.1.1 Net longwave radiation functions

Quadratic equations were the best fit for both, incoming and outgoing longwave radiation during clear-sky conditions, improving noticeably the predictions for temperatures below $0°C$, particularly useful for regions at high elevations (Figs. 15a and 15c). The net longwave equation, resulting from algebraically subtracting $LW_{IN} - LW_{OUT}$, showed a very small quadratic

545 coefficient, which was neglected to adopt a simpler linear equation (Fig. 15c).

---

[1] ratio $Positives\,correctly\,classified/Total\,positives$
[1] ratio $Negatives\,incorrectly\,classified/Total\,negatives$

(a) Incoming longwave radiation

(b) Outgoing longwave radiation

(c) Net longwave radiation
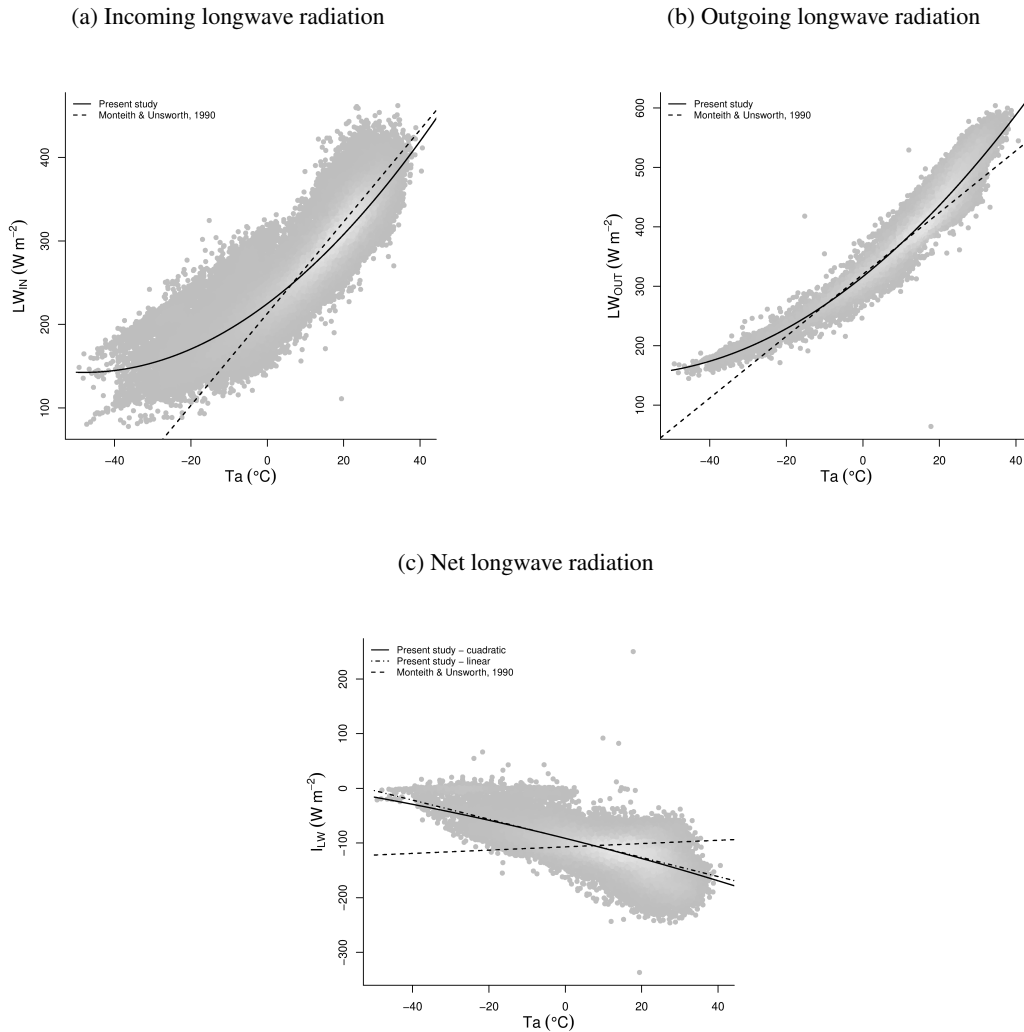
Figure 15. Clear-sky longwave radiation as a function of air temperature. (a) Clear-sky incoming longwave radiation. (b) Clear-sky outgoing longwave radiation. (c) Clear-sky Net longwave radiation.

6.1.2 Snowfall probability

The performance of the snowfall occurrence calculation resulted in an AUC of 0.97 (Fig. 16), which considering a maximum value of 1.0, suggests this method is highly accurate.
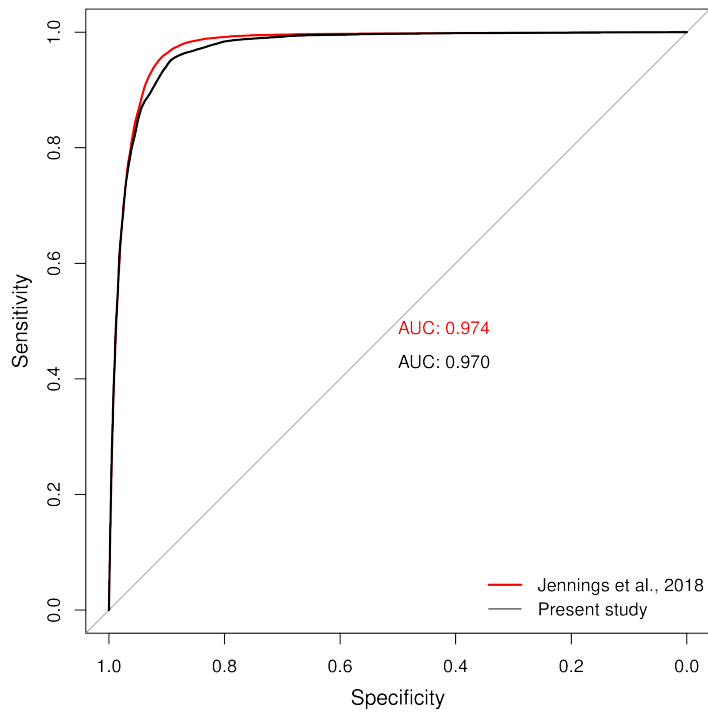
Figure 16. Evaluation of the predicted snowfall probability using a ROC curve.

6.1.3 Snow cover fraction and Snow-albedo correction

550 The simple hyperbolic function used to describe the response of the snow cover fraction to the size of the snowpack suggests that the inflection starts when the SWE reaches 140mm, and most of the variation in snow cover (up to 80%) happens in the first 1000mm of SWE. Moreover, the standard deviations of SWE aggregated by biomes show that in the sampled period values higher than 1000 mm are uncommon (Fig. 17a).

The snow ageing function suggests that a reduction of about 50% of the albedo can happen in the first 10 days without new
555 snow falling and the lowest albedo can reach 0.4 (Fig. 32b).

30

(a) Snow cover fraction

(b) Snow ageing
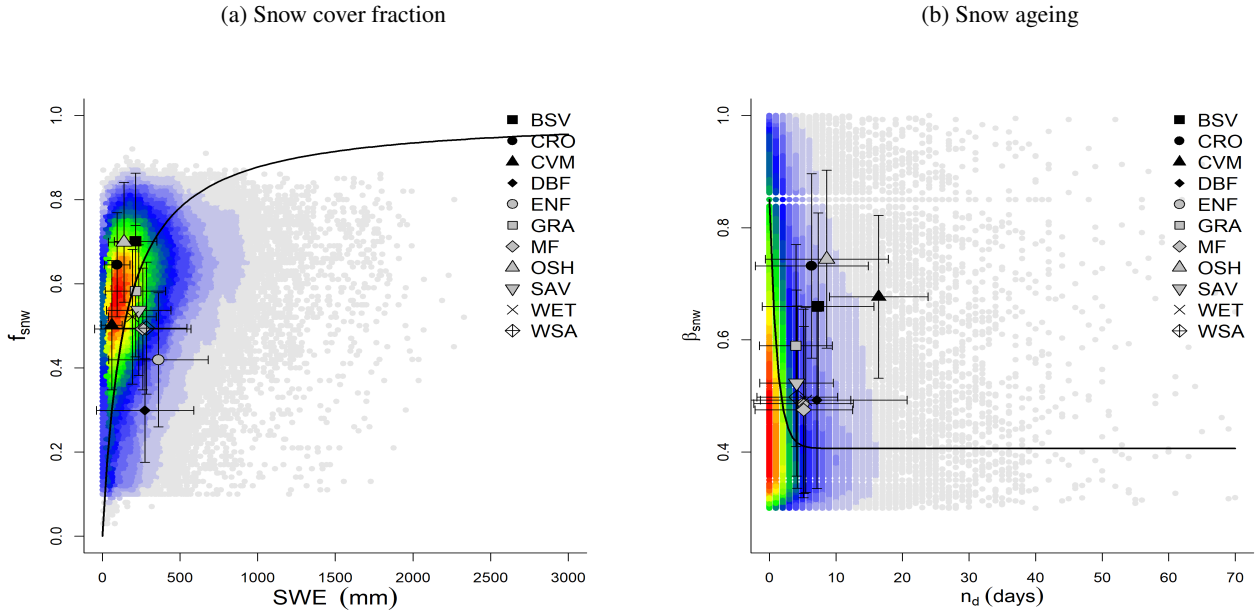
Figure 17. Ground-based observations of snow against satellite retrievals. The color scale shows point density; red indicates higher density. (a) Daily snow cover fraction from MODIS (f_{snw}) vs. daily SNOTEL SWE. The black line shows the optimized Eq.(27). (b) MODIS albedo (β_{snw}) when the snow cover exceeds 70% vs. Days without fresh snowfall (n_d) from the daily SNOTEL SWE. The black line shows the optimized Eq.(26).

6.1.4 Pedotransfer functions

From the models tested (Table 2), the non-linear equations from Balland et al. (2008), which were fit to the largest dataset outperformed the other models. Further optimization of these equations (Eq. A25a,A25b,A25c) using the full dataset employed for this evaluation yielded a slight improvement of around 10% for field capacity (θ_{33}) and saturation (θ_{sat}) (Fig. 20). The new parameters are detailed in Table A1.

$$\theta_{1500} = \theta_{33} \left(c_{wp} + (d_{wp} - c_{wp}) \, CLAY^{0.5} \right) \tag{67a}$$

$$\theta_{33} = \theta_{sat} \left(c_{fc} + (d_{fc} - c_{fc}) \, CLAY^{0.5} \right) e^{\frac{a_{fc} SAND - b_{fc} SOM}{\theta_{sat}}} \tag{67b}$$

$$\theta_{sat} = 1 - \frac{\rho_b}{\rho_p} \tag{67c}$$

$$K_{sat} = 10^{a_{ks} + b_{ks} \, log_{10}(\rho_p - \rho_b) + c_{ks} SAND} \tag{67d}$$

Were θ_{1500} is wilting point (water held at 1500kPa), θ_{33} is field capacity (water held at 33kPa), θ_{sat} is saturation, K_{sat} the saturated hydraulic conductivity, and, SAND, CLAY and SOM refer to sand, clay and organic matter contents (%). a, b, c are constants with the subscripts referring to wilting point, field capacity or hydraulic saturated conductivity respectively, ρ_b is the

bulk density, and ρ_p is the particle density, calculated as follows (Balland et al., 2008):

$$\rho_p = \frac{1}{\frac{SOM}{1.3} + \frac{1-SOM}{2.65}} \tag{68}$$

Table 3. Updated parameters for the Balland et al. (2008) PTFs

	a_x	b_x	c_x	d_x
θ_{1500}	−	−	0.2018	0.7809
θ_{33}	-0.0547	-0.0010	0.4760	0.9402
K_{sat}	-2.6539	3.0924	4.2146	−
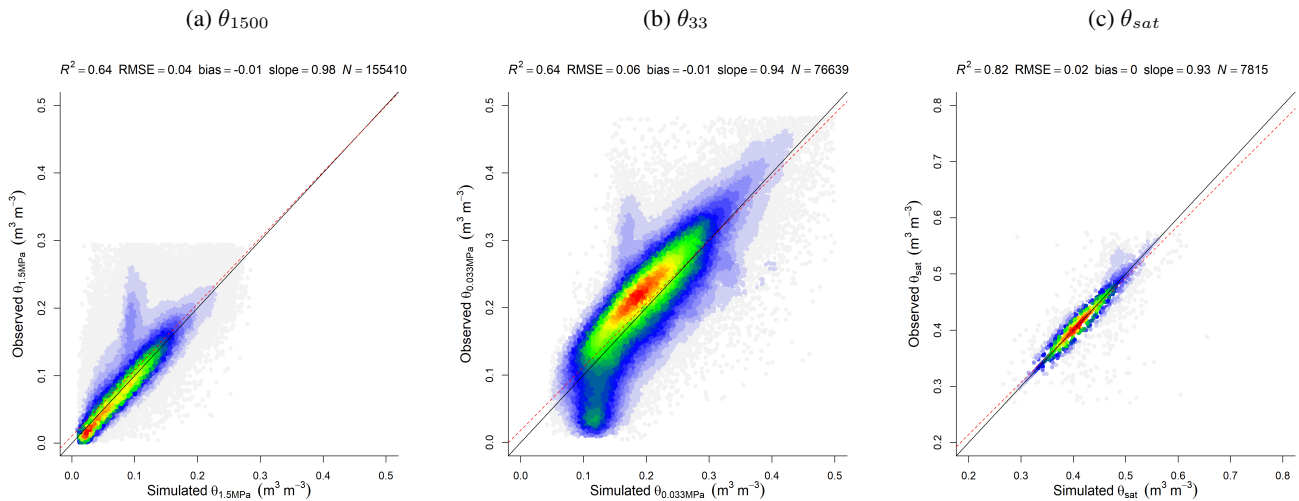
Figure 18. Correlation of observed and simulated values of soil hydro-physical properties. The color scale shows point density; red indicates higher density. (a) Permanent wilting point (θ_{1500}). (b) Field capacity (θ_{33}). (c) Soil porosity or saturation point (θ_{sat}).

K_{sat} estimated by the Saxton and Rawls (2006) PFT was the best performing model, however, it leads to unrealistic values when the drainable porosity ($\theta_{sat} - \theta_{33}$) is relatively high. Thus a simple saturating curve was adopted here, which yields similar estimations to Saxton and Rawls (2006) at the lower end of the drainable porosity but it flattens at a fitted K_{sat} maximum of 623 $mm\,h^{-1}$.

$R^2 = 0.42$ RMSE = 207.14 bias = -5.04 slope = 0.97 $N = 18066$
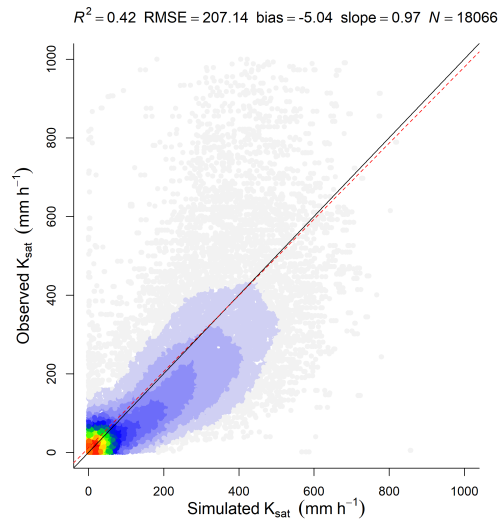
Figure 19. Correlation of observed and simulated values of saturated hydraulic conductivity K_{sat}. The color scale shows point density; red indicates higher density.

6.2 Fluxes

6.2.1 Net longwave radiation

The evaluation of I_{LW} shows the values clustering around -100 and 0 $W\,m^2$, nonetheless the simple linear model was able to explain 70% of the variance with a very low bias (-0.11) (Fig. 20).

$R^2 = 0.7$ RMSE = 23.13 bias = -0.11 slope = 1.01 $N = 457157$
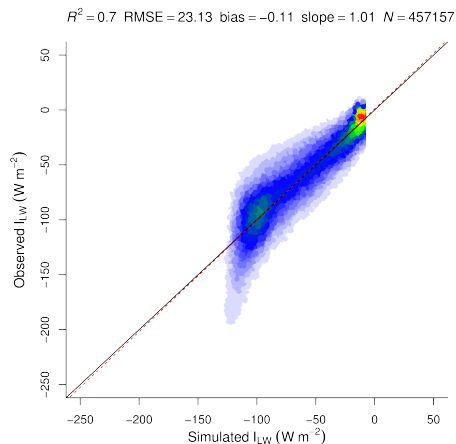
Figure 20. Correlation of observed and simulated values of I_{LW}, with data from all the sites pooled. The color scale shows point density; red indicates higher density.

33

6.2.2 Daytime Net Radiation

The Daytime net radiation, or positive net radiation was compared against 87 EC sites distributed over mountain regions covering several biomes. The comparison, using all the data pooled at daily resolution shows that the model is able to explain more than 70% of the observations' variance with a very small bias (Fig. 21). The evaluation also shows that the highest overestimation happens in ecosystems with sparse vegetation (BSV biome).

(a) SPLASHv1.0 daytime net radiation

$R^2 = 0.88$ RMSE $= 2.291$ bias $= 0.841$ slope $= 0.949$ $N = 559569$

(b) SPLASHv2.0 daytime net radiation

$R^2 = 0.87$ RMSE $= 2.21$ bias $= 0.021$ slope $= 0.999$ $N = 559569$
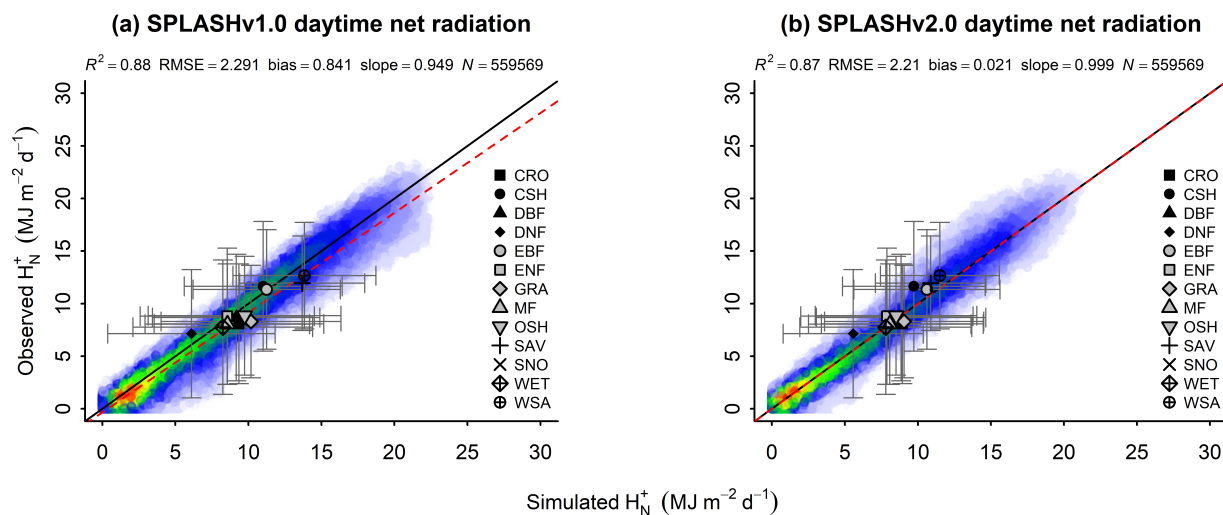
Figure 21. Correlation of observed and simulated values of H_N^+ with data from all the sites pooled. The color scale shows point density; red indicates higher density. (a) simulations with SPLASH v1.0. (b) simulations with SPLASH v2.0.

The seasonal patterns of H_N^+ averaged by climate zone show a classic bell-shaped curve, peaking during the summer months, the greater deviations from the mean appear in climate zones with no dry season (Cfb, Dfc). SPLASH simulations ~~are reproducing~~ reproduce the observations more closely than the VIC results in most of the climate zones, noticeably outperforming VIC in climate zones with dry ~~summer~~ summers (Csa, Csb). SPLASH overestimation ~~happen~~ happens primarily in cold deserts during summer months (BWk), while underestimation ~~are~~ is noticeable in temperate zones with no dry season (Cfa) and in the hot steppe (BSh), both during summer months~~as well~~. (Fig 22).

34
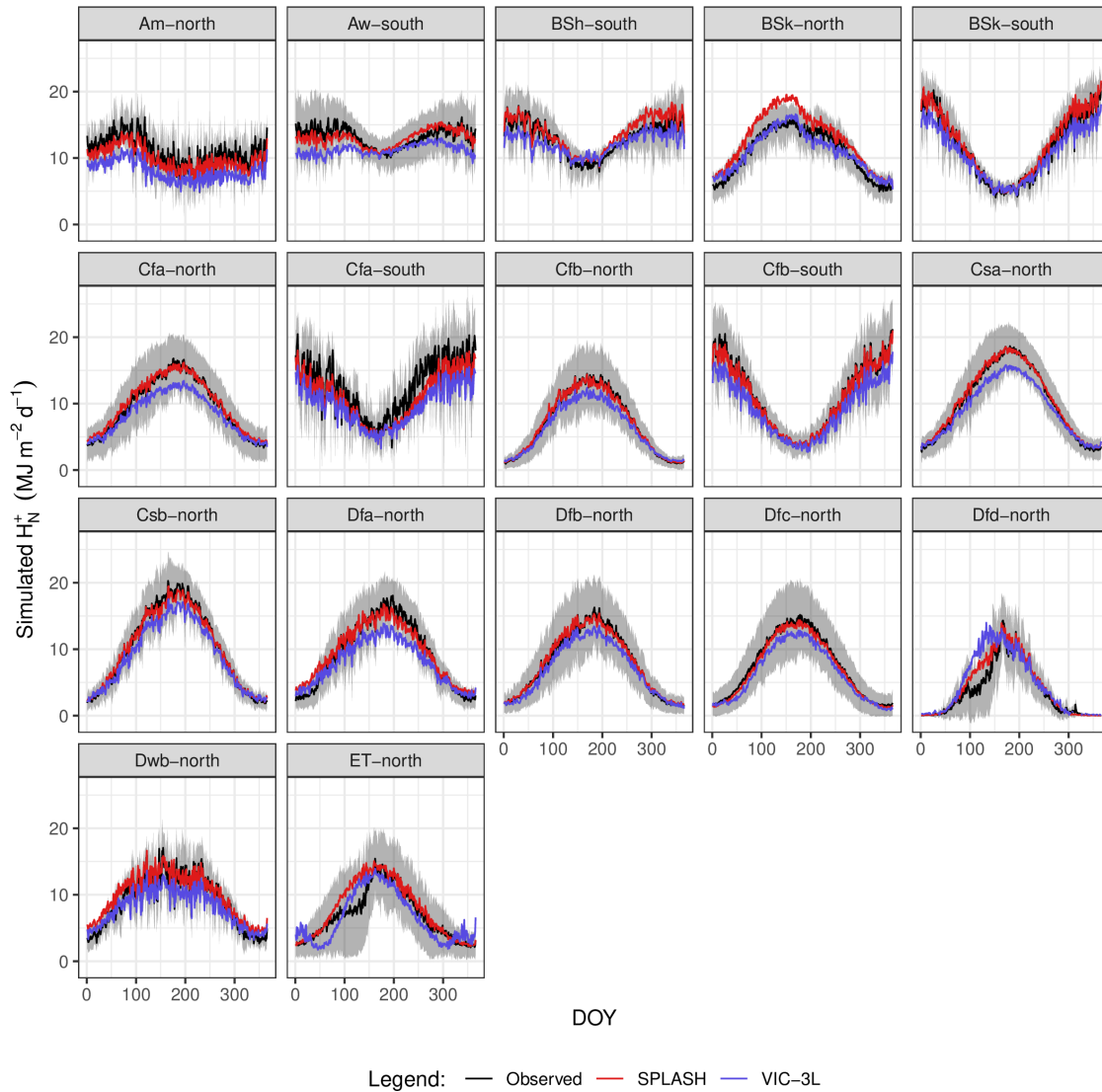
Figure 22. Mean seasonal cycle of H_N^+ per climate zone. The gray areas show one SD from the observed mean. Climate zones are described in table (A2).

6.2.3 Evapotranspiration

The performance evaluation of E_n^a using the data of all the EC stations ~~located in the mountains~~ shows the model reproducing ~~44~~50% of the variance of daily observations with a small bias and the slope of the regression of observations simulations equal to ~~0.9~~0.072. The standard deviation of the data aggregated by biome, in the observation axis, shows that at daily timestep E_n^a is highly variable, and there is no clear difference between woody and herbaceous ecosystems. The evaluation shows a greater

35

underestimation for evergreen broadleaf forests (EBF), while the greater overestimation happens in deciduous broadleaf forests (DBF). Furthermore the lowest E_n^a is shown by ecosystems with sparse vegetation (~~BSV~~OSH) and the highest by EBF (Fig. 23).

(a) SPLASHv1.0 daily evapotranspiration

$R^2 = 0.4$ RMSE = 1.422 bias = 0.482 slope = 0.631 $N = 504782$

(b) SPLASHv2.0 daily evapotranspiration

$R^2 = 0.5$ RMSE = 1.164 bias = -0.072 slope = 0.775 $N = 504782$

Figure 23. Correlation of observed and simulated values of E_n^a with data from all the sites pooled. The color scale shows point density; red indicates higher density. (a) simulations with SPLASH v1.0. (b) simulations with SPLASH v2.0.

The seasonal patterns of E_n^a broadly follow the pattern of H_N^+ in zones with no water limitations (Cf* and Cf* types), the polar tundra exhibits similar patterns but with a higher difference between summer and winter months. While arid zones (BS* and BW* types) show a very different pattern compared to H_N^+. SPLASH simulations correctly reproduced most of the seasonal patterns, and for certain climate zones (BSk, Csb, Dsc) outperformed VIC simulations. Although SPLASH captures the overall seasonal patterns, it overestimates E_n^a in Dsc sites, while, similarly to the VIC results, it underestimates E_n^a in the polar tundra (ET) and in the Cfb sites in the southern hemisphere (Fig. 24).

Figure 24. Mean seasonal cycle of E_n^a per climate zone. The gray areas show one SD from the observed mean. Climate zones are described in table (A2).

At a global scale, SPLASH produces major spatial patterns that roughly follow the distribution of the Köppen-Geiger climate zones. In northern latitudes ~~like Alaska~~ it overestimates E_n^a during summer months, nonetheless, it outperforms VIC-3L which 605   ~~is producing~~ produces high values during winter (Fig. 25).
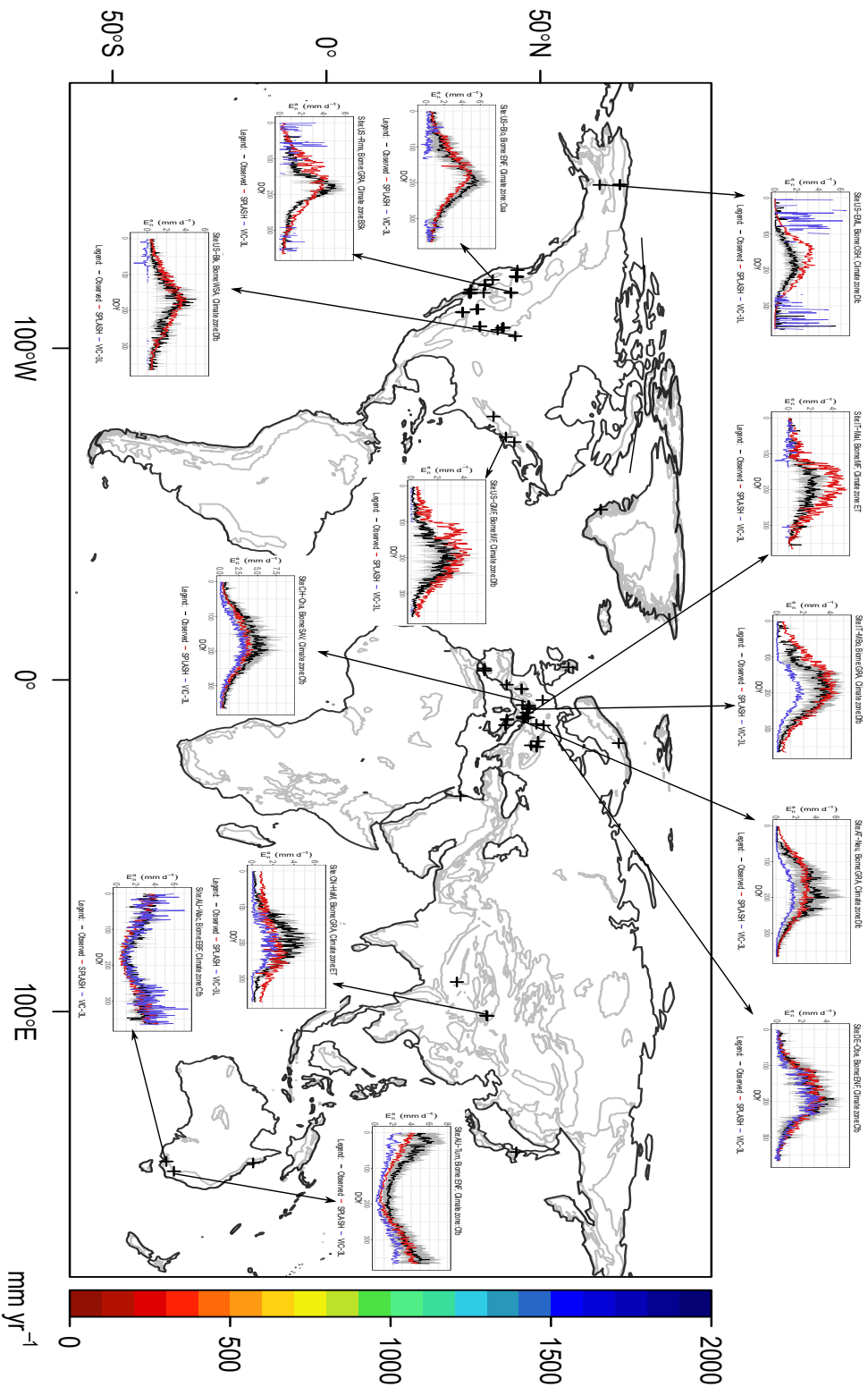
Figure 25. Spatial patterns of mean annual E^a for the period 2010-2016 at 5km resolution along with site-simulation examples from the mountains. Inset plots show seasonal cycles where observations are in black, SPLASH v2.0 simulations are in red and VIC 3L simulations are in blue. The grey areas show one SD from the observed mean.

The simulations, with the long-term data from Rietholzbach, exhibit a good overall agreement with the lysimeter-based observations (Fig. 26e). However, a minor but systematic overestimation happens during the spring months. Here, the spatial patterns produced by SPLASH show higher magnitudes on south-facing slopes, and, at the valley bottom close to the outlet, coinciding with the area where a small forest is present (Seneviratne et al., 2012) (Fig. 43c). These patterns contrast with the spatially distributed LE, calculated from Landsat 5 retrievals, which shows a more uniform LE, except for a few forest patches, where LE spikes (Fig. 26d). Both datasets barely agree over the small forest at the valley bottom.

(a) Slope

(b) Aspect

(c) SPLASH annual Evapotranspiration

(d) SEBAL/Landsat 5 mean LE

(e) Monthly evapotranspiration time series
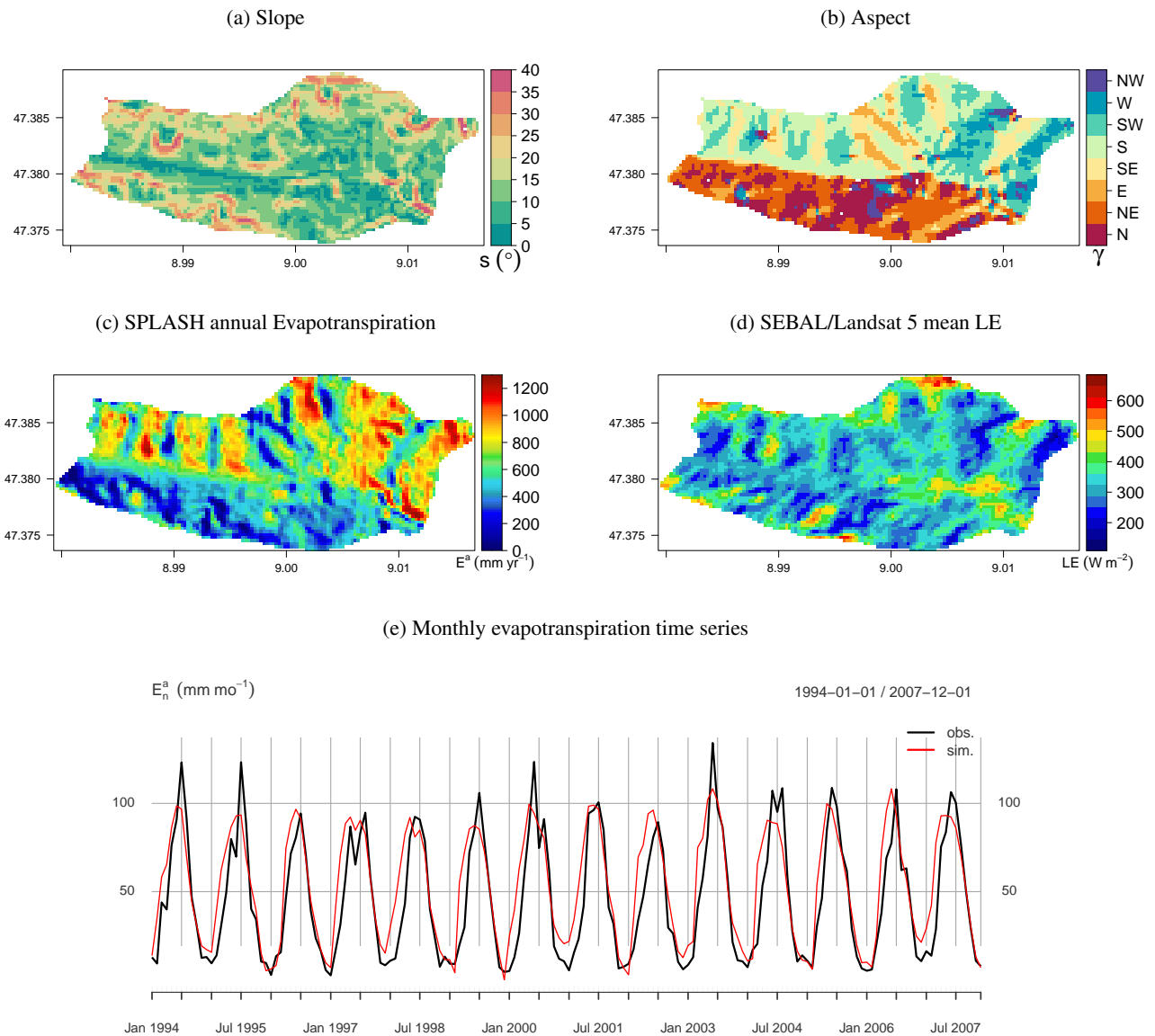
Figure 26. Spatial and temporal patterns of evapotranspiration in a small wet temperate watershed, Rietholzbach - Switzerland. (a) Slope in degrees. (b) Slope orientation, N stands for north, S for south and so on. (c) Mean annual simulated evapotranspiration 1994-2007. (d) Mean instantaneous LE from L5's clear-sky pixels during 1994-2007. (e) Time series of monthly evapotranspiration, simulated and lysimeter-based observations.

In the tropical watershed, the spatial patterns of E_n^a produced by SPLASH (Fig. 27c) show a better agreement with the RS LE than in the temperate watershed, as shown by some emergent coldspots in the northern part of the watershed (Fig. 27e).

Moreover, in both datasets, slopes facing the equator show higher magnitudes compared to flat areas, however, in the SPLASH

615 results, this difference is stronger than in the RS LE estimation.
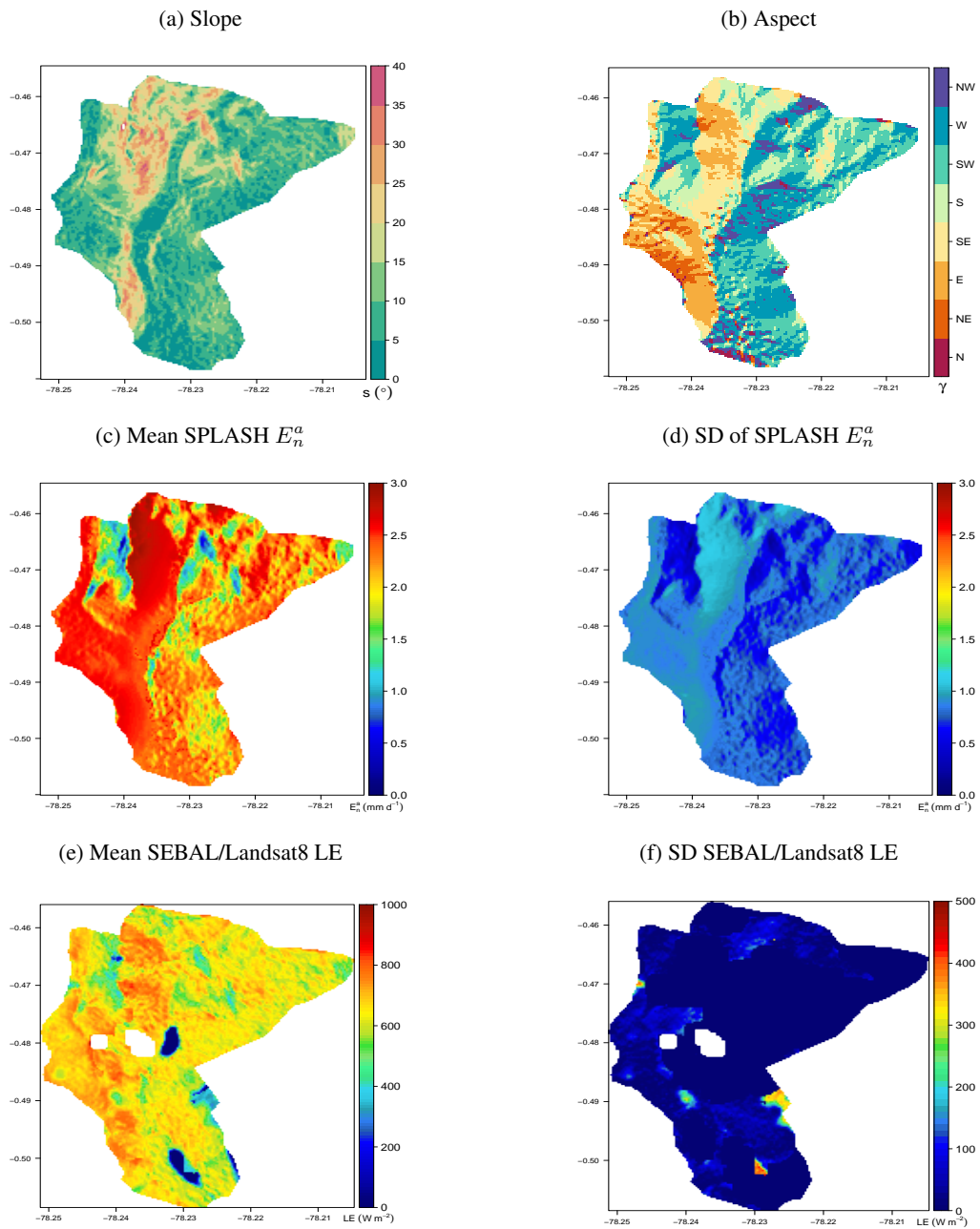
Figure 27. Spatial patterns of daily evapotranspiration in a wet tropical watershed, Jatunhuayco - Ecuador. (a) Slope in degrees. (b) Slope orientation, N stands for north, S for south and so on. (c) Mean daily evapotranspiration during 2014. (d) Standard deviation of the daily evapotranspiration during 2014). (e) Mean instantaneous LE from L8's clear-sky pixels during 2014. (f) Standard deviation of the instantaneous LE from L8's clear-sky pixels during 2014.

6.2.4 Condensation

SPLASH model showed the poorest performance simulating C_n, it was able to capture around ~~10~~18% of the variance, with a bias of ~~-0.621~~0.913. The slope of the regression observations-simulations points to overestimations at high simulated values. Most of the observations seem to cluster in the 0-10 $mm\,yr^{-1}$, the greater underestimation happens in broadleaf evergreen forests while C_n is overestimated in barren/sparse vegetated ecosystems~~28)~~.

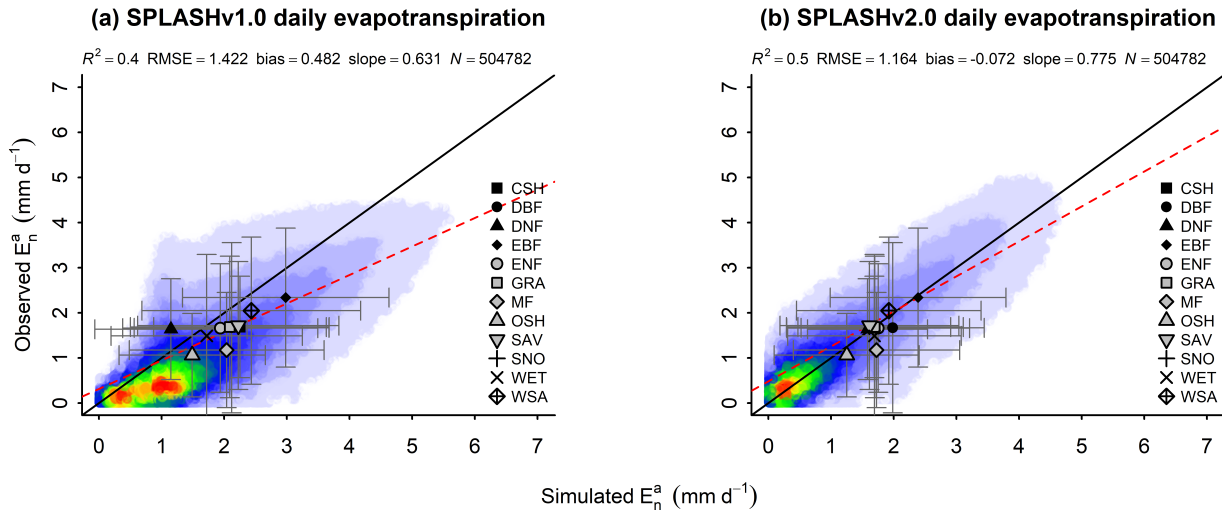**(a) SPLASHv1.0 annual condensation** **(b) SPLASHv2.0 annual condensation**
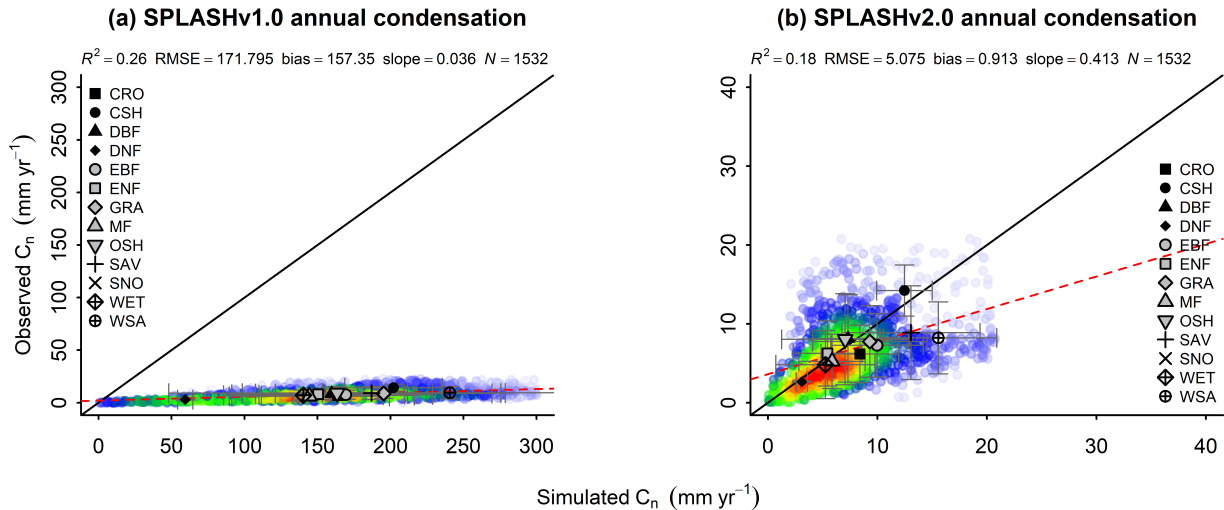
Figure 28. Correlation of observed and simulated values of C_n with data from all the sites pooled. The color scale shows point density; red indicates higher density. (a) simulations with SPLASH v1.0. (b) simulations with SPLASH v2.0.

Just arid climate zones (B* types) showed seasonal patterns of C_n, and potentially important magnitudes, both dimensions captured by SPLASH. However, the SPLASH model is still underestimating C_n in the hot steppe (BSh) and overestimating C_n in the cold steppe and desert (e.g. BSk and BWk). In some climate zones with no apparent seasonal pattern and with random peaks through the year (e.g. Cfc and Dsc) SPLASH model shows a smother prediction, underestimating all the peaks. Compared to the VIC simulations, the SPLASH model seems to reproduce the general patterns more reasonably (Fig. 29).
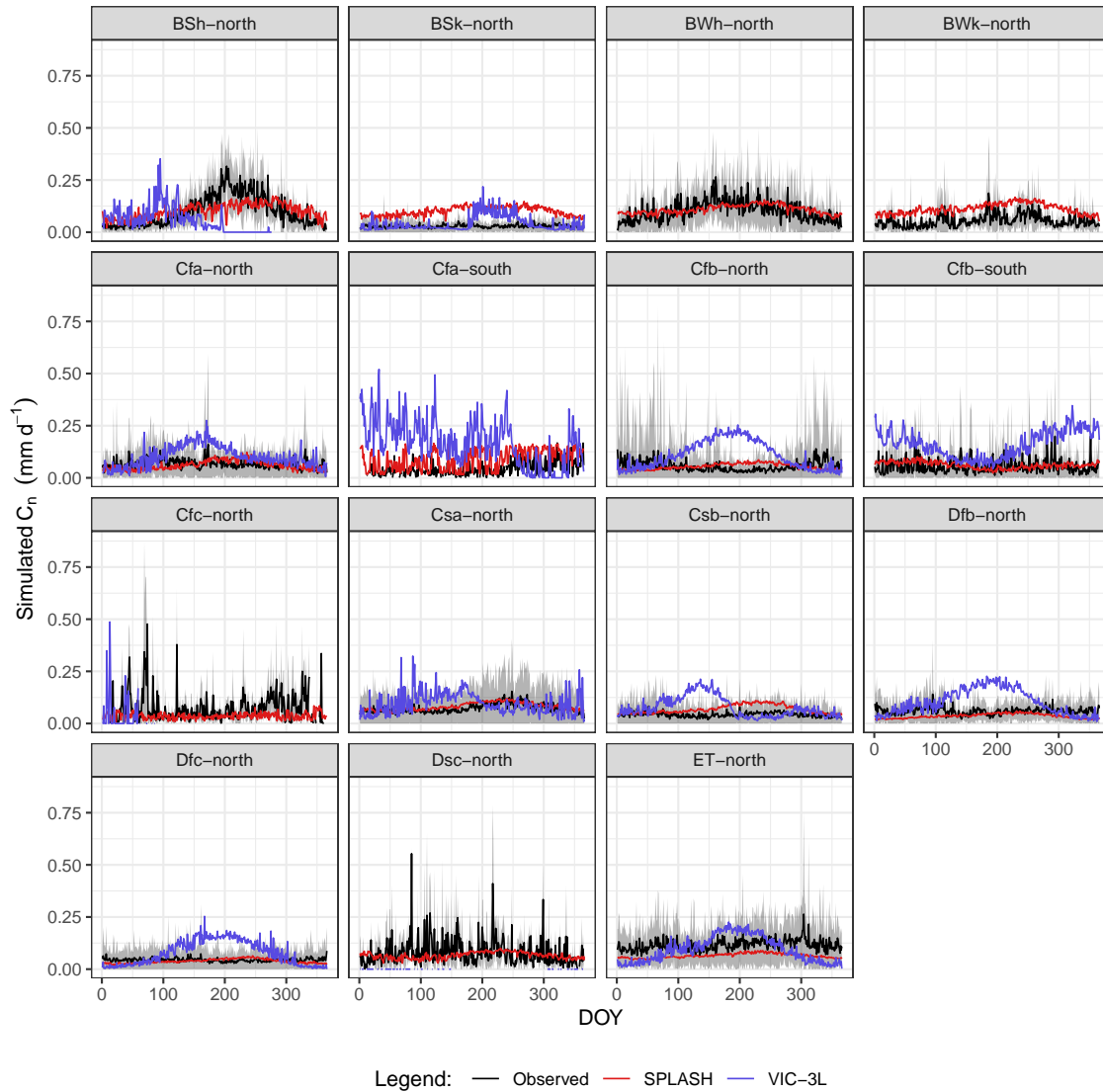
Figure 29. Mean seasonal cycle of C_n per climate zone. The gray areas show one SD from the observed mean. Climate zones are described in table (A2).

6.2.5 Snowfall

The seasonal patterns of Sf show differences in the magnitudes between climate zones with and without dry season only in temperate types (Cfb, Csb), while wet continental (Df*) types did not show noticeable differences with their dry counterparts (Ds*). Arid climates (B*), on the other hand, showed the lowest magnitudes. The patterns simulated by SPLASH match almost

630 perfectly with the observations for all the climate zones, in agreement with the VIC simulations as well. Some underestimation is noticeable at the end of the winter in the wet temperate zone (Cfb) (Fig. 30).
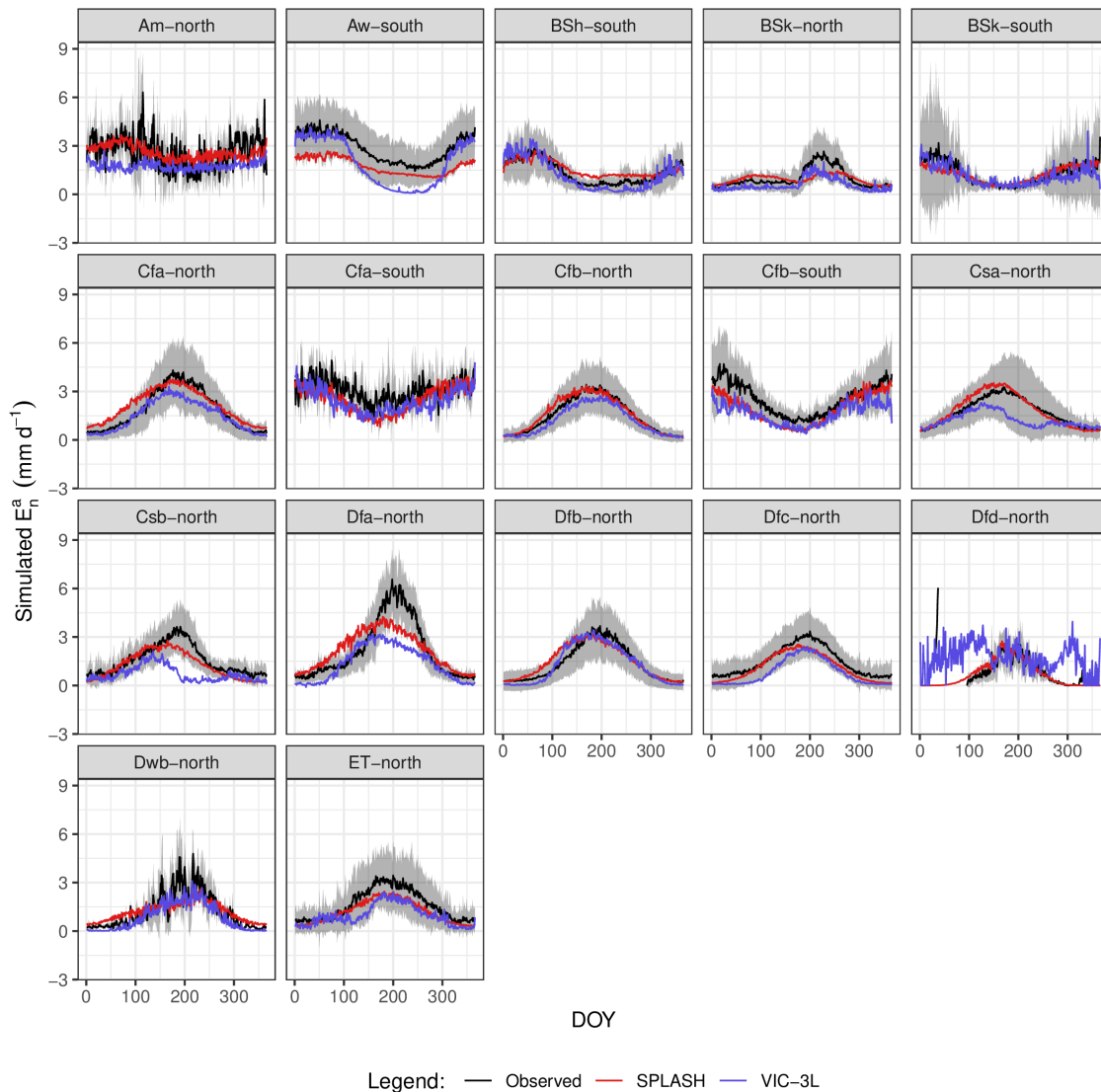

Figure 30. Mean seasonal cycle of Sf per climate zone. The gray areas show one SD from the observed mean. Climate zones are described in table (A2).

6.2.6 Snowmelt

Seasonal patterns of Sm appear more clearly in the continental climate zones (D* types) with an expected peak at the beginning of spring, the other climate zones apparently don't show a general pattern. SPLASH model was able to simulate the start of the

635 melting process in all the climate zones, however, it captures the seasonal pattern only in wet continental climates (Df*), while ~~overestimates~~ overestimating Sm in their dry counterparts (Ds*). Overall the seasonal patterns from SPLASH seem to agree with the simulations better than the results of the VIC model, which shows a temporal lag in the start and peak of the melting period (Fig. 31).

Figure 31. Mean seasonal cycle of Sm per climate zone. The gray areas show one SD from the observed mean. Climate zones are described in table (A2).

6.2.7 Surface Runoff and lateral flow

640   The SPLASH simulations of total streamflow (TSF) ($RO + q_{out}$) in the watersheds were able to explain 71% of the variation while the estimations of surface runoff accounted for 69% of the variation. The bias in both analyses shows a systematic underestimation of this flux, especially at the lower end (Fig. ~~??~~32).

(a) Total Streamflow   (b) Surface Runoff

$R^2 = 0.71$ RMSE $= 395.83$ bias $= -116.01$ slope $= 0.99$ $N = 13406$

$R^2 = 0.69$ RMSE $= 364.24$ bias $= -52.98$ slope $= 0.88$ $N = 13406$
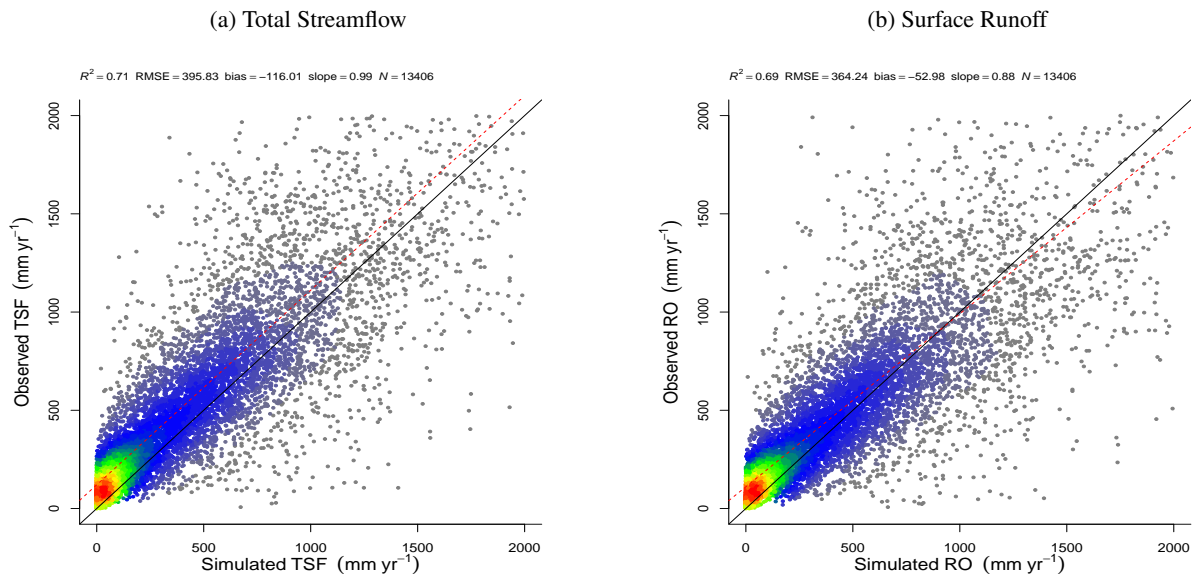
Figure 32. Correlation of observed and simulated values of Discharge with data from all the watersheds pooled. The color scale shows point density; red indicates higher density. (a) Total Streamflow. (b) Surface Runoff

SPLASH simulations of TSF and RO in the same watersheds as VIC showed that although VIC achieved slightly better performance, SPLASH can achieve very similar R^2 values. The slope of simulated vs. observed data suggests that SPLASH, 645   without any local calibration, can reach 80% of the accuracy of VIC calibrated with historical data (Fig. 33).
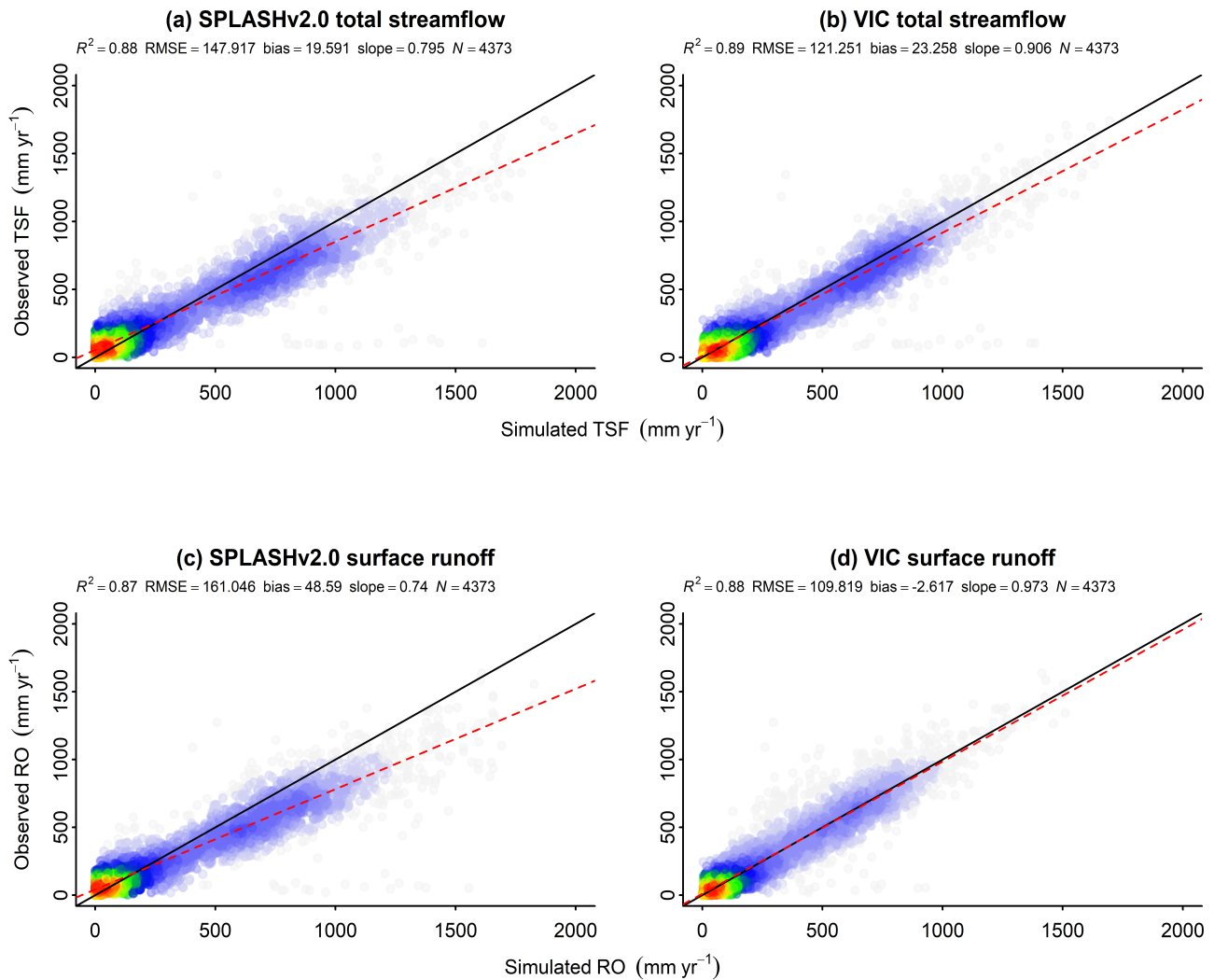
Figure 33. Correlation of observed and simulated values of Discharge with data from all the watersheds pooled. The color scale shows point density; red indicates higher density. (a) Total Streamflow. (b) Surface Runoff

Tracking down the source of the systematic underestimation by analysing in detail the time series of observed and simulated TSF from Rietholzbach, the underestimation appeared greater during winter months when the precipitation is below the average. On the other hand, when the precipitation is peaking, overestimation occurs in some years seemingly without showing any systematic pattern (Fig. 34f).

650   The simulated time series of baseflow index BFI $\left(\frac{q_{out}}{q_{out}+RO}\right)$ roughly follows the temporal dynamics of the observations. Overestimations appear in the winter months due to the underestimations of surface RO during these months (Fig. 34e).

Furthermore, the spatial patterns resulting from the simulation show the runoff is higher in areas surrounding the stream, which emerges from the flux accumulation at the valley bottom (Fig. 34b).

Moreover, the lateral flow is mostly produced in the north-facing slopes and in some areas next to the main stream, upslope from the main outlet. The BFI is close to 1 in most of the watershed, except in areas close to the stream, suggesting that most of the simulated hydrological response is subsurface flow (Fig. 34a).

(a) Mean baseflow index

(b) Spatial patterns of mean annual runoff

(c) Spatial patterns of mean annual baseflow

(d) Time series of precipitation

(e) Time series of monthly baseflow index

(f) Time series of total streamflow
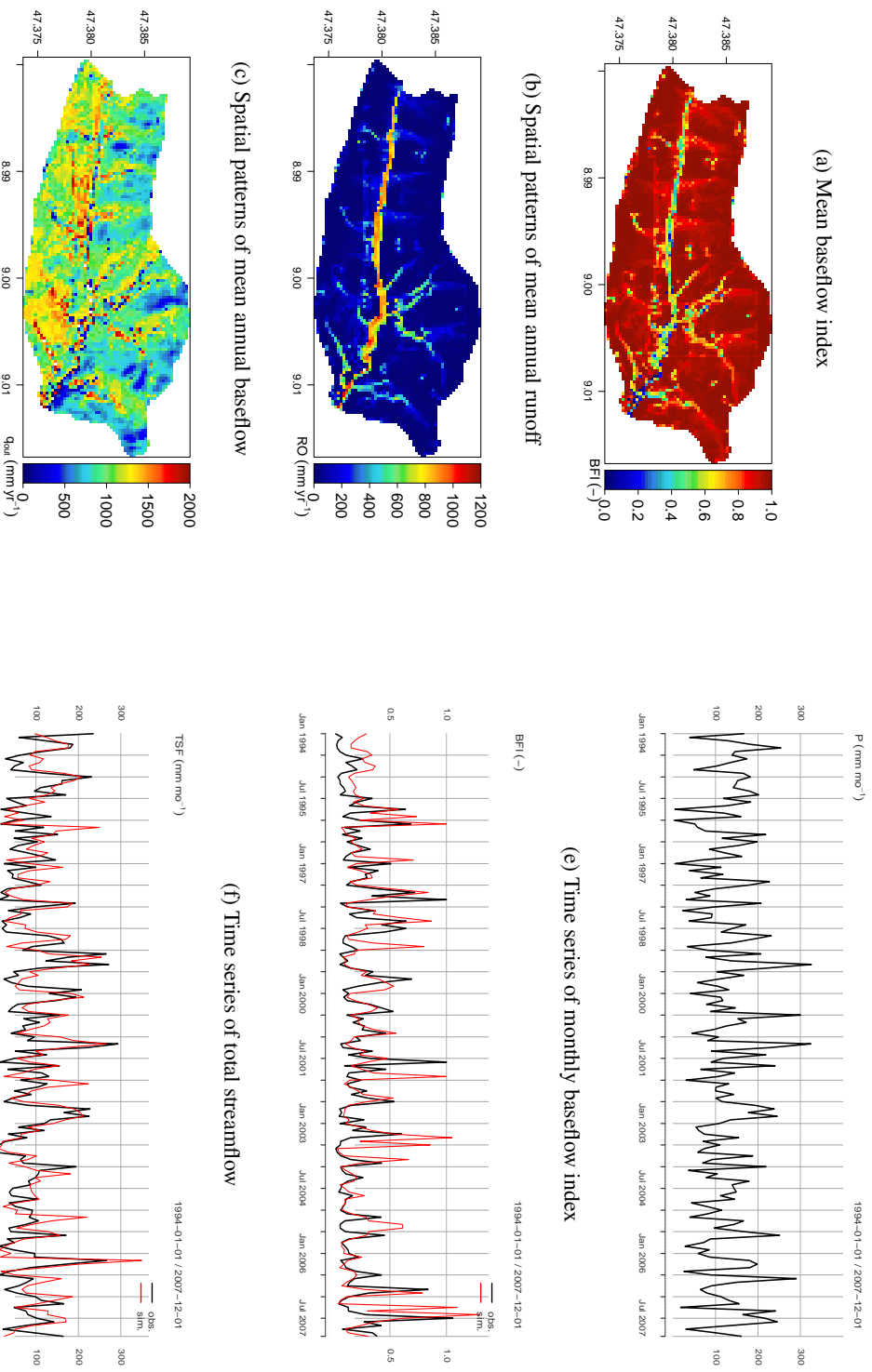
Figure 34. Spatial and temporal patterns of runoff in a small wet temperate watershed, Rietholzbach - Switzerland. (a) Spatial patterns of mean soil water content in the first 2m during 1994-2007. (b) Spatial patterns of mean annual runoff during 1994-2007. (c) Spatial patterns of mean annual baseflow during 1994-2007. (d) Time series of precipitation 1994-2007. (e) Time series of SWC in the first 1m of depth during 1994-2007. (f) Time series of total streamflow during 1994-2007

50

The monthly means of BFI from the long-term data from Rietholzbach suggest that the underestimation of surface RO is indeed systematic and the major discrepancies appear in November and December (Fig. 35).
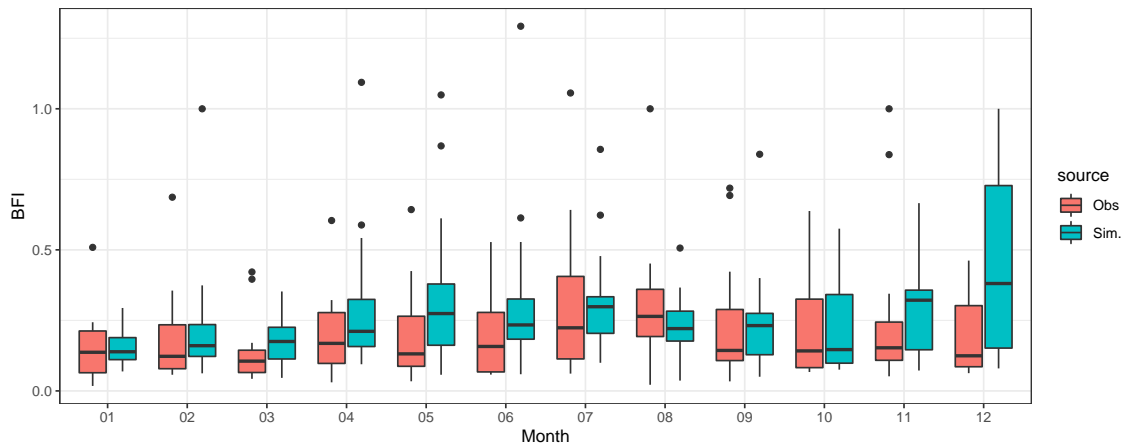
Figure 35. Mean monthly BFI 1994-2007 in a small wet temperate watershed, Rietholzbach - Switzerland for the period 1994-2007

At daily timestep, the results of the simulation in the tropical watershed, show that the performance of SPLASH simulating
660   fast storm response is poor, the model fails in capturing the expected runoff peaks during relatively big storms at daily timescale (Fig. 36e). Nonetheless, the spatial patterns generated by SPLASH in this small watershed, reproduce mostly saturation excess runoff in areas close to the streams (Fig. 47a), while the simulated lateral flow ~~appear~~ appears stable, spatially and over time (Figs. (47c) and (47d)).
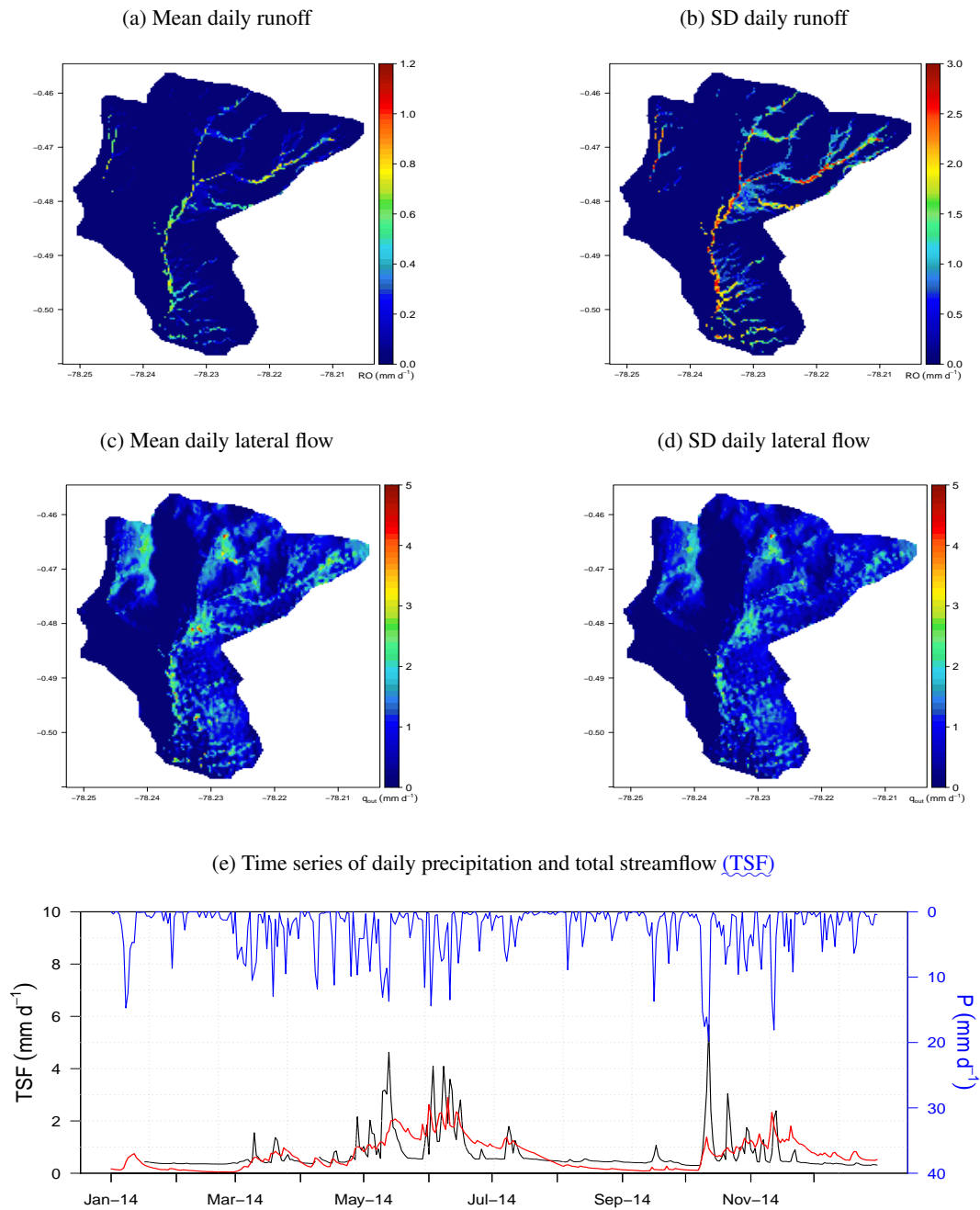
Figure 36. Spatial and temporal patterns of daily fluxes in a tropical small watershed, Jatunhuayco - Ecuador (a) Mean daily runoff during 2014. (b) Standard deviation of the daily runoff in 2014). (c) Mean daily lateral flow during 2014. (d) Standard deviation of the daily lateral flow during 2014 (e) Time series of daily precipitation and total streamflow during 2014

6.3 Storages

6.3.1 Snow water equivalent

The simple formulations proposed to simulate SWE were able to explain 88% of the observed variation ~~across~~ 127 SNOTEL sites located in mountain regions~~, the~~ . The mean value of the observations aggregated by biome ~~, show the~~ shows that SWE ~~storage~~ in evergreen needle-leaf forests (ENF) is the largest among the biomes, while the lowest value was from open/deciduous canopies (OSH,DBF). The bias suggests that SPLASH is underestimating SWE at low values, however, the huge variation of the observations in all ~~the biomes suggest~~ biomes suggests that the differences are not significant (Fig. 37).
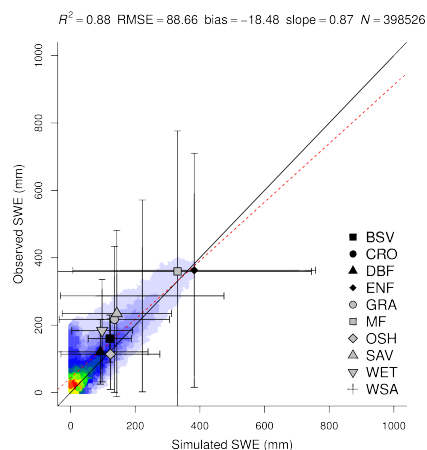
Figure 37. Correlation of observed and simulated values of daily SWE, values of all sites pooled. The color scale shows point density; red indicates higher density.

The seasonal patterns of SWE depict the well-known bell-shaped curve during winter with great deviations from the seasonal mean. Here, the sites in the temperate climate zones without dry season showed the greatest deviation (Cfb). SPLASH model was able to reproduce the seasonal patterns in all the climate zones. It underestimates, to different degrees, the averages within the range of the observations, which contrasts with the overestimation of the VIC simulations. Nonetheless, SPLASH captures almost perfectly the length of the snow-covered period, failing only in the Cfb zone, where it overestimates SWE during the melting period, here VIC outperforms SPLASH (Fig. 38).
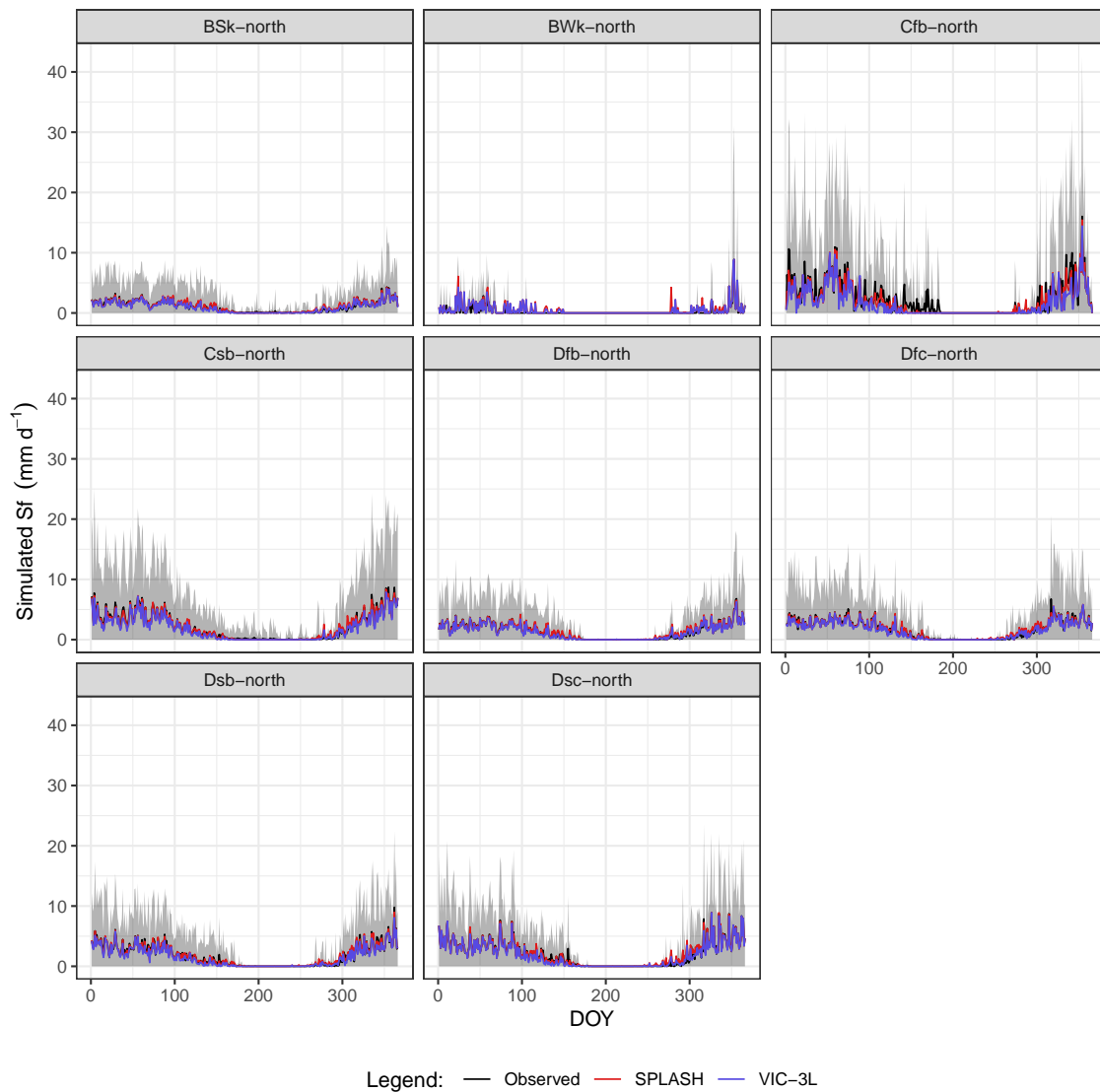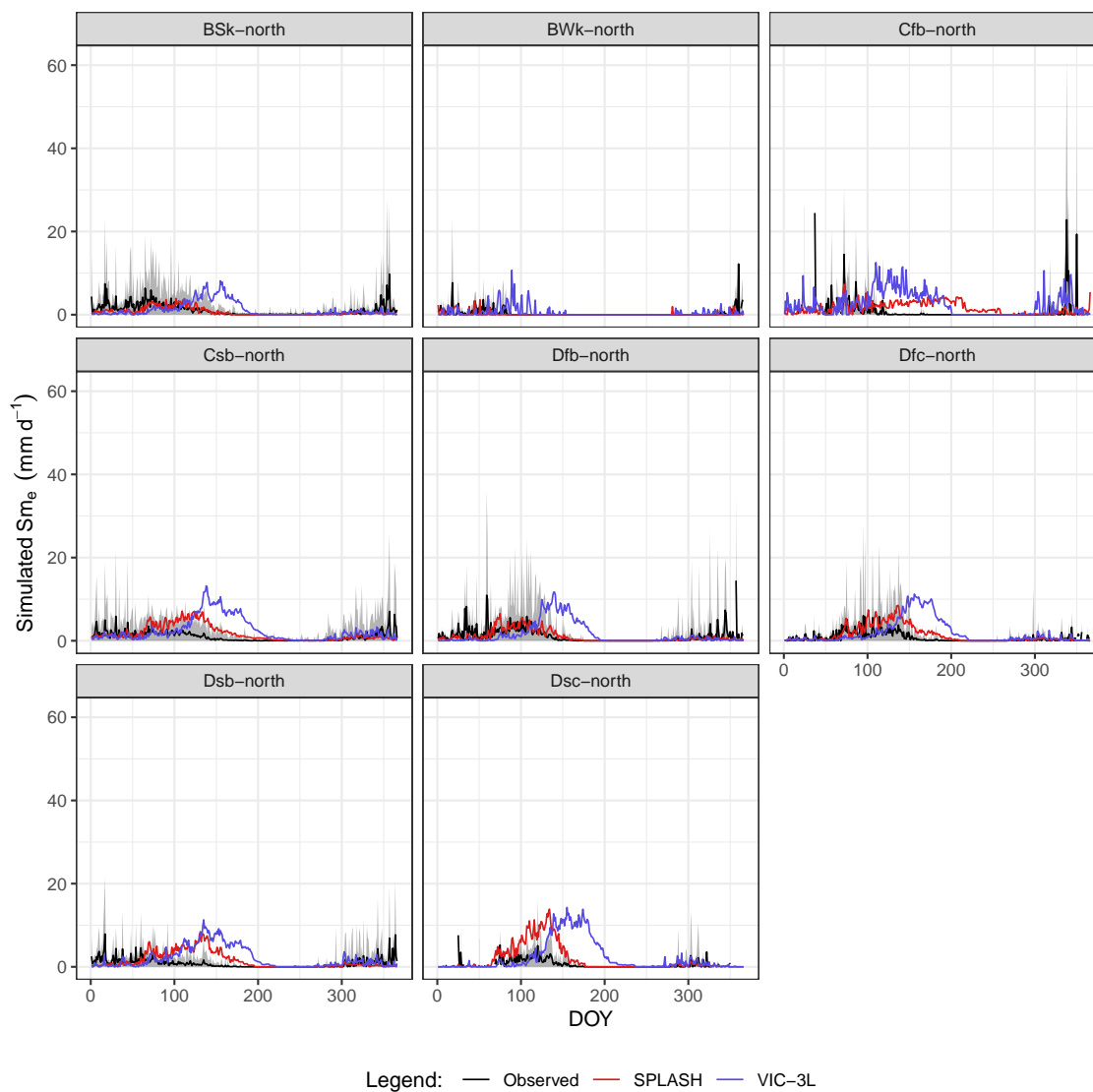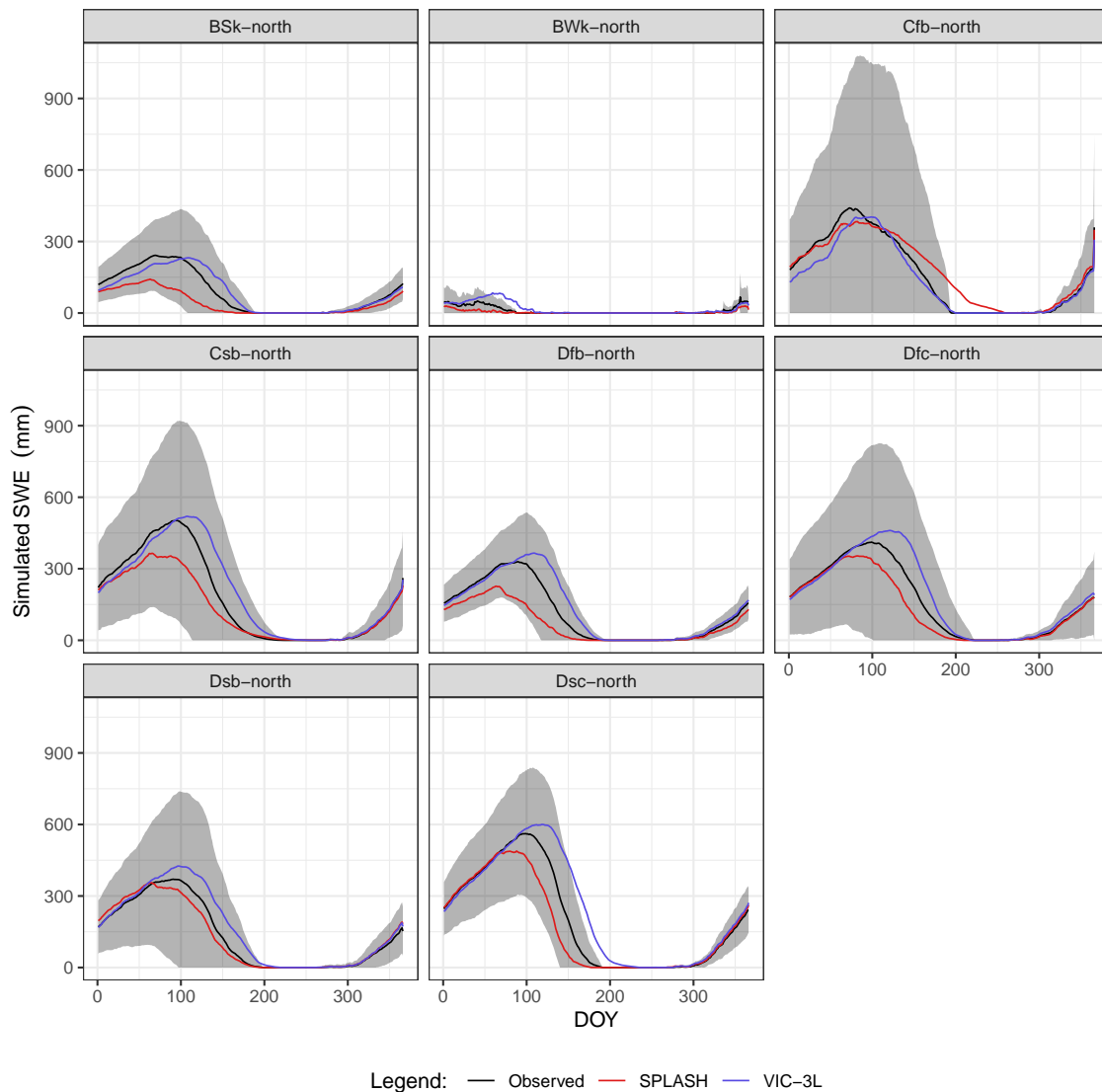
Figure 38. Mean seasonal cycle of SWE per climate zone. The gray areas show one SD from the observed mean. Climate zones are described in table (A2).

The spatially distributed high-resolution simulation, over North America, showed strong patterns defined by the topography, with higher SWE over the mountain regions, and variations according to the slope exposure. A well-defined lower boundary for the snow-covered area emerged in the eastern US, around $40°$ of latitude, coinciding with the transition from climates Cfa to Dfa, while on mountain summits the simulated SWE fades at around $35°$ (Fig. 39).
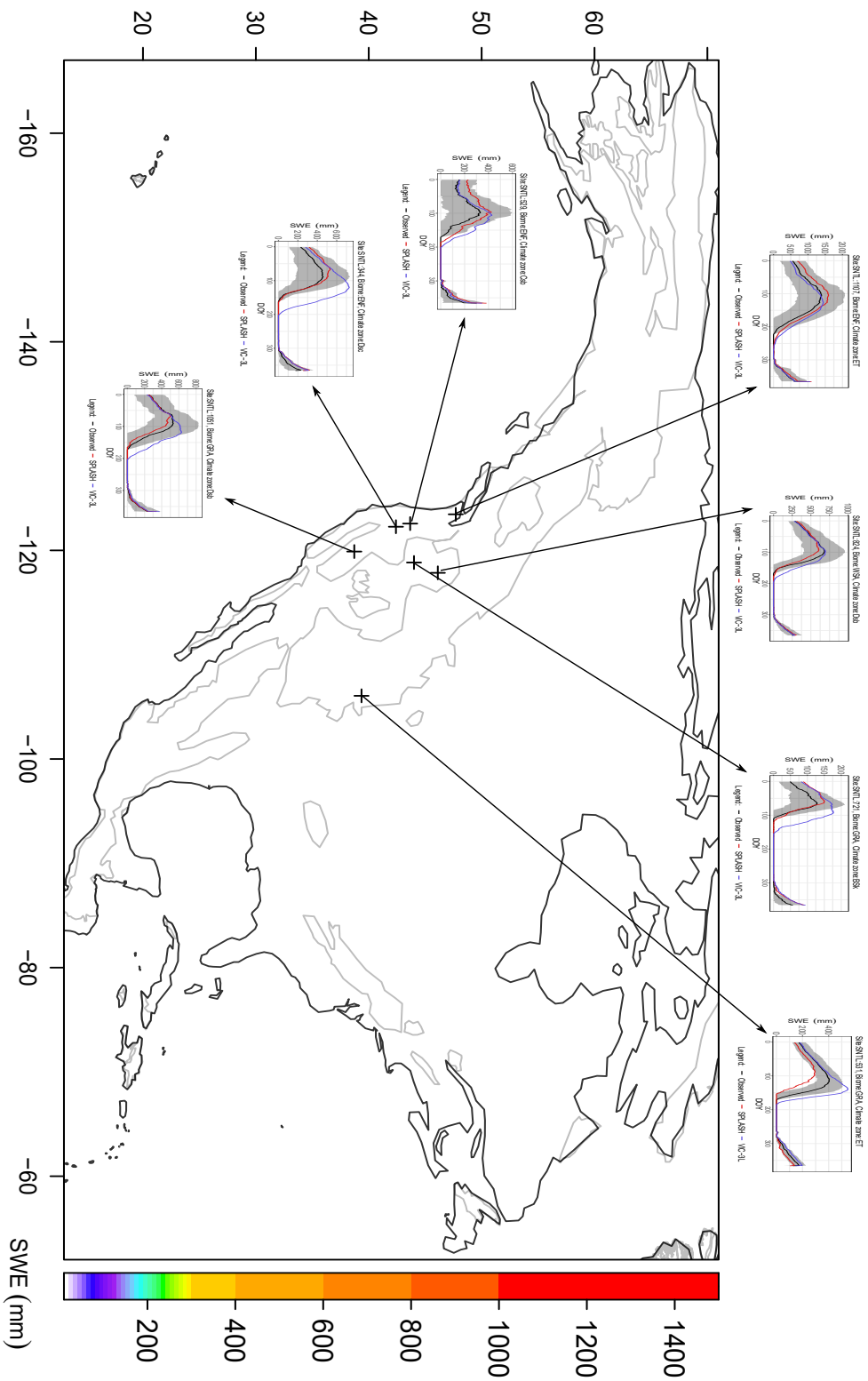
Figure 39. Spatial patterns of mean monthly maximum SWE for the period 2010-2016 over North-America at 1km resolution, along with site-simulation examples from the mountains. The gray areas show one SD from the observed mean.

6.3.2 Soil water content

The performance evaluation of daily SWC was done with data from stations measuring soil moisture deeper than ~~30cm~~ 30 cm located in the mountain regions, resulting in ~~37~~ 16 EC (Fig. 40a) and 127 SNOTEL (Fig. 40b) stations. Comparison among biomes was not possible due to the different depths of measurement in each station, this shows for example, because of mostly superficial measurements, wetlands at the lower end of the observations axis (Fig. 40b). Nevertheless, the SPLASH model was able to explain 86% of the variation in the EC dataset which is around 7 times smaller than the SNOTEL dataset where SPLASH explained 54% of the variation. The evaluation also shows that SWC was overestimated by the SPLASH model in Grassland ecosystems (GRA) and in open shrublands (OSH) (Fig. 40).

(a) EC sites   (b) SNOTEL sites
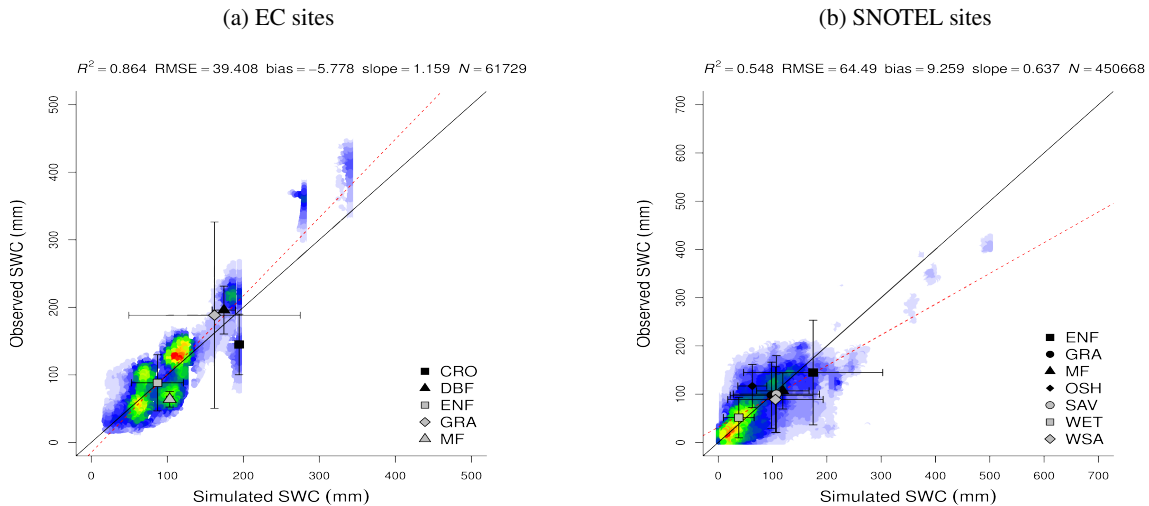
Figure 40. Correlation of observed and simulated values of daily SWC, values of all sites pooled. The color scale shows point density; red indicates higher density.

The seasonal patterns of Θ, extracted from the data and simulations at SNOTEL sites, show a sinusoidal shape in all the climate zones. The highest point appears during the first half of the spring, and the lowest point by the end of the summer. Most of the climate zones show huge deviations from the mean, especially the zones without dry season (e.g. Cfb, Dfc), except for the cold desert (BWk) where this variation is smaller.

SPLASH model shows a reasonable agreement of the seasonal pattern for climate zones with warm and dry summers (i.e. Csb, Dsb) and for the cold steppe (BSk). At these climate zones, SPLASH reproduces the seasonality in a better way than VIC. In some continental climates (Dfb, Dfc, Dsc), SPLASH produce a similar pattern to the observed mean but downshifted inside the expected deviation. At these climate zones, the VIC model approaches the observed mean only during spring-summer months. In the Warm-summer temperate climate with no dry season (Cfb), SPLASH is not able to reproduce the seasonal pattern, the amplitude of the sinusoidal shape is too small to match the observations. Here, VIC agrees with the

56

observations briefly during winter. In the cold desert (BWk) SPLASH does not produce a seasonal pattern, the average through
700   the year remains close to the minimum. Here VIC overestimates Θ during spring and produces negative values during the
spring and summer months (Fig. 41).
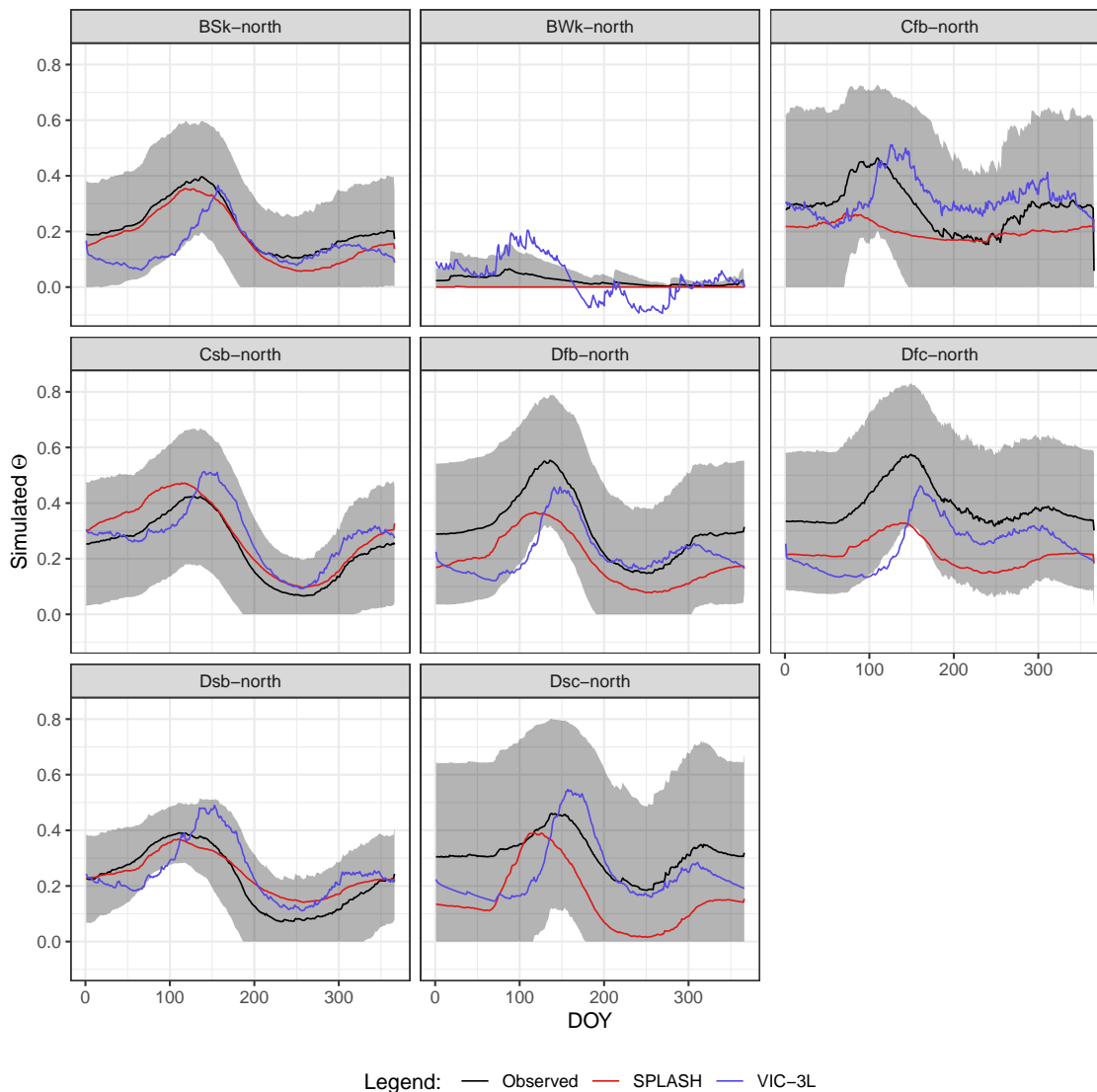
Figure 41. Mean seasonal cycle of Θ per climate zone. The gray areas show one SD from the observed mean. Climate zones are described
in table (A2).

The spatially distributed simulation of relative soil moisture saturation shows that the patterns of the annual average roughly
follow the global climate zones distribution. At this resolution, the model was incapable of reproducing the streams and most
of the mountain regions ~~emerge~~ emerged as areas half to low saturated (Fig. 42).

57
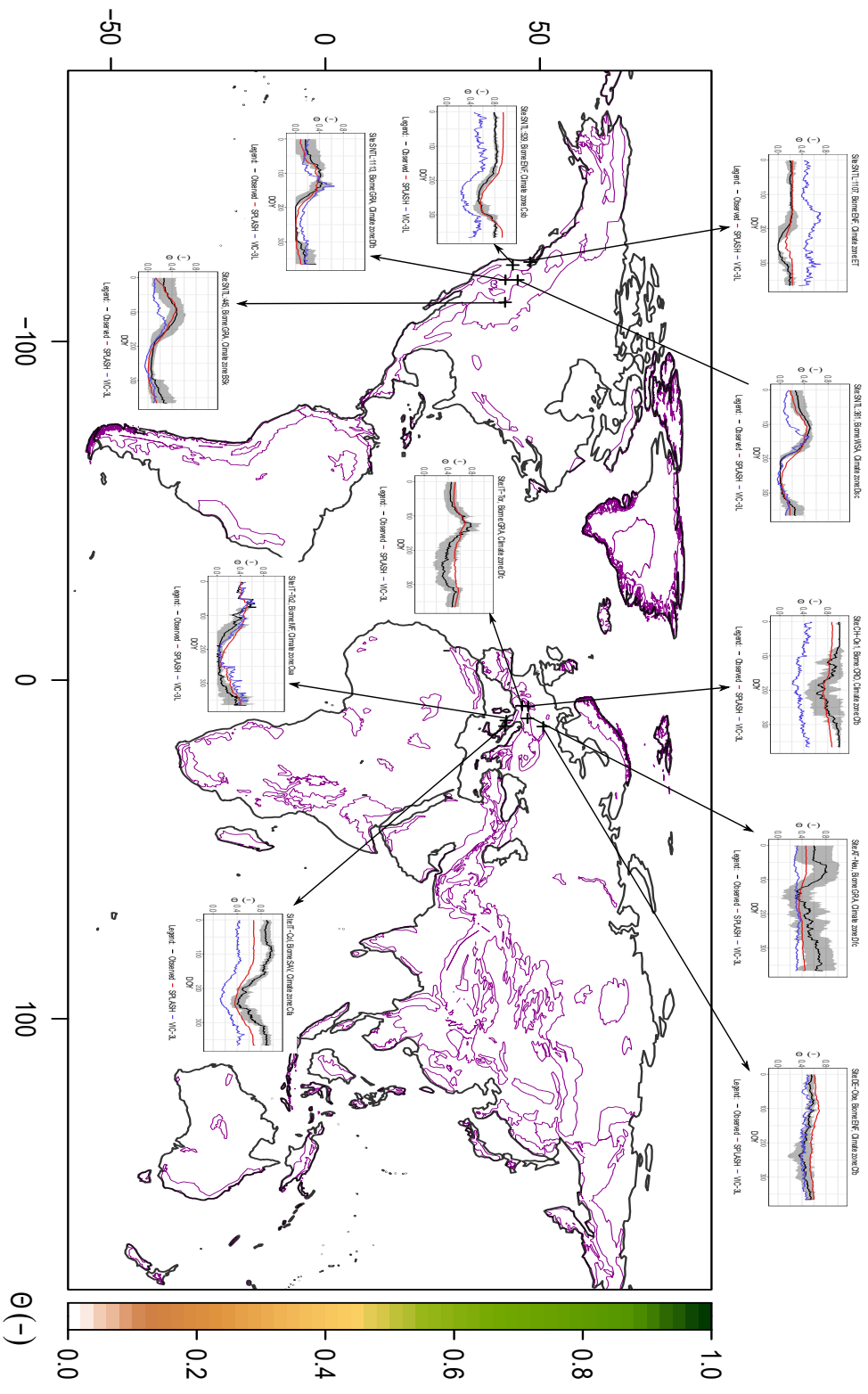
Figure 42. Spatial patterns of mean annual Θ for the period 2010-2016 at 5km resolution along with site-simulation examples from the mountains. The grey areas show one SD from the observed mean.

58

705   The spatial patterns of the total soil water content in the temperate watershed show an emergent accumulation at the valley bottom, shaping the stream. Here, the s.d. is very small, suggesting the valley bottom remains wet most of the year (Fig. 43d).

The different patterns over north and south-facing slopes, show the former with more water content over the latter, but more variations over time. The emergent variations in the north-facing slope are shaped by the inclination of the slope, while on the south-facing slope, this pattern seems to follow the aspect (Fig. 43c).

710   The time series of soil water content over the first meter of depth ~~were~~ was poorly reproduced by SPLASH, in some years the simulation matches the observations (e.g. 2006), however, in most of the years the droughts are underestimated and the peaks are overestimated (Fig. 43e).

(a) Slope

(b) Aspect

(c) SPLASH mean W_n

(d) SPLASH SD W_n

(e) Monthly swc 1m time series
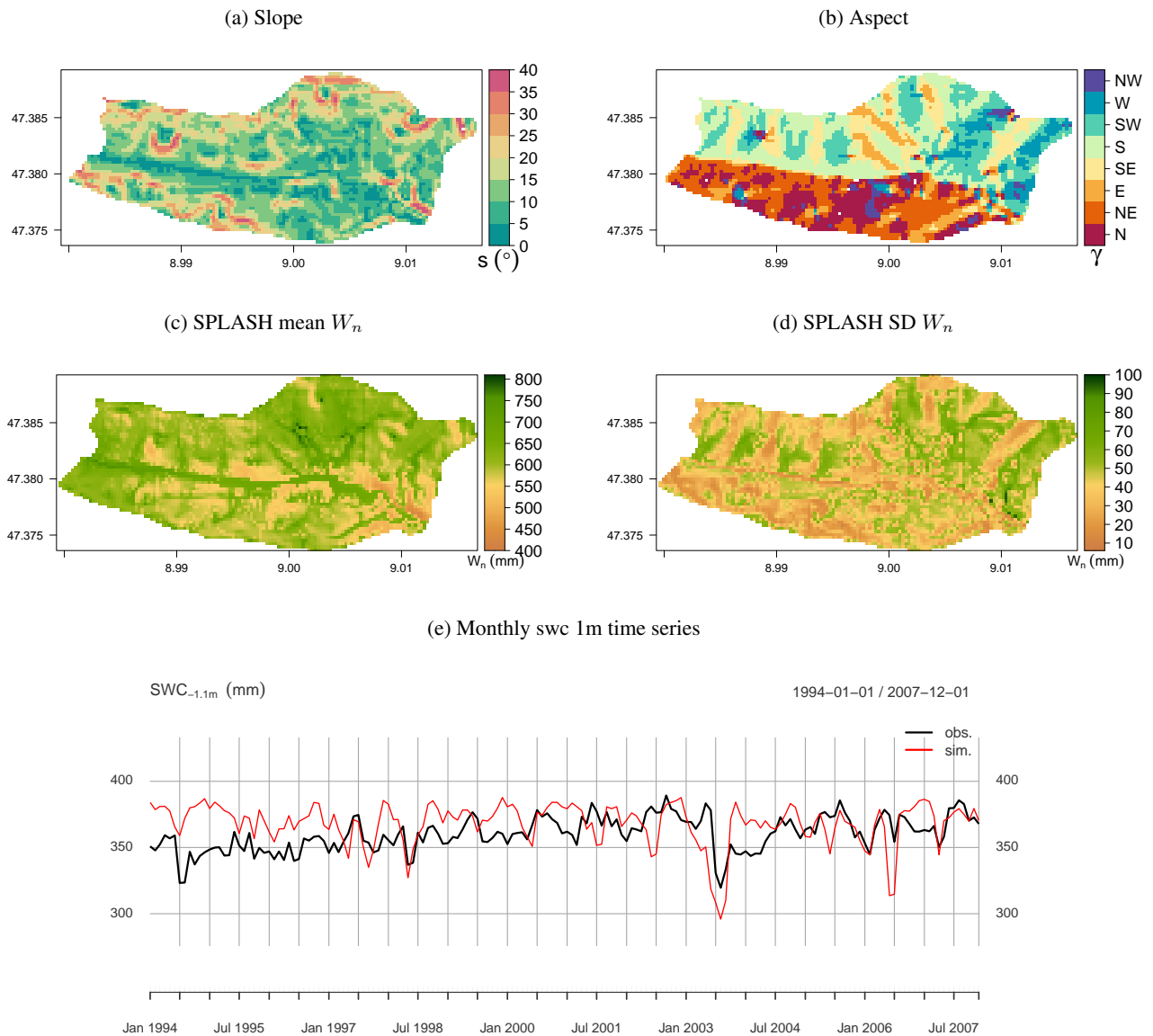
Figure 43. Spatial and temporal patterns of soil water content in a small wet temperate watershed, Rietholzbach - Switzerland. (a) Slope in degrees. (b) Slope orientation, N stands for north, S for south and so on. (c) Mean annual simulated soil water content in the whole column during 1994-2007. (d) The standard deviation of the daily soil water content in the whole column during 1994-2007. (e) Time series of monthly soil water content, simulated and observed over the first 1 m. of depth.

In the tropical watershed, the spatial patterns of the daily average W_n show the emergent stream at the valley bottom, according to the simulations the daily water content here is more variable than in the rest of the watershed (Fig. 44d), contrary

715 to the temperate watershed where this pattern was opposite. Here the east-west aspects ~~are defining~~ define the spatial patterns, the eastern ~~flank~~ flanks show less water content than their ~~Western~~ western counterparts (Fig. 44c).

(a) Slope

(b) Aspect

(c) Mean SPLASH wn

(d) SD of SPLASH wn
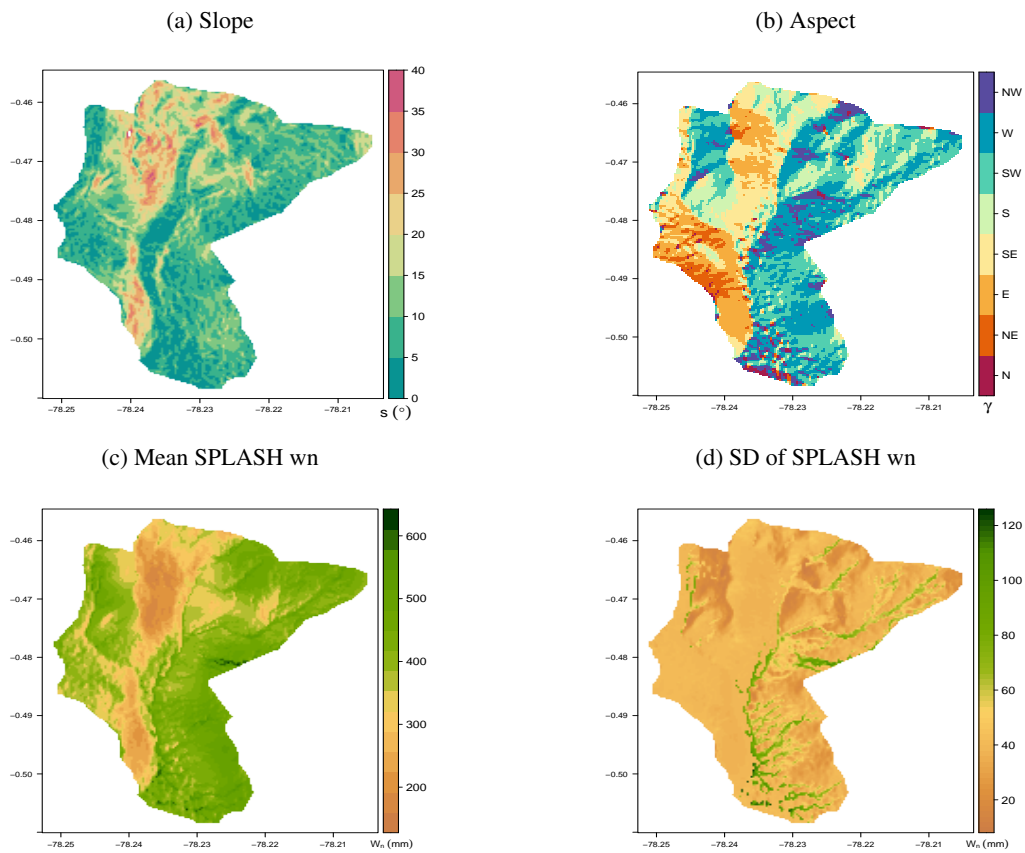
Figure 44. Spatial patterns of daily soil water content in a wet tropical watershed, Jatunhuayco - Ecuador. (a) Slope in degrees. (b) Slope orientation, N stands for north, S for south and so on. (c) Mean daily soil water content during 2014. (d) Standard deviation of the daily soil water content during 2014).

7 Discussion

The updated SPLASH model ~~exhibited a~~ showed reasonable agreement with the observations in all the fluxes analysed here without any local calibration or prescribed land-cover information. The data requirements to run the model (precipitation, solar 720 radiation, air temperature, elevation and soil texture) are modest; the open-source code, compiled in a ready-to-use package, facilitates replication.

The analytical approach used to solve the energy and water fluxes allowed the model to run with high-resolution data on global scales without using statistical–dynamical flux parameterizations, or hydrological unit responses. Emergent patterns

produced by the model follow the natural accumulation of soil moisture downslope. Most of the fluxes and storages analysed here agree with — and sometimes outperform— the more complex VIC-3L model, which was chosen for comparison due to its wide use in ecohydrological applications, and its well-known good performance.

SPLASH assumes background albedo, a parameter particularly crucial due to its synergy with water fluxes, to be constant for all biomes. This contrasts with the VIC model, which uses monthly albedo per vegetation class (Gao et al., 2009). Nonetheless, SPLASH showed overall good agreement of H_n^+ with the observations, suggesting that the snow effect on the albedo is much stronger than the effects of the phenology in snow-covered regions (Xiao et al., 2017). This global albedo assumption, however, is more likely to be the cause of the discrepancy of H_n^+ in ecosystems with sparse vegetation cover (e.g. BSV and OSH), where the extent of exposed soil and its moisture status modify the albedo (Campbell and Norman, 1998; Barry, 2008).

Although the ground heat flux is ignored by the model, an improvement in the calculation of H_n^+ is noticed relative to the previous version (Davis et al., 2017), where the overestimation in the arid desert (BWh) is fixed with the new parameterization of the longwave radiation, and the overestimation in the polar tundra (ET) is corrected by the new included feedback snow-albedo.

Simulated actual evapotranspiration (E_n^a) is underestimated to various degrees in all biomes. As model performance for H_n^+ is high, this suggests that the E_n^a discrepancies are related to the empirical parameterization of the water supply/uptake (S_W). Theoretically, this should be driven by the soil-to-leaf water potentials gradient ($\Delta\psi$) (Prentice et al., 2014), thus, reflecting different plant strategies to deal with drought. However, when this idea was tested during the development stage, the performance of the simulations decreased (Fig. 45c), probably due to the calculation method used for the leaf-water potential, and its assumptions (both taken from the literature): canopy well coupled to the atmosphere at pre-dawn, thus $T_s = Ta$; and the relative water content of the leaf close to saturation (Appendix A4).

Although in this version of SPLASH, ~~I~~we propose a physically-based calculation for the upper threshold of S_W, its response to the water deficit is conceptualized as a linear function, which has been reported as the most simple and reasonable empirical description (e.g. Federer (1982)). Nonetheless, several authors report more complex formulations depicting, convex (Campbell and Norman, 1998), concave (Metselaar and de Jong van Lier, 2007) or trapezoidal (Feddes and Raats, 2004) shapes. Some of these formulations were tested during the development stage of the model, with no significant improvement over the simple linear formulation (Fig. 45).

From this experimentation, the assumption made on the maximum supply rate S_c as the maximum rate of evaporation yielded the best approximations. This assumption makes more sense in bare-ground areas, however, in vegetated areas, this value should be reflecting the plant controls on transpiration, which ideally, needs to be addressed with ideas based on Eco-evolutionary optimality theory (Harrison et al., 2021).

(a) Campbell water uptake eq.

$R^2 = 0.33$ RMSE = 1.832 bias = 0.746 slope = 0.403 $N = 225728$

(b) Metselaar water stress eq.

$R^2 = 0.341$ RMSE = 1.43 bias = 0.356 slope = 0.502 $N = 225728$

(c) $\Delta\psi$ water uptake eq.

$R^2 = 0.22$ RMSE = 1.65 bias = -0.58 slope = 0.59 $N = 559569$
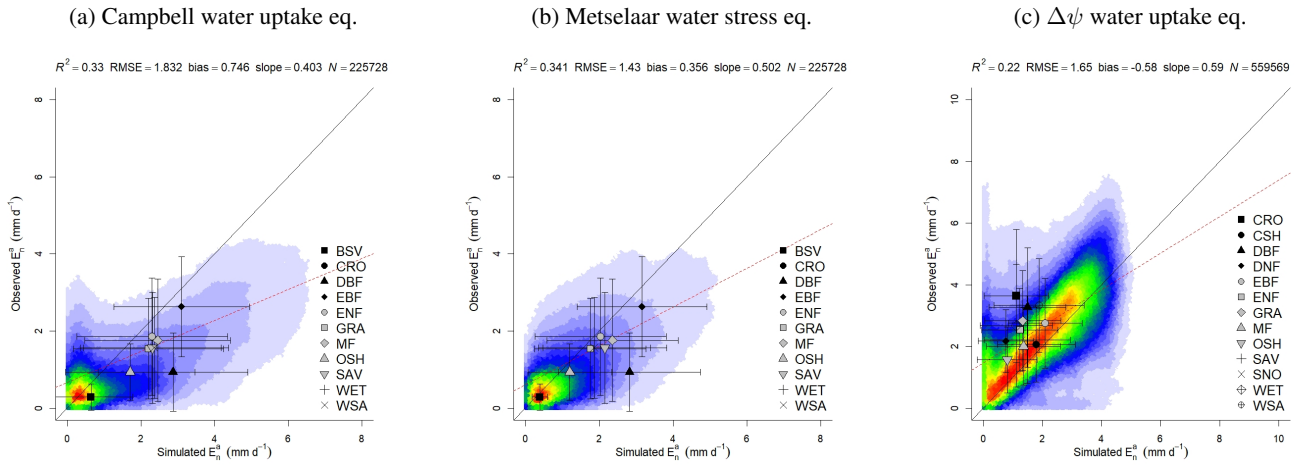
Figure 45. Simulation experiments against EC observations using different soil water stress/water uptake functions. The color scale shows point density; red indicates higher density. (a) Using Campbell and Norman (1998) water uptake function in mountain sites. (b) Using Metselaar and de Jong van Lier (2007) water stress function and a constant $Sc = 1.05\,(mm\,h^{-1})$ (Federer, 1982) in mountain sites. (c) Using the gradient of water potentials soil-leaf $\Delta\psi$ to drive the water uptake in all the FLUXNET database.

Since SPLASH seems to reproduce the evapotranspiration better over non-water limited areas, in such areas, slopes facing the equator (south-facing slopes in the northern hemisphere) should, in theory, show higher values than their opposite-facing counterparts, which receive less radiation (Körner, 2021; Chapin et al., 2011).

This spatial pattern is indeed produced by SPLASH in the Rietholzbach experimental catchment. However, here the latent heat calculated from the Landsat5 retrievals does not show any strong differences between north and south-facing slopes. It is still unclear if the spatial patterns from Landsat are correct, the SEBAL algorithm used the calculate LE is limited to clear-sky pixels only, thus a large amount of data was excluded from the calculation, furthermore, this algorithm computes an instantaneous $\frac{LE}{Rn-G}$ (at the satellite overpass), then, it assumes this proportion is constant through the day, so the daily E^a can be calculated from the daily accumulated Rn measured on the ground (Bastiaanssen et al., 1998a). Therefore, a more accurate estimation from SEBAL would involve terrain-corrected independent calculations of Rn at Landsat spatial resolution, which were unavailable at the time of this comparison. Land use in Rietholzbach also plays a key role in shaping the spatial patterns of LE as well.

SPLASH in theory reflects the environment the plants experience. The spin-up routine produces an initial state of equilibrium, thus in areas with natural vegetation the spatial patterns produced by SPLASH should reflect this vegetation cover to some degree. This is shown in the agreement (to some extent) of the spatial patterns of E_n^a produced by SPLASH compared with the Landsat8 LE in the tropical watershed, which always had natural vegetation. This microclimatic gradient created by the slope and aspect is particularly important to explain outlier populations existing beyond their major distribution zone, which can colonize their surroundings during rapid climatic changes (Chapin et al., 2011).

Although the results presented here are encouraging, more rigorous comparisons are needed to evaluate how well the fluxes produced by SPLASH reflect patterns of naturally occurring vegetation.

The less-than-optimal performance of SPLASH simulating condensation is mainly due to the lack of other environmental variables needed to calculate the dew point and surface temperature, such as air humidity, wind speed, and aerodynamic resistance. Nonetheless, the simple assumption made to estimate this flux (10% of H_N^-) reproduces the seasonal Cn better than VIC. The major discrepancies of VIC's Cn happen during the spring-summer months suggesting that some of the heat lost as Cn (latent) is actually lost from the surface by convection, cooling the leaves. The yearly magnitudes of dew formed by Cn suggest that its impact on the water balance is ~~minimum~~ minimal in most climate zones, except for hot arid climate zones (BSh), where Cn has ecological importance, in agreement with the observations reported by Guo et al. (2016) and Yu et al. (2020).

The size of the snowpack (SWE) simulated by SPLASH agrees more than 80% with the observations, however, its seasonal patterns show a systematic underestimation in most of the climate zones. Since the seasonal patterns of the snowfall (Sf) produced by SPLASH match the observations in all the climate zones, and, the snowmelt (Sm) is reasonably well predicted in the steppe (BSk) and the wet continental climates (Df*). In these climate zones, the discrepancies seem to be due to the redistribution of snow by the wind, which is greatly dependent on the structure of the vegetation (Barry, 2008; Pomeroy and Brun, 2001) and it is not considered by the model. In dry continental and temperate climates (Ds*, Csb), on the other hand, SPLASH systematically underestimates SWE, here the cause is more likely to be neglecting the "cold content" of the snow, which in turn causes an overestimation of Sm. This effect is stronger at high elevations where the temperature is lower, here VIC delivers better estimations than SPLASH (Fig. 45). Moreover, ~~although~~ despite the discrepancies in the simulated magnitudes at these sites, the duration of the snow-covered period is reasonably predicted, considering that the multi-annual variation can be up to one month (Körner, 2021).
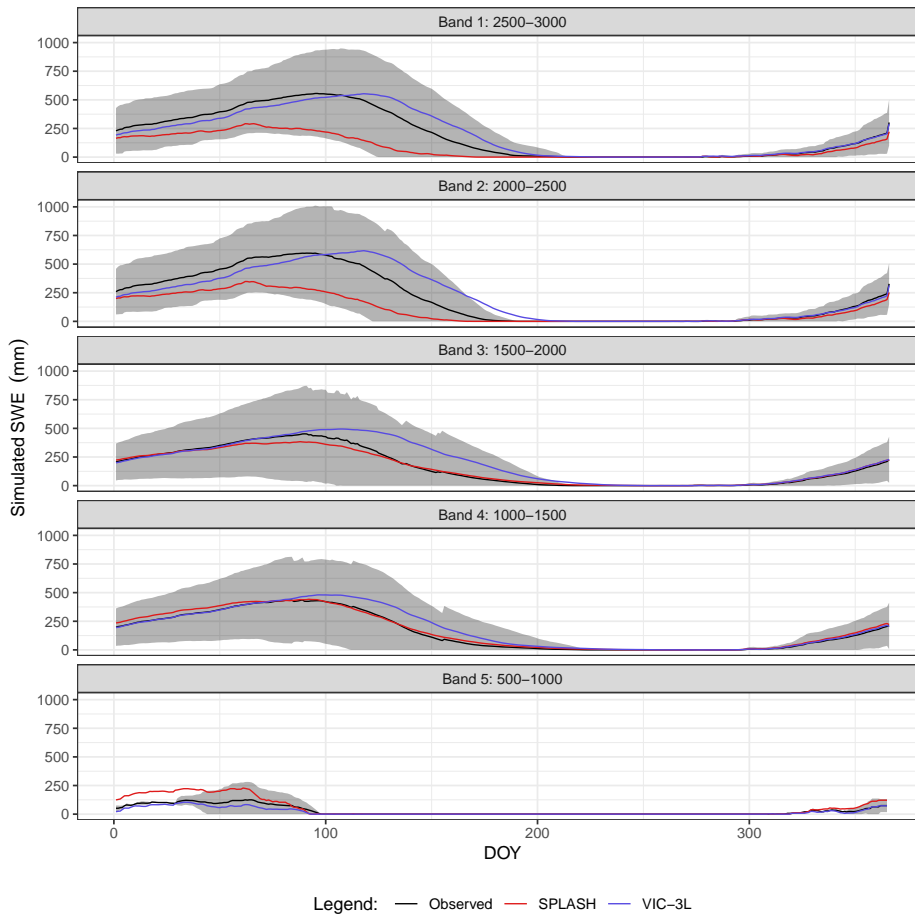
Figure 46. Mean seasonal cycle of SWE over dry temperate climates (Csb) per elevation band. Results aggregated every 500 masl. The lines show the means, while the gray shaded area shows the ~~mean ±~~ sd.

Although in theory, different sets of parameters in the snow-albedo functions, depending on the complexity of the canopy, should yield more accurate predictions (e.g. Romanov (2003)), the performance of SPLASH simulating SWE ~~show~~ shows
795   that one set of parameters is able to deliver reasonable approximations for all types of biomes, such approximation was possible using roughly 10^6 of RS/ground datapoints spawned over 15 years in 315 stations during the optimization process. The use of one set of parameters is nothing new and it has been used for a long time, however, in previous studies, the number of observations and available tools ~~were limiting~~ limited the spatial representativity of these calibrations (Clark et al., 2017). Nonetheless, the parameters found in SPLASH for the snow-albedo decay function, are consistent with the values proposed in
800   the Noah model by Livneh et al. (2010), although in SPLASH there are no different sets of parameters for accumulation and melt seasons.

The spatial patterns of the surface runoff generated by SPLASH in the small watersheds show that most of this flux is generated in the saturated zone in the valley bottom, in agreement with what is expected in montane regions (Grayson and Blöschl, 2000; Weizu and Freer, 1995).

805 Moreover, the spatial patterns of BFI produced by SPLASH in Rietholzbach agree with previous studies which show that most of the streamflow is produced by subsurface flow, specially interflow (Von Freyberg et al., 2014; Gurtz et al., 2003). However, the poor performance of SPLASH simulating the daily surface runoff in the Andean catchment, suggest that the assumption made for the event duration doesn't hold for this area, or the saturated zone close to the stream, which controls this flux in Andean catchments (Correa et al., 2020) is underestimated.

810 Although the simulations of soil moisture are overall reasonable and the results mostly matched the temporal dynamics of the observations, two recurrent errors were observed among the simulations, or a combination of these errors, the resultant soil moisture appears up or downshifted randomly (1st error), or the amplitude of the variations is different from what is observed (2nd error).

The first type of error seems to be related to the estimation of the bucket size, which in turn is defined by the pedotransfer 815 functions and soil data. Although the pedotransfer functions were optimized with a global dataset, which covers a wide spectrum of textural classes with a wide range of SOM combinations, the empirical nature of these equations is a well-documented source of error (Pachepsky et al., 2015; Van Looy et al., 2017; Paschalis et al., 2022). This error might explain why the evapotranspiration and total streamflow agree with the observations in Rietholzbach, but the performance of the soil moisture simulation was very poor.

820 The second type of error was less recurrent with the SNOTEL dataset, which includes actual measurements of soil properties, suggesting that the data obtained from SoilGrids for the EC sites might be a source of this error. The coarser volumetric fraction (stoniness), particularly, can reduce the size of the bucket dramatically here. However, a rigorous evaluation and sensitivity analysis is needed to define this source of error in a broader modelling context.

The spatial patterns of soil moisture at a global scale show how the assumption of the model of a maximum depth breaks the 825 hydrological connectivity in large watersheds. Here, the model forces the water to flow down instead of laterally if the bedrock is not in the first two meters of depth. On the other hand, in small watersheds, the hydrological connectivity emerges from the conceptualization of the model accumulating the moisture at the valley bottom and shaping the streams.

Furthermore, the lateral flow simulated by SPLASH is strongly related ~~with~~ to the soil water content, consistent with what has been reported in Rietholzbach (Teuling et al., 2010) and in Andean watersheds (Crespo et al., 2011).

830 The exponential decay of the saturated conductivity with depth, widely used in TOPMODEL-type models, was deliberately excluded from the model. The saturated hydraulic conductivity is highly dependent on the organic matter content and was calculated using a weighted average (by depth) of SOM as an input. ~~Ssince~~ Since SOM generally decreases exponentially with depth (Kramer and Gleixner, 2008; Hobley and Wilson, 2016; Bai et al., 2016) this estimated K_{sat} should be reproducing the decay to some degree. However, the available data used for the optimization of the pedotransfer functions calculating K_{sat} was 835 biased towards sandy and loamy-sand soils, affecting the performance in the rest of the textural classes.

The lateral flow equation proposed here is based on the profile transmissivity, originally proposed by TOPMODEL and the assumption of steady-state flow. However, it's been reported that the steady-state flow assumption holds better in wet catchments with high hydraulic gradients. In dry catchments or during dry periods, areas of the catchment may lose their hydrological connectivity (Woods et al., 1997; Tague and Band, 2001).

840   Analyzing the response of the lateral flow to soil moisture generated by SPLASH the minimum q_{out} reflects the stable gravity-driven drainage (which in shallow soils defines the baseflow), while the maximum q_{out} appears as pulses product of individual precipitation events mimicking the behaviour of the interflow. This response is consistent in both, wet and arid sites in different magnitudes.

In VIC3-L, however, q_{out} reaches values in the order of hundreds (truncated in the figure) while soil moisture is not even

845   saturated. In the comparable region of the analysis, the upper envelope of the scattered points shows a linear threshold and a sharp transition to a plateau. The flux here seems to display relatively high values when the soil moisture is close to the wilting point, which is theoretically impossible.

(a) SPLASH ENF/Csb site

(b) VIC-3L ENF/Csb site

(c) SPLASH GRA/Bsk site

(d) VIC-3L GRA/Bsk site
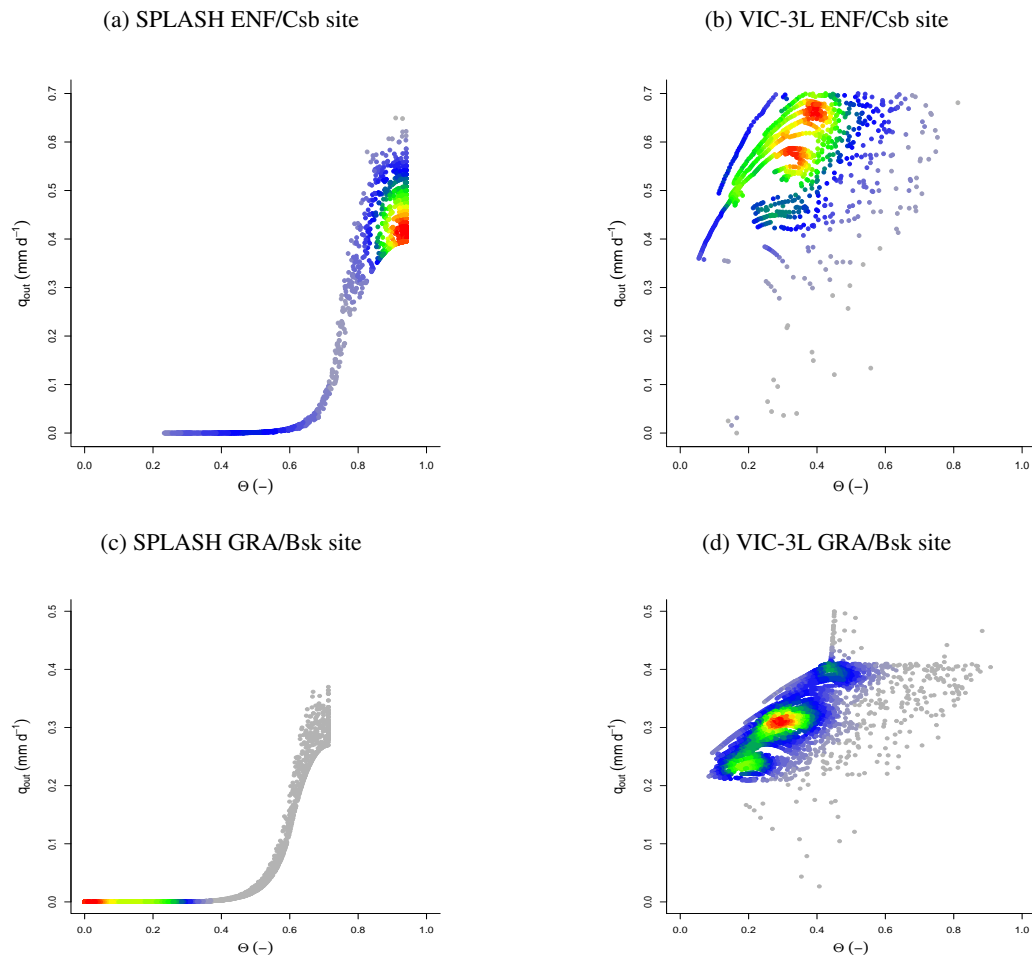
Figure 47. Emergent response of the lateral flow to soil moisture from an ENF in a temperate climate, with a dry and warm summer (Csb) (Site site SNTL:529), simulated from: (a) SPLASH. (b) VIC-3L. The same relationship from a GRA in an arid cold steppe (Bsk) (Site site SNTL:871), simulated from: (c) SPLASH. (d) VIC-3L.

Despite the limitations discussed, the updated SPLASH model provides fast and parsimonious means to generate robust estimates of water and energy budgets across regions, regardless of their topographic complexity and spatial scale. The calibration-free approach enhances the model's portability and the ecological interpretability of the results. Moreover, since the structure of the model contains fewer moving parts than any other LSMs, it facilitates formulating ecologically-driven working hypotheses on why results do not match the observations in case of big discrepancies. With targeted refinements, SPLASH could become an even more robust tool for ecohydrological modeling and for exploring hydrological impacts of global change.

Appendix A: Derivations and extended mathematical analysis

A1   Recession constant

Analysing the flux from one cell, according to the linear reservoir model (Eq. 42) and the BC model (Eq.39), the maximum (initial) lateral flux will happen when the soil is saturated. In the same way, it will be close to zero at field capacity. Thus, if we
870 set the volume of the drainable porosity, ~~equals~~ equal to the total volume drained by Eq. (42):

$$(W_{sat} - W_{fc})\, Ai = \int\limits_{0}^{t} Q_{sat} K_b{}^t dt \tag{A1}$$

Then, solving both, Eq.(42) and Eq.(A1) for t, we can set:

$$\frac{1}{\ln(K_b)} \ln\left(\frac{Q_{fc}}{Q_{sat}}\right) = \frac{1}{\ln(K_b)} \ln\left(\frac{Ai\,(W_{sat} - W_{fc})\ln(K_b)}{Q_{sat}} + 1\right) \tag{A2}$$

Therefore, solving Eq. (A2) for K_b, we get:

875 $$K_b = e^{\frac{Q_{fc} - Q_{sat}}{Ai\,(W_{sat} - W_{fc})}} \tag{A3}$$

A2 Actual field capacity

Replacing Eq. (55), Eq. (56b) and Eq.(57) in Eq.(54):

$$A(\theta)^{-B} - \rho_w\, g\, \theta\,(1000z) = 0 \tag{A4}$$

Then, converting units to SI and simplifying, we can substitute:

$$c = \frac{1000}{\rho_w\, g} \tag{A5}$$

Where 1000 is a factor to correct the units. This can be rearranged to,

$$c\,\frac{A}{z} = \frac{\theta}{\theta^{-B}} \tag{A6}$$

Thus, solving Eq.(A3) for θ:

$$\theta = \left(\frac{c\,A}{z}\right)^{\frac{1}{1+B}} \tag{A7}$$

A3 Comparable quantities from the VIC-3L model

A3.1 H_N^+ from $\overline{I_N}$

VIC-3L provides daily $\overline{I_N}\,(W\,m^{-2})$ as output, so, the comparable quantity representing the total input of energy can be found as:

$$H_N^+ = 86400\,\overline{I_N} + H_N^- \tag{A8}$$

Among the outputs from the VIC-3L model are $I_{SW}max$ and I_{LW}, so, if at solar noon ($h = 0$) $I_{SW} = I_{SW}max$, and, at $h = h_n$, $I_{SW} = I_{LW}$, then:

$$I_{SW}max\,\cos h_n = I_{LW} \qquad\qquad \Rightarrow h_n = \arccos \frac{I_{LW}}{I_{SW}max} \tag{A9}$$

$I_{SW} = I_{LW}$, and $I_{SW} = 0$ at $h = h_s$ implies as well the line:

$$0 = I_{SW}max - \left(\frac{I_{SW}max - I_{LW}}{h_s}\right) h_n \tag{A10}$$

Which solving for h_s yields:

$$h_s = h_n\left(1 + \frac{I_{LW}}{I_{SW}max}\right) \tag{A11}$$

Then, the area representing H_N^- is:

$$H_N^- = \frac{86400}{\pi}\,(\pi - h_s)I_{LW} + \frac{(h_s - h_n)I_{LW}}{2} \tag{A12}$$

A3.2 C_n from latent heat components

900 VIC-3L provides the daily average of the net latent heat as output, along its components used to melt/refreeze soil and snow, so C_n was computed simply as the remnant negative latent heat after the components were subtracted from the net latent heat, in the way

$$C_n = (OUT_{LATENT} + OUT_{FUSION} + OUT_{MELT\ ENERGY} + OUT_{RFRZ\ ENERGY}) * (86.4/2260) - OUT_{EVAP} \quad \text{(A13)}$$

Here, the factor $(86.4/2260)$ transforms from $W\,m^{-2}$ to $mm\,d^{-1}$ assuming constant water density and vaporization heat of

905 $2260kJ/kg$.

A4 Water uptake/water stress functions

A4.1 Water uptake from $\Delta\psi$

Transpiration can be defined following Campbell and Norman (1998) as:

$$E = S_W = \left(\frac{\psi_s - \psi_L}{R_p}\right) \quad \text{(A14)}$$

910 Where, ψ_s is the soil water potential, ψ_L the leaf water potential and R_p the total plant hydraulic resistance, from the root to the leaf.

Then, without soil moisture limitations ($\psi_s = 0$), the transpiration becomes:

$$E_{max} = D_p = \left(\frac{-\psi_L}{R_p}\right) \quad \text{(A15)}$$

Then, solving Eq. (A15) for R_p and replacing in Eq. (A14):

915 $$S_W = D_p \left(1 - \frac{-\psi_s}{\psi_L}\right) \quad \text{(A16)}$$

Where $,\psi_L$ is found using the first law of thermodynamics: $dU = dQ - PdV$. Where dU is the change in internal energy, dQ is the instantaneous heat input and PdV is the work done at constant pressure.

So, if $\psi = \frac{U}{Vw}$, and $PdV = \frac{-nRT}{P}dP$ from the ideal gas law, assuming $dQ = 0$ at pre-dawn, then:

$$\psi_L = \frac{1}{Vw}\int_{P1}^{P2} \frac{nRT}{P}dP = \frac{RT}{Vw}\ln\frac{e_L^a}{e_L^s} \quad \text{(A17)}$$

920 Where, Vw is the molar volume, e_L^a and e_L^s are the actual and saturation vapour pressure at the leaf surface, its proportion was assumed as 0.98 (Nobel, 1983).

A4.2 Water uptake from Campbell and Norman (1998)

$$S_W = D_p \left(1 - \frac{2}{3}\frac{\psi_s}{\psi_L}\right) \quad \text{(A18)}$$

71

A4.3 Water stress function from Metselaar and de Jong van Lier (2007)

$$S_W = Sc \frac{\Theta^{a+1} - \Theta_W^{a+1}}{\Theta_l^{a+1} - \Theta_W^{a+1}} \tag{A19}$$

Where:

$$\Theta = \frac{\theta - \theta_r}{\theta_s - \theta_{wp}} \tag{A20}$$

$$\Theta_l = \frac{\theta_l - \theta_r}{\theta_s - \theta_{wp}} \tag{A21}$$

$$\Theta_W = \frac{\theta_{wp} - \theta_r}{\theta_s - \theta_{wp}} \tag{A22}$$

$$\theta_l = \theta_{wp} + A * (\theta_s - \theta_{wp}) \tag{A23}$$

$$\alpha = 3 + 2\lambda \tag{A24}$$

Here, λ is a parameter for the BC water retention model, A is an empirical parameter defining the curvature of the function, θ_{wp}, θ_s, θ, θ_r are the volumetric water content at wilting point, saturation, actual and residual respectively, and $Sc = 1.05(mm\,h^{-1})$ after (Federer, 1982).

A4.4 Rainfall event duration

Pareto distribution, higher frequency events last between 0-1 hrs 80% lower 6 rainy hours, 6hrs chosen parameter

(a) Relative frequency

(b) Cumulative Distribution
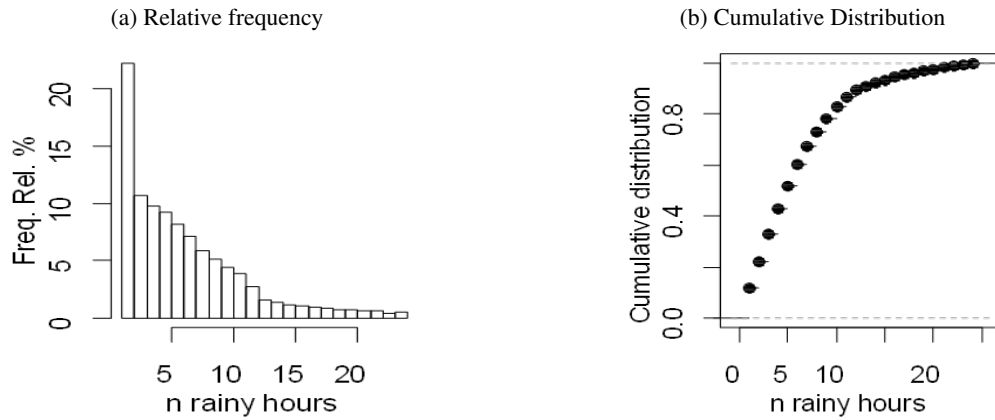
Figure A1. Distribution of daily rainy-hour counts from GsMap global hourly data 2000-2014. (a) Relative frequencies. (b) Cumulative probability

A5 Pedotransfer functions

From the models tested (Table 2), the equations from Balland et al. (2008), which use the largest dataset and non-linear formulations outperformed the other models with the explained variance exceeding 60% for permanent wilting point (θ_{1500}), field capacity (θ_{33}) and saturation (θ_{sat}) (Fig.A2).
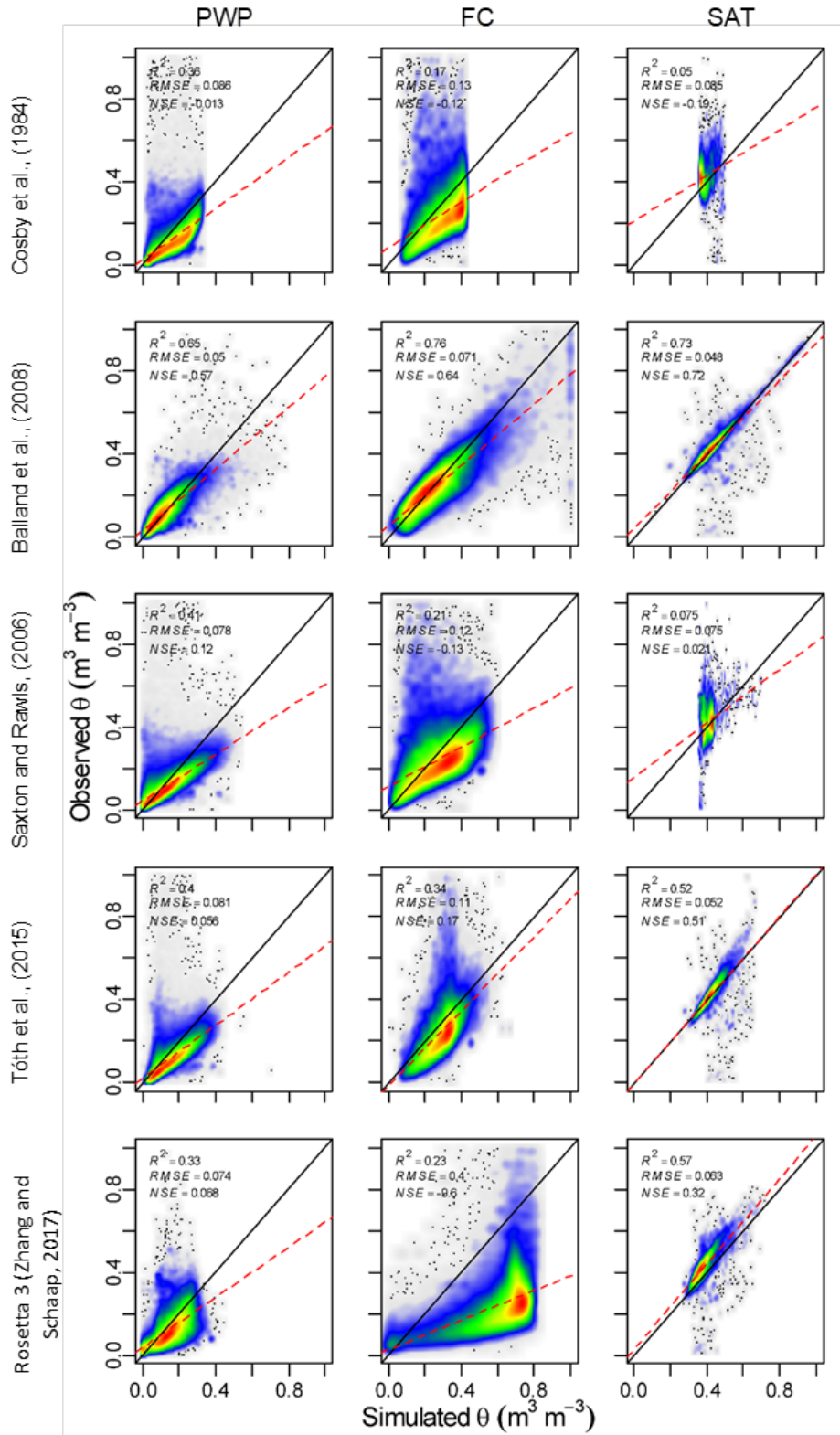
Figure A2. Evaluation of different pedotransfer functions to estimate θ_{1500}, θ_{33} and θ_{sat}, n = 68567.

The PTFs for computing K_{sat} showed poor performances for all the models, most of the measurements seem to cluster around 0 to 50 $mm\,h^{-1}$ which is only captured by the Cosby et al. (1984) model. Overall, the explained variance of all the models didn't reach the 10%, (Fig. A3). Here, K_{sat} values exceeding 526 $mm\,h^{-1}$ were considered as outliers (percentile 90%) and excluded from the analysis, similar maximum values were presented by Van Looy et al. (2017).
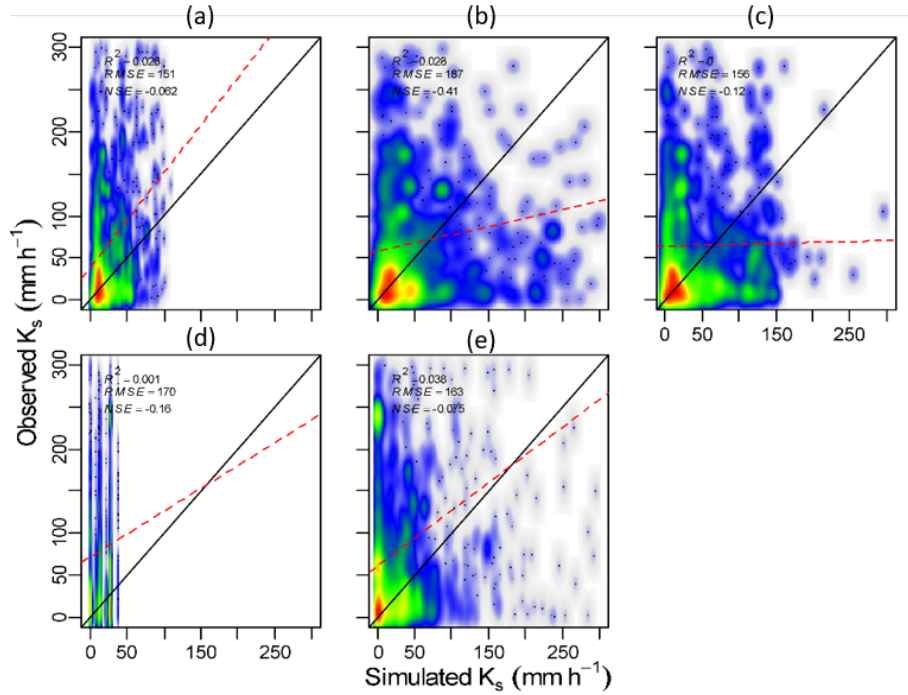
Figure A3. Evaluation of different pedotransfer functions to estimate K_{sat}. (a) Cosby et al. (1984). (b) Balland et al. (2008). (c) Saxton and Rawls (2006). (d) Tóth et al. (2015). (e) Rosetta 3 (Zhang and Schaap, 2017).

945   K_{sat} estimated by the Saxton and Rawls (2006) PFT was the best performing model, however, it leads to unrealistic values when the drainable porosity ($\theta_{sat} - \theta_{33}$) is relatively high. So, a simple exponential saturating curve was adopted here, which yields similar estimations to Saxton and Rawls (2006) at the lower end of the drainable porosity but it flattens at a fitted K_{sat} maximum of 623 $mm\,h^{-1}$.

Furthermore, to improve these estimations, the equations from Balland et al. (2008) (Eq. A25a,A25b,A25c,A25d) were
950   optimized using the full dataset employed for this evaluation resulting in the parameters detailed in Table A1.

$$\theta_{1500} = \theta_{33}\left(c_{wp} + (d_{wp} - c_{wp})\,CLAY^{0.5}\right) \tag{A25a}$$

$$\theta_{33} = \theta_{sat}\left(c_{fc} + (d_{fc} - c_{fc})\,CLAY^{0.5}\right)e^{\frac{a_{fc}SAND - b_{fc}SOM}{\theta_{sat}}} \tag{A25b}$$

$$\theta_{sat} = 1 - \frac{\rho_b}{\rho_p} \tag{A25c}$$

$$K_{sat} = 10^{a_{ks} + b_{ks}\,log_{10}(\rho_p - \rho_b) + c_{ks}SAND} \tag{A25d}$$

955 Were θ_{1500} is wilting point (water held at 1500kPa), θ_{33} is field capacity (water held at 33kPa), θ_{sat} is saturation, K_{sat} the saturated hydraulic conductivity, and, SAND, CLAY and SOM refer to sand, clay and organic matter contents (%). a, b, c are constants with the subscripts referring to wilting point, field capacity or hydraulic saturated conductivity respectively, ρ_b is the bulk density, and ρ_p is the particle density, calculated as follows (Balland et al., 2008):

$$\rho_p = \frac{1}{\frac{SOM}{1.3} + \frac{1-SOM}{2.65}} \tag{A26}$$

Table A1. Updated parameters for the Balland et al. (2008) PTFs

	a_x	b_x	c_x	d_x
θ_{1500}	–	–	0.2018	0.7809
θ_{33}	-0.0547	-0.0010	0.4760	0.9402
K_{sat}	-2.6539	3.0924	4.2146	–

Table A1. IGBP Biomes and their description

Biome	Code	Description
Evergreen Needleleaf Forests	ENF	Dominated by evergreen conifer trees (canopy >2m). Tree cover >60%.
Evergreen Broadleaf Forests	EBF	Dominated by evergreen broadleaf and palmate trees (canopy >2m). Tree cover >60%.
Deciduous Needleleaf Forests	DNF	Dominated by deciduous needleleaf (larch) trees (canopy >2m). Tree cover >60%.
Deciduous Broadleaf Forests	DBF	Dominated by deciduous broadleaf trees (canopy >2m). Tree cover >60%.
Mixed Forests	MF	Dominated by neither deciduous nor evergreen (40-60% of each) tree type (canopy >2m). Tree cover >60%.
Closed Shrublands	CSH	Dominated by >60% cover. woody perennials (1-2m height)
Open Shrublands	OSH	Dominated by 10-60% cover. woody perennials (1-2m height)
Woody Savannas	WSA	Tree cover 30-60% (canopy >2m).
Savannas	SAV	Tree cover 10-30% (canopy >2m).
Grasslands	GRA	Dominated by herbaceous annuals (<2m).
Permanent Wetlands	WET	Permanently inundated lands with 30-60% water cover and >10% vegetated cover.
Croplands	CRO	At least 60% of area is cultivated cropland.
Cropland/Natural Vegetation Mosaics	CNV	Mosaics of small-scale cultivation 40-60% with natural tree, shrub, or herbaceous vegetation.
Permanent Snow and Ice	SNO	At least 60% of area is covered by snow and ice for at least 10 months of the year.
Barren	BSV	At least 60% of area is non-vegetated barren (sand, rock, soil) areas with less than 10% vegetation.

Table A2. Köppen-Geiger climate zones after Beck et al. (2018). Where, T_{cold} is the air temperature of the coldest month (°C); T_{hot} is the air temperature of the warmest month (°C); T_{mon10} is the number of months with air temperature > 10 °C (unitless); P_{dry} is the precipitation in the driest month ($mm\,mo^{-1}$); P_{sdry} is the precipitation in the driest month in summer ($mm\,mo^{-1}$); P_{wdry} is precipitation in the driest month in winter ($mm\,mo^{-1}$); P_{swet} is precipitation in the wettest month in summer ($mm\,mo^{-1}$); P_{wwet} is precipitation in the wettest month in winter ($mm\,mo^{-1}$). $P_{threshold}$ = 2×MAT if >70% of precipitation falls in winter, $P_{threshold}$ =2×MAT+28 if >70% of precipitation falls in summer, otherwise $P_{threshold}$ = 2×MAT+14.

1st level	2nd level	3rd level	Description	Criteria
			Tropical	Not (B) and $T_{cold} \leq 18\ P_{dry}$
	f		Rainforest	$P_{dry} \geq 60$
A	m		Monsoon	Not (Af) and $P_{dry} \geq 100 - MAP/25$
	w		Savanna (Dry winter)	Not (Af) and $P_{dry} < 100 - MAP/25$
	s		Savanna (Dry summer)	Not (Af) and $P_{dry} < P_{wwet}/3$
			Arid	$MAP < 10 \times P_{threshold}$
	W		Desert	$MAP < 5 \times P_{threshold}$
B	S		Steppe	$MAP \geq 5 \times P_{threshold}$
		h	- Hot	$MAP \geq 18$
		k	- Cold	$MAP < 18$
			Temperate	Not (B) $T_{hot} > 10$ and $0 < T_{cold} < 18$
	s		Dry summer	$P_{sdry} < 40$ and $P_{sdry} < P_{wwet}/3$
	w		Dry winter	$P_{sdry} < P_{swet}/10$
C	f		No dry season	Not (Cs) or (Cw)
		a	- Hot summer	$T_{hot} \geq 22$
		b	- Warm summer	Not (a) and $T_{mon} \geq 4$
		c	- Cold summer	Not (a or b) and $1 \leq T_{mon10} < 4$
			Continental	Not (B) $T_{hot} > 10$ and $0 < T_{cold} \leq 0$
	s		Dry summer	$P_{sdry} < 40$ and $P_{sdry} < P_{wwet}/3$
	w		Dry winter	$P_{wdry} < P_{swet}/10$
	f		No dry season	Not (Ds) or (Dw)
D		a	- Hot summer	$T_{hot} \geq 22$
		b	- Warm summer	Not (a) and $T_{mon} \geq 4$
		c	- Cold summer	Not (a, b, or d)
		d	- Very cold winter	Not (a or b) and $T_{cold} < -38$
			Polar	Not (B) $T_{hot} \leq 10$
E	T		Tundra	$T_{hot} > 0$
	F		Frost	$T_{hot} \leq 0$

Table A3: Eddy covariance stations used in the performance evaluation. Where Lat. is latitude (°), Lon. is longitude (°), Net. is the network, here FLX, EUR and AME stand for Fluxnet, Europeflux and Ameriflux respectively. Climate refers to the Köppen-Geiger climate zone, Biome as defined by the IGBP (Table A1) (Friedl et al., 2019). Elev. is the elevation in masl, Slop. and Asp. are the slope (°) and aspect (°) respectively and Au. is the upslope draining area (km^2)

Station	Lat.	Lon.	Net.	Climate	Biome	Period	Elev.	Slop.	Asp	Au	Reference
AT-Neu	47.12	11.32	FLX	Dfc	GRA	2002-2012	981	10	135	0.50	Wohlfahrt et al. (2008)
AU-Rob	-17.12	145.63	FLX	Cfa	EBF	2014-2014	712	1	126	1.88	Bristow et al. (2016)
AU-Tum	-35.66	148.15	FLX	Cfb	ENF	2001-2014	1243	2	26	0.08	Leuning et al. (2005)
AU-Wac	-37.43	145.19	FLX	Cfb	EBF	2005-2008	704	0	311	0.01	Kilinc et al. (2013)
BE-Jal	50.56	6.07	EUR	Cfb	MF	2006-2007	480	1	198	1.49	− − −
CH-Cha	47.21	8.41	FLX	Cfb	SAV	2005-2014	392	0	331	0.07	Merbold et al. (2014)
CH-Dav	46.82	9.86	FLX	ET	MF	1997-2014	1628	22	271	0.01	Zielis et al. (2014)
CH-Fru	47.12	8.54	FLX	Cfb	GRA	2005-2014	974	1	262	0.02	Imer et al. (2013)
CH-Lae	47.48	8.37	FLX	Cfb	MF	2004-2014	679	18	180	0.02	Etzold et al. (2011)
CH-Oe1	47.29	7.73	FLX	Cfb	CRO	2002-2008	454	0	78	0.02	Ammann et al. (2009)
CH-Oe2	47.29	7.73	FLX	Cfb	CRO	2004-2014	454	0	78	0.02	Dietiker et al. (2010)
CN-Dan	30.50	91.07	FLX	ET	GRA	2004-2005	4316	1	128	0.70	Shi et al. (2006)
CN-Ha2	37.61	101.33	FLX	ET	GRA	2003-2005	3205	0	186	0.06	− − −
CN-HaM	37.37	101.18	FLX	ET	GRA	2002-2004	3985	9	97	0.01	Kato et al. (2006)
CZ-BK1	49.50	18.54	FLX	Dfb	ENF	2004-2014	833	9	62	0.01	Acosta et al. (2013)
CZ-BK2	49.49	18.54	FLX	Dfb	MF	2004-2012	859	5	125	0.03	Sigut et al.
DE-Lkb	49.10	13.30	FLX	Cfb	GRA	2009-2013	1305	5	160	0.01	Lindauer et al. (2014)
DE-Obe	50.78	13.72	FLX	Cfb	ENF	2008-2014	767	3	336	0.01	− − −
DK-NuF	64.13	-51.39	FLX	ET	GRA	2008-2009	46	4	343	0.01	Westergaard-Nielsen et al. (2013)
ES-LgS	37.10	-2.97	FLX	Csa	SAV	2007-2009	2250	3	322	0.06	Reverter et al. (2010)
ES-LJu	36.93	-2.75	EUR	Csa	OSH	2004-2013	1610	3	309	0.01	− − −
ES-Ln2	36.97	-3.48	FLX	Csa	SAV	2009-2009	2180	9	186	0.01	Serrano-Ortiz et al. (2011)
ES-VDA	42.15	1.45	EUR	Cfb	SAV	2004-2008	1759	2	318	0.09	− − −
FR-Lq1	45.64	2.74	EUR	Cfb	SAV	2004-2010	1031	4	257	0.96	− − −
FR-Lq2	45.64	2.74	EUR	Cfb	SAV	2006-2010	1031	4	257	0.96	− − −
GL-NuF	64.13	-51.39	EUR	ET	GRA	2008-2014	46	4	343	0.01	López-Blanco et al. (2017)
HU-Mat	47.85	19.73	EUR	Cfb	SAV	2004-2008	302	4	236	0.03	− − −
IL-Yat	31.35	35.05	EUR	BSh	ENF	2001-2009	647	1	245	0.03	− − −
IT-Amp	41.90	13.61	EUR	Cfa	SAV	2002-2008	836	1	202	0.15	− − −
IT-Col	41.85	13.59	FLX	Cfa	SAV	1996-2014	1571	11	222	0.12	Valentini et al. (1996)
IT-La2	45.95	11.29	FLX	Cfb	ENF	2000-2002	1375	4	183	0.01	Marcolla et al. (2003)
IT-Lav	45.96	11.28	FLX	Cfb	ENF	2003-2014	1403	5	213	0.02	− − −
IT-Mal	46.11	11.70	EUR	ET	MF	2003-2006	1660	8	142	0.08	− − −
IT-MBo	46.01	11.05	FLX	Dfb	GRA	2003-2013	1557	3	112	0.65	Marcolla et al. (2011)
IT-Ren	46.59	11.43	FLX	Dfc	WSA	1998-2013	1761	11	221	0.03	Montagnani et al. (2009)
IT-To1	42.19	11.92	EUR	Csa	MF	2004-2006	367	7	3	0.01	− − −
IT-To2	42.19	11.92	EUR	Csa	MF	2004-2006	367	7	3	0.01	− − −
IT-Tol	42.19	11.92	EUR	Csa	MF	2005-2006	367	7	3	0.01	− − −
IT-Tor	45.84	7.58	FLX	Dfc	GRA	2008-2014	2133	15	231	0.03	Galvagno et al. (2013)
JP-MBF	44.39	142.32	FLX	Dfb	WSA	2003-2005	580	2	88	0.02	− − −
SE-St1	68.35	19.05	EUR	ET	WET	2012-2014	352	0	101	0.33	− − −
SK-Ta1	49.16	20.26	EUR	Dfc	WSA	2006-2007	1010	7	130	0.06	− − −
SK-Ta2	49.13	20.11	EUR	Dfc	WSA	2007-2007	1268	9	187	0.58	− − −
SK-Tat	49.12	20.16	EUR	Dfc	WSA	2005-2007	1043	7	133	0.19	− − −

Continuation of Table A3

Station	Lat.	Lon	Net.	Climate	Biome	Period	Elev.	Slop.	Asp	Au	Reference
UK-Gri	56.61	-3.80	EUR	Cfc	ENF	2000-2006	359	2	0	0.23	– – –
US-ADR	36.77	-116.69	AME	BWk	BSV	2011-2017	852	0	158	0.11	?
US-Blk	44.16	-103.65	AME	Dfb	WSA	2004-2008	1762	4	135	0.09	Novick et al. (2016)
US-Blo	38.90	-120.63	FLX	Csa	ENF	1997-2007	1330	2	251	0.01	Goldstein et al. (2000)
US-CaV	39.06	-79.42	AME	Cfb	WSA	2004-2010	978	2	293	0.03	Meyers (2016)
US-CPk	41.07	-106.12	AME	Dfc	GRA	2009-2013	2758	0	73	0.02	Chu et al. (2018a)
US-CZ2	37.03	-119.26	AME	Csb	WSA	2010-2016	1181	3	91	0.05	Goulden (2018a)
US-CZ3	37.07	-119.20	AME	Csb	ENF	2008-2016	2020	2	231	0.01	Goulden (2018b)
US-CZ4	37.07	-118.99	AME	Dsc	WSA	2009-2016	2712	1	158	0.05	Goulden (2018c)
US-EML	63.88	-149.25	AME	Dfc	OSH	2008-2018	675	1	0	0.01	Belshe et al. (2012)
US-Fmf	35.14	-111.73	AME	Csb	GRA	2005-2010	2198	0	81	0.03	Amiro et al. (2010)
US-Fwf	35.45	-111.77	AME	Csb	GRA	2005-2010	2309	2	0	1.14	Amiro et al. (2010)
US-GBT	41.37	-106.24	FLX	Dfc	GRA	1999-2006	3193	3	182	0.05	Zeller and Nikolov (2000)
US-GLE	41.37	-106.24	FLX	Dfc	GRA	2004-2014	3193	3	182	0.05	Frank et al. (2014)
US-GMF	41.97	-73.23	AME	Dfb	MF	1999-2004	500	3	73	0.02	Chu et al. (2018b)
US-HBK	43.94	-71.72	AME	Dfb	DBF	2016-2019	396	6	356	0.01	Kelsey and Green (2020)
US-ICh	68.61	-149.30	AME	Dfc	OSH	2007-2011	950	3	271	0.01	Euskirchen et al. (2012a)
US-ICs	68.61	-149.31	AME	Dfc	OSH	2007-2011	898	1	281	0.57	Euskirchen et al. (2017)
US-ICt	68.61	-149.30	AME	Dfc	OSH	2007-2011	918	5	261	0.01	Euskirchen et al. (2012b)
US-Me1	44.58	-121.50	FLX	Csb	GRA	2004-2005	893	4	79	0.02	Irvine et al. (2007)
US-Me2	44.45	-121.56	FLX	Csb	ENF	2002-2014	1259	1	166	0.01	Campbell et al. (2004)
US-Me3	44.32	-121.61	AME	Csb	WSA	2004-2009	1006	0	49	0.04	Barr et al. (2013a)
US-Me4	44.50	-121.62	AME	Csb	ENF	1996-2000	956	7	274	0.03	Anthoni et al. (1999)
US-Me5	44.44	-121.57	AME	Csb	ENF	2000-2002	1189	2	208	0.81	Anthoni et al. (2002)
US-Me6	44.32	-121.61	FLX	Csb	WSA	2010-2014	999	0	65	23.80	Ruehr et al. (2012)
US-MRf	44.65	-123.55	AME	Csb	ENF	2006-2011	265	6	246	0.02	Chu et al. (2018c)
US-NR1	40.03	-105.55	FLX	Dfc	WSA	1998-2014	3039	7	83	0.03	Monson et al. (2002)
US-Rls	43.14	-116.74	AME	BSk	GRA	2014-2018	1611	5	343	0.02	Fellows et al. (2020)
US-Rms	43.06	-116.75	AME	BSk	GRA	2014-2018	2116	3	324	0.01	Fellows et al. (2020)
US-Rws	43.17	-116.71	AME	BSk	GRA	2014-2018	1437	4	349	0.07	Fellows et al. (2020)
US-SCf	33.81	-116.77	AME	Csa	ENF	2006-2015	1739	4	176	0.01	Goulden (2018d)
US-SCg	33.74	-117.69	AME	Csa	OSH	2006-2016	440	3	9	0.01	Goulden (2018e)
US-SCs	33.73	-117.70	AME	Csa	GRA	2006-2016	470	4	96	0.02	Goulden (2018f)
US-SCw	33.60	-116.45	AME	BWh	OSH	2006-2016	1290	2	263	0.01	Goulden (2018g)
US-SO2	33.37	-116.62	AME	Csa	SAV	1997-2006	1423	5	188	0.39	Barr et al. (2013b)
US-SO3	33.38	-116.62	AME	Csa	GRA	1997-2006	1480	7	201	0.01	Baldocchi et al. (2015)
US-SO4	33.38	-116.64	AME	Csa	GRA	2004-2006	1416	3	206	0.01	Baldocchi et al. (2015)
US-SRC	31.91	-110.84	AME	BSk	OSH	2008-2014	985	1	304	3.06	Wolf et al. (2016)
US-SRG	31.79	-110.83	FLX	BSk	GRA	2008-2014	1288	3	308	0.39	Scott et al. (2015)
US-SRM	31.82	-110.87	FLX	BSk	GRA	2004-2014	1112	1	295	0.05	Barron-Gafford et al. (2013)
US-Vcm	35.89	-106.53	AME	Cfb	GRA	2007-2019	2984	7	334	0.01	Anderson-Teixeira et al. (2011)
US-Vcp	35.86	-106.60	AME	Cfb	GRA	2007-2019	2503	9	255	0.19	Anderson-Teixeira et al. (2011)
US-Vcs	35.92	-106.61	AME	Cfb	WSA	2016-2019	2775	3	165	0.01	Remy et al. (2019)

Table A4: SNOTEL stations used in the performance evaluation. Where Lat. is latitude (°), Lon. is longitude (°), Climate refers to the Köppen-Geiger climate zone, Biome as defined by the IGBP (Table A1) (Friedl et al., 2019). Elev. is the elevation in masl, Slop. and Asp. are the slope (°) and aspect (°) respectively, Au. is the upslope draining area (km^2), and SM sens. is the depth of the soil profile (m) where the soil moisture was measured.

Station	Lat.	Lon	Climate	Biome	Period	Elev.	Slop.	Asp	Au	SM sens.	Site name
SNTL:1243	40.86	-115.22	BSk	GRA	2014-2015	1997	4	200	0.53	0.49	Dry Creek - NV
SNTL:1242	39.25	-119.88	Dsb	SAV	2014-2015	1979	0	116	25.64	0.49	Little Valley - NV
SNTL:1244	40.86	-115.12	Dsb	GRA	2014-2015	2365	7	148	8.50	0.49	Pole Canyon - NV
SNTL:1236	39.66	-110.38	BSk	GRA	2014-2015	2501	11	162	0.04	0.49	Corral - UT
SNTL:1248	37.60	-112.93	Dsb	GRA	2014-2015	2453	8	208	0.04	0.49	Suu Ranch - UT
SNTL:1214	40.46	-112.25	Dfb	GRA	2013-2015	1987	10	318	0.04	0.98	Bevans Cabin - UT
SNTL:1153	37.87	-109.45	Dsb	WSA	2013-2015	2720	6	1	5.66	0.49	Buckboard Flat - UT
SNTL:1215	38.48	-109.29	Dsb	GRA	2013-2015	2677	10	299	0.04	0.49	Lasal Mountain-Lower - UT
SNTL:1225	40.68	-111.22	Dfb	SAV	2013-2015	2600	5	302	0.04	0.49	Redden Mine Lwr - UT
SNTL:1217	39.50	-111.73	BSk	GRA	2013-2015	2196	14	4	0.08	0.49	Rees Flat - UT
SNTL:1155	39.46	-114.65	BSk	SAV	2012-2015	2297	13	21	0.04	0.49	Bird Creek - NV
SNTL:1207	41.89	-115.86	Dfb	GRA	2012-2012	2105	7	329	0.20	0.49	Merritt Mountain - NV
SNTL:1192	40.84	-110.66	Dfc	SAV	2012-2015	2935	2	63	47.60	0.49	Buck Pasture - UT
SNTL:1184	38.79	-111.69	BSk	SAV	2012-2015	2559	6	82	0.13	0.49	Gooseberry RS Up - UT
SNTL:992	40.89	-110.83	Dfc	GRA	2011-2015	2675	3	281	0.40	0.49	Bear River RS - UT
SNTL:1149	38.50	-111.77	BSk	GRA	2011-2015	2681	0	192	159.55	0.49	Fish Lake Utah - UT
SNTL:1145	41.25	-111.41	Dfb	SAV	2011-2015	2200	10	180	0.32	0.49	Kilfoil Creek - UT
SNTL:1159	48.95	-118.99	Dfc	WSA	2011-2015	1633	7	307	0.04	0.49	Gold Axe Camp - WA
SNTL:1144	47.98	-114.35	Dfc	WSA	2010-2014	1722	9	208	0.04	0.98	Blacktail Mtn - MT
SNTL:1117	40.84	-110.01	Dfc	WSA	2010-2015	3119	4	30	0.20	0.49	Spirit Lk - UT
SNTL:1113	41.89	-111.57	Dfb	GRA	2010-2015	1929	10	100	0.12	0.49	Tony Grove RS - UT
SNTL:1130	43.67	-109.38	Dfc	GRA	2010-2014	2560	7	167	0.04	0.98	Castle Creek - WY
SNTL:1123	40.51	-105.77	Dfc	WSA	2009-2014	3041	7	118	0.12	0.49	Long Draw Resv - CO
SNTL:1080	48.93	-121.20	Dsc	SAV	2009-2014	1776	19	12	0.11	0.49	Brown Top - WA
SNTL:1129	45.99	-120.81	Dsc	WSA	2009-2015	1633	8	170	0.11	0.20	Indian Rock - WA
SNTL:1107	47.71	-123.46	ET	ENF	2008-2014	1484	13	231	0.11	0.20	Buckinghorse - WA
SNTL:1085	46.87	-121.53	Dsc	WSA	2007-2011	1597	23	182	0.11	0.49	Cayuse Pass - WA
SNTL:1081	47.86	-117.04	Dsb	MF	2006-2014	1283	17	46	0.18	0.49	Ragged Mountain - ID
SNTL:999	48.76	-121.70	Dfc	ENF	2006-2009	1072	14	220	0.04	0.98	Marten Ridge - WA
SNTL:1056	41.36	-111.49	Dfb	GRA	2005-2015	2503	3	194	0.04	0.98	Lightning Ridge - UT
SNTL:1051	38.72	-119.89	Dsb	GRA	2004-2015	2477	9	213	0.08	0.49	Burnside Lake - CA
SNTL:1049	38.68	-119.96	Dsc	SAV	2004-2015	2443	3	172	0.08	0.49	Forestdale Creek - CA
SNTL:1043	48.86	-118.40	Dfb	ENF	2003-2014	1426	13	325	0.11	0.20	Sentinel Butte - WA
SNTL:1013	41.79	-111.55	Dfb	GRA	2002-2015	2257	4	254	0.04	0.49	Temple Fork - UT
SNTL:989	46.81	-116.85	Dsb	ENF	2001-2015	1432	2	267	0.04	0.49	Moscow Mountain - ID
SNTL:926	43.73	-113.83	Dfc	GRA	2001-2014	2901	8	334	0.08	0.49	Smiley Mountain - ID
SNTL:979	44.38	-116.34	Dsb	GRA	2001-2014	1499	7	205	0.88	0.49	Van Wyck - ID
SNTL:990	48.88	-121.26	Dfc	ENF	2001-2008	1106	14	55	0.18	0.98	Beaver Pass - WA
SNTL:985	46.24	-117.39	Dsb	GRA	2000-2014	1219	10	339	0.04	0.49	Sourdough Gulch - WA
SNTL:978	43.76	-116.10	Dsb	GRA	1999-2014	1932	13	336	0.04	0.49	Bogus Basin - ID
SNTL:2029	43.29	-116.84	BSk	GRA	1999-2014	1706	7	151	0.04	0.98	Reynolds Creek - ID
SNTL:942	47.04	-121.94	Dfc	ENF	1999-2013	1271	17	205	0.07	0.49	Burnt Mountain - WA
SNTL:974	47.94	-123.43	Dsc	ENF	1999-2014	1527	24	216	0.07	0.49	Waterhole - WA
SNTL:939	39.03	-106.08	Dfc	GRA	1998-2008	3157	5	338	0.12	0.98	Rough And Tumble - CO
SNTL:921	35.70	-105.81	Dfb	GRA	1997-2000	2502	7	290	0.91	0.49	Elk Cabin - NM

Station	Lat.	Lon	Climate	Biome	Period	Elev.	Slop.	Asp	Au	SM sens.	Site name
SNTL:914	37.85	-105.44	Dfc	SAV	1996-2001	2941	9	66	0.04	0.49	Medano Pass - CO
SNTL:907	37.52	-112.27	Dfb	GRA	1995-2004	2712	12	202	0.04	0.49	Agua Canyon - UT
SNTL:896	40.87	-111.72	Dsb	SAV	1994-2009	2209	8	283	0.12	0.49	Hardscrabble - UT
SNTL:895	43.77	-114.42	Dfb	SAV	1993-2005	1923	8	136	1.66	0.49	Chocolate Gulch - ID
SNTL:633	38.67	-119.61	Dsb	GRA	1991-2001	2531	6	10	0.17	0.49	Monitor Pass - CA
SNTL:387	37.66	-107.80	Dfb	SAV	1990-1995	2718	6	169	0.21	0.49	Cascade #2 - CO
SNTL:623	47.15	-116.27	Dsb	ENF	1990-1998	1374	11	330	0.04	0.49	Mica Creek - ID
SNTL:871	42.01	-115.00	BSk	GRA	1990-2002	2170	3	229	0.04	0.49	Wilson Creek - ID
SNTL:599	46.36	-121.08	Dsc	GRA	1990-2004	1560	3	44	0.04	0.20	Lost Horse - WA
SNTL:783	47.18	-114.33	Dfc	WSA	1989-1997	1874	11	27	0.47	0.98	Sleeping Woman - MT
SNTL:707	47.88	-117.09	Dsb	ENF	1986-1998	1432	9	272	0.04	0.49	Quartz Peak - WA
SNTL:522	40.91	-109.96	Dfc	GRA	1985-1995	2780	2	191	0.57	0.49	Hickerson Park - UT
SNTL:694	38.88	-112.25	Dfb	SAV	1985-1995	2662	27	10	0.08	0.49	Pine Creek - UT
SNTL:778	38.67	-119.82	Dsb	SAV	1984-1996	1848	11	97	0.04	0.49	Spratt Creek - CA
SNTL:425	46.56	-115.29	Dsc	WSA	1984-1988	1816	1	25	0.04	0.49	Crater Meadows - ID
SNTL:340	39.45	-119.94	Dsb	SAV	1984-1994	2510	8	18	0.12	0.49	Big Meadow - NV
SNTL:454	41.66	-115.32	BSk	GRA	1984-1997	2220	13	46	0.04	0.49	Draw Creek - NV
SNTL:734	47.38	-121.06	Dsc	WSA	1984-1998	1322	4	23	0.04	0.49	Sasse Ridge - WA
SNTL:735	46.47	-114.63	Dsc	ENF	1983-1988	1886	7	251	0.04	0.49	Savage Pass - ID
SNTL:356	38.61	-119.92	Dsc	SAV	1981-1991	2458	3	316	0.04	0.49	Blue Lakes - CA
SNTL:463	38.85	-120.08	Dsb	WSA	1981-1993	2332	19	182	0.42	0.49	Echo Peak - CA
SNTL:724	39.00	-120.13	Dsb	ENF	1981-1994	2322	8	37	0.08	0.49	Rubicon #2 - CA
SNTL:834	39.30	-120.18	Dsb	ENF	1981-1994	1983	6	52	0.25	0.49	Truckee #2 - CA
SNTL:445	41.97	-118.19	BSk	GRA	1981-1992	1908	18	135	0.12	0.49	Disaster Peak - NV
SNTL:652	39.32	-119.89	Dsc	GRA	1981-1990	2682	18	343	0.04	0.49	Mt Rose Ski Area - NV
SNTL:849	39.13	-114.96	BSk	GRA	1981-1991	2804	21	234	0.04	0.49	Ward Mountain - NV
SNTL:784	39.19	-120.27	Dsb	GRA	1980-1991	2442	8	117	0.17	0.49	Squaw Valley G.C. - CA
SNTL:848	39.14	-120.22	Dsb	ENF	1980-1992	2055	3	128	3.36	0.49	Ward Creek #3 - CA
SNTL:531	39.36	-106.06	ET	GRA	1980-1990	3474	7	225	0.04	0.98	Hoosier Pass - CO
SNTL:688	40.40	-105.85	Dfc	GRA	1980-1985	2752	2	79	63.23	0.49	Phantom Valley - CO
SNTL:312	44.30	-115.23	Dsc	WSA	1980-1988	2145	1	48	0.04	0.49	Banner Summit - ID
SNTL:424	44.44	-111.99	Dfc	WSA	1980-1988	2103	5	46	0.19	0.49	Crab Creek - ID
SNTL:550	44.05	-115.44	Dsc	WSA	1980-1998	2154	7	323	0.04	0.49	Jackson Peak - ID
SNTL:752	46.95	-116.34	Dsb	WSA	1980-1981	975	2	42	0.69	0.49	Sherwin - ID
SNTL:395	43.23	-121.81	Dsb	WSA	1980-1992	1478	1	104	0.04	0.98	Chemult Alternate - OR
SNTL:529	43.67	-122.57	Csb	ENF	1980-1985	1502	3	267	0.04	0.98	Holland Meadows - OR
SNTL:647	45.27	-117.69	Dsc	ENF	1980-1992	1755	5	43	0.04	0.98	Moss Springs - OR
SNTL:653	45.27	-117.17	Dsc	SAV	1980-1992	2410	9	16	0.04	0.98	Mt. Howard - OR
SNTL:706	42.32	-120.83	Dsb	SAV	1980-1994	1743	3	278	0.67	0.98	Quartz Mountain - OR
SNTL:721	44.01	-118.84	BSk	GRA	1980-1999	1612	1	208	0.69	0.20	Rock Springs - OR
SNTL:729	43.61	-122.12	Dsb	ENF	1980-1985	1286	1	189	0.12	0.49	Salt Creek Falls - OR
SNTL:756	42.96	-121.18	Dsb	WSA	1980-1994	1749	3	39	0.04	0.20	Silver Creek - OR
SNTL:557	38.48	-112.39	Dsc	SAV	1980-1992	2773	14	352	0.84	0.49	Kimberly Mine - UT
SNTL:679	46.78	-121.75	Dfc	ENF	1980-1983	1563	9	216	0.15	0.49	Paradise - WA
SNTL:711	48.52	-120.74	Dsc	ENF	1980-1987	1490	19	41	0.04	0.49	Rainy Pass - WA
SNTL:824	46.12	-117.85	Dsb	WSA	1980-1994	1685	2	30	0.04	0.49	Touchet - WA
SNTL:508	38.85	-119.94	Dsb	WSA	1979-1992	2359	8	10	0.08	0.49	Hagans Meadow - CA
SNTL:539	39.45	-120.29	Dsb	WET	1979-1991	2127	0	130	0.08	0.49	Independence Camp - CA
SNTL:541	39.43	-120.31	Dsb	WSA	1979-1992	2541	12	48	0.04	0.49	Independence Lake - CA
SNTL:587	38.44	-119.37	Dsb	GRA	1979-1990	2819	0	300	9.89	0.49	Lobdell Lake - CA

Continuation of Table A4

Station	Lat.	Lon	Climate	Biome	Period	Elev.	Slop.	Asp	Au	SM sens.	Site name
SNTL:771	38.31	-119.60	Dsc	SAV	1979-1991	2673	12	28	0.04	0.49	Sonora Pass - CA
SNTL:846	38.07	-119.23	Dsc	GRA	1979-1991	2878	8	152	0.04	0.49	Virginia Lakes Ridge - CA
SNTL:682	39.05	-107.87	Dfc	SAV	1979-1984	3035	5	260	0.17	0.49	Park Reservoir - CO
SNTL:484	42.05	-111.60	Dfc	GRA	1979-1992	2481	5	271	0.28	0.49	Franklin Basin - ID
SNTL:490	43.87	-114.71	Dsc	SAV	1979-1984	2676	7	107	0.04	0.49	Galena Summit - ID
SNTL:594	47.46	-115.70	Dsb	WSA	1979-1988	1581	10	10	0.04	0.49	Lookout - ID
SNTL:645	48.06	-116.23	Dsc	ENF	1979-1984	1603	8	202	0.07	0.49	Mosquito Ridge - ID
SNTL:749	43.21	-111.69	Dfb	MF	1979-1988	2026	10	39	0.08	0.49	Sheep Mtn. - ID
SNTL:770	42.95	-111.36	Dfb	WSA	1979-1989	2072	9	36	0.20	0.49	Somsen Ranch - ID
SNTL:774	42.76	-116.90	Dsb	GRA	1979-1988	1981	13	37	0.28	0.49	South Mtn. - ID
SNTL:532	36.72	-106.26	Dfc	GRA	1979-1982	3048	1	63	0.04	0.49	Hopewell - NM
SNTL:615	39.16	-119.90	Dsb	WSA	1979-1992	2403	9	41	0.04	0.49	Marlette Lake - NV
SNTL:344	42.41	-122.27	Dsc	ENF	1979-1992	1609	4	125	0.16	0.98	Billie Creek Divide - OR
SNTL:361	44.83	-118.19	Dsc	WSA	1979-1987	1783	19	164	0.08	0.49	Bourne - OR
SNTL:523	45.70	-118.11	Dsb	ENF	1979-1991	1499	7	12	0.15	0.98	High Ridge - OR
SNTL:759	42.75	-118.69	Dsb	GRA	1979-1998	2130	2	277	0.04	0.98	Silvies - OR
SNTL:821	44.66	-118.43	Dsb	WSA	1979-1991	1569	6	334	0.04	0.49	Tipton - OR
SNTL:339	38.30	-112.36	Dfc	SAV	1979-1992	3154	2	311	0.21	0.49	Big Flat - UT
SNTL:364	38.51	-112.02	Dfc	GRA	1979-1992	3003	1	148	0.04	0.49	Box Creek - UT
SNTL:455	41.41	-111.54	Dfc	GRA	1979-1992	2530	1	90	0.12	0.49	Dry Bread Pond - UT
SNTL:495	38.80	-111.68	BSk	GRA	1979-1992	2421	6	282	0.04	0.49	Gooseberry RS - UT
SNTL:832	47.23	-120.29	Dsc	SAV	1979-1993	1670	4	55	0.58	0.20	Trough - WA
SNTL:358	44.68	-107.58	Dfc	GRA	1979-1986	2849	6	301	0.11	0.98	Bone Springs Div - WY
SNTL:613	48.80	-113.67	Dfc	WSA	1977-1993	1493	16	172	0.04	0.20	Many Glacier - MT
SNTL:781	46.78	-110.62	Dfc	WSA	1967-1972	2468	4	339	0.04	0.98	Spur Park - MT
SNTL:554	42.27	-110.80	Dfc	GRA	1964-1965	2493	6	122	0.20	0.49	Kelley R.S. - WY
SNTL:342	42.65	-109.26	Dfc	GRA	1963-1977	2767	3	251	0.87	0.49	Big Sandy Opening - WY
SNTL:822	43.75	-110.06	Dfc	GRA	1961-1974	2919	5	199	0.23	0.49	Togwotee Pass - WY
SCAN:2160	41.78	-113.82	BSk	GRA	2010-2014	1778	2	172	0.16	0.98	Grouse Creek - UT
SCAN:2149	37.78	-118.42	BWk	GRA	2009-2014	1884	4	249	0.13	0.98	Marble Creek - CA
SCAN:2142	36.37	-115.78	BSk	OSH	2008-2015	2391	8	201	0.04	0.98	Trough Springs - NV
SCAN:2074	42.02	-121.39	BSk	CRO	2003-2014	1247	0	198	0.28	0.98	Lynhart Ranch - OR

Table A5: GSIM hydrometric stations used in the streamflow performance evaluation. Where Lat. is latitude (°), Lon. is longitude (°), Climate refers to the three largest Köppen-Geiger climate zones in the watershed, Biome refers to the three largest biomes in the watershed, as defined by the IGBP (Table A1) (Friedl et al., 2019). Elev. is the elevation range in masl. Area is the watershed area (km^2) and River lists the river name and country.

Station	Lat	Lon	Climate	Biome	Period	Elev	Area	River
CA_0000351	48.52	-89.18	Dfb: 98.9%; Dfc: 1.1%	MF: 56.8%; WSA: 37.8%; DBF: 5.4%	1980-2014	341-514	104.70	North Current River - CA
CA_0000373	48.85	-86.61	Dfc: 77.4%; Dfb: 22.6%	MF: 83.1%; WSA: 10.1%; ENF: 6.7%	1980-2014	211-536	1324.17	Little Pic River - CA
CA_0000391	47.00	-84.52	Dfb: 100%	MF: 56%; DBF: 39.5%; WSA: 3.7%	1980-2014	239-601	1227.64	Batchawana River - CA
CA_0000395	47.06	-84.43	Dfb: 100%	DBF: 100%	1980-2014	370-521	10.36	Norberg Creek - CA
CA_0000396	47.05	-84.41	Dfb: 100%	DBF: 100%	1980-2014	373-521	8.03	Norberg Creek - CA
CA_0000397	47.04	-84.41	Dfb: 100%	DBF: 100%	1980-2014	387-521	5.05	Norberg Creek - CA
CA_0001119	46.37	-74.50	Dfb: 52.3%; Dfc: 47.7%	MF: 100%	1980-2013	447-732	39.90	Saintlouis Ruisseau A 03 Km De La River - CA
CA_0001273	46.44	-73.46	Dfb: 97.2%; Dfc: 2.8%	MF: 96.2%; WSA: 3.2%; DBF: 0.6%	1980-2013	275-663	186.00	Mastigouche River - CA
CA_0001411	47.26	-71.14	Dfc: 100%	MF: 89.2%; WSA: 9.6%; ENF: 1.2%	1980-2013	581-1065	269.00	Montmorency River - CA
CA_0001418	47.27	-71.14	Dfc: 100%	MF: 85.7%; WSA: 14.3%	1980-2013	581-904	9.17	Eaux Volees Ruisseau Des Pres De La River - CA
CA_0001423	47.12	-70.82	Dfc: 88.2%; Dfb: 11.8%	MF: 76.2%; WSA: 15.5%; DBF: 4.5%	1980-1994	288-1106	974.00	Sainteanne Du Nord River - CA
CA_0001527	49.88	-70.93	Dfc: 100%	WSA: 53.3%; ENF: 31.6%; SAV: 8.5%	1980-2007	248-975	1717.00	Manouane River - CA
CA_0001556	49.33	-70.98	Dfc: 100%	MF: 71%; ENF: 23.7%; WSA: 5.4%	1980-1994	383-603	277.00	Shipshaw River - CA
CA_0001566	47.94	-71.38	Dfc: 100%	MF: 81.2%; ENF: 9.1%; WSA: 8.8%	1980-2013	559-1037	495.00	Pikauba River - CA
CA_0001679	48.81	-57.78	Dfc: 100%	WSA: 68.8%; SAV: 31.2%	1980-2014	327-584	12.90	Copper Pond Brook - CA
CA_0002036	49.66	-114.13	Dfc: 75%; Dfb: 24.6%; ET: 0.4%	GRA: 65.4%; ENF: 19.9%; WSA: 12.6%	1980-1993	1201-2293	144.00	Todd Creek - CA
CA_0002038	49.60	-114.41	Dfc: 97.3%; ET: 2.7%	WSA: 37.5%; ENF: 37.2%; GRA: 23.4%	1980-2012	1282-2458	402.70	Crowsnest River - CA
CA_0002041	49.47	-114.13	Dfc: 93.4%; Dfb: 6.3%; ET: 0.3%	WSA: 32.4%; ENF: 26.5%; GRA: 24%	1980-2012	1236-2356	179.00	Mill Creek - CA
CA_0002047	49.49	-114.14	Dfc: 93.9%; Dfb: 5.1%; ET: 0.9%	ENF: 31.7%; GRA: 31.2%; WSA: 26.4%	1980-2013	1198-2498	820.70	Castle River - CA
CA_0002048	49.81	-114.18	Dfc: 91.2%; ET: 8.6%; Dfb: 0.2%	WSA: 44.5%; ENF: 36.6%; GRA: 17.4%	1980-2008	1280-2757	1446.10	Oldman River - CA
CA_0002051	49.90	-114.43	Dfc: 89.4%; ET: 10.6%	WSA: 42.6%; ENF: 40.4%; GRA: 16.2%	1980-1995	1505-2669	143.00	Dutch Creek - CA
CA_0002052	49.84	-114.42	Dfc: 96.7%; ET: 3.3%	ENF: 53.1%; WSA: 34.6%; GRA: 11.7%	1980-2013	1466-2511	217.60	Racehorse Creek - CA
CA_0002053	49.40	-114.34	Dfc: 99.1%; ET: 0.9%	ENF: 45.6%; SAV: 18.5%; GRA: 18.4%	1980-2014	1354-2420	375.30	Castle River - CA

Station	Lat	Lon	Climate	Biome	Period	Elev	Area	River
CA_0002055	49.60	-114.40	Dfc: 99.1%; ET: 0.9%	WSA: 40.4%; ENF: 32.3%; GRA: 24.2%	1980-2014	1335-2322	63.30	Gold Creek - CA
CA_0002057	49.31	-114.08	Dfc: 100%	GRA: 50%; SAV: 28.9%; WSA: 18.4%	1980-2012	1589-2235	24.00	Pincher Creek - CA
CA_0002059	49.76	-114.24	Dfc: 99.3%; ET: 0.7%	GRA: 46.1%; ENF: 33%; WSA: 20.9%	1980-2013	1406-2293	74.00	Todd Creek - CA
CA_0002064	49.64	-113.80	Dfc: 52.1%; Dfb: 47.9%	GRA: 61.4%; ENF: 16.4%; WSA: 11.4%	1980-2012	1102-1770	255.80	Beaver Creek - CA
CA_0002072	50.02	-113.71	Dfc: 72.9%; Dfb: 27%; ET: 0.1%	GRA: 54.2%; WSA: 21.2%; ENF: 10.8%	1980-2013	1001-2368	1180.60	Willow Creek - CA
CA_0002079	50.20	-114.21	Dfc: 99.7%; ET: 0.3%	WSA: 46.3%; ENF: 36.5%; GRA: 7.8%	1980-1995	1315-2229	162.00	Willow Creek - CA
CA_0002087	50.14	-113.94	Dfc: 99.4%; Dfb: 0.4%; ET: 0.1%	GRA: 45.2%; WSA: 31.9%; ENF: 16.6%	1980-1997	1172-2368	727.00	Willow Creek - CA
CA_0002088	50.24	-114.35	Dfc: 99.2%; ET: 0.8%	ENF: 54.2%; WSA: 30.8%; GRA: 9.3%	1980-2014	1478-2229	65.30	Willow Creek - CA
CA_0002089	50.13	-113.85	Dfc: 96%; Dfb: 3.9%; ET: 0.1%	GRA: 49.8%; WSA: 29.3%; ENF: 15.2%	1980-2012	1079-2368	832.90	Willow Creek - CA
CA_0002091	50.12	-113.75	Dfb: 93.8%; Dfc: 6.2%	GRA: 52%; CRO: 48%	1980-2013	1038-1381	85.70	Na - CA
CA_0002133	49.11	-113.84	Dfc: 93.1%; ET: 4%; Dfb: 2.9%	GRA: 39.3%; WSA: 24.4%; ENF: 16.3%	1980-2012	1274-2699	612.70	Waterton River - CA
CA_0002135	49.10	-113.70	Dfc: 94.8%; ET: 4.9%; Dfb: 0.4%	GRA: 41.8%; WSA: 22.3%; ENF: 19.5%	1980-2014	1340-2940	319.20	Belly River - CA
CA_0002166	49.23	-113.96	Dfc: 92.1%; ET: 7.9%	GRA: 71.6%; ENF: 10.8%; SAV: 9.5%	1980-2013	1460-2483	47.90	Yarrow Creek - CA
CA_0002198	48.83	-113.52	Dfc: 93%; ET: 7%	GRA: 65.7%; WSA: 15%; ENF: 9.8%	1980-1994	1454-2757	168.00	Swiftcurrent Creek - CA
CA_0002206	49.03	-113.54	Dfc: 100%	WSA: 44.4%; ENF: 34%; GRA: 14.6%	1980-1992	1436-2267	93.80	Lee Creek - CA
CA_0002264	49.74	-110.04	Dfb: 74.1%; Dfc: 25.9%	CRO: 88%; GRA: 5.4%; ENF: 2.2%	1980-1993	998-1390	75.10	Mackay Creek - CA
CA_0002279	51.43	-116.19	ET: 67.8%; Dfc: 32.2%	GRA: 29.1%; BSV: 26.5%; ENF: 17.2%	1980-2014	1541-2978	422.40	Bow River - CA
CA_0002280	51.43	-116.17	ET: 80.2%; Dfc: 19.8%	GRA: 46.7%; BSV: 20.9%; ENF: 12.8%	1980-2014	1618-3093	306.10	Pipestone River - CA
CA_0002284	51.24	-115.84	ET: 78%; Dfc: 22%	GRA: 49.5%; WSA: 17.3%; BSV: 16.8%	1980-1996	1449-2904	124.00	Johnston Creek - CA
CA_0002292	51.10	-115.67	ET: 69.7%; Dfc: 30.3%	GRA: 53.9%; WSA: 33.9%; ENF: 7.8%	1980-1996	1622-2762	109.00	Brewster Creek - CA
CA_0002293	51.22	-115.81	ET: 69.2%; Dfc: 30.8%	GRA: 33.3%; WSA: 32.9%; ENF: 17.3%	1980-1996	1449-3155	147.00	Redearth Creek - CA
CA_0002294	51.16	-115.55	ET: 50.1%; Dfc: 49.9%	GRA: 44.1%; WSA: 36.5%; ENF: 11.4%	1980-2014	1432-3079	750.60	Spray River - CA
CA_0002299	51.06	-115.43	Dfc: 65.3%; ET: 34.7%	WSA: 62.7%; GRA: 28.8%; ENF: 8.5%	1980-2012	1643-2693	40.90	Goat Creek - CA
CA_0002303	51.29	-115.53	ET: 77%; Dfc: 23%	GRA: 55.5%; WSA: 20.9%; ENF: 14.8%	1980-1996	1571-3043	454.00	Cascade River - CA
CA_0002314	50.70	-115.12	ET: 56.1%; Dfc: 43.9%	GRA: 37.1%; ENF: 24.8%; BSV: 20%	1980-2012	1621-3026	362.00	Kananaskis River - CA

Continuation of Table A5

Station	Lat	Lon	Climate	Biome	Period	Elev	Area	River
CA_0002319	50.79	-115.30	ET: 70.5%; Dfc: 29.5%	GRA: 59.5%; BSV: 21.6%; WSA: 18.9%	1980-1992	1898-2876	29.00	Mud Lake - CA
CA_0002321	50.95	-115.15	Dfc: 60%; ET: 40%	ENF: 50%; WSA: 31.2%; GRA: 18.8%	1980-2012	1711-2473	9.10	Marmot Creek - CA
CA_0002328	51.04	-115.03	Dfc: 53.9%; ET: 46.1%	GRA: 36.7%; ENF: 26.9%; WSA: 22.6%	1980-2012	1342-3026	899.00	Kananaskis River - CA
CA_0002330	51.30	-115.18	ET: 73.4%; Dfc: 26.6%	GRA: 67.3%; BSV: 11.9%; WSA: 11%	1980-1993	1625-2834	211.00	Ghost River - CA
CA_0002334	51.28	-114.84	Dfc: 82.9%; ET: 17.1%	ENF: 51.7%; WSA: 22.7%; GRA: 20.4%	1980-2012	1292-2764	332.50	Waiparous Creek - CA
CA_0002336	51.27	-114.93	Dfc: 81.9%; ET: 18.1%	ENF: 36.3%; GRA: 31.7%; WSA: 26.5%	1980-2012	1328-2660	484.50	Ghost River - CA
CA_0002345	51.00	-114.94	Dfc: 91%; ET: 9%	ENF: 79.3%; GRA: 12.1%; WSA: 8.6%	1980-2012	1654-2320	36.90	Jumpingpound Creek - CA
CA_0002355	50.86	-114.79	ET: 50.3%; Dfc: 49.7%	GRA: 54%; WSA: 22.8%; ENF: 18.2%	1980-1995	1534-2911	437.00	Elbow River - CA
CA_0002356	50.79	-114.92	ET: 71.9%; Dfc: 28.1%	GRA: 74.3%; WSA: 20.6%; BSV: 3.3%	1980-1995	1757-2778	129.00	Little Elbow River - CA
CA_0002375	50.41	-114.50	Dfc: 76%; ET: 24%	ENF: 46.9%; WSA: 28%; GRA: 21.6%	1980-2012	1426-2939	773.60	Highwood River - CA
CA_0002378	50.29	-114.59	Dfc: 83.7%; ET: 16.3%	ENF: 53.3%; WSA: 35.2%; GRA: 11.5%	1980-2012	1680-2629	165.50	Cataract Creek - CA
CA_0002379	50.47	-114.21	Dfc: 98.1%; ET: 1.9%	GRA: 29.5%; WSA: 25.7%; CRO: 21.1%	1980-2014	1208-2353	231.90	Pekisko Creek - CA
CA_0002382	50.48	-114.43	Dfc: 78.9%; ET: 21.1%	GRA: 41.7%; ENF: 28%; WSA: 19.7%	1980-2012	1365-2606	137.40	Trap Creek - CA
CA_0002424	51.66	-115.13	Dfc: 100%	WSA: 66.7%; GRA: 33.3%	1980-1995	1432-1620	5.44	Deer Creek - CA
CA_0002425	51.66	-115.41	ET: 70.4%; Dfc: 29.6%	GRA: 46.8%; WSA: 24.5%; BSV: 16.6%	1980-2012	1513-3052	941.40	Red Deer River - CA
CA_0002506	52.04	-116.38	ET: 81.9%; Dfc: 18.1%	GRA: 45.2%; BSV: 34.3%; WSA: 13.3%	1980-1996	1406-3027	515.00	Siffleur River - CA
CA_0002511	51.88	-116.69	ET: 73.2%; Dfc: 26.8%	BSV: 38.5%; GRA: 25.7%; WSA: 13.3%	1980-2013	1635-2968	248.00	Mistaya River - CA
CA_0002513	52.00	-116.47	ET: 69.3%; Dfc: 30.7%	GRA: 34.5%; BSV: 32.8%; SNO: 13.1%	1980-2014	1355-3333	1923.20	North Saskatchewan River - CA
CA_0002514	51.80	-116.58	ET: 91.5%; Dfc: 8.5%	BSV: 48.8%; GRA: 32.6%; WSA: 11.6%	1980-2013	1728-2842	21.00	Silverhorn Creek - CA
CA_0002517	51.99	-115.43	ET: 51.3%; Dfc: 48.7%	GRA: 34.4%; ENF: 30.9%; WSA: 22.3%	1980-1992	1365-3136	1340.00	Clearwater River - CA
CA_0002527	52.37	-115.42	Dfc: 66.5%; ET: 33.5%	ENF: 61.2%; GRA: 20.2%; WSA: 16%	1980-2013	1083-2986	1853.60	Ram River - CA
CA_0002531	52.28	-116.00	Dfc: 60.9%; ET: 39.1%	ENF: 67.9%; GRA: 21.3%; WSA: 10.2%	1980-2013	1463-2596	347.30	North Ram River - CA
CA_0002536	52.76	-116.36	Dfc: 98.4%; ET: 1.6%	ENF: 87.7%; WSA: 12%; SAV: 0.3%	1980-2013	1316-2149	218.70	Brown Creek - CA
CA_0002539	52.87	-116.60	Dfc: 59.6%; ET: 40.4%	ENF: 61.3%; GRA: 18.1%; WSA: 14.2%	1980-1990	1341-2682	495.00	Cardinal River - CA
CA_0002950	52.60	-101.04	Dfc: 91.5%; Dfb: 8.5%	WSA: 44.9%; MF: 29.2%; ENF: 18.5%	1980-1993	316-762	170.00	Bell River - CA

Station	Lat	Lon	Climate	Biome	Period	Elev	Area	River
CA_0003014	50.48	-99.48	Dfb: 85.7%; Dfc: 14.3%	DBF: 44.4%; CRO: 16.7%; WSA: 16.7%	1980-2014	469-704	9.20	Pelican Creek - CA
CA_0003558	52.86	-118.11	ET: 61.1%; Dfc: 38.9%	ENF: 39.4%; GRA: 32.5%; WSA: 16%	1980-2012	1051-2769	628.50	Miette River - CA
CA_0003561	52.93	-118.03	ET: 73.9%; Dfc: 26.1%	GRA: 47.1%; ENF: 21.7%; BSV: 16.3%	1980-1997	1032-3151	908.00	Maligne River - CA
CA_0003562	52.22	-117.23	ET: 100%	SNO: 57.4%; BSV: 42.6%	1980-2012	1943-3390	29.30	Sunwapta River - CA
CA_0003564	52.72	-117.92	ET: 63.1%; Dfc: 36.9%	GRA: 31.9%; BSV: 29%; WSA: 14.9%	1980-1996	1148-3094	598.00	Whirlpool River - CA
CA_0003566	53.16	-118.03	ET: 68.1%; Dfc: 31.9%	GRA: 43.3%; ENF: 28.5%; WSA: 17.5%	1980-1993	1118-2752	1580.00	Snake Indian River - CA
CA_0003567	53.52	-117.95	Dfc: 56.8%; ET: 43.2%	ENF: 70.4%; WSA: 16.6%; GRA: 12.4%	1980-2013	1270-2512	959.80	Wildhay River - CA
CA_0003574	53.68	-118.24	Dfc: 54.9%; ET: 45.1%	ENF: 55.8%; WSA: 23.1%; GRA: 19.9%	1980-2012	1414-2415	93.00	Little Berland River - CA
CA_0003590	53.16	-117.26	Dfc: 100%	ENF: 100%	1980-2014	1289-1627	25.90	Wampus Creek - CA
CA_0003591	53.16	-117.24	Dfc: 100%	ENF: 100%	1980-1990	1280-1616	14.00	Deerlick Creek - CA
CA_0003592	53.15	-117.23	Dfc: 100%	ENF: 100%	1980-1992	1309-1636	17.10	Eunice Creek - CA
CA_0003598	53.08	-117.20	ET: 60%; Dfc: 40%	ENF: 42.5%; GRA: 36.4%; WSA: 13.9%	1980-2012	1415-2611	329.60	Mcleod River - CA
CA_0003600	53.25	-117.36	Dfc: 83.4%; ET: 16.6%	ENF: 79.6%; WSA: 10.5%; GRA: 9.6%	1980-2012	1235-2366	384.00	Gregg River - CA
CA_0003619	53.00	-116.66	Dfc: 100%	WSA: 92.6%; ENF: 7.4%	1980-2013	1338-1555	102.70	Lovett River - CA
CA_0003647	55.42	-114.81	Dfc: 100%	WSA: 88.9%; WET: 11.1%	1980-2012	590-595	23.70	Lily Creek - CA
CA_0003651	54.80	-115.47	Dfc: 100%	ENF: 52.9%; WSA: 43.3%; MF: 3.8%	1980-2014	973-1348	155.10	Swan River - CA
CA_0003714	57.19	-124.90	ET: 58.4%; Dfc: 27.5%; Dsc: 14.1%	ENF: 35.3%; GRA: 27.9%; WSA: 27.1%	1980-2012	766-2661	1690.00	Akie River - CA
CA_0003720	56.13	-124.80	Dfc: 59.7%; ET: 35.2%; Dsc: 5.1%	WSA: 48.6%; ENF: 30.4%; GRA: 18.8%	1980-2013	809-2274	1950.00	Osilinka River - CA
CA_0003728	54.53	-122.61	Dfc: 100%	ENF: 47.3%; MF: 37.5%; DBF: 7.5%	1980-2012	760-1267	310.00	Chuchinka Creek - CA
CA_0003732	55.95	-122.66	Dfc: 90.3%; ET: 9.7%	ENF: 79.8%; WSA: 12.6%; GRA: 7.5%	1980-2013	769-1936	741.00	Carbon Creek - CA
CA_0003742	55.54	-121.60	Dfc: 100%	ENF: 51%; DBF: 20.4%; MF: 20.4%	1980-2014	650-1602	82.40	Dickebusch Creek - CA
CA_0003743	55.15	-120.92	Dfc: 100%	ENF: 86.2%; MF: 6.9%; WSA: 6.9%	1980-2001	946-1254	29.50	Quality Creek - CA
CA_0003747	55.09	-120.94	Dfc: 97.8%; ET: 2.2%	ENF: 87.1%; WSA: 6.7%; GRA: 3%	1980-2012	865-1922	486.00	Flatbed Creek - CA
CA_0003749	55.70	-121.63	Dfc: 100%	ENF: 33.3%; MF: 31%; WSA: 31%	1980-1998	747-1295	22.90	Windrem Creek - CA
CA_0003753	56.27	-120.95	Dfc: 100%	WSA: 47.8%; SAV: 16.6%; GRA: 12.7%	1980-1992	689-866	298.00	Stoddart Creek - CA
CA_0003773	56.17	-117.60	Dfc: 100%	CRO: 100%	1980-2011	589-653	8.10	Na - CA
CA_0003779	53.93	-118.82	Dfc: 73.3%; ET: 26.7%	ENF: 62.5%; WSA: 25.2%; GRA: 11.3%	1980-2014	1151-2581	702.90	Muskeg River - CA

Station	Lat	Lon	Climate	Biome	Period	Elev	Area	River
CA_0003780	54.52	-118.96	Dfc: 100%	ENF: 53.4%; WSA: 28.4%; MF: 17.4%	1980-2013	825-1599	842.20	Cutbank River - CA
CA_0003784	54.84	-119.39	Dfc: 100%	MF: 72.5%; WSA: 16.4%; ENF: 6.7%	1980-2011	720-1285	493.80	Pinto Creek - CA
CA_0003927	61.19	-136.98	Dfc: 66.7%; Dsc: 33.3%	WSA: 85.7%; SAV: 14.3%	1980-2014	945-1044	190.00	Giltana Creek - CA
CA_0003932	60.11	-136.93	ET: 81.5%; Dsc: 18.5%	GRA: 65.7%; OSH: 18.6%; WSA: 10.9%	1980-2014	726-1934	375.00	Takhanne River - CA
CA_0003933	60.12	-137.08	ET: 72.2%; Dsc: 27.8%	GRA: 54.6%; OSH: 12.8%; BSV: 10.7%	1980-2014	592-2035	1750.00	Tatshenshini River - CA
CA_0003943	57.22	-129.11	ET: 96.5%; Dsc: 3.5%	GRA: 40.4%; BSV: 23.4%; SNO: 21.3%	1980-1996	1212-2015	29.20	Unnamed Creek - CA
CA_0003944	57.25	-129.05	ET: 100%	GRA: 72.7%; BSV: 27.3%	1980-1996	1499-1982	16.60	Klappan River - CA
CA_0003951	57.53	-130.18	ET: 63.8%; Dsc: 36.2%	GRA: 39.2%; ENF: 36.3%; WSA: 14.1%	1980-1996	821-2330	1250.00	Iskut River - CA
CA_0003953	57.04	-130.40	ET: 69.5%; Dsc: 20.4%; Dfc: 10.1%	GRA: 37%; SNO: 25.5%; BSV: 17.2%	1980-1995	427-2284	844.00	More Creek - CA
CA_0003954	56.92	-130.72	ET: 69.5%; Dfc: 30.5%	SNO: 64.8%; GRA: 15.4%; ENF: 10.1%	1980-1994	486-2060	311.00	Forrest Kerr Creek - CA
CA_0003956	56.11	-129.48	ET: 50.2%; Dfc: 49.1%; Dsc: 0.7%	GRA: 46.9%; SNO: 20.6%; BSV: 11.9%	1980-2012	342-2314	218.00	Surprise Creek - CA
CA_0003960	56.97	-129.47	ET: 87.1%; Dsc: 12.9%	GRA: 58.5%; WSA: 15.2%; ENF: 14.7%	1980-1996	991-1984	118.00	Craven Creek - CA
CA_0003963	56.29	-129.23	Dsc: 70%; Dfc: 15%; ET: 15%	ENF: 75%; GRA: 25%	1980-2011	532-1473	8.64	Kelly Creek - CA
CA_0003978	56.04	-129.93	ET: 53%; Dfc: 46.5%; Dfb: 0.5%	SNO: 43.2%; GRA: 24.3%; ENF: 21.2%	1980-1999	87-2317	350.00	Bear River - CA
CA_0003979	56.35	-130.69	ET: 50.6%; Dfc: 46.4%; Dsc: 2.2%	SNO: 28.1%; ENF: 27.8%; GRA: 26%	1980-1996	123-2366	1480.00	Unuk River - CA
CA_0003982	55.43	-127.72	Dsc: 78.3%; ET: 12.3%; Dsb: 5.6%	ENF: 72.6%; GRA: 11.6%; MF: 10.4%	1980-2014	286-1839	1880.00	Kispiox River - CA
CA_0003984	55.46	-127.85	Dsc: 81.1%; ET: 18.9%	ENF: 79.4%; GRA: 17.6%; BSV: 2.9%	1980-2014	579-1717	19.10	Compass Creek - CA
CA_0003987	54.41	-125.43	Dsc: 82%; Dfc: 18%	ENF: 61.3%; WSA: 34.2%; GRA: 4.2%	1980-2013	863-1574	808.00	Pinkut Creek - CA
CA_0003993	53.93	-127.45	Dfc: 65.8%; ET: 34.2%; Dsc: 0.1%	ENF: 43.7%; GRA: 23.1%; WSA: 15.1%	1980-2013	912-2243	732.00	Nanika River - CA
CA_0003994	54.12	-127.43	Dfc: 59.9%; ET: 33.9%; Dsc: 6.2%	ENF: 40.6%; GRA: 23.3%; WSA: 17.5%	1980-2013	761-2469	1900.00	Morice River - CA
CA_0004004	54.65	-127.12	Dsc: 72.5%; ET: 27.5%	ENF: 66.7%; GRA: 11.7%; WSA: 11.3%	1980-2012	674-2116	125.00	Goathorn Creek - CA
CA_0004007	54.81	-127.20	Dsc: 64.5%; ET: 35.5%	ENF: 40.7%; GRA: 29.6%; BSV: 18.5%	1980-2012	560-2114	13.20	Simpson Creek - CA
CA_0004008	54.40	-126.65	Dsc: 86.3%; Dfc: 12.4%; ET: 1.4%	ENF: 54.2%; WSA: 41.7%; GRA: 2.4%	1980-2015	611-1550	565.00	Buck Creek - CA
CA_0004009	54.80	-127.11	Dsc: 71.1%; ET: 16.5%; Dfc: 12.4%	ENF: 66.7%; WSA: 23.2%; GRA: 6%	1980-1996	540-1859	256.00	Canyon Creek - CA
CA_0004015	54.61	-127.50	ET: 45.5%; Dsc: 42.9%; Dfc: 11.6%	ENF: 52.3%; GRA: 20.4%; WSA: 10.1%	1980-2014	710-2355	367.00	Telkwa River - CA

Station	Lat	Lon	Climate	Biome	Period	Elev	Area	River
CA_0004020	55.30	-127.62	Dsc: 91.2%; Dfc: 5.9%; Dsb: 2.9%	ENF: 89.3%; MF: 10.7%	1980-2014	438-1418	21.20	Two Mile Creek - CA
CA_0004022	55.23	-127.57	Dsc: 59.1%; ET: 40.9%	GRA: 47.1%; ENF: 35.3%; BSV: 17.6%	1980-1996	473-1949	10.80	Station Creek - CA
CA_0004027	54.78	-127.47	Dsc: 66.7%; ET: 33.3%	ENF: 52.9%; WSA: 41.2%; GRA: 5.9%	1980-2013	954-1721	9.97	M3 Creek - CA
CA_0004042	54.99	-128.81	Dfc: 87.5%; Dsc: 6.2%; ET: 6.2%	ENF: 78.6%; WSA: 14.3%; GRA: 7.1%	1980-2013	563-1534	7.16	Clarence Creek - CA
CA_0004058	52.36	-126.81	Dfc: 65.1%; ET: 25.3%; Dfb: 9.6%	ENF: 58.2%; GRA: 19.2%; SNO: 8.9%	1980-1996	186-1984	92.50	Clayton Falls Creek - CA
CA_0004069	53.56	-127.95	Dfc: 56.3%; ET: 35.3%; Dfb: 8.4%	GRA: 34.9%; ENF: 23.9%; SNO: 22.1%	1980-2013	68-2144	556.00	Kemano River - CA
CA_0004074	54.22	-128.22	Dfc: 95.8%; Dfb: 4.2%	ENF: 57.9%; GRA: 26.3%; WSA: 15.8%	1980-2009	404-1495	12.70	Kilometre 189 Creek - CA
CA_0004101	49.45	-123.11	Dfc: 50.3%; Dfb: 45.5%; Cfb: 4.2%	ENF: 96.9%; WSA: 2.3%; GRA: 0.8%	1980-2003	310-1501	69.90	Capilano River - CA
CA_0004102	49.45	-123.10	Dfb: 51.3%; Dfc: 46.1%; Cfb: 2.6%	ENF: 98.5%; WSA: 1.5%	1980-2003	364-1503	41.40	Eastcap Creek - CA
CA_0004135	50.11	-123.43	Dfc: 57.4%; ET: 29.1%; Dfb: 13.5%	SNO: 26%; GRA: 25.3%; ENF: 25.2%	1980-2014	283-2640	1200.00	Elaho River - CA
CA_0004136	50.08	-123.04	Dfc: 64.1%; ET: 28.7%; Dfb: 4.4%	ENF: 38.1%; GRA: 23.2%; BSV: 21.5%	1980-2012	694-2499	297.00	Cheakamus River - CA
CA_0004139	49.52	-123.00	Dfc: 57%; Dfb: 41.3%; Cfb: 1.7%	ENF: 94.1%; GRA: 2.9%; WSA: 2.9%	1980-2011	271-1471	63.00	Seymour River - CA
CA_0004141	49.50	-122.97	Dfc: 51.7%; Dfb: 43%; Cfb: 5.3%	ENF: 95.4%; GRA: 2.3%; WSA: 2.3%	1980-2012	233-1471	82.90	Seymour River - CA
CA_0004149	49.79	-123.42	Dfc: 73.5%; Dfb: 21.8%; Cfb: 3.1%	ENF: 48.2%; GRA: 25.9%; BSV: 13.6%	1980-2013	74-2301	147.00	Clowhom River - CA
CA_0004159	51.37	-124.76	ET: 45.9%; Dsc: 33.5%; Dfc: 18.5%	ENF: 31.2%; BSV: 24.2%; WSA: 19.2%	1980-1995	632-3051	1960.00	Homathko River - CA
CA_0004161	51.41	-124.93	ET: 57.8%; Dfc: 20.2%; Dsc: 16.8%	BSV: 28.2%; GRA: 27%; ENF: 24.5%	1980-1995	704-3659	1550.00	Mosley Creek - CA
CA_0004162	51.67	-124.41	Dsc: 45.5%; Dfc: 28.6%; ET: 20.4%	WSA: 56.8%; ENF: 31%; BSV: 7.9%	1980-2014	854-2615	486.00	Homathko River - CA
CA_0004163	51.42	-124.51	ET: 42.5%; Dsc: 37%; Dfc: 18.1%	ENF: 34.1%; WSA: 22.7%; BSV: 22.6%	1980-1995	817-3051	1550.00	Homathko River - CA
CA_0004169	51.07	-126.36	Dfc: 78.6%; Dfb: 15.3%; Cfb: 5.1%	ENF: 47%; GRA: 27.7%; WSA: 12%	1980-2010	158-1669	54.30	Kippan Creek - CA
CA_0004219	48.64	-124.29	Cfb: 100%	ENF: 100%	1980-2012	394-842	8.12	Renfrew Creek - CA
CA_0004220	48.72	-124.23	Cfb: 58.2%; Csb: 40%; Dfc: 1.8%	ENF: 100%	1980-2012	299-986	28.00	Harris Creek - CA
CA_0004227	49.29	-124.58	Dfc: 47.6%; Csb: 32.3%; Dsc: 7.7%	ENF: 91%; WSA: 6.2%; GRA: 2.8%	1980-2001	185-1603	135.00	Little Qualicum River - CA
CA_0004257	49.02	-124.19	Csb: 36.9%; Dfc: 27.2%; Dsb: 18.4%	ENF: 100%	1980-2014	344-1328	62.20	Jump Creek - CA
CA_0004284	49.25	-125.58	Cfb: 54.3%; Cfc: 24.3%; Dfc: 21.4%	ENF: 98.3%; GRA: 1.7%	1980-2013	75-1174	38.60	Tofino Creek - CA
CA_0004289	49.06	-124.13	Csb: 31.4%; Dsb: 30.4%; Dfc: 15.7%	ENF: 100%	1980-2014	283-1346	211.00	South Nanaimo River - CA

Station	Lat	Lon	Climate	Biome	Period	Elev	Area	River
CA_0004301	49.82	-125.99	Dfc: 71.6%; Cfb: 25.7%; Cfc: 2.7%	ENF: 100%	1980-2013	220-1419	60.00	Heber River - CA
CA_0004324	49.86	-125.81	Dfc: 75.4%; Cfb: 16%; ET: 6.4%	ENF: 71.7%; WSA: 16.4%; GRA: 11.9%	1980-2013	301-1845	132.00	Elk River - CA
CA_0004326	49.93	-125.51	Cfb: 44.2%; Dfb: 29.2%; Dfc: 26.6%	ENF: 83%; WSA: 14.8%; GRA: 2.2%	1980-2013	311-1513	84.20	Quinsam River - CA
CA_0004331	49.75	-125.34	Dfc: 100%	ENF: 100%	1980-2005	1007-1337	8.37	Piggott Creek - CA
CA_0004339	50.14	-126.17	Dfc: 74.1%; ET: 14.8%; Dfb: 11.1%	ENF: 68%; WSA: 24%; GRA: 8%	1980-2012	577-1630	14.60	Zeballos River - CA
CA_0004345	50.44	-126.58	Dfc: 58%; Cfb: 28.1%; Cfc: 10.7%	ENF: 98.8%; GRA: 0.6%; WSA: 0.4%	1980-2012	109-1539	365.00	Tsitika River - CA
CA_0004349	50.42	-126.58	Dfc: 76.1%; Cfc: 9.1%; Cfb: 8%	ENF: 97.5%; WSA: 2.5%	1980-1999	206-1448	46.10	Catherine Creek - CA
CA_0004351	50.73	-127.88	Cfc: 74.5%; Cfb: 25.5%	ENF: 97.6%; EBF: 2.4%	1980-2012	236-503	22.30	Pugh Creek - CA
CA_0004364	53.26	-125.41	Dfc: 81.7%; Dsc: 12.3%; ET: 6%	WSA: 78.8%; ENF: 19.3%; GRA: 1.9%	1980-2006	1022-1826	150.00	Van Tine Creek - CA
CA_0004365	53.65	-127.54	ET: 62.2%; Dfc: 37.8%	GRA: 50.4%; ENF: 26.6%; WSA: 10.1%	1980-2013	880-2026	86.50	Laventie Creek - CA
CA_0004366	53.80	-126.36	ET: 56.7%; Dsc: 43.3%	GRA: 35.6%; WSA: 34.5%; ENF: 28.7%	1980-1995	896-2078	53.40	Macivor Creek - CA
CA_0004375	53.66	-126.99	Dfc: 73.3%; ET: 26.7%	ENF: 57.1%; GRA: 28.6%; WSA: 14.3%	1980-2013	1001-1637	7.72	Whitesail Middle Creek - CA
CA_0004380	53.90	-126.95	Dfc: 84%; ET: 12.6%; Dsc: 3.4%	ENF: 49.5%; WSA: 38.1%; GRA: 7.9%	1980-2015	927-2147	369.00	Nadina River - CA
CA_0004381	54.18	-125.49	Dsc: 96.8%; Dfc: 3.2%	WSA: 61.1%; ENF: 33.9%; GRA: 2.4%	1980-2004	697-1415	771.00	Endako River - CA
CA_0004397	55.98	-126.68	Dfc: 65.8%; ET: 19.8%; Dsc: 14.4%	ENF: 71.6%; WSA: 14.6%; GRA: 12%	1980-2012	779-2083	403.00	Driftwood River - CA
CA_0004402	53.31	-120.25	ET: 64.5%; Dfc: 35.5%	WSA: 31.3%; GRA: 27.3%; BSV: 25.2%	1980-2013	782-2722	409.00	Dore River - CA
CA_0004406	52.99	-119.01	ET: 61.4%; Dfc: 38.6%	GRA: 40%; WSA: 20.3%; ENF: 18.5%	1980-2013	1030-3108	1710.00	Fraser River - CA
CA_0004407	52.92	-118.80	ET: 66.9%; Dfc: 33.1%	GRA: 46.4%; BSV: 23.4%; WSA: 16%	1980-1995	1082-2985	458.00	Moose River - CA
CA_0004408	53.44	-120.22	ET: 61.6%; Dfc: 38.4%	GRA: 43%; WSA: 26.8%; ENF: 25.4%	1980-2013	983-2296	253.00	Mckale River - CA
CA_0004411	52.84	-119.27	ET: 62.8%; Dfc: 36.8%; Dfb: 0.4%	GRA: 56.6%; WSA: 20.5%; ENF: 17.8%	1980-1998	806-2339	132.00	Swift Creek - CA
CA_0004412	53.68	-120.59	Dfc: 55.1%; ET: 44.9%	WSA: 38.3%; GRA: 32.8%; ENF: 25.4%	1980-2013	704-2360	1260.00	Morkill River - CA
CA_0004416	54.30	-120.98	Dfc: 87%; ET: 13%	WSA: 45%; GRA: 27.2%; ENF: 22.2%	1980-2013	954-2194	103.00	Muller Creek - CA
CA_0004419	54.61	-123.24	Dfc: 98.5%; Dsc: 1.5%	WSA: 62.2%; ENF: 34%; GRA: 3.9%	1980-1998	811-1059	303.00	Muskeg River - CA
CA_0004420	53.26	-121.41	Dfc: 87.4%; ET: 12.6%	ENF: 64.3%; WSA: 26.1%; GRA: 9.5%	1980-1995	909-2150	458.00	Bowron River - CA
CA_0004433	53.16	-122.48	Dfc: 95.7%; Dfb: 3.4%; ET: 0.9%	WSA: 49.8%; ENF: 41.3%; MF: 8.4%	1980-1999	589-1862	1910.00	Cottonwood River - CA
CA_0004436	52.97	-122.51	Dfc: 95.2%; Dfb: 4.8%	WSA: 81.9%; ENF: 12.6%; GRA: 3.4%	1980-2013	483-1471	1550.00	Baker Creek - CA

89

Station	Lat	Lon	Climate	Biome	Period	Elev	Area	River
CA_0004443	52.91	-121.77	Dfc: 93.5%; ET: 6.5%	WSA: 64.8%; ENF: 35.2%	1980-2013	1088-1955	127.00	Little Swift River - CA
CA_0004451	53.86	-122.57	Dfc: 97.5%; Dfb: 2.5%	MF: 51%; ENF: 34.3%; WSA: 14.7%	1980-1999	681-1203	60.20	Tabor Creek - CA
CA_0004452	52.64	-122.41	Dfc: 73.7%; Dfb: 26.3%	ENF: 59.5%; WSA: 40.5%	1980-1995	823-1394	37.30	Alix Creek - CA
CA_0004453	52.83	-122.54	Dfc: 91.8%; Dfb: 8.2%	WSA: 68.8%; ENF: 24.2%; MF: 6.4%	1980-1993	796-1401	99.10	Deserters Creek - CA
CA_0004459	52.99	-123.80	Dfc: 98.8%; ET: 1.2%	WSA: 86.1%; ENF: 10.8%; GRA: 3.1%	1980-1995	964-1706	992.00	Baezaeko River - CA
CA_0004469	52.29	-121.07	Dfc: 80.5%; ET: 19.5%	ENF: 52.7%; WSA: 25.9%; GRA: 16.7%	1980-2013	889-2400	790.00	Horsefly River - CA
CA_0004474	52.32	-121.41	Dfc: 97.7%; Dfb: 1.3%; ET: 1%	WSA: 74.7%; ENF: 17.4%; GRA: 8%	1980-2012	803-2064	548.00	Moffat Creek - CA
CA_0004475	52.28	-121.00	Dfc: 95.6%; Dfb: 2.4%; ET: 2.1%	ENF: 75.1%; WSA: 21.2%; MF: 1.9%	1980-2014	863-2098	431.00	Mckinley Creek - CA
CA_0004478	52.95	-122.40	Dfb: 100%	WSA: 42.9%; ENF: 28.6%; GRA: 14.3%	1980-1994	617-834	7.25	Dragon Creek - CA
CA_0004480	52.37	-121.36	Dfc: 60.1%; Dfb: 38.3%; ET: 1.6%	ENF: 74.5%; WSA: 17.4%; MF: 6.1%	1980-1990	783-2121	416.00	Little Horsefly River - CA
CA_0004501	51.61	-121.23	Dfc: 99.1%; Dfb: 0.9%	WSA: 69.5%; ENF: 29.5%; GRA: 0.7%	1980-1997	991-1614	912.00	Bridge Creek - CA
CA_0004502	51.73	-120.01	Dfc: 69.4%; ET: 28.1%; Dfb: 2.5%	ENF: 64%; WSA: 19%; GRA: 15%	1980-1994	847-2431	52.50	Spahats Creek - CA
CA_0004509	51.62	-120.67	Dfc: 100%	ENF: 60%; WSA: 40%	1980-2011	1175-1861	79.40	Windy Creek - CA
CA_0004521	50.72	-120.03	Dfb: 54%; Dfc: 44.4%; BSk: 1.6%	WSA: 50%; ENF: 44.4%; GRA: 2.8%	1980-2009	870-1438	55.70	Paul Creek - CA
CA_0004527	51.18	-120.13	Dfc: 69%; Dfb: 28.1%; ET: 2.3%	ENF: 64.7%; WSA: 29.8%; GRA: 4.8%	1980-2014	381-2217	1140.00	Barriere River - CA
CA_0004531	51.12	-120.21	Dfc: 80.5%; Dfb: 19.5%	WSA: 74.4%; ENF: 20.5%; GRA: 5.1%	1980-2013	617-1623	135.00	Fishtrap Creek - CA
CA_0004541	52.12	-119.30	Dfc: 81.1%; ET: 13.5%; Dfb: 5.4%	WSA: 38.1%; ENF: 30.4%; GRA: 25.4%	1980-2013	685-2331	272.00	Blue River - CA
CA_0004567	51.25	-119.94	Dfc: 79.6%; Dfb: 16.1%; ET: 4.4%	ENF: 58.1%; WSA: 33.7%; GRA: 7.8%	1980-2013	571-2217	624.00	Barriere River - CA
CA_0004570	51.13	-120.12	Dfc: 70.7%; Dfb: 29.3%	ENF: 54.6%; WSA: 40.5%; MF: 2.7%	1980-1996	388-2075	515.00	Louis Creek - CA
CA_0004572	51.35	-119.88	Dfc: 88.5%; ET: 8.6%; Dfb: 3%	ENF: 59.2%; WSA: 29.2%; GRA: 10.9%	1980-2013	803-2217	166.00	Harper Creek - CA
CA_0004574	51.43	-120.20	Dfc: 85.7%; Dfb: 14.3%	ENF: 50.6%; WSA: 45.8%; MF: 3.4%	1980-2013	399-1679	443.00	Lemieux Creek - CA
CA_0004579	50.30	-118.82	Dfc: 70.2%; Dfb: 26%; ET: 3.8%	ENF: 67.4%; WSA: 19.9%; GRA: 10.5%	1980-2013	455-2687	2000.00	Shuswap River - CA
CA_0004590	50.35	-118.55	Dfc: 75.1%; Dfb: 18.7%; ET: 6.2%	ENF: 60.3%; WSA: 19.3%; GRA: 17.1%	1980-2013	600-2687	1130.00	Shuswap River - CA
CA_0004608	50.30	-118.86	Dfc: 56.9%; Dfb: 43.1%	ENF: 58.3%; WSA: 33.9%; GRA: 6.4%	1980-2013	483-1934	769.00	Bessette Creek - CA
CA_0004609	50.28	-118.95	Dfb: 62.3%; Dfc: 37.7%	ENF: 76.7%; WSA: 17.2%; MF: 5.2%	1980-2013	505-1844	70.90	Vance Creek - CA

Station	Lat	Lon	Climate	Biome	Period	Elev	Area	River
CA_0004610	50.25	-118.96	Dfc: 65.2%; Dfb: 34.8%	ENF: 57.2%; WSA: 35.6%; GRA: 6.2%	1980-2011	495-1934	632.00	Bessette Creek - CA
CA_0004613	50.26	-118.63	Dfc: 74.2%; Dfb: 24.8%; ET: 1.1%	ENF: 80.1%; WSA: 15%; GRA: 3.8%	1980-1990	525-2352	503.00	Cherry Creek - CA
CA_0004614	50.53	-118.97	Dfb: 63.6%; Dfc: 36.4%	ENF: 86.9%; WSA: 9.5%; SAV: 2.5%	1980-1990	431-1760	191.00	Trinity Creek - CA
CA_0004616	50.89	-119.73	Dfc: 78%; Dfb: 22%	ENF: 92.6%; WSA: 7.4%	1980-2002	634-1765	69.70	Hiuihill Creek - CA
CA_0004620	51.43	-119.47	Dfc: 81.1%; Dfb: 18.9%	ENF: 85.7%; WSA: 14.3%	1980-1998	422-1580	14.70	Fisher Creek - CA
CA_0004640	50.50	-119.56	Dfc: 56%; BSk: 25.5%; Dfb: 18.5%	WSA: 53.7%; ENF: 34.4%; GRA: 10.3%	1980-2013	588-1914	1030.00	Salmon River - CA
CA_0004641	50.69	-119.33	Dfc: 47.7%; Dfb: 34.7%; BSk: 17.6%	WSA: 46.7%; ENF: 40.6%; GRA: 10.6%	1980-2011	353-1914	1550.00	Salmon River - CA
CA_0004644	50.94	-118.80	Dfc: 68.1%; Dfb: 25.9%; ET: 6%	ENF: 55.6%; WSA: 20.4%; GRA: 18.5%	1980-2014	367-2708	932.00	Eagle River - CA
CA_0004647	51.26	-118.95	Dfc: 66.2%; Dfb: 24.4%; ET: 9.4%	ENF: 57.4%; WSA: 19.4%; GRA: 15.8%	1980-2013	365-2568	805.00	Seymour River - CA
CA_0004687	50.29	-119.96	Dfc: 85%; Dfb: 8.6%; BSk: 6.4%	WSA: 70.8%; ENF: 22.9%; GRA: 6.2%	1980-2002	1000-1914	143.00	Salmon River - CA
CA_0004688	50.91	-119.53	Dfc: 60%; Dfb: 40%	ENF: 94.1%; WSA: 5.9%	1980-2010	400-1719	26.20	Corning Creek - CA
CA_0004707	50.52	-119.85	Dfc: 73.4%; BSk: 14.5%; Dfb: 12.1%	WSA: 61.3%; ENF: 28.3%; SAV: 7.5%	1980-1994	708-1705	64.30	Monte Creek - CA
CA_0004710	50.93	-118.47	Dfc: 58%; Dfb: 38%; ET: 4%	ENF: 90%; DBF: 5%; GRA: 2.5%	1980-1994	556-2189	30.20	South Pass Creek - CA
CA_0004712	50.70	-119.20	Dfb: 73.7%; Dfc: 26.3%	ENF: 100%	1980-2014	626-1299	20.80	East Canoe Creek - CA
CA_0004714	50.82	-119.68	Dfc: 64.9%; Dfb: 35.1%	ENF: 59%; WSA: 36.1%; MF: 3.3%	1980-2013	384-1777	297.00	Chase Creek - CA
CA_0004721	50.88	-120.97	Dfc: 75.5%; Dfb: 17%; BSk: 7.6%	WSA: 66.4%; ENF: 28.9%; GRA: 4.7%	1980-2014	546-1855	479.00	Criss Creek - CA
CA_0004728	50.88	-121.42	Dfc: 70.1%; Dfb: 17.3%; BSk: 10%	WSA: 52.4%; ENF: 35.8%; GRA: 10.9%	1980-1994	591-2254	658.00	Hat Creek - CA
CA_0004739	50.90	-120.98	Dfc: 80.4%; Dfb: 14.5%; BSk: 5.1%	WSA: 77.5%; ENF: 14.5%; GRA: 7.9%	1980-2014	554-1741	878.00	Deadman River - CA
CA_0004771	51.04	-121.44	Dfc: 67.8%; Dfb: 22.4%; BSk: 9.7%	WSA: 67.4%; ENF: 29.6%; GRA: 2.7%	1980-1996	728-1697	479.00	Loon Creek - CA
CA_0004773	51.26	-121.68	Dfc: 89.6%; ET: 10.4%	WSA: 69.2%; GRA: 16.9%; ENF: 12.3%	1980-1996	1143-2168	36.40	Fiftynine Creek - CA
CA_0004774	50.74	-121.58	Dfc: 90.6%; Dfb: 9.4%	WSA: 66.7%; GRA: 18.8%; ENF: 14.6%	1980-1998	1131-1914	32.90	Ambusten Creek - CA
CA_0004777	50.73	-121.64	Dfc: 91.9%; ET: 8.1%	ENF: 73.1%; WSA: 19.2%; GRA: 3.8%	1980-1998	1193-2110	31.90	Anderson Creek - CA
CA_0004778	50.68	-120.57	Dfc: 53%; BSk: 47%	WSA: 62.5%; ENF: 20%; GRA: 17.5%	1980-1996	628-1860	143.00	Cherry Creek - CA
CA_0004780	50.98	-121.40	Dfc: 91.7%; Dfb: 4.3%; BSk: 4%	WSA: 68.2%; GRA: 18.4%; ENF: 13.5%	1980-1994	885-1749	141.00	Scottie Creek - CA
CA_0004782	51.01	-120.75	Dfc: 100%	WSA: 93.8%; GRA: 6.2%	1980-1994	1120-1855	46.60	Heller Creek - CA

Continuation of Table A5

Station	Lat	Lon	Climate	Biome	Period	Elev	Area	River
CA_0004785	51.15	-120.86	Dfc: 100%	WSA: 85.5%; GRA: 13.9%; ENF: 0.6%	1980-2015	1078-1525	98.90	Joe Ross Creek - CA
CA_0004786	51.43	-120.62	Dfc: 100%	WSA: 83.9%; ENF: 16.1%	1980-1994	1149-1489	20.40	Mcdonald Creek - CA
CA_0004789	50.84	-121.24	Dfc: 80.2%; Dfb: 10.5%; BSk: 9.3%	WSA: 67.6%; ENF: 27%; GRA: 5.4%	1980-2013	770-1661	50.50	Arrowstone Creek - CA
CA_0004790	50.84	-121.15	Dfc: 78.9%; Dfb: 10.5%; BSk: 10.5%	WSA: 70.6%; ENF: 23.5%; GRA: 5.9%	1980-2011	943-1628	10.60	Dairy Creek - CA
CA_0004798	50.14	-121.03	Dsc: 73.1%; Dsb: 24.4%; BSk: 1.8%	ENF: 64.8%; WSA: 32.4%; GRA: 2.7%	1980-2014	542-2150	775.00	Spius Creek - CA
CA_0004799	50.49	-120.86	Dfc: 100%	WSA: 66.5%; GRA: 30.2%; BSV: 1.7%	1980-1996	1120-1829	139.00	Witches Brook - CA
CA_0004800	50.11	-120.80	Dsc: 51.4%; Dsb: 35.1%; BSk: 6.4%	ENF: 48.9%; WSA: 47.6%; GRA: 3%	1980-2014	598-1989	917.00	Coldwater River - CA
CA_0004805	49.96	-120.13	Dfc: 100%	WSA: 72.3%; ENF: 22.3%; GRA: 5.4%	1980-2013	1458-1929	87.60	Pennask Creek - CA
CA_0004824	50.36	-120.81	Dfc: 95.1%; BSk: 4.4%; Dfb: 0.5%	WSA: 73.5%; GRA: 17.8%; ENF: 8%	1980-2014	955-1907	871.00	Guichon Creek - CA
CA_0004829	49.85	-120.91	Dsc: 83.7%; Dsb: 13.3%; Dfc: 2.7%	ENF: 66.5%; WSA: 30.3%; GRA: 2.9%	1980-2014	919-1989	316.00	Coldwater River - CA
CA_0004830	50.18	-120.38	Dfc: 58.4%; BSk: 30%; Dfb: 11.6%	WSA: 50.4%; GRA: 36.5%; ENF: 12.3%	1980-2014	736-1929	1500.00	Nicola River - CA
CA_0004836	50.61	-120.91	Dfc: 100%	WSA: 81.9%; GRA: 17.4%; ENF: 0.6%	1980-2014	1189-1931	78.20	Guichon Creek - CA
CA_0004840	50.14	-120.28	Dfc: 60%; BSk: 33.5%; Dfb: 6.6%	WSA: 52.3%; GRA: 34.4%; ENF: 11.4%	1980-1996	826-1929	241.00	Spahomin Creek - CA
CA_0004843	50.11	-119.98	Dfc: 97.1%; BSk: 2.9%	WSA: 81.8%; GRA: 9.5%; ENF: 8.8%	1980-2001	1110-1820	85.00	Beak Creek - CA
CA_0004845	50.33	-120.92	Dfc: 100%	GRA: 77.8%; WSA: 22.2%	1980-1998	1313-1719	32.20	Chataway Creek - CA
CA_0004846	50.15	-120.88	Dfc: 86.5%; BSk: 9.3%; Dfb: 4.2%	WSA: 74.3%; GRA: 16.5%; ENF: 8.6%	1980-2015	580-1907	1230.00	Guichon Creek - CA
CA_0004847	49.95	-121.10	Dsc: 87.9%; Dsb: 12.1%	ENF: 69.2%; WSA: 27.7%; GRA: 3.1%	1980-2011	932-2019	178.00	Spius Creek - CA
CA_0004850	51.38	-123.63	ET: 66%; Dfc: 34%	BSV: 32.6%; ENF: 24.5%; GRA: 21.4%	1980-2013	1323-2929	1520.00	Taseko River - CA
CA_0004851	51.67	-124.15	ET: 45.1%; Dsc: 44.5%; Dfc: 10.4%	ENF: 62.7%; WSA: 22.9%; GRA: 12.4%	1980-2014	1256-2140	98.80	Lingfield Creek - CA
CA_0004859	51.25	-123.10	ET: 91.2%; Dfc: 8.8%	GRA: 48.9%; WSA: 26.5%; BSV: 23%	1980-2013	1702-2737	232.00	Big Creek - CA
CA_0004894	52.11	-121.94	Dfc: 71.7%; Dfb: 28.3%	WSA: 66.5%; ENF: 25.5%; GRA: 8%	1980-2010	736-1081	192.00	Borland Creek - CA
CA_0004895	52.08	-121.99	Dfb: 56.7%; Dfc: 43.3%	ENF: 60.5%; WSA: 36.1%; GRA: 3.2%	1980-2013	615-1609	1990.00	San Jose River - CA
CA_0004898	52.15	-122.56	Dfc: 100%	WSA: 52.3%; ENF: 46.5%; SAV: 1.3%	1980-1994	990-1280	82.70	Meldrum Creek - CA
CA_0004900	52.43	-122.29	Dfc: 85.6%; Dfb: 14.4%	WSA: 55%; ENF: 45%	1980-2014	725-1312	99.00	Sheridan Creek - CA
CA_0004925	50.91	-121.72	Dfc: 98.5%; ET: 1.5%	ENF: 83.9%; WSA: 16.1%	1980-1998	1326-2020	37.10	Pavilion Creek - CA
CA_0004929	50.84	-121.90	Dfc: 89.4%; Dfb: 10.6%	ENF: 50%; WSA: 50%	1980-1994	904-1919	36.30	Lee Creek - CA

Station	Lat	Lon	Climate	Biome	Period	Elev	Area	River
CA_0004933	50.67	-121.97	ET: 42.1%; Dsc: 34.6%; Dfc: 17.5%	GRA: 32%; WSA: 30.6%; ENF: 24.7%	1980-2014	275-2712	885.00	Cayoosh Creek - CA
CA_0004934	50.67	-121.97	Dsc: 32.7%; Dsb: 24.9%; ET: 23%	ENF: 37.1%; WSA: 29.2%; GRA: 24.1%	1980-2013	244-2668	1020.00	Seton River - CA
CA_0004947	50.86	-123.45	ET: 63.1%; Dfc: 36.9%	SNO: 64%; GRA: 18.4%; BSV: 14.6%	1980-2013	1381-2815	144.00	Bridge River - CA
CA_0004949	50.91	-122.24	Dfc: 43.2%; ET: 40%; Dsc: 14.5%	WSA: 49.2%; GRA: 20.9%; ENF: 14.9%	1980-2013	795-2711	581.00	Yalakom River - CA
CA_0004950	50.96	-122.30	Dfc: 93.2%; ET: 4.3%; Dsc: 2.5%	WSA: 53.9%; ENF: 25.5%; GRA: 20.6%	1980-1994	1013-2101	86.40	Junction Creek - CA
CA_0004951	50.73	-122.94	ET: 46.6%; Dsc: 40.4%; Dfc: 13%	GRA: 38.4%; BSV: 25.2%; ENF: 17.3%	1980-2013	1029-2621	312.00	Hurley River - CA
CA_0004952	50.82	-123.20	ET: 61.1%; Dfc: 38%; Dfb: 0.8%	GRA: 28.6%; SNO: 26.6%; BSV: 24.9%	1980-2011	763-2815	708.00	Bridge River - CA
CA_0004991	49.54	-121.12	Dsc: 78%; Dfc: 14.3%; Dsb: 7.7%	ENF: 52.3%; WSA: 29.5%; GRA: 16.8%	1980-2014	881-1886	85.50	Coquihalla River - CA
CA_0004993	49.95	-121.86	Dsc: 43.9%; Dfc: 28.4%; Dsb: 17.1%	ENF: 36%; GRA: 32.3%; WSA: 20%	1980-2014	322-2559	712.00	Nahatlatch River - CA
CA_0005014	50.12	-122.95	Dfc: 49.4%; ET: 28.8%; Dsc: 11.2%	ENF: 40.4%; GRA: 24.5%; BSV: 14.6%	1980-2012	657-2536	89.70	Fitzsimmons Creek - CA
CA_0005027	49.08	-121.46	Dfc: 76.3%; Dfb: 19.7%; Dsb: 2.5%	ENF: 64.4%; GRA: 15.9%; WSA: 6.9%	1980-2014	619-2384	335.00	Chilliwack River - CA
CA_0005044	49.07	-121.70	Dfc: 75.8%; Dfb: 22.1%; Cfb: 2.1%	ENF: 66%; GRA: 20.1%; SAV: 5.7%	1980-2014	312-2079	160.00	Slesse Creek - CA
CA_0005045	49.19	-122.16	Dfb: 82%; Cfb: 10.2%; Dfc: 7.8%	ENF: 98.3%; MF: 1.7%	1980-2007	78-1261	117.00	Norrish Creek - CA
CA_0005070	49.10	-121.66	Dfc: 74.6%; Dfb: 23%; Dsb: 1.3%	ENF: 67.1%; GRA: 15.8%; WSA: 5.8%	1980-2013	357-2384	650.00	Chilliwack River - CA
CA_0005083	49.49	-122.79	Dfc: 67%; Dfb: 33%	ENF: 73.8%; GRA: 16.2%; WSA: 7.5%	1980-2012	335-1723	52.50	Coquitlam River - CA
CA_0005086	49.56	-122.32	Dfc: 73.7%; Dfb: 23.6%; ET: 2.7%	ENF: 37%; GRA: 29.7%; WSA: 13.8%	1980-2011	194-2097	290.00	Stave River - CA
CA_0005087	49.24	-122.13	Dfb: 89.9%; Dfc: 8.6%; Cfb: 1.4%	ENF: 100%	1980-2006	350-1261	78.20	Norrish Creek - CA
CA_0005101	51.30	-116.97	Dfc: 56.5%; ET: 43.1%; Dfb: 0.4%	ENF: 30.3%; GRA: 27.7%; WSA: 20.2%	1980-2014	787-3161	1850.00	Kicking Horse River - CA
CA_0005106	50.90	-116.41	Dfc: 54.2%; ET: 43.6%; Dfb: 2.2%	WSA: 29%; GRA: 28.5%; ENF: 24.9%	1980-2014	804-2968	1460.00	Spillimacheen River - CA
CA_0005128	51.14	-116.74	Dfc: 62.5%; ET: 25%; Dfb: 12.5%	ENF: 35.7%; WSA: 35.7%; SAV: 21.4%	1980-1998	914-2272	8.03	Carbonate Creek - CA
CA_0005134	50.32	-115.86	Dfc: 56.1%; ET: 27.2%; Dfb: 16.7%	WSA: 45.4%; ENF: 25.8%; GRA: 22.2%	1980-1996	807-2837	891.00	Columbia River - CA
CA_0005142	51.44	-116.37	ET: 72.5%; Dfc: 27.5%	GRA: 37%; BSV: 37%; WSA: 13.2%	1980-1996	1610-3161	119.00	Kicking Horse River - CA
CA_0005163	51.48	-116.97	ET: 51.4%; Dfc: 48.2%; Dfb: 0.4%	GRA: 32.1%; WSA: 19.9%; BSV: 19.5%	1980-2015	914-3030	587.00	Blaeberry River - CA
CA_0005164	51.61	-117.74	ET: 63.7%; Dfc: 36.3%	GRA: 30.8%; BSV: 26.5%; SNO: 17.1%	1980-1995	1112-3225	135.00	Gold River - CA
CA_0005165	51.68	-117.72	ET: 58.5%; Dfc: 41.3%; Dfb: 0.1%	GRA: 34.3%; BSV: 20%; ENF: 15.9%	1980-2013	837-3225	429.00	Gold River - CA

Station	Lat	Lon	Climate	Biome	Period	Elev	Area	River
CA_0005166	51.65	-116.74	ET: 64.1%; Dfc: 35.9%	GRA: 29.9%; BSV: 27%; WSA: 25.1%	1980-1996	1154-2944	230.00	Blaeberry River - CA
CA_0005167	51.53	-116.90	ET: 51.6%; Dfc: 48.4%	GRA: 43.2%; WSA: 22%; ENF: 20.5%	1980-2014	1035-2641	80.50	Split Creek - CA
CA_0005169	51.51	-117.47	Dfc: 57.2%; ET: 41.2%; Dfb: 1.6%	ENF: 30.4%; GRA: 29.8%; BSV: 16.2%	1980-2014	796-3105	1150.00	Beaver River - CA
CA_0005173	52.73	-119.38	ET: 57.8%; Dfc: 42.2%	GRA: 29.4%; SNO: 22.9%; WSA: 18.8%	1980-2013	975-2952	305.00	Canoe River - CA
CA_0005184	51.67	-118.60	Dfc: 66.2%; ET: 24.8%; Dfb: 9%	ENF: 34.7%; WSA: 26%; GRA: 24.9%	1980-2014	622-2745	934.00	Goldstream River - CA
CA_0005185	51.01	-118.09	Dfc: 65.1%; ET: 27.7%; Dfb: 7.3%	ENF: 34.2%; GRA: 27.6%; WSA: 19.5%	1980-2014	511-2921	1150.00	Illecillewaet River - CA
CA_0005189	51.66	-118.10	ET: 54.4%; Dfc: 45.6%	GRA: 43%; BSV: 24.2%; SNO: 13.4%	1980-1998	1028-2745	139.00	Stitt Creek - CA
CA_0005190	51.64	-118.67	Dfc: 77.7%; ET: 16.6%; Dfb: 5.7%	ENF: 42%; GRA: 26%; WSA: 16.6%	1980-2005	744-2253	112.00	Kirbyville Creek - CA
CA_0005195	50.77	-117.68	Dfc: 57.4%; ET: 32.1%; Dfb: 10.6%	GRA: 35.2%; ENF: 18.7%; WSA: 17.1%	1980-1996	474-3045	1020.00	Incomappleux River - CA
CA_0005199	50.28	-117.73	Dfc: 91.9%; Dfb: 6.7%; ET: 1.4%	GRA: 34.1%; ENF: 32.9%; WSA: 30.1%	1980-2013	737-2416	330.00	Kuskanax Creek - CA
CA_0005201	50.73	-117.73	Dfc: 59.7%; Dfb: 40.3%	ENF: 87.3%; WSA: 11.1%; SAV: 1.6%	1980-2013	545-2138	96.70	Beaton Creek - CA
CA_0005226	49.01	-117.95	Dfc: 53.9%; Dfb: 35.1%; Dsb: 8.3%	ENF: 60.8%; WSA: 38.3%; MF: 0.8%	1980-2015	687-2224	347.00	Big Sheep Creek - CA
CA_0005255	49.05	-117.29	Dfc: 59.5%; Dfb: 29.3%; Dsc: 6.5%	ENF: 59.9%; WSA: 32.7%; GRA: 4.2%	1980-2014	609-2234	1240.00	Salmo River - CA
CA_0005258	49.91	-118.13	Dfc: 81.8%; Dfb: 18.2%	ENF: 79.3%; WSA: 16.3%; GRA: 1.8%	1980-2013	623-2052	204.00	Barnes Creek - CA
CA_0005265	49.45	-118.04	Dfc: 58.7%; Dfb: 41.3%	ENF: 72.1%; WSA: 27%; GRA: 0.9%	1980-2015	720-2130	81.60	Deer Creek - CA
CA_0005281	49.90	-118.19	Dfc: 82.3%; Dfb: 17.7%	ENF: 53.2%; WSA: 42.5%; GRA: 3.8%	1980-2013	555-2167	298.00	Inonoaklin Creek - CA
CA_0005285	49.23	-117.24	Dfc: 82.7%; Dfb: 17.3%	ENF: 62.9%; WSA: 25.8%; GRA: 5.6%	1980-2013	898-2048	56.70	Hidden Creek - CA
CA_0005288	50.34	-117.52	Dfc: 97%; ET: 3%	GRA: 56.6%; WSA: 24.9%; ENF: 17.9%	1980-1996	1088-2425	113.00	Kuskanax Creek - CA
CA_0005293	50.79	-118.08	Dfc: 77.9%; ET: 17.9%; Dfb: 4.2%	GRA: 26.4%; ENF: 23.3%; WSA: 22.1%	1980-2011	818-2674	99.60	Cranberry Creek - CA
CA_0005299	50.89	-116.05	Dfc: 70.4%; ET: 29.6%	ENF: 36%; WSA: 31.4%; GRA: 25.1%	1980-2014	1179-2862	416.00	Kootenay River - CA
CA_0005303	50.66	-115.53	Dfc: 55.1%; ET: 44.9%	GRA: 38.5%; WSA: 29.4%; ENF: 14.7%	1980-1999	1330-2909	69.70	Albert River - CA
CA_0005304	50.53	-115.62	Dfc: 61.7%; ET: 38.3%	GRA: 33.6%; WSA: 28.2%; ENF: 25.4%	1980-1995	1104-3204	653.00	Palliser River - CA
CA_0005306	49.49	-115.37	Dfc: 84.3%; ET: 12.2%; Dfb: 3.5%	WSA: 37.2%; ENF: 33.4%; GRA: 19.1%	1980-2014	894-3043	1520.00	Bull River - CA
CA_0005345	49.61	-116.17	Dfc: 80.2%; ET: 16.1%; Dfb: 3.7%	WSA: 37.2%; ENF: 31.3%; GRA: 26.4%	1980-1995	972-2759	1480.00	St Mary River - CA
CA_0005369	49.71	-115.90	Dfc: 83.5%; ET: 8.7%; Dfb: 7.9%	WSA: 73.7%; GRA: 12.7%; SAV: 7%	1980-2014	1048-2516	135.00	Mather Creek - CA

Station	Lat	Lon	Climate	Biome	Period	Elev	Area	River
CA_0005370	49.74	-116.44	Dfc: 88.8%; ET: 11.2%	WSA: 36.2%; GRA: 31%; ENF: 27.7%	1980-2014	1155-2530	208.00	St Mary River - CA
CA_0005371	49.19	-115.44	Dfc: 81%; Dfb: 19%	ENF: 71.1%; WSA: 25.9%; GRA: 2.3%	1980-1995	1041-2085	313.00	Caven Creek - CA
CA_0005376	49.70	-116.03	Dfc: 90.7%; ET: 9.3%	WSA: 51%; ENF: 30.2%; SAV: 12.8%	1980-1999	1360-2421	102.00	Mark Creek - CA
CA_0005377	49.66	-116.07	Dfc: 82.5%; ET: 17.5%	WSA: 46.7%; ENF: 25.8%; GRA: 14%	1980-1998	1234-2539	148.00	Matthew Creek - CA
CA_0005383	49.09	-116.46	Dfc: 75.4%; Dfb: 24.3%; ET: 0.3%	ENF: 55.7%; WSA: 37.6%; GRA: 4.5%	1980-1995	643-2412	1180.00	Goat River - CA
CA_0005384	49.91	-116.95	Dfc: 79.6%; ET: 11.9%; Dfb: 8.5%	ENF: 41.3%; WSA: 28.1%; GRA: 24.4%	1980-2014	739-2684	442.00	Kaslo River - CA
CA_0005385	49.00	-116.18	Dfc: 73.8%; Dfb: 25.8%; Dsc: 0.4%	ENF: 56.7%; WSA: 38.6%; GRA: 3.7%	1980-2013	822-2284	1480.00	Moyie River - CA
CA_0005386	50.26	-116.97	Dfc: 73.3%; ET: 13.6%; Dfb: 13.1%	ENF: 40.3%; GRA: 31.8%; WSA: 20%	1980-2014	564-2692	1640.00	Lardeau River - CA
CA_0005395	49.20	-116.53	Dfc: 78.5%; Dfb: 21.5%	ENF: 59.5%; WSA: 36.7%; MF: 2.5%	1980-2014	825-2082	57.00	Duck Creek - CA
CA_0005400	49.00	-116.57	Dfc: 78.6%; Dfb: 19.8%; Dsc: 0.9%	ENF: 85.4%; WSA: 10.5%; GRA: 2.2%	1980-2013	539-1967	242.00	Boundary Creek - CA
CA_0005444	49.16	-116.45	Dfc: 80.9%; Dfb: 19.1%	ENF: 83.8%; WSA: 16.2%	1980-2014	846-2040	78.30	Arrow Creek - CA
CA_0005450	49.70	-116.92	Dfc: 71.7%; ET: 9.4%; Dsb: 8.8%	WSA: 34.8%; ENF: 26.5%; GRA: 25.8%	1980-1992	759-2602	87.30	Coffee Creek - CA
CA_0005460	49.10	-116.44	Dfc: 58.3%; Dfb: 41.7%	ENF: 90%; SAV: 10%	1980-2014	811-1794	6.22	Sullivan Creek - CA
CA_0005462	49.34	-116.71	Dfc: 73.9%; Dfb: 26.1%	ENF: 61.1%; WSA: 38.9%	1980-1999	767-1978	12.70	Twin Bays Creek - CA
CA_0005464	50.64	-117.05	Dfc: 58.1%; ET: 38%; Dfb: 3.8%	GRA: 36.6%; WSA: 19.9%; BSV: 19.8%	1980-2014	597-3124	1310.00	Duncan River - CA
CA_0005465	49.42	-115.94	Dfc: 99.6%; Dfb: 0.2%; ET: 0.2%	ENF: 53.6%; WSA: 42.4%; GRA: 3.6%	1980-2014	1189-2284	239.00	Moyie River - CA
CA_0005472	50.08	-116.78	Dfc: 63.2%; ET: 35.9%; Dfb: 0.9%	GRA: 40.6%; WSA: 29.6%; ENF: 15%	1980-2014	887-2978	585.00	Fry Creek - CA
CA_0005473	50.16	-116.58	ET: 50.2%; Dfc: 49.8%	GRA: 37.4%; BSV: 26.2%; WSA: 23%	1980-2004	1371-2906	119.00	Carney Creek - CA
CA_0005474	49.87	-117.12	Dfc: 75.8%; ET: 24.2%	GRA: 44.9%; ENF: 25.4%; WSA: 24.6%	1980-2014	1242-2684	92.30	Keen Creek - CA
CA_0005477	50.63	-117.54	Dfc: 83.3%; ET: 11.1%; Dfb: 5.6%	ENF: 38.5%; WSA: 30.8%; GRA: 23.1%	1980-2013	1006-2503	8.84	Humphries Creek - CA
CA_0005496	49.64	-117.00	Dfc: 85.2%; Dfb: 14.8%	ENF: 43.5%; WSA: 43.5%; GRA: 13%	1980-2000	747-2136	15.00	Laird Creek - CA
CA_0005502	49.59	-117.24	Dfc: 77.8%; Dsc: 11.1%; Dfb: 10.1%	WSA: 57.1%; ENF: 38.1%; GRA: 4.8%	1980-2014	803-2106	52.90	Duhamel Creek - CA
CA_0005503	49.59	-117.06	Dfc: 84.2%; Dfb: 11.8%; Dsc: 3.9%	ENF: 60.3%; WSA: 39.7%	1980-1994	672-2183	42.20	Harrop Creek - CA
CA_0005534	49.62	-117.06	Dfc: 93.6%; Dfb: 6.4%	WSA: 70.7%; ENF: 26.8%; GRA: 2.4%	1980-2014	897-2175	27.20	Redfish Creek - CA
CA_0005571	49.57	-117.65	Dfc: 53.8%; Dfb: 46.2%	ENF: 81.8%; WSA: 18.2%	1980-1994	523-1933	5.70	Mcfayden Creek - CA
CA_0005573	49.50	-117.26	Dfc: 70.6%; Dfb: 29.4%	ENF: 75%; WSA: 25%	1980-2015	968-1794	9.07	Anderson Creek - CA

Station	Lat	Lon	Climate	Biome	Period	Elev	Area	River
CA_0005598	49.70	-117.45	Dfc: 86.7%; Dfb: 9.6%; ET: 3.7%	ENF: 47.9%; WSA: 36.4%; GRA: 14%	1980-2014	782-2462	181.00	Lemon Creek - CA
CA_0005600	49.47	-117.52	Dfb: 62.5%; Dfc: 37.5%	WSA: 57.1%; ENF: 42.9%	1980-1993	848-1637	5.59	Smoky Creek - CA
CA_0005602	50.11	-117.49	Dfc: 84.6%; Dfb: 15.4%	ENF: 76.9%; WSA: 23.1%	1980-1998	1074-1948	6.70	Cadden Creek - CA
CA_0005605	49.48	-117.36	Dfc: 73.7%; Dfb: 26.3%	ENF: 87.5%; WSA: 12.5%	1980-1998	1002-1890	11.10	Sandy Creek - CA
CA_0005606	49.52	-117.21	Dfc: 100%	ENF: 45.7%; WSA: 42.9%; GRA: 11.4%	1980-2014	1283-2180	47.70	Five Mile Creek - CA
CA_0005622	49.87	-114.87	Dfc: 72.7%; ET: 27.3%	WSA: 42%; GRA: 28.6%; ENF: 21.4%	1980-2015	1202-3040	1840.00	Elk River - CA
CA_0005624	49.89	-114.87	Dfc: 76.5%; ET: 23.5%	WSA: 49.2%; GRA: 25.7%; ENF: 15.7%	1980-2014	1235-2813	621.00	Fording River - CA
CA_0005625	49.84	-114.86	Dfc: 97.5%; ET: 2.5%	WSA: 42.5%; ENF: 39.6%; GRA: 8.2%	1980-1999	1214-2337	83.90	Grave Creek - CA
CA_0005626	49.73	-114.86	Dfc: 96%; ET: 3.9%; Dfb: 0.1%	WSA: 44.8%; ENF: 33.8%; GRA: 15.2%	1980-1996	1151-2509	637.00	Michel Creek - CA
CA_0005627	50.20	-114.88	Dfc: 61.1%; ET: 38.9%	WSA: 46%; GRA: 35.4%; ENF: 10.6%	1980-1995	1688-2813	104.00	Fording River - CA
CA_0005628	49.89	-114.83	Dfc: 78.3%; ET: 21.7%	WSA: 39%; GRA: 33.3%; ENF: 22.1%	1980-2014	1290-2725	138.00	Line Creek - CA
CA_0005630	49.58	-114.95	Dfc: 100%	ENF: 88.9%; WSA: 11.1%	1980-2014	1531-2036	6.40	Hosmer Creek - CA
CA_0005631	50.38	-114.92	Dfc: 56.2%; ET: 43.8%	GRA: 35.9%; ENF: 26.7%; WSA: 21.8%	1980-1996	1566-3040	334.00	Elk River - CA
CA_0005632	49.51	-114.68	Dfc: 100%	ENF: 51%; GRA: 21.6%; WSA: 19.6%	1980-1995	1532-2270	35.90	Michel Creek - CA
CA_0005633	50.17	-114.86	Dfc: 61.4%; ET: 38.6%	BSV: 36.1%; WSA: 31.9%; GRA: 27.8%	1980-1995	1630-2602	43.00	Kilmarnock Creek - CA
CA_0005635	49.21	-119.99	Dfc: 62.2%; Dsc: 17.1%; ET: 14.3%	WSA: 39%; ENF: 37.1%; GRA: 23%	1980-2013	488-2542	1050.00	Ashnola River - CA
CA_0005638	49.46	-120.50	Dsc: 76.7%; Dsb: 11.6%; Dfc: 9.4%	ENF: 52.1%; WSA: 29.8%; GRA: 15.9%	1980-2013	645-2390	1810.00	Similkameen River - CA
CA_0005653	49.46	-120.52	Dsc: 59.5%; Dsb: 23%; Dfc: 9.8%	WSA: 48%; ENF: 45.8%; GRA: 5.9%	1980-2013	660-2085	1780.00	Tulameen River - CA
CA_0005658	49.37	-120.57	Dsc: 74.1%; Dsb: 22.5%; Dfc: 3.4%	ENF: 61.8%; WSA: 34%; GRA: 3.6%	1980-1998	882-1917	185.00	Whipsaw Creek - CA
CA_0005661	49.66	-120.34	Dfc: 79.6%; Dsc: 11.2%; BSk: 9.2%	WSA: 67.2%; GRA: 21.6%; ENF: 11.2%	1980-2013	947-1759	263.00	Siwash Creek - CA
CA_0005666	49.26	-119.83	BSk: 54.5%; Dfc: 40.5%; Dfb: 5%	WSA: 69.3%; ENF: 25.1%; GRA: 5%	1980-2013	514-2156	181.00	Keremeos Creek - CA
CA_0005668	49.36	-120.07	Dfc: 87.1%; BSk: 12.9%	WSA: 51.5%; ENF: 41.9%; GRA: 6.6%	1980-2013	676-2105	388.00	Hedley Creek - CA
CA_0005678	49.10	-120.58	Dsc: 92%; ET: 3.4%; Dfc: 2.8%	GRA: 38.1%; WSA: 29.7%; ENF: 29.2%	1980-2013	1128-2390	566.00	Pasayten River - CA
CA_0005679	49.09	-120.67	Dsc: 97.7%; Dsb: 1.6%; Dfc: 0.4%	ENF: 74.9%; WSA: 15.6%; GRA: 6.2%	1980-2013	1116-2254	408.00	Similkameen River - CA
CA_0005680	49.47	-120.98	Dsc: 88.8%; Dfc: 11.2%	ENF: 86.1%; WSA: 11.3%; GRA: 2.1%	1980-2011	1141-2085	253.00	Tulameen River - CA

Station	Lat	Lon	Climate	Biome	Period	Elev	Area	River
CA_0005703	50.30	-119.21	Dfb: 57.4%; Dfc: 42.6%	ENF: 62.4%; WSA: 31.8%; GRA: 3.5%	1980-1999	638-1831	55.70	Bx Creek - CA
CA_0005705	50.04	-119.24	Dfc: 100%	WSA: 74.7%; ENF: 20.7%; GRA: 4.6%	1980-1996	1346-1620	62.40	Vernon Creek - CA
CA_0005719	49.43	-119.75	Dfc: 57.6%; BSk: 41.9%; Dfb: 0.6%	ENF: 64.4%; WSA: 33.6%; GRA: 2.1%	1980-2013	817-2079	101.00	Shatford Creek - CA
CA_0005723	49.83	-119.79	Dfc: 64.4%; BSk: 20.1%; Dfb: 15.5%	ENF: 50.8%; WSA: 45.8%; GRA: 3.4%	1980-2011	631-1860	182.00	Trepanier Creek - CA
CA_0005733	49.89	-119.42	Dfc: 49.9%; BSk: 26.8%; Dfb: 23.3%	ENF: 37.3%; WSA: 30.5%; GRA: 20.2%	1980-1996	386-1650	221.00	Kelowna Creek - CA
CA_0005743	50.24	-119.27	Dfb: 39.8%; Dfc: 36.1%; BSk: 24.1%	WSA: 44.3%; ENF: 34.3%; GRA: 13.1%	1980-2013	392-1620	569.00	Vernon Creek - CA
CA_0005754	49.88	-119.41	Dfc: 76.3%; Dfb: 19.1%; BSk: 4.5%	ENF: 52.4%; WSA: 41.9%; GRA: 4.5%	1980-2013	387-2060	795.00	Mission Creek - CA
CA_0005768	49.71	-120.01	Dfc: 87.7%; BSk: 7.7%; Dfb: 4.6%	ENF: 58.9%; WSA: 41.1%	1980-2014	1065-1841	34.60	Camp Creek - CA
CA_0005772	50.07	-119.67	Dfc: 100%	WSA: 59.2%; ENF: 40.8%	1980-1994	1363-1677	31.30	Terrace Creek - CA
CA_0005776	50.26	-119.08	Dfb: 65.2%; Dfc: 34.8%	ENF: 67%; WSA: 25.8%; MF: 7.2%	1980-2011	690-1620	60.60	Coldstream Creek - CA
CA_0005777	50.01	-119.25	Dfc: 100%	WSA: 45%; ENF: 30%; GRA: 25%	1980-2004	1314-1456	12.70	Bulman Creek - CA
CA_0005780	49.34	-119.58	Dfc: 71.3%; BSk: 18%; Dfb: 10.7%	ENF: 48.7%; WSA: 43.3%; GRA: 6.7%	1980-2010	373-1814	89.90	Shuttleworth Creek - CA
CA_0005791	50.26	-119.31	Dfb: 43.9%; Dfc: 31.7%; BSk: 24.3%	WSA: 39.8%; ENF: 33.8%; GRA: 15.3%	1980-1999	360-1771	751.00	Vernon Creek - CA
CA_0005795	49.99	-119.61	Dfc: 84.4%; BSk: 15.6%	ENF: 68.7%; WSA: 31.3%	1980-1996	922-1822	76.10	Lambly Creek - CA
CA_0005798	49.62	-119.42	Dfc: 100%	WSA: 61.2%; ENF: 38.8%	1980-1999	1571-1957	35.50	Penticton Creek - CA
CA_0005800	49.25	-119.32	Dfc: 99.5%; BSk: 0.5%	ENF: 66.1%; WSA: 33.9%	1980-2014	1277-2166	117.00	Vaseux Creek - CA
CA_0005802	49.79	-119.85	Dfc: 57.5%; BSk: 39.7%; Dfb: 2.7%	ENF: 83.1%; WSA: 16.9%	1980-2011	956-1645	40.70	Greata Creek - CA
CA_0005803	50.21	-119.54	Dfc: 89.2%; Dfb: 9.8%; BSk: 1%	ENF: 74.4%; WSA: 23.9%; GRA: 1.7%	1980-2013	735-1984	114.00	Whiteman Creek - CA
CA_0005815	49.08	-119.50	Dfc: 46.1%; BSk: 32.3%; Dfb: 21.6%	WSA: 53.3%; ENF: 37.1%; GRA: 7.6%	1980-2015	302-2134	227.00	Inkaneep Creek - CA
CA_0005826	49.99	-118.87	Dfc: 100%	WSA: 65.4%; ENF: 34.6%	1980-1998	1831-2060	16.10	Loch Katrine Creek - CA
CA_0005827	50.00	-119.07	Dfc: 100%	WSA: 67%; ENF: 28.2%; GRA: 4.9%	1980-2010	1276-1823	70.70	Belgo Creek - CA
CA_0005839	49.17	-118.98	Dfc: 69.4%; Dfb: 23.3%; BSk: 7.3%	ENF: 51.4%; WSA: 47.7%; GRA: 0.9%	1980-2014	646-2181	1890.00	West Kettle River - CA
CA_0005851	49.70	-119.09	Dfc: 98.6%; Dfb: 0.9%; ET: 0.5%	WSA: 56.4%; ENF: 41.4%; GRA: 2.2%	1980-2013	1043-2181	233.00	West Kettle River - CA
CA_0005854	49.57	-119.05	Dfc: 78.3%; Dfb: 21.7%	ENF: 69.7%; WSA: 25.4%; GRA: 4.8%	1980-2013	934-2170	145.00	Trapping Creek - CA
CA_0005857	49.48	-119.11	Dfc: 81.4%; Dfb: 16.7%; BSk: 1.8%	ENF: 53.8%; WSA: 44.8%; GRA: 1.4%	1980-1996	827-2181	1170.00	West Kettle River - CA

Station	Lat	Lon	Climate	Biome	Period	Elev	Area	River
CA_0005858	49.59	-118.31	Dfc: 81.3%; Dfb: 18.7%	ENF: 58.6%; WSA: 39.7%; GRA: 1.7%	1980-2012	924-2166	221.00	Burrell Creek - CA
CA_0005861	49.37	-118.85	Dfc: 60.4%; Dfb: 39.6%	ENF: 65%; WSA: 35%	1980-2011	808-2085	28.50	Lost Horse Creek - CA
CA_0005862	49.00	-114.48	Dfc: 99.3%; Dfb: 0.4%; ET: 0.3%	ENF: 37.7%; WSA: 32%; GRA: 22.3%	1980-2013	1219-2427	1110.00	Flathead River - CA
CA_0005863	49.03	-114.58	Dfc: 100%	ENF: 44.3%; WSA: 31%; GRA: 14.6%	1980-1992	1403-2175	118.00	Couldrey Creek - CA
CA_0005864	49.09	-114.54	Dfc: 98.8%; ET: 1.2%	GRA: 47.3%; ENF: 25%; WSA: 24.1%	1980-1996	1320-2336	145.00	Howell Creek - CA
CA_0005865	49.09	-114.55	Dfc: 100%	ENF: 54.7%; GRA: 29.5%; WSA: 12.9%	1980-2014	1338-2236	92.80	Cabin Creek - CA
CA_0005880	60.08	-133.86	Dsc: 93.6%; ET: 4.7%; BSk: 1.7%	WSA: 79%; ENF: 17.3%; GRA: 2.4%	1980-1993	645-1866	1770.00	Lubbock River - CA
CA_0005883	59.84	-135.01	ET: 53.8%; Dsc: 46.2%	GRA: 42.8%; SNO: 30.8%; WSA: 9.9%	1980-1993	669-1944	240.00	Lindeman Creek - CA
CA_0005885	60.13	-134.88	ET: 61.6%; Dsc: 38.4%	GRA: 48.9%; BSV: 17.4%; WSA: 10.9%	1980-2014	640-2139	864.00	Wheaton River - CA
CA_0005886	59.95	-134.33	ET: 56%; Dsc: 44%	GRA: 43.7%; WSA: 18.7%; BSV: 12.9%	1980-2014	715-1986	989.00	Tutshi River - CA
CA_0005887	59.59	-134.39	ET: 70.2%; Dsc: 29.8%	GRA: 26.9%; SNO: 25.7%; BSV: 22.5%	1980-1993	697-2103	717.00	Fantail River - CA
CA_0005888	59.43	-134.21	ET: 83.2%; Dsc: 16.8%	GRA: 56.4%; ENF: 16.8%; WSA: 14.9%	1980-1993	808-1931	269.00	Wann River - CA
CA_0005891	60.61	-134.46	Dsc: 59.8%; ET: 19.5%; BSk: 19.1%	WSA: 66.3%; ENF: 24%; GRA: 5.8%	1980-1995	656-1844	1700.00	Mclintock River - CA
CA_0005895	60.73	-135.49	ET: 68.3%; Dsc: 31.7%	GRA: 44.4%; WSA: 29.5%; OSH: 22.5%	1980-2014	859-2024	648.00	Ibex River - CA
CA_0005900	59.91	-132.91	Dsc: 54.2%; ET: 45.8%	WSA: 43.2%; GRA: 30.5%; ENF: 19.5%	1980-1993	872-1934	1910.00	Gladys River - CA
CA_0005901	60.01	-132.14	Dsc: 96.7%; Dfb: 3.3%	ENF: 52%; WSA: 48%	1980-2014	812-1238	1580.00	Morely River - CA
CA_0005904	61.39	-134.37	ET: 51.6%; Dsc: 39.7%; Dfc: 8.7%	WSA: 60.3%; GRA: 25.6%; OSH: 9.3%	1980-1996	780-1965	515.00	South Big Salmon River - CA
CA_0005906	62.57	-137.01	Dfc: 88%; ET: 12%	WSA: 47.6%; SAV: 34.1%; OSH: 17.1%	1980-2014	506-1876	1800.00	Big Creek - CA
CA_0005908	62.20	-134.39	Dsc: 53.7%; ET: 30.8%; Dfc: 15.5%	WSA: 66.4%; ENF: 11.1%; GRA: 10.4%	1980-2009	633-1934	552.00	Drury Creek - CA
CA_0005911	62.92	-130.54	ET: 60.9%; Dfc: 36.2%; Dsc: 2.9%	SAV: 38.3%; GRA: 22.3%; OSH: 18%	1980-1996	939-2290	997.00	South Macmillan River - CA
CA_0005920	61.35	-139.17	ET: 95.1%; Dfc: 4.9%	GRA: 41.1%; BSV: 37.9%; OSH: 8.7%	1980-2014	901-2916	654.00	Duke River - CA
CA_0005935	64.00	-137.57	Dfc: 89.7%; ET: 9.6%; Dsc: 0.6%	WSA: 52.1%; SAV: 32.3%; OSH: 13.4%	1980-1994	658-1736	860.00	Little South Klondike River - CA
CA_0005950	60.29	-129.02	Dfc: 99.6%; ET: 0.4%	ENF: 75.8%; WSA: 24.2%	1980-1993	725-1529	435.00	Tom Creek - CA
CA_0005957	59.76	-129.13	Dsc: 58.4%; ET: 38.6%; Dfc: 2.9%	ENF: 37.6%; GRA: 29.6%; WSA: 27.5%	1980-1995	719-2101	1700.00	Blue River - CA
CA_0005958	59.12	-129.83	ET: 58.6%; Dsc: 41.4%	GRA: 47.8%; WSA: 34.5%; ENF: 5.3%	1980-2013	815-1998	882.00	Cottonwood River - CA
CA_0005972	59.34	-125.94	ET: 48%; Dfc: 47.9%; Dsc: 4.1%	WSA: 41.7%; GRA: 34.7%; ENF: 15.7%	1980-2014	541-2142	1170.00	Trout River - CA

Station	Lat	Lon	Climate	Biome	Period	Elev	Area	River
CA_0005973	59.60	-126.67	Dfc: 100%	WSA: 79.6%; ENF: 19.7%; MF: 0.7%	1980-1996	568-1176	77.80	Geddes Creek - CA
CA_0005974	59.45	-126.23	Dfc: 100%	MF: 45.9%; ENF: 35.9%; WSA: 17%	1980-2014	475-1473	209.00	Teeter Creek - CA
CA_0005976	59.37	-125.07	Dfc: 98.9%; ET: 1.1%	ENF: 67.7%; WSA: 18.9%; MF: 9.2%	1980-1995	390-1685	1780.00	Grayling River - CA
CA_0005986	58.03	-122.72	Dfc: 100%	ENF: 78.5%; MF: 19.8%; DBF: 1.6%	1980-2012	529-1093	335.00	Bougie Creek - CA
CA_0005987	58.11	-122.72	Dfc: 100%	ENF: 73.2%; MF: 23.5%; DBF: 2.3%	1980-2014	552-1077	109.00	Adsett Creek - CA
CA_0005994	62.21	-128.76	ET: 84%; Dfc: 16%	GRA: 41.2%; OSH: 34.3%; SAV: 20.8%	1980-1992	1020-2138	216.00	Mac Creek - CA
CA_0005995	62.37	-128.68	ET: 98.9%; Dfc: 1.1%	GRA: 46.2%; BSV: 30%; SAV: 11.2%	1980-1992	1210-2089	34.30	Lened Creek - CA
CA_0005997	61.56	-124.81	Dfc: 54.1%; ET: 45.9%	GRA: 61.2%; SAV: 19.8%; OSH: 17.3%	1980-2014	896-1840	495.00	Prairie Creek - CA
CA_0006022	63.30	-129.79	ET: 100%	OSH: 43.1%; GRA: 40.6%; BSV: 15.9%	1980-1992	1247-2121	219.00	Tsichu River - CA
CA_0006027	62.77	-126.69	ET: 90.2%; Dfc: 9.8%	GRA: 42.4%; BSV: 38.4%; OSH: 16.6%	1980-1990	901-2413	1420.00	Silverberry River - CA
CA_0006072	64.90	-138.28	ET: 57.1%; Dfc: 41.5%; Dsc: 1.4%	OSH: 71.1%; GRA: 25.6%; BSV: 3.1%	1980-2014	940-2108	1180.00	Blackstone River - CA
CA_0006242	49.65	-110.01	Dfc: 100%	GRA: 48.2%; ENF: 32.7%; CRO: 12.5%	1980-2014	1186-1436	111.00	Battle Creek - CA
US_0000044	45.23	-70.20	Dfb: 96.3%; Dfc: 3.7%	MF: 56.2%; DBF: 41.7%; ENF: 1.4%	1980-2016	344-1192	516.00	Dead River - US
US_0000045	45.31	-70.24	Dfb: 94.9%; Dfc: 5.1%	MF: 66.5%; DBF: 32.1%; WSA: 1.3%	1980-2016	326-1024	193.00	Spencer Stream - US
US_0000051	44.86	-70.49	Dfb: 100%	DBF: 69.8%; MF: 30.2%	1980-2016	310-900	25.30	Sandy River - US
US_0000057	44.88	-71.06	Dfb: 98.3%; Dfc: 1.7%	DBF: 83%; MF: 17%	1980-2016	412-1004	152.00	Diamond River - US
US_0000058	44.78	-71.13	Dfb: 96.9%; Dfc: 3.1%	DBF: 50%; MF: 45.6%; ENF: 3.7%	1980-2016	378-1092	1046.00	Androscoggin River - US
US_0000059	44.67	-71.18	Dfb: 97.2%; Dfc: 2.8%	DBF: 53.1%; MF: 42.8%; ENF: 3.3%	1980-2016	363-1092	1177.00	Androscoggin River Below Bog Brook - US
US_0000060	44.44	-71.19	Dfb: 97.5%; Dfc: 2.5%	DBF: 54.9%; MF: 40.5%; ENF: 2.8%	1980-2016	275-1101	1361.00	Androscoggin River - US
US_0000314	42.08	-73.07	Dfb: 100%	DBF: 80.8%; MF: 19.2%	1980-2016	250-582	91.70	West Branch Farmington River - US
US_0000338	42.47	-73.20	Dfb: 100%	DBF: 79%; WSA: 12.7%; MF: 4.9%	1980-2016	321-672	57.60	East Branch Housatonic River - US
US_0000433	42.32	-74.44	Dfb: 100%	DBF: 86.1%; WSA: 9%; MF: 4.9%	1980-2016	359-1167	237.00	Schoharie Creek - US
US_0000437	42.41	-74.45	Dfb: 100%	DBF: 72.5%; MF: 15%; WSA: 12.5%	1980-2016	387-668	10.90	Platter Kill - US
US_0000438	42.43	-74.47	Dfb: 100%	DBF: 91.8%; WSA: 6.6%; MF: 1.6%	1980-2016	369-796	16.20	Mine Kill - US
US_0000458	41.87	-74.49	Dfb: 100%	DBF: 100%	1980-2016	328-1084	38.30	Rondout Creek - US
US_0000585	42.14	-74.65	Dfb: 100%	DBF: 95.8%; WSA: 4.2%	1980-2016	405-1084	163.00	East Branch Delaware River - US
US_0000587	42.11	-74.73	Dfb: 100%	DBF: 100%	1980-2016	437-1018	25.20	Mill Brook - US

Station	Lat	Lon	Climate	Biome	Period	Elev	Area	River
US_0000588	42.12	-74.82	Dfb: 100%	DBF: 92.3%; WSA: 7.7%	1980-2016	421-942	33.20	Tremper Kill - US
US_0000827	42.39	-77.36	Dfb: 100%	WSA: 51.6%; DBF: 38.2%; SAV: 4.1%	1980-1995	367-656	66.80	Fivemile Creek - US
US_0000987	39.27	-79.26	Dfb: 100%	DBF: 60.5%; WSA: 33.3%; GRA: 5.6%	1980-2010	804-1236	48.70	Stony River - US
US_0000988	39.37	-79.18	Dfb: 100%	DBF: 71.1%; WSA: 28.1%; SAV: 0.7%	1980-2016	620-1015	42.60	Abram Creek - US
US_0001004	38.98	-79.23	Dfb: 92.9%; Dfa: 7.1%	DBF: 91.7%; WSA: 5.5%; SAV: 1.8%	1980-2016	378-1444	310.00	N F South Branch Potomac River - US
US_0001005	38.99	-79.18	Dfb: 88%; Dfa: 12%	DBF: 85.1%; WSA: 7.2%; SAV: 4.4%	1980-2016	308-1444	651.00	South Branch Potomac River - US
US_0001007	39.01	-78.96	Dfb: 55.2%; Dfa: 44.8%	DBF: 88.3%; WSA: 7%; SAV: 4.4%	1980-2016	273-1213	277.00	S F South Branch Potomac River - US
US_0001568	34.81	-83.31	Cfa: 74.7%; Cfb: 24.4%; Dfb: 0.9%	MF: 58.4%; DBF: 39.6%; WSA: 2%	1980-2016	410-1361	207.00	Chattooga River - US
US_0001569	34.89	-83.53	Cfa: 65.9%; Cfb: 27.3%; Dfb: 6.8%	DBF: 86.8%; MF: 12.7%; WSA: 0.5%	1980-2016	607-1571	58.40	Tallulah River - US
US_0001570	34.73	-83.38	Cfa: 85.9%; Cfb: 11.6%; Dfb: 2.5%	DBF: 68%; MF: 27.6%; WSA: 4.2%	1980-2016	448-1571	184.40	Tallulah River - US
US_0001942	34.70	-83.73	Cfa: 90.2%; Cfb: 9.8%	DBF: 55.3%; MF: 43.3%; WSA: 1.4%	1980-2016	461-1135	44.70	Chattahoochee River - US
US_0002093	34.57	-84.47	Cfa: 100%	DBF: 83.3%; WSA: 16.7%	1980-2015	432-755	9.99	Fausett Creek - US
US_0002122	34.26	-84.60	Cfa: 100%	DBF: 67.6%; WSA: 29.8%; SAV: 1.6%	1980-2016	291-674	56.50	Shoal Creek - US
US_0002372	38.81	-79.88	Dfb: 100%	DBF: 91%; GRA: 4.3%; WSA: 4.2%	1980-2016	596-1406	185.00	Tygart Valley River - US
US_0002373	38.92	-79.88	Dfb: 100%	DBF: 86.3%; WSA: 7.5%; GRA: 4.7%	1980-2004	583-1406	271.00	Tygart Valley River - US
US_0002374	39.03	-79.94	Dfb: 100%	DBF: 83.3%; WSA: 11.6%; GRA: 3.9%	1980-2016	522-1406	406.00	Tygart Valley River - US
US_0002375	39.04	-80.07	Dfb: 98.2%; Dfa: 1.8%	DBF: 98.6%; WSA: 1.4%	1980-2016	554-1104	148.00	Middle Fork River - US
US_0002390	39.07	-79.62	Dfb: 100%	DBF: 88.8%; WSA: 6.5%; MF: 2.7%	1980-2016	587-1422	349.00	Dry Fork - US
US_0002391	39.14	-79.42	Dfb: 100%	DBF: 62.4%; WSA: 31.4%; MF: 3.1%	1980-2016	958-1298	54.70	Blackwater River - US
US_0002392	39.13	-79.47	Dfb: 100%	DBF: 55.2%; WSA: 39.3%; MF: 3.1%	1980-2016	942-1298	85.90	Blackwater River - US
US_0002395	39.10	-79.68	Dfb: 99.9%; Dfa: 0.1%	DBF: 86.1%; MF: 13%; WSA: 0.9%	1980-1993	503-1436	213.00	Shavers Fork - US
US_0002396	39.12	-79.68	Dfb: 99.8%; Dfa: 0.2%	DBF: 81.8%; WSA: 10.1%; MF: 6.7%	1980-2016	493-1436	722.00	Cheat River - US
US_0002397	39.35	-79.67	Dfb: 98.5%; Dfa: 1.5%	DBF: 84.8%; WSA: 9.1%; MF: 5.1%	1980-1996	443-1436	939.00	Cheat River - US
US_0002548	38.54	-79.83	Dfb: 100%	DBF: 96.7%; MF: 1.5%; GRA: 0.9%	1980-2015	838-1337	133.00	Greenbrier River - US
US_0002549	38.19	-80.13	Dfb: 100%	DBF: 92.7%; WSA: 3.4%; SAV: 2.2%	1980-2016	645-1448	540.00	Greenbrier River - US

Station	Lat	Lon	Climate	Biome	Period	Elev	Area	River
US_0002550	37.68	-80.46	Dfb: 73.2%; Dfa: 26.8%	DBF: 69%; WSA: 13.1%; GRA: 10.1%	1980-1998	572-1078	80.80	Second Creek - US
US_0002556	38.38	-80.48	Dfb: 100%	DBF: 93.7%; MF: 5.3%; GRA: 0.7%	1980-2016	696-1374	128.00	Williams River - US
US_0002558	38.30	-80.53	Dfb: 100%	DBF: 90.2%; MF: 9.8%	1980-2016	735-1369	80.40	Cranberry River - US
US_0002560	38.29	-80.64	Dfb: 100%	DBF: 95%; MF: 2.9%; WSA: 1.2%	1980-2016	619-1374	529.00	Gauley River - US
US_0002561	38.22	-80.89	Dfb: 92.9%; Dfa: 7.1%	DBF: 91.8%; WSA: 4.5%; MF: 1.9%	1980-2003	479-1374	806.00	Gauley River - US
US_0002564	38.26	-81.02	Dfa: 88.6%; Dfb: 11.4%	DBF: 90.9%; WSA: 7.7%; GRA: 0.7%	1980-2016	387-727	40.20	Peters Creek - US
US_0002565	38.23	-81.18	Dfb: 79.5%; Dfa: 20.5%	DBF: 90.4%; WSA: 6.3%; GRA: 1.7%	1980-2016	257-1374	1317.00	Gauley River - US
US_0002567	38.60	-80.49	Dfb: 93.1%; Dfa: 6.9%	DBF: 99.3%; WSA: 0.4%; MF: 0.2%	1980-2016	370-1434	266.00	Elk River - US
US_0002573	37.97	-81.52	Dfa: 77.3%; Dfb: 22.7%	DBF: 89.8%; GRA: 9.3%; WSA: 0.9%	1980-2016	321-902	62.80	Clear Fork - US
US_0002593	37.43	-82.35	Cfa: 100%	DBF: 100%	1980-2016	329-580	6.20	Grapevine Creek - US
US_0003020	36.75	-83.26	Cfa: 92.7%; Dfb: 7.3%	DBF: 98.9%; WSA: 1.1%	1980-2004	406-984	55.80	Martins Fork - US
US_0003103	35.96	-83.17	Dfb: 39.1%; Cfa: 33%; Cfb: 27.9%	DBF: 79.4%; WSA: 10.2%; SAV: 6.5%	1980-2016	330-1883	666.00	Pigeon River - US
US_0003106	36.18	-82.46	Dfb: 46.4%; Cfa: 34%; Cfb: 19.5%	DBF: 87.7%; WSA: 9.1%; SAV: 1.8%	1980-2016	483-1938	805.00	Nolichucky River - US
US_0003165	36.43	-83.40	Cfa: 65.5%; Dfb: 18.3%; Dfa: 16.2%	DBF: 70.8%; WSA: 16.3%; SAV: 10.9%	1980-2016	352-1386	1474.00	Clinch River - US
US_0003169	36.54	-83.63	Cfa: 87.3%; Dfb: 7.9%; Dfa: 4.8%	DBF: 53.5%; WSA: 31.2%; SAV: 12%	1980-2016	350-1137	685.00	Powell River - US
US_0003181	34.88	-83.72	Cfa: 78.4%; Cfb: 21.6%	DBF: 76.8%; MF: 19.2%; WSA: 4%	1980-2016	613-1223	39.50	Hiwassee River - US
US_0003186	34.84	-83.94	Cfa: 91%; Cfb: 8.6%; Dfb: 0.3%	DBF: 64.1%; MF: 19.2%; WSA: 16.3%	1980-2016	573-1319	74.80	Nottely River - US
US_0004649	44.08	-104.06	Dfb: 93.3%; Dfc: 6.7%	WSA: 52.6%; GRA: 23.7%; SAV: 23.7%	1980-2016	1918-2117	10.20	Beaver Creek - US
US_0004650	43.86	-104.11	Dfb: 98.1%; Dfc: 1.7%; BSk: 0.2%	GRA: 53.4%; SAV: 23.9%; WSA: 18.8%	1980-2016	1377-2117	110.00	Stockade Beaver Creek - US
US_0004657	43.43	-103.48	Dfb: 49.5%; BSk: 49.5%; Dfa: 1.1%	GRA: 97.7%; URB: 0.8%; SAV: 0.8%	1980-2016	1070-1720	136.00	Fall River - US
US_0004658	43.58	-103.48	Dfb: 100%	GRA: 77.6%; ENF: 9.4%; SAV: 8.8%	1980-2015	1301-1819	45.60	Beaver Creek - US
US_0004659	43.47	-103.31	Dfb: 64.4%; BSk: 30.8%; Dfa: 4.9%	GRA: 90.3%; ENF: 4.5%; SAV: 3.2%	1980-2016	973-1819	127.00	Beaver Creek - US
US_0004661	43.72	-103.37	Dfb: 100%	GRA: 78%; WSA: 11.7%; SAV: 6%	1980-2016	1244-2075	105.00	French Creek - US
US_0004663	43.87	-103.34	Dfb: 89.5%; Dwb: 10.5%	WSA: 59.3%; GRA: 34%; ENF: 6.6%	1980-2016	1177-2008	58.50	Battle Creek - US
US_0004664	43.76	-103.36	Dfb: 100%	GRA: 54.3%; WSA: 39%; ENF: 6.7%	1980-2016	1270-1731	26.80	Grace Coolidge Creek - US
US_0004667	43.98	-103.35	Dfb: 88.9%; Dwb: 10.6%; Dfc: 0.4%	WSA: 75.5%; GRA: 20.9%; ENF: 2.5%	1980-2016	1224-2162	163.00	Spring Creek - US

Station	Lat	Lon	Climate	Biome	Period	Elev	Area	River
US_0004670	44.13	-103.86	Dfb: 70.6%; Dfc: 29.4%	WSA: 100%	1980-2016	1937-2159	7.84	Rhoads Fork - US
US_0004673	44.08	-103.58	Dfb: 89.1%; Dfc: 10.9%	WSA: 81.4%; GRA: 17%; SAV: 1.1%	1980-2016	1466-2166	293.00	Rapid Creek Above Pactola Reservoir - US
US_0004674	44.08	-103.48	Dfb: 89.6%; Dfc: 9.9%; Dwb: 0.4%	WSA: 82.4%; GRA: 15.5%; SAV: 1%	1980-2016	1398-2166	321.00	Rapid Creek - US
US_0004675	44.05	-103.31	Dfb: 79.9%; Dwb: 11.2%; Dfc: 8.6%	WSA: 82.3%; GRA: 15.4%; SAV: 0.9%	1980-2016	1077-2166	374.00	Rapid Creek - US
US_0004679	44.14	-103.45	Dfb: 100%	WSA: 82.5%; ENF: 9.8%; GRA: 7.7%	1980-2016	1358-1955	94.20	Boxelder Creek - US
US_0004680	44.13	-103.30	Dfb: 84.5%; Dwb: 13.3%; Dwa: 2.2%	WSA: 77%; GRA: 11.6%; ENF: 11.4%	1980-2009	1063-1955	127.00	Boxelder Creek - US
US_0004693	44.52	-104.08	Dfb: 94.7%; Dfa: 3.4%; Dfc: 1.9%	WSA: 61.1%; GRA: 35%; ENF: 2.2%	1980-2016	1108-2138	274.00	Sand Creek - US
US_0004696	44.30	-103.87	Dfb: 94.7%; Dfc: 5.3%	WSA: 93%; GRA: 6.6%; ENF: 0.4%	1980-2016	1656-2157	64.80	Spearfish Creek - US
US_0004698	44.35	-103.94	Dfb: 100%	WSA: 97.1%; GRA: 2.9%	1980-2016	1626-2063	27.80	Little Spearfish Creek - US
US_0004699	44.40	-103.89	Dfb: 97.5%; Dfc: 2.5%	WSA: 94.2%; GRA: 5.4%; ENF: 0.4%	1980-2009	1407-2157	143.00	Spearfish Creek - US
US_0004700	44.48	-103.86	Dfb: 95.2%; Dfa: 2.6%; Dfc: 2.2%	WSA: 91%; GRA: 7.9%; ENF: 0.7%	1980-2016	1141-2157	165.00	Spearfish Creek - US
US_0004705	44.44	-103.63	Dfb: 100%	WSA: 65.7%; GRA: 28.2%; URB: 2.8%	1980-2016	1127-2080	56.50	Whitewood Creek - US
US_0004711	44.34	-103.64	Dfb: 100%	WSA: 85%; GRA: 15%	1980-2016	1524-1820	15.70	Bear Butte Creek - US
US_0004887	39.16	-105.31	Dfc: 51.7%; BSk: 31.9%; Dfb: 8.9%	GRA: 86.6%; WSA: 7.5%; SAV: 5%	1980-2016	2177-4227	1615.10	South Platte River - US
US_0004889	39.21	-105.27	Dfc: 52.1%; BSk: 29.6%; Dfb: 11.2%	GRA: 84.1%; WSA: 9.5%; SAV: 5.4%	1980-2007	2086-4227	1740.10	South Platte River - US
US_0004890	39.17	-105.12	Dfb: 66.2%; Dfc: 33.8%	GRA: 44.8%; WSA: 36.2%; SAV: 15%	1980-2016	2307-3089	106.00	Trout Creek - US
US_0004905	39.65	-105.17	Dfb: 54.9%; Dfc: 38.7%; ET: 5.5%	WSA: 60.4%; GRA: 21.4%; ENF: 12%	1980-2016	1740-4009	176.00	Bear Creek - US
US_0005681	36.68	-104.79	Dfb: 58.4%; BSk: 24.6%; Dfc: 16.6%	GRA: 68.8%; SAV: 27.1%; WSA: 3.7%	1980-2016	1978-3818	301.00	Vermejo River - US
US_0005682	36.55	-105.27	Dfc: 51.8%; Dfb: 48.2%	GRA: 83.6%; WSA: 15.6%; ENF: 0.8%	1980-2010	2512-3647	73.80	Moreno Creek - US
US_0005683	36.49	-105.27	Dfb: 89.7%; Dfc: 10.3%	GRA: 59.2%; WSA: 40.3%; SAV: 0.4%	1980-2010	2512-3360	56.00	Cieneguilla Creek - US
US_0005684	36.52	-105.28	Dfc: 67.3%; Dfb: 32.7%	WSA: 76.2%; GRA: 23.8%	1980-2010	2512-3578	10.50	Sixmile Creek - US
US_0005685	36.53	-105.23	Dfb: 68.8%; Dfc: 31.2%	GRA: 68%; WSA: 31.4%; ENF: 0.3%	1980-2016	2497-3647	167.00	Cimarron River - US
US_0005686	36.52	-104.98	Dfb: 68.1%; Dfc: 28.9%; BSk: 3%	GRA: 62.3%; WSA: 35.9%; SAV: 1.3%	1980-2016	2038-3663	294.00	Cimarron River - US
US_0005687	36.57	-104.95	Dfb: 65.3%; Dfc: 21.4%; BSk: 13.4%	GRA: 78.8%; SAV: 12.4%; WSA: 8.8%	1980-2016	2081-3671	171.00	Ponil Creek - US
US_0005694	35.92	-105.16	Dfb: 90.7%; Dfc: 6.8%; BSk: 2.5%	GRA: 73.1%; WSA: 26.4%; ENF: 0.4%	1980-2016	2090-3303	215.00	Coyote Creek - US
US_0006466	38.22	-106.09	Dfc: 75.1%; BSk: 18.6%; ET: 6.2%	GRA: 63.8%; WSA: 28.9%; SAV: 7.2%	1980-2007	2662-3781	45.40	Kerber Creek - US

Station	Lat	Lon	Climate	Biome	Period	Elev	Area	River
US_0006486	36.90	-105.25	Dfc: 98.9%; ET: 1.1%	GRA: 48%; SAV: 26.7%; WSA: 22.7%	1980-2016	2889-3864	25.10	Costilla Creek - US
US_0006487	36.90	-105.26	Dfc: 78.5%; ET: 21.5%	GRA: 58.2%; SAV: 28.4%; WSA: 13.4%	1980-2016	2905-3832	16.60	Casias Creek - US
US_0006489	36.87	-105.28	Dfc: 91.6%; ET: 8.4%	GRA: 54.2%; SAV: 25.3%; WSA: 19.5%	1980-2016	2868-3832	54.60	Costilla Creek - US
US_0006490	36.97	-105.51	Dfc: 74.1%; Dfb: 17.9%; BSk: 5.1%	GRA: 57.5%; SAV: 22.3%; WSA: 18.5%	1980-2016	2458-3865	195.00	Costilla Creek - US
US_0006494	36.70	-105.57	Dfc: 72%; Dfb: 25.3%; BSk: 1.9%	WSA: 43.4%; GRA: 38.1%; ENF: 9.8%	1980-2016	2338-3877	113.00	Red River - US
US_0006496	36.68	-105.65	Dfc: 61.3%; Dfb: 22%; BSk: 16.2%	GRA: 45.2%; WSA: 39.9%; SAV: 7.3%	1980-2016	2219-3877	185.00	Red River - US
US_0006498	36.54	-105.56	Dfc: 84.8%; Dfb: 15.2%	WSA: 63.3%; GRA: 25.8%; ENF: 7%	1980-2016	2477-3795	36.20	River Hondo - US
US_0006501	36.44	-105.50	Dfb: 51.8%; Dfc: 46.6%; BSk: 1.6%	WSA: 79.8%; GRA: 10.8%; ENF: 8.9%	1980-2016	2337-3693	66.60	River Pueblo De Taos - US
US_0006502	36.51	-105.53	Dfc: 82.1%; Dfb: 14.9%; ET: 3%	WSA: 48.3%; GRA: 36.2%; SAV: 8.6%	1980-2016	2577-3829	16.60	River Lucero - US
US_0006504	36.30	-105.58	Dfb: 66.4%; Dfc: 26.2%; BSk: 7.4%	WSA: 80%; ENF: 11%; GRA: 8.6%	1980-2016	2229-3568	83.00	River Grande Del Rancho - US
US_0006508	36.17	-105.60	Dfb: 53.6%; Dfc: 46.4%	WSA: 72.1%; GRA: 14.4%; ENF: 13.5%	1980-2016	2470-3732	101.00	River Pueblo - US
US_0006509	36.21	-105.91	Dfb: 43.3%; BSk: 28.9%; Dfc: 27.7%	WSA: 55.7%; GRA: 28.7%; ENF: 7.6%	1980-2016	1823-3828	305.00	Embudo Creek - US
US_0006515	36.32	-106.60	Dfb: 46.7%; BSk: 37%; Dfc: 16.1%	GRA: 76.4%; SAV: 15.1%; WSA: 7.5%	1980-2016	1928-3723	1500.00	River Chama - US
US_0006517	36.35	-106.04	Dfb: 45.2%; BSk: 42.1%; Dfc: 12.6%	GRA: 67.2%; SAV: 16.6%; WSA: 16.1%	1980-2016	1953-3241	419.00	River Ojo Caliente - US
US_0006519	35.96	-105.90	Dfb: 42.7%; Dfc: 33.2%; BSk: 24.1%	GRA: 50.2%; WSA: 26.1%; ENF: 12.4%	1980-2016	2031-3674	86.00	Santa Cruz River - US
US_0006520	35.85	-105.89	Dfb: 62.4%; Dfc: 30.4%; BSk: 7.2%	GRA: 73.8%; WSA: 15.9%; ENF: 5.6%	1980-2012	2141-3686	25.00	River Nambe - US
US_0006521	35.85	-105.91	Dfb: 60.2%; Dfc: 27.8%; BSk: 12%	GRA: 69.6%; WSA: 14.8%; SAV: 10.4%	1980-2016	2043-3686	34.10	River Nambe - US
US_0006522	35.74	-105.90	Dfb: 73.3%; Dfc: 15.6%; BSk: 11.1%	GRA: 42.5%; ENF: 20%; WSA: 20%	1980-2016	2203-3495	11.70	Tesuque Creek - US
US_0006523	35.73	-105.91	Dfb: 86.7%; BSk: 13.3%	GRA: 60.9%; WSA: 39.1%	1980-2009	2251-3101	7.61	Little Tesuque Creek - US
US_0006526	35.69	-105.82	Dfb: 58.5%; Dfc: 41.5%	GRA: 70.2%; ENF: 12.8%; WSA: 8.5%	1980-2016	2525-3578	13.50	Santa Fe River - US
US_0006527	35.69	-105.84	Dfb: 69.9%; Dfc: 30.1%	GRA: 78.5%; ENF: 9.2%; WSA: 6.2%	1980-2016	2426-3578	18.20	Santa Fe River - US
US_0006528	35.55	-106.23	BSk: 82.9%; Dfb: 14.7%; Dfc: 2.5%	GRA: 83.6%; SAV: 7.7%; URB: 5.6%	1980-2016	1697-3578	231.00	Santa Fe River - US
US_0006534	35.73	-106.76	Dfb: 78.5%; BSk: 13.5%; Dfc: 8.1%	WSA: 55.1%; GRA: 43.9%; SAV: 0.7%	1980-1996	1900-3208	235.00	River Guadalupe - US
US_0006560	35.78	-105.66	Dfc: 79%; Dfb: 21%	WSA: 76.9%; GRA: 13.6%; ENF: 9.5%	1980-2016	2515-3634	53.20	River Mora - US
US_0006561	35.71	-105.68	Dfc: 69.9%; Dfb: 30.1%	WSA: 72%; GRA: 19.7%; ENF: 8.3%	1980-2016	2344-3695	189.00	Pecos River - US

Station	Lat	Lon	Climate	Biome	Period	Elev	Area	River
US_0006563	35.65	-105.32	Dfb: 82.2%; Dfc: 17.8%	WSA: 75.3%; GRA: 23.9%; ENF: 0.8%	1980-2016	2174-3494	84.00	Gallinas Creek - US
US_0006575	33.34	-105.73	Dfb: 100%	GRA: 58.6%; WSA: 39.7%; ENF: 1.7%	1980-2016	2254-3391	18.30	River Ruidoso - US
US_0006576	33.33	-105.63	Cfb: 62.9%; Dfb: 31.8%; BSk: 5.3%	GRA: 52.6%; WSA: 35.5%; SAV: 5%	1980-2016	1992-3391	120.00	River Ruidoso - US
US_0006577	33.39	-105.72	Dfb: 100%	GRA: 92%; CSH: 8%	1980-2016	2385-3192	8.14	Eagle Creek - US
US_0006602	32.85	-107.97	BSk: 70.9%; Dsb: 29.1%	SAV: 43.5%; GRA: 23.3%; CSH: 19%	1980-2016	1813-3049	184.00	Mimbres River - US
US_0006603	33.14	-105.90	Cfb: 35.7%; Dfb: 31.1%; BSk: 24.5%	WSA: 45%; GRA: 36.9%; SAV: 12.5%	1980-2016	1681-2709	120.00	Tularosa Creek - US
US_0006610	39.85	-105.75	Dfc: 57.5%; ET: 42.5%	GRA: 69.7%; WSA: 21.2%; SAV: 9.1%	1980-2016	2993-3839	10.50	Fraser River - US
US_0006661	39.55	-106.40	Dfc: 76.7%; ET: 23.1%; Dfb: 0.1%	WSA: 43.3%; GRA: 33.9%; SAV: 12.1%	1980-2016	2478-4016	186.00	Eagle River - US
US_0006683	39.21	-106.80	Dfc: 68.9%; ET: 31.1%	WSA: 38.4%; SAV: 29%; GRA: 26.8%	1980-2016	2682-3845	41.70	Hunter Creek - US
US_0006709	38.66	-106.85	Dfc: 82.7%; ET: 13.3%; Dfb: 3.6%	GRA: 47.1%; WSA: 25.9%; SAV: 24.3%	1980-2016	2465-3973	289.00	East River - US
US_0006735	38.18	-107.75	Dfc: 42.5%; Dfb: 26.5%; BSk: 15.6%	SAV: 45.5%; GRA: 40%; WSA: 7.8%	1980-2016	2119-3968	149.00	Uncompahgre River - US
US_0006855	40.13	-111.02	Dfb: 67.9%; Dfc: 32.1%	SAV: 58.7%; GRA: 41.3%	1980-1994	2371-2938	43.00	Strawberry River - US
US_0006948	37.04	-107.88	Dfc: 39%; Dfb: 34.6%; BSk: 15.3%	WSA: 41%; GRA: 36.8%; SAV: 20.2%	1980-2016	1844-4088	1090.00	Animas River - US
US_0006955	36.74	-108.25	BSk: 66.4%; Dfb: 23.9%; Dfc: 4.5%	GRA: 85.6%; SAV: 7.7%; OSH: 4.6%	1980-2015	1605-3804	583.00	La Plata River - US
US_0006973	34.02	-109.46	Dsb: 53.1%; Dsc: 34.7%; Dfb: 12.2%	GRA: 45.6%; WSA: 42.2%; ENF: 12.2%	1980-2016	2555-3328	29.10	Little Colorado River - US
US_0006984	35.28	-108.55	BSk: 88.8%; Dfb: 11.2%	GRA: 97%; SAV: 3%	1980-2016	2170-2624	71.40	River Nutria - US
US_0006995	34.67	-111.01	Dsb: 93.3%; BSk: 6.7%	WSA: 54.1%; SAV: 33.4%; ENF: 10.7%	1980-1993	1927-2404	317.00	Clear Creek - US
US_0007035	36.71	-114.70	BWh: 100%	GRA: 100%	1980-2016	528-549	40.00	Muddy River - US
US_0007048	36.12	-114.90	BWk: 44.2%; BWh: 43.4%; BSk: 11.1%	OSH: 41.5%; BSV: 28.3%; URB: 22.2%	1980-2016	414-3379	1586.00	Lv Wash - US
US_0007051	34.54	-113.45	BSk: 86.4%; BWh: 10.1%; BSh: 3.3%	GRA: 40.6%; OSH: 35.6%; SAV: 22.3%	1980-2016	609-2128	601.00	Burro Creek - US
US_0007053	34.31	-113.35	BSk: 67.3%; BWh: 19%; BSh: 12.4%	OSH: 54.6%; GRA: 20.9%; SAV: 20.5%	1980-2016	435-2113	1129.00	Santa Maria River - US
US_0007056	33.06	-108.54	BSk: 80.3%; Dsb: 17.9%; Dfb: 1.6%	SAV: 46.8%; GRA: 37.3%; WSA: 6.7%	1980-2016	1454-3174	1864.00	Gila River - US
US_0007057	33.17	-108.65	Dsb: 57%; BSk: 43%	SAV: 70.1%; GRA: 25.6%; CSH: 2.1%	1980-2016	1755-3131	69.00	Mogollon Creek - US
US_0007068	33.06	-109.44	BSk: 88%; Csb: 8.9%; Dsb: 3%	SAV: 35.1%; GRA: 24.1%; OSH: 19.9%	1980-2016	1171-2839	622.00	Eagle Creek - US
US_0007076	33.00	-110.77	BSk: 66.9%; BWk: 14.9%; Dsb: 6.5%	OSH: 44.7%; GRA: 24.5%; SAV: 21%	1980-2004	617-3227	382.00	Gila River - US
US_0007084	32.84	-110.63	BSk: 86.8%; BSh: 13.1%; Csa: 0.1%	OSH: 69.3%; GRA: 20.2%; SAV: 10.3%	1980-2016	732-2293	537.00	Aravaipa Creek - US

Station	Lat	Lon	Climate	Biome	Period	Elev	Area	River
US_0007152	34.32	-112.06	BSk: 88.9%; Csa: 7%; Csb: 4.1%	GRA: 53.9%; SAV: 20%; OSH: 13.4%	1980-2016	1070-2277	585.00	Agua Fria River - US
US_0007153	34.02	-112.17	BSk: 76.2%; BSh: 12.1%; Csa: 7.4%	GRA: 49.2%; OSH: 24.7%; SAV: 17.2%	1980-2016	564-2281	1111.00	Agua Fria River - US
US_0007488	42.79	-118.87	BSk: 75.5%; Dsb: 12.9%; Dsc: 11.6%	GRA: 100%	1980-2016	1371-2875	200.00	Donner Und Blitzen River - US
US_0008472	48.42	-116.50	Dsb: 63.3%; Dsc: 35.8%; Dfc: 0.9%	ENF: 46.8%; WSA: 34.7%; GRA: 14.1%	1980-2016	647-2131	124.00	Pack River - US
US_0008473	48.45	-116.90	Dsb: 58%; Dsc: 18.3%; Dfc: 12.8%	ENF: 78.4%; WSA: 14.8%; GRA: 4.7%	1980-2006	727-2128	611.00	Priest River - US
US_0008474	48.22	-116.91	Dsb: 70.5%; Dsc: 13.9%; Dfc: 8.4%	ENF: 77.3%; WSA: 16.2%; GRA: 3.3%	1980-2016	643-2128	902.00	Priest River - US
US_0008483	47.71	-115.98	Dsb: 98.8%; Dsc: 1.2%	ENF: 97.2%; WSA: 2.4%; MF: 0.4%	1980-2016	830-1775	335.00	Nf Coeur D Alene River - US
US_0008484	47.57	-116.25	Dsb: 97.1%; Dsc: 2.9%	ENF: 96.2%; WSA: 3.2%; GRA: 0.2%	1980-2016	665-1975	895.00	Nf Coeur D Alene River - US
US_0008528	47.74	-120.37	Dsb: 54.8%; Dsc: 45.2%	ENF: 45.9%; GRA: 33.9%; WSA: 14.4%	1980-2016	426-1946	92.40	Mad River - US
US_0008570	43.86	-110.59	Dfc: 99.6%; ET: 0.4%	GRA: 39.4%; WSA: 31.2%; SAV: 24.9%	1980-2016	2060-3450	807.00	Snake River - US
US_0008583	43.14	-110.98	Dfc: 83.7%; Dfb: 16.3%	GRA: 49.6%; WSA: 26.2%; SAV: 24.1%	1980-2016	1837-3319	448.00	Greys River - US
US_0008606	43.44	-111.73	Dfb: 84.5%; BSk: 14.8%; Dfc: 0.6%	GRA: 84.4%; SAV: 8.9%; WSA: 4.1%	1980-2016	1619-2821	568.00	Willow Creek - US
US_0008652	43.49	-114.06	Dsb: 24.8%; Dfc: 24.2%; Dfb: 20.2%	GRA: 86.2%; SAV: 12.4%; BSV: 1%	1980-2016	1652-3415	248.00	Little Wood River - US
US_0008672	43.50	-115.31	Dsb: 56%; Dsc: 44%	GRA: 61%; SAV: 35.9%; WSA: 2.1%	1980-2016	1302-2988	635.00	Sf Boise River - US
US_0008685	43.57	-118.21	BSk: 75%; Dsb: 22.6%; Dsc: 2.4%	GRA: 81.7%; WSA: 15%; SAV: 1.9%	1980-2016	1032-2412	1100.00	Malheur River - US
US_0008687	43.91	-118.15	BSk: 60%; Dsb: 31.6%; Dsc: 8.4%	GRA: 75.7%; WSA: 17.1%; SAV: 4.3%	1980-2016	1000-2329	440.00	North Fork Malheur River - US
US_0008696	44.91	-116.00	Dsc: 99.6%; Dsb: 0.4%	WSA: 42.3%; SAV: 34.5%; GRA: 22.2%	1980-2016	1619-2557	48.90	Lake Fork Payette River - US
US_0008698	44.52	-116.05	Dsb: 53.9%; Dsc: 46.1%	WSA: 48.1%; GRA: 32.9%; SAV: 16.6%	1980-2015	1469-2557	616.00	Nf Payette River - US
US_0008710	44.29	-116.78	Dsa: 54%; Dsb: 25.7%; BSk: 20.3%	GRA: 99.2%; BSV: 0.6%; CRO: 0.2%	1980-2016	696-1547	288.00	Crane Creek - US
US_0008720	44.95	-116.87	Dsb: 51.2%; Dsa: 21.9%; Dsc: 18.5%	GRA: 52.8%; SAV: 20%; WSA: 17.8%	1980-1996	621-2717	230.00	Pine Creek - US
US_0008723	44.22	-114.93	Dsc: 83.7%; Dfc: 16.3%	GRA: 56.3%; WSA: 24.7%; SAV: 17.3%	1980-2016	1905-2993	147.00	Valley Creek - US
US_0008726	44.30	-114.48	Dfc: 96.6%; Dfb: 3.4%	SAV: 57.7%; GRA: 19.2%; WSA: 15.4%	1980-2016	1936-2626	6.29	Bruno Creek - US
US_0008766	46.37	-116.16	Dsb: 100%	ENF: 74.8%; WSA: 11.9%; GRA: 10.1%	1980-2016	467-1782	243.00	Lolo Creek - US

960 *Author contributions.* Conceptualization, coding and first draft writing:DS. All authors provided scientific input, reviewed and edited the final manuscript

Competing interests. The authors declare no competing interests

Disclaimer. TEXT

References

970   Abatzoglou, J. T.: Development of gridded surface meteorological data for ecological applications and modelling, International Journal of Climatology, 33, 121–131, https://doi.org/10.1002/joc.3413, http://doi.wiley.com/10.1002/joc.3413, 2013.

Abatzoglou, J. T., Dobrowski, S. Z., Parks, S. A., and Hegewisch, K. C.: TerraClimate, a high-resolution global dataset of monthly climate and climatic water balance from 1958–2015, Scientific Data, 5, 170 191, https://doi.org/10.1038/sdata.2017.191, http://www.nature.com/articles/sdata2017191, 2018.

975   Acosta, M., Pavelka, M., Montagnani, L., Kutsch, W., Lindroth, A., Juszczak, R., and Janouš, D.: Soil surface CO2 efflux measurements in Norway spruce forests: Comparison between four different sites across Europe — from boreal to alpine forest, Geoderma, 192, 295–303, https://doi.org/10.1016/j.geoderma.2012.08.027, https://doi.org/10.1016{%}2Fj.geoderma.2012.08.027https://linkinghub.elsevier.com/retrieve/pii/S0016706112003229, 2013.

Allen, R. G.: Assessing Integrity of Weather Data for Reference Evapotranspiration Estimation, Journal of Irrigation and
980   Drainage Engineering, 122, 97–106, https://doi.org/10.1061/(ASCE)0733-9437(1996)122:2(97), http://ascelibrary.org/doi/10.1061/{%}28ASCE{%}290733-9437{%}281996{%}29122{%}3A2{%}2897{%}29, 1996.

Allen, R. G., Trezza, R., and Tasumi, M.: Analytical integrated functions for daily solar radiation on slopes, Agricultural and Forest Meteorology, 139, 55–73, https://doi.org/10.1016/j.agrformet.2006.05.012, https://linkinghub.elsevier.com/retrieve/pii/S0168192306001511, 2006.

985   Amatulli, G., Domisch, S., Tuanmu, M.-n., Parmentier, B., Ranipeta, A., Malczyk, J., and Jetz, W.: A suite of global, cross-scale topographic variables for environmental and biodiversity modeling, Scientific Data, 5, 180 040, https://doi.org/10.1038/sdata.2018.40, http://www.nature.com/articles/sdata201840, 2018.

Amiro, B. D., Barr, A. G., Barr, J. G., Black, T. A., Bracho, R., Brown, M., Chen, J., Clark, K. L., Davis, K. J., Desai, A. R., Dore, S., Engel, V., Fuentes, J. D., Goldstein, A. H., Goulden, M. L., Kolb, T. E., Lavigne, M. B., Law, B. E., Margolis, H. A., Martin, T.,
990   McCaughey, J. H., Misson, L., Montes-Helu, M., Noormets, A., Randerson, J. T., Starr, G., and Xiao, J.: Ecosystem carbon dioxide fluxes after disturbance in forests of North America, Journal of Geophysical Research, 115, G00K02, https://doi.org/10.1029/2010JG001390, http://doi.wiley.com/10.1029/2010JG001390, 2010.

Ammann, C., Spirig, C., Leifeld, J., and Neftel, A.: Assessment of the nitrogen and carbon budget of two managed temperate grassland fields, Agriculture, Ecosystems and Environment, 133, 150–162, https://doi.org/10.1016/j.agee.2009.05.006, https://doi.org/10.1016, 2009.

995   Anderson-Teixeira, K. J., Delong, J., Fox, A., Brese, D. A., and Litvak, M.: Differential responses of production and respiration to temperature and moisture drive the carbon balance across a climatic gradient in New Mexico, Global Change Biology, 17, 410–424, https://doi.org/10.1111/j.1365-2486.2010.02269.x, https://onlinelibrary.wiley.com/doi/10.1111/j.1365-2486.2010.02269.x, 2011.

Anthoni, P. M., Law, B. E., and Unsworth, M. H.: Carbon and water vapor exchange of an open-canopied ponderosa pine ecosystem, Agricultural and Forest Meteorology, 95, 151–168, https://doi.org/10.1016/S0168-1923(99)00029-5, https://linkinghub.elsevier.com/retrieve/
1000   pii/S0168192399000295, 1999.

Anthoni, P. M., Unsworth, M. H., Law, B. E., Irvine, J., Baldocchi, D. D., Tuyl, S. V., and Moore, D.: Seasonal differences in carbon and water vapor exchange in young and old-growth ponderosa pine ecosystems, Agricultural and Forest Meteorology, 111, 203–222, https://doi.org/10.1016/S0168-1923(02)00021-7, https://linkinghub.elsevier.com/retrieve/pii/S0168192302000217, 2002.

Assouline, S.: Infiltration into soils: Conceptual approaches and solutions, Water Resources Research, 49, 1755–1772,
1005   https://doi.org/10.1002/wcr.20155, 2013.

Bai, J., Zhang, G., Zhao, Q., Lu, Q., Jia, J., Cui, B., and Liu, X.: Depth-distribution patterns and control of soil organic carbon in coastal salt marshes with different plant covers, Scientific Reports, 6, https://doi.org/10.1038/srep34835, 2016.

Baldocchi, D., Sturtevant, C., and Contributors, F.: Does day and night sampling reduce spurious correlation between canopy photosynthesis and ecosystem respiration?, Agricultural and Forest Meteorology, 207, 117–126, https://doi.org/10.1016/j.agrformet.2015.03.010, https://linkinghub.elsevier.com/retrieve/pii/S016819231500088X, 2015.

Balland, V., Pollacco, J. A., and Arp, P. A.: Modeling soil hydraulic properties for a wide range of soil conditions, Ecological Modelling, 219, 300–316, https://doi.org/10.1016/j.ecolmodel.2008.07.009, http://linkinghub.elsevier.com/retrieve/pii/S0304380008003505, 2008.

Barr, A., Richardson, A., Hollinger, D., Papale, D., Arain, M., Black, T., Bohrer, G., Dragoni, D., Fischer, M., Gu, L., Law, B., Margolis, H., McCaughey, J., Munger, J., Oechel, W., and Schaeffer, K.: Use of change-point detection for friction–velocity threshold evaluation in eddy-covariance studies, Agricultural and Forest Meteorology, 171-172, 31–45, https://doi.org/10.1016/j.agrformet.2012.11.023, https://linkinghub.elsevier.com/retrieve/pii/S0168192312003607, 2013a.

Barr, A., Richardson, A., Hollinger, D., Papale, D., Arain, M., Black, T., Bohrer, G., Dragoni, D., Fischer, M., Gu, L., Law, B., Margolis, H., McCaughey, J., Munger, J., Oechel, W., and Schaeffer, K.: Use of change-point detection for friction–velocity threshold evaluation in eddy-covariance studies, Agricultural and Forest Meteorology, 171-172, 31–45, https://doi.org/10.1016/j.agrformet.2012.11.023, https://linkinghub.elsevier.com/retrieve/pii/S0168192312003607, 2013b.

Barron-Gafford, G. A., Scott, R. L., Jenerette, G. D., Hamerlynck, E. P., and Huxman, T. E.: Landscape and environmental controls over leaf and ecosystem carbon dioxide fluxes under woody plant expansion, Journal of Ecology, 101, 1471–1483, https://doi.org/10.1111/1365-2745.12161, https://onlinelibrary.wiley.com/doi/10.1111/1365-2745.12161, 2013.

Barry, R. G.: The parameterization of surface albedo for sea ice and its snow cover, Progress in Physical Geography, 20, 63–79, 1996.

Barry, R. G.: Mountain Weather and Climate, Cambridge University Press, 3rd ed. edn., 2008.

Bastiaanssen, W., Menenti, M., Feddes, R., and Holtslag, A.: A remote sensing surface energy balance algorithm for land (SEBAL). 1. Formulation, Journal of Hydrology, 212-213, 198–212, https://doi.org/10.1016/S0022-1694(98)00253-4, https://linkinghub.elsevier.com/retrieve/pii/S0022169498002534, 1998a.

Bastiaanssen, W., Pelgrum, H., Wang, J., Ma, Y., Moreno, J., Roerink, G., and van der Wal, T.: A remote sensing surface energy balance algorithm for land (SEBAL). 2. Validation, Journal of Hydrology, 212-213, 213–229, https://doi.org/10.1016/S0022-1694(98)00254-6, https://linkinghub.elsevier.com/retrieve/pii/S0022169498002546, 1998b.

Batjes, N. H., Ribeiro, E., and van Oostrum, A.: Standardised soil profile data to support global mapping and modelling (WoSIS snapshot 2019), Earth System Science Data, 12, 299–320, https://doi.org/10.5194/essd-12-299-2020, https://essd.copernicus.org/articles/12/299/2020/, 2020.

Beck, H. E., Zimmermann, N. E., McVicar, T. R., Vergopolan, N., Berg, A., and Wood, E. F.: Present and future Köppen-Geiger climate classification maps at 1-km resolution, Scientific Data, 5, 1–12, https://doi.org/10.1038/sdata.2018.214, http://www.nature.com/articles/sdata2018214, 2018.

Beck, H. E., Wood, E. F., Pan, M., Fisher, C. K., Miralles, D. G., van Dijk, A. I. J. M., McVicar, T. R., and Adler, R. F.: MSWEP V2 Global 3-Hourly 0.1° Precipitation: Methodology and Quantitative Assessment, Bulletin of the American Meteorological Society, 100, 473–500, https://doi.org/10.1175/BAMS-D-17-0138.1, https://journals.ametsoc.org/view/journals/bams/100/3/bams-d-17-0138.1.xml, 2019.

Beldring, S., Gottschalk, L., Seibert, J., and Tallaksen, L.: Distribution of soil moisture and groundwater levels at patch and catchment scales, Agricultural and Forest Meteorology, 98-99, 305–324, https://doi.org/10.1016/S0168-1923(99)00103-3, http://linkinghub.elsevier.com/retrieve/pii/S0168192399001033https://linkinghub.elsevier.com/retrieve/pii/S0168192399001033, 1999.

Belshe, E. F., Schuur, E. A. G., Bolker, B. M., and Bracho, R.: Incorporating spatial heterogeneity created by permafrost thaw into a landscape carbon estimate, Journal of Geophysical Research: Biogeosciences, 117, https://doi.org/10.1029/2011JG001836, http://doi.wiley.com/10.1029/2011JG001836, 2012.

Bergström, S.: The HBV model, in: Computer Models of Watershed Hydrology, edited by Singh, V., pp. 443–476, Water Resources Publications, Highlands Ranch, CO., 1995.

Beven, K. J. and Kirby, M. J.: A physically based, variable contributing area model of basin hydrology, Hydrological Sciences Bulletin, 24, 43–69, https://doi.org/10.1080/02626667909491834, http://www.scopus.com/inward/record.url?eid=2-s2.0-0018441920{&}partnerID=40{&}md5=515af4414abd2835228006eedf683f18http://www.tandfonline.com/doi/abs/10.1080/02626667909491834, 1979.

Bristow, M., Hutley, L. B., Beringer, J., Livesley, S. J., Edwards, A. C., and Arndt, S. K.: Quantifying the relative importance of greenhouse gas emissions from current and future savanna land use change across northern Australia, Biogeosciences Discussions, pp. 1–47, https://doi.org/10.5194/bg-2016-191, https://doi.org/10.5194{%}2Fbg-2016-191, 2016.

Brooks, R. H. and Corey, A. T.: Hydraulic Properties of Porous Media, Transactions of the ASAE, 7, https://doi.org/10.13031/2013.40684, 1964.

Buytaert, W., De Bièvre, B., Wyseure, G., and Deckers, J.: The use of the linear reservoir concept to quantify the impact of changes in land use on the hydrology of catchments in the Andes Use of linear reservoir concept to quantify the impact of changes in land use on the hydrology of catchments in the Andes, Hydrology and Earth System Sciences, 8, 108–114, https://doi.org/10.5194/hess-8-108-2004, 2004.

Campbell, G. S. and Norman, J. M.: An Introduction to Environmental Biophysics, Springer New York, New York, NY, https://doi.org/10.1007/978-1-4612-1626-1, https://www.agronomy.org/publications/jeq/abstracts/6/4/JEQ0060040474ahttp://link.springer.com/10.1007/978-1-4612-1626-1, 1998.

Campbell, J. L., Sun, O. J., and Law, B. E.: Disturbance and net ecosystem production across three climatically distinct forest landscapes, Global Biogeochemical Cycles, 18, n/a–n/a, https://doi.org/10.1029/2004GB002236, http://doi.wiley.com/10.1029/2004GB002236, 2004.

Chapin, F. S. I., Matson, P. A., and Vitousek, P. M.: Principles of Terrestrial Ecosystem Ecology, Springer New York, New York, NY, https://doi.org/10.1007/978-1-4419-9504-9, http://link.springer.com/10.1007/978-1-4419-9504-9, 2011.

Chen, A., Li, W., Li, W., and Liu, X.: An observational study of snow aging and the seasonal variation of snow albedo by using data from Col de Porte, France, Chinese Science Bulletin, 59, 4881–4889, https://doi.org/10.1007/s11434-014-0429-9, 2014.

Chu, H., Baldocchi, D. D., Poindexter, C., Abraha, M., Desai, A. R., Bohrer, G., Arain, M. A., Griffis, T., Blanken, P. D., O'Halloran, T. L., Thomas, R. Q., Zhang, Q., Burns, S. P., Frank, J. M., Christian, D., Brown, S., Black, T. A., Gough, C. M., Law, B. E., Lee, X., Chen, J., Reed, D. E., Massman, W. J., Clark, K., Hatfield, J., Prueger, J., Bracho, R., Baker, J. M., and Martin, T. A.: Temporal Dynamics of Aerodynamic Canopy Height Derived From Eddy Covariance Momentum Flux Data Across North American Flux Networks, Geophysical Research Letters, 45, 9275–9287, https://doi.org/10.1029/2018GL079306, https://onlinelibrary.wiley.com/doi/10.1029/2018GL079306, 2018a.

Chu, H., Baldocchi, D. D., Poindexter, C., Abraha, M., Desai, A. R., Bohrer, G., Arain, M. A., Griffis, T., Blanken, P. D., O'Halloran, T. L., Thomas, R. Q., Zhang, Q., Burns, S. P., Frank, J. M., Christian, D., Brown, S., Black, T. A., Gough, C. M., Law, B. E., Lee, X., Chen, J., Reed, D. E., Massman, W. J., Clark, K., Hatfield, J., Prueger, J., Bracho, R., Baker, J. M., and Martin, T. A.: Temporal Dynamics of Aerodynamic Canopy Height Derived From Eddy Covariance Momentum Flux Data Across North American Flux Networks, Geophysical Research Letters, 45, 9275–9287, https://doi.org/10.1029/2018GL079306, https://onlinelibrary.wiley.com/doi/10.1111/gcb.14559https://onlinelibrary.wiley.com/doi/10.1029/2018GL079306, 2018b.

Chu, H., Baldocchi, D. D., Poindexter, C., Abraha, M., Desai, A. R., Bohrer, G., Arain, M. A., Griffis, T., Blanken, P. D., O'Halloran, T. L., Thomas, R. Q., Zhang, Q., Burns, S. P., Frank, J. M., Christian, D., Brown, S., Black, T. A., Gough, C. M., Law, B. E., Lee, X., Chen, J., Reed, D. E., Massman, W. J., Clark, K., Hatfield, J., Prueger, J., Bracho, R., Baker, J. M., and Martin, T. A.: Temporal Dynamics of Aerodynamic Canopy Height Derived From Eddy Covariance Momentum Flux Data Across North American Flux Networks, Geophysical Research Letters, 45, 9275–9287, https://doi.org/10.1029/2018GL079306, https://onlinelibrary.wiley.com/doi/10.1029/2018GL079306, 2018c.

Clark, M. P., Bierkens, M. F. P., Samaniego, L., Woods, R. A., Uijlenhoet, R., Bennett, K. E., Pauwels, V. R. N., Cai, X., Wood, A. W., and Peters-Lidard, C. D.: The evolution of process-based hydrologic models: historical challenges and the collective quest for physical realism, Hydrology and Earth System Sciences, 21, 3427–3440, https://doi.org/10.5194/hess-21-3427-2017, https://www.hydrol-earth-syst-sci.net/21/3427/2017/, 2017.

Corps of Engineers: Summary report of the snow investigations, snow hydrology, Army Engineer Division, Portland, US., 1956.

Correa, A., Ochoa-Tocachi, B. F., Birkel, C., Ochoa-Sánchez, A., Zogheib, C., Tovar, C., and Buytaert, W.: A concerted research effort to advance the hydrological understanding of tropical páramos, Hydrological Processes, 34, 4609–4627, https://doi.org/10.1002/hyp.13904, 2020.

Cosby, B. J., Hornberger, G. M., Clapp, R. B., and Ginn, T. R.: A Statistical Exploration of the Relationships of Soil Moisture Characteristics to the Physical Properties of Soils, Water Resources Research, 20, 682–690, https://doi.org/10.1029/WR020i006p00682, http://doi.wiley.com/10.1029/WR020i006p00682, 1984.

Cramer, W. and Prentice, I. C.: Simulation of regional soil moisture deficits on a European scale, Norwegian Journal of Geography, 12, 149–151, https://doi.org/10.1080/00291958808552193, http://www.tandfonline.com/doi/abs/10.1080/00291958808552193?journalCode=sgeo20{#}.VSZBV{_}msVHU, 1988.

Crespo, P. J., Feyen, J., Buytaert, W., Bücker, A., Breuer, L., Frede, H.-G., and Ramírez, M.: Identifying controls of the rainfall–runoff response of small catchments in the tropical Andes (Ecuador), Journal of Hydrology, 407, 164–174, https://doi.org/10.1016/j.jhydrol.2011.07.021, https://linkinghub.elsevier.com/retrieve/pii/S002216941100477X, 2011.

Davis, T. W., Prentice, I. C., Stocker, B. D., Thomas, R. T., Whitley, R. J., Wang, H., Evans, B. J., Gallego-Sala, A. V., Sykes, M. T., and Cramer, W.: Simple process-led algorithms for simulating habitats (SPLASH v.1.0): robust indices of radiation, evapotranspiration and plant-available moisture, Geoscientific Model Development, 10, 689–708, https://doi.org/10.5194/gmd-10-689-2017, https://www.geosci-model-dev.net/10/689/2017/, 2017.

Dickinson, R. E., Henderson-Sellers, A., Kennedy, P. J., and Wilson, M. F.: Biosphere-Atmosphere Transfer Scheme (BATS) for the NCAR Community Climate Model, 1986.

Dietiker, D., Buchmann, N., and Eugster, W.: Testing the ability of the {DNDC} model to predict {CO}2 and water vapour fluxes of a {S}wiss cropland site, Agriculture, Ecosystems & Environment, 139, 396–401, https://doi.org/10.1016/j.agee.2010.09.002, https://doi.org/10.1016{%}2Fj.agee.2010.09.002, 2010.

Dirmeyer, P. A., Gao, X., Zhao, M., Guo, Z., Oki, T., and Hanasaki, N.: GSWP-2: Multimodel analysis and implications for our perception of the land surface, Bulletin of the American Meteorological Society, 87, 1381–1397, https://doi.org/10.1175/BAMS-87-10-1381, 2006.

Do, H. X., Gudmundsson, L., Leonard, M., and Westra, S.: The Global Streamflow Indices and Metadata Archive (GSIM)-Part 1: The production of a daily streamflow archive and metadata, Earth System Science Data, 10, 765–785, https://doi.org/10.5194/essd-10-765-2018, 2018.

Dunkerley, D.: Identifying individual rain events from pluviograph records: a review with analysis of data from an Australian dryland site, Hydrological Processes, 22, 5024–5036, https://doi.org/10.1002/hyp.7122, http://doi.wiley.com/10.1002/hyp.7122, 2008.

Etzold, S., Ruehr, N. K., Zweifel, R., Dobbertin, M., Zingg, A., Pluess, P., Häsler, R., Eugster, W., and Buchmann, N.: The Carbon Balance of Two Contrasting Mountain Forest Ecosystems in {S}witzerland: Similar Annual Trends, but Seasonal Differences, Ecosystems, 14, 1289–1309, https://doi.org/10.1007/s10021-011-9481-3, https://doi.org/10.1007{%}2Fs10021-011-9481-3, 2011.

Euskirchen, E. S., Bret-Harte, M. S., Scott, G. J., Edgar, C., and Shaver, G. R.: Seasonal patterns of carbon dioxide and water fluxes in three representative tundra ecosystems in northern Alaska, Ecosphere, 3, art4, https://doi.org/10.1890/ES11-00202.1, http://doi.wiley.com/10.1890/ES11-00202.1, 2012a.

Euskirchen, E. S., Bret-Harte, M. S., Scott, G. J., Edgar, C., and Shaver, G. R.: Seasonal patterns of carbon dioxide and water fluxes in three representative tundra ecosystems in northern Alaska, Ecosphere, 3, art4, https://doi.org/10.1890/ES11-00202.1, http://doi.wiley.com/10.1890/ES11-00202.1, 2012b.

Euskirchen, E. S., Bret-Harte, M. S., Shaver, G. R., Edgar, C. W., and Romanovsky, V. E.: Long-Term Release of Carbon Dioxide from Arctic Tundra Ecosystems in Alaska, Ecosystems, 20, 960–974, https://doi.org/10.1007/s10021-016-0085-9, http://link.springer.com/10.1007/s10021-016-0085-9, 2017.

Fan, Y., Miguez-Macho, G., Weaver, C. P., Walko, R., and Robock, A.: Incorporating water table dynamics in climate modeling: 1. Water table observations and equilibrium water table simulations, Journal of Geophysical Research: Atmospheres, 112, 1–17, https://doi.org/10.1029/2006JD008111, http://doi.wiley.com/10.1029/2006JD008111, 2007.

Fawcett, T.: An introduction to ROC analysis, Pattern Recognition Letters, 27, 861–874, https://doi.org/10.1016/j.patrec.2005.10.010, https://linkinghub.elsevier.com/retrieve/pii/S016786550500303X, 2006.

Feddes, R. A. and Raats, P. A.: Parameterizing the soil - water - plant root system, in: Unsaturated-zone Modeling: Progress, Challenges and Applications, edited by Feddes, R., de Rooij, G., and van Dam, J., Springer Netherlands, 2004.

Federer, C. A.: Spatial Variation of Net Radiation, Albedo and Surface Temperature of Forests, Journal of Applied Meteorology, 7, 789–795, https://doi.org/10.1175/1520-0450(1968)007<0789:SVONRA>2.0.CO;2, http://journals.ametsoc.org/doi/10.1175/1520-0450(1968)007{%}3C0789:SVONRA{%}3E2.0.CO;2, 1968.

Federer, C. A.: Transpirational supply and demand: Plant, soil, and atmospheric effects evaluated by simulation, Water Resources Research, 18, 355–362, https://doi.org/10.1029/WR018i002p00355, http://doi.wiley.com/10.1029/WR018i002p00355, 1982.

Fellows, A. W., Flerchinger, G. N., Seyfried, M. S., Biederman, J. A., and Lohse, K. A.: Winter CO 2 Efflux From Sagebrush Shrublands Distributed Across the Rain-to-Snow Transition Zone, Journal of Geophysical Research: Biogeosciences, 125, https://doi.org/10.1029/2019JG005325, https://onlinelibrary.wiley.com/doi/10.1029/2019JG005325, 2020.

Frank, J. M., Massman, W. J., Ewers, B. E., Huckaby, L. S., and Negrõn, J. F.: Ecosystem CO2/H2O fluxes are explained by hydraulically limited gas exchange during tree mortality from spruce bark beetles, Journal of Geophysical Research: Biogeosciences, 119, 1195–1215, https://doi.org/10.1002/2013JG002597, https://doi.org/10.1002, 2014.

Friedl, M., Gray, J., and Sulla-Menashe, D.: MCD12Q2 MODIS/Terra+Aqua Land Cover Dynamics Yearly L3 Global 500m SIN Grid V006 [Data set], https://doi.org/10.5067/MODIS/MCD12Q2.006, 2019.

Gallego-Sala, A. V. and Prentice, I. C.: Blanket peat biome endangered by climate change, Nature Climate Change, 3, 152–155, https://doi.org/10.1038/nclimate1672, http://www.nature.com/doifinder/10.1038/nclimate1672, 2012.

Galvagno, M., Wohlfahrt, G., Cremonese, E., Rossini, M., Colombo, R., Filippa, G., Julitta, T., Manca, G., Siniscalco, C., Morra Di Cella, U., and Migliavacca, M.: Phenology and carbon dioxide source/sink strength of a subalpine grassland in response to an excep-

tionally short snow season, Environmental Research Letters, 8, 25 008, https://doi.org/10.1088/1748-9326/8/2/025008, https://doi.org/10.1088{%}2F1748-9326{%}2F8{%}2F2{%}2F025008, 2013.

Gao, H., Tang, Q., Shi, X., Zhu, C., Bohn, T., Su, F., Sheffield, J., Pan, M., Lettenmaier, D., and Wood, E. F.: Water budget record from Variable Infiltration Capacity (VIC) model. Algorithm Theoretical Basis Document, Version 1.2, in: Algorithm theoretical basis document for terrestrial water cycle data records, pp. 120–173, Department of Civil and Environmental Engineering, University of Washington., http://scholar.google.com/scholar?hl=en{&}btnG=Search{&}q=intitle:Water+Budget+Record+from+Variable+Infiltration+Capacity+(+VIC+)+Model{#}2, 2009.

Goldstein, A. H., Hultman, N. E., Fracheboud, J. M., Bauer, M. R., Panek, J. A., Xu, M., Qi, Y., Guenther, A. B., and Baugh, W.: Effects of climate variability on the carbon dioxide, water, and sensible heat fluxes above a ponderosa pine plantation in the Sierra Nevada (CA), Agricultural and Forest Meteorology, 101, 113–129, https://doi.org/10.1016/S0168-1923(99)00168-9, https://doi.org/10.1016{%}2Fs0168-1923{%}2899{%}2900168-9, 2000.

Goulden, M. U. I.: AmeriFlux US-CZ2 Sierra Critical Zone, Sierra Transect, Ponderosa Pine Forest, Soaproot Saddle, https://doi.org/10.17190/AMF/1419510, https://www.osti.gov/biblio/1419510https://www.osti.gov/servlets/purl/1419510, 2018a.

Goulden, M. U. I.: AmeriFlux US-CZ3 Sierra Critical Zone, Sierra Transect, Sierran Mixed Conifer, P301, https://doi.org/10.17190/AMF/1419512, https://www.osti.gov/biblio/1419512https://www.osti.gov/servlets/purl/1419512, 2018b.

Goulden, M. U. I.: AmeriFlux US-CZ4 Sierra Critical Zone, Sierra Transect, Subalpine Forest, Shorthair, https://doi.org/10.17190/AMF/1419511, https://www.osti.gov/biblio/1419511https://www.osti.gov/servlets/purl/1419511, 2018c.

Goulden, M. U. o. C. I.: AmeriFlux US-SCf Southern California Climate Gradient - Oak/Pine Forest, https://doi.org/10.17190/AMF/1419503, https://www.osti.gov/biblio/1419503https://www.osti.gov/servlets/purl/1419503, 2018d.

Goulden, M. U. o. C. I.: AmeriFlux US-SCg Southern California Climate Gradient - Grassland, https://doi.org/10.17190/AMF/1419502, https://www.osti.gov/biblio/1419502https://www.osti.gov/servlets/purl/1419502, 2018e.

Goulden, M. U. o. C. I.: AmeriFlux US-SCs Southern California Climate Gradient - Coastal Sage, https://doi.org/10.17190/AMF/1419501, https://www.osti.gov/biblio/1419501https://www.osti.gov/servlets/purl/1419501, 2018f.

Goulden, M. U. o. C. I.: AmeriFlux US-SCw Southern California Climate Gradient - Pinyon/Juniper Woodland, https://doi.org/10.17190/AMF/1419504, https://www.osti.gov/biblio/1419504https://www.osti.gov/servlets/purl/1419504, 2018g.

Grayson, R. B. and Blöschl, G.: Spatial patterns in catchment hydrology: observations and modelling, Cambridge University Press, 2000.

Guo, X., Zha, T., Jia, X., Wu, B., Feng, W., Xie, J., Gong, J., Zhang, Y., and Peltola, H.: Dynamics of Dew in a Cold Desert-Shrub Ecosystem and Its Abiotic Controls, Atmosphere, 7, 32, https://doi.org/10.3390/atmos7030032, http://www.mdpi.com/2073-4433/7/3/32, 2016.

Gupta, H. V. and Kling, H.: On typical range, sensitivity, and normalization of Mean Squared Error and Nash-Sutcliffe Efficiency type metrics, Water Resources Research, 47, 2–4, https://doi.org/10.1029/2011WR010962, http://doi.wiley.com/10.1029/2011WR010962, 2011.

Gurtz, J., Zappa, M., Jasper, K., Lang, H., Verbunt, M., Badoux, A., and Vitvar, T.: A comparative study in modelling runoff and its components in two mountainous catchments, Hydrological Processes, 17, 297–311, https://doi.org/10.1002/hyp.1125, https://onlinelibrary.wiley.com/doi/10.1002/hyp.1125, 2003.

Hall, D. K., Salomonson, V. V., and Riggs., G. A.: MODIS/Terra Snow Cover Daily L3 Global 500m Grid. Version 6., https://doi.org/10.5067/MODIS/MOD10A1.006, 2016.

Harder, P. and Pomeroy, J. W.: Hydrological model uncertainty due to precipitation-phase partitioning methods, Hydrological Processes, 28, 4311–4327, https://doi.org/10.1002/hyp.10214, 2014.

Harrison, S. P., Prentice, I. C., Barboni, D., Kohfeld, K. E., Ni, J., and Sutra, J.-p.: Ecophysiological and bioclimatic foundations for a global plant functional classification, Journal of Vegetation Science, 21, 300–317, https://doi.org/10.1111/j.1654-1103.2009.01144.x, http://doi.wiley.com/10.1111/j.1654-1103.2009.01144.x, 2010.

Harrison, S. P., Cramer, W., Franklin, O., Prentice, I. C., Wang, H., Brännström, Å., Boer, H., Dieckmann, U., Joshi, J., Keenan, T. F., Lavergne, A., Manzoni, S., Mengoli, G., Morfopoulos, C., Peñuelas, J., Pietsch, S., Rebel, K. T., Ryu, Y., Smith, N. G., Stocker, B. D., and Wright, I. J.: Eco-evolutionary optimality as a means to improve vegetation and land-surface models, New Phytologist, https://doi.org/10.1111/nph.17558, https://onlinelibrary.wiley.com/doi/10.1111/nph.17558, 2021.

Hengl, T., Mendes de Jesus, J., Heuvelink, G. B. M., Ruiperez Gonzalez, M., Kilibarda, M., Blagotić, A., Shangguan, W., Wright, M. N., Geng, X., Bauer-Marschallinger, B., Guevara, M. A., Vargas, R., MacMillan, R. A., Batjes, N. H., Leenaars, J. G. B., Ribeiro, E., Wheeler, I., Mantel, S., and Kempen, B.: SoilGrids250m: Global gridded soil information based on machine learning, PLOS ONE, 12, e0169 748, https://doi.org/10.1371/journal.pone.0169748, http://dx.plos.org/10.1371/journal.pone.0169748https://dx.plos.org/10.1371/journal.pone.0169748, 2017.

Hilberts, A. G. J., Troch, P. A., and Paniconi, C.: Storage-dependent drainable porosity for complex hillslopes, Water Resources Research, 41, 1–13, https://doi.org/10.1029/2004WR003725, http://doi.wiley.com/10.1029/2004WR003725, 2005.

Hillel, D.: Environmental Soil Physics: Fundamentals, Applications, and Environmental Considerations, Academic Press, 1998.

Hino, M., Odaka, Y., Nadaoka, K., and Sato, A.: Effect of initial soil moisture content on the vertical infiltration process — A guide to the problem of runoff-ratio and loss, Journal of Hydrology, 102, 267–284, https://doi.org/10.1016/0022-1694(88)90102-3, http://linkinghub.elsevier.com/retrieve/pii/0022169488901023https://linkinghub.elsevier.com/retrieve/pii/0022169488901023, 1988.

Hirschi, M., Michel, D., Lehner, I., and Seneviratne, S. I.: A site-level comparison of lysimeter and eddy covariance flux measurements of evapotranspiration, Hydrology and Earth System Sciences, 21, 1809–1825, https://doi.org/10.5194/hess-21-1809-2017, https://hess.copernicus.org/articles/21/1809/2017/, 2017.

Hobley, E. U. and Wilson, B.: The depth distribution of organic carbon in the soils of eastern Australia, Ecosphere, 7, 1–21, https://doi.org/10.1002/ecs2.1214, 2016.

IFAS: Florida Soil Characterization Retrieval System, https://soils.ifas.ufl.edu/flsoils/FLSoilsData.zip, 2007.

Imer, D., Merbold, L., Eugster, W., and Buchmann, N.: Temporal and spatial variations of soil CO2, CH4 and N2O fluxes at three differently managed grasslands, Biogeosciences, 10, 5931–5945, https://doi.org/10.5194/bg-10-5931-2013, https://doi.org/10.5194{%}2Fbg-10-5931-2013, 2013.

Irvine, J., Law, B. E., and Hibbard, K. A.: Postfire carbon pools and fluxes in semiarid ponderosa pine in Central Oregon, Global Change Biology, 13, 1748–1760, https://doi.org/10.1111/j.1365-2486.2007.01368.x, https://doi.org/10.1111{%}2Fj.1365-2486.2007.01368.x, 2007.

Jarvis, A., Reuter, H., Nelson, A., and Guevara, E.: Hole-filled SRTM for the globe Version 4, available from the CGIAR-CSI SRTM 90m Database, http://srtm.csi.cgiar.org, 2008.

Jennings, K. S., Winchell, T. S., Livneh, B., and Molotch, N. P.: Spatial variation of the rain-snow temperature threshold across the Northern Hemisphere, Nature Communications, 9, 1–9, https://doi.org/10.1038/s41467-018-03629-7, http://dx.doi.org/10.1038/s41467-018-03629-7, 2018.

Jones, H. G.: Plants and Microclimate, Cambridge University Press, Cambridge, https://doi.org/10.1017/CBO9780511845727, http://ebooks.cambridge.org/ref/id/CBO9780511845727, 2013.

1230 Kao, S.-C., Ashfaq, M., Rastogi, D., Gangrade, S., Uria Martinez, R., Fernandez, A., Konapala, G., Voisin, N., Zhou, T., Xu, W., Gao, H., Zhao, B., and Zhao, G.: The Third Assessment of the Effects of Climate Change on Federal Hydropower, Tech. rep., Oak Ridge National Laboratory (ORNL), Oak Ridge, TN (United States), https://doi.org/10.2172/1887712, https://www.osti.gov/servlets/purl/1887712/, 2022.

Karger, D. N., Conrad, O., Böhner, J., Kawohl, T., Kreft, H., Soria-Auza, R. W., Zimmermann, N. E., Linder, H. P., and Kessler, M.: Climatologies at high resolution for the earth's land surface areas, Scientific Data, 4, 170 122, https://doi.org/10.1038/sdata.2017.122,
1235 http://www.nature.com/articles/sdata2017122, 2017.

Kato, T., Tang, Y., Gu, S., Hirota, M., Du, M., Li, Y., and Zhao, X.: Temperature and biomass influences on interannual changes in CO 2 exchange in an alpine meadow on the Qinghai-Tibetan Plateau, Global Change Biology, 12, 1285–1298, https://doi.org/10.1111/j.1365-2486.2006.01153.x, https://doi.org/10.1111{%}2Fj.1365-2486.2006.01153.xhttps://onlinelibrary.wiley.com/doi/10.1111/j.1365-2486.2006.01153.x, 2006.

1240 Kelsey, E. P. S. U. and Green, M. C. W. R. U.: AmeriFlux US-HBK Hubbard Brook Experimental Forest, https://doi.org/10.17190/AMF/1634881, https://www.osti.gov/biblio/1634881https://www.osti.gov/servlets/purl/1634881, 2020.

Kienzle, S. W.: A new temperature based method to separate rain and snow, Hydrological Processes, 22, 5067–5085, https://doi.org/10.1002/hyp.7131, http://jamsb.austms.org.au/courses/CSC2408/semester3/resources/ldp/abs-guide.pdfhttp://doi.wiley.com/10.1002/hyp.7131, 2008.

1245 Kilinc, M., Beringer, J., Hutley, L. B., Tapper, N. J., and McGuire, D. A.: Carbon and water exchange of the world's tallest angiosperm forest, Agricultural and Forest Meteorology, 182-183, 215–224, https://doi.org/10.1016/j.agrformet.2013.07.003, https://doi.org/10.1016{%}2Fj.agrformet.2013.07.003https://linkinghub.elsevier.com/retrieve/pii/S0168192313001834, 2013.

Kopp, G. and Lean, J. L.: A new, lower value of total solar irradiance: Evidence and climate significance, Geophysical Research Letters, 38, 1–7, https://doi.org/10.1029/2010GL045777, 2011.

1250 Körner, C.: Plant ecology at high elevations, Alpine Plant Life, pp. 1–7, https://doi.org/10.1007/978-3-642-98018-3_1, 1999.

Körner, C.: Alpine Plant Life, Springer International Publishing, Cham, Switzerland, 3rd edn., https://doi.org/10.1007/978-3-030-59538-8, http://link.springer.com/10.1007/978-3-642-98018-3{_}1http://link.springer.com/10.1007/978-3-642-98018-3http://link.springer.com/10.1007/978-3-030-59538-8, 2021.

Kramer, C. and Gleixner, G.: Soil organic matter in soil depth profiles: Distinct carbon preferences of microbial groups during carbon
1255 transformation, Soil Biology and Biochemistry, 40, 425–433, https://doi.org/10.1016/j.soilbio.2007.09.016, 2008.

Kramer, P. J. and Boyer, J. S.: Water Relations of Plants and Soils, Academic Press, New York, 1995.

Ladson, A. R., Brown, R., Neal, B., and Nathan, R.: A standard approach to baseflow separation using the Lyne and Hollick filter, Australian Journal of Water Resources, 17, 25–34, https://doi.org/10.7158/W12-028.2013.17.1, 2013.

Laipelt, L., Henrique Bloedow Kayser, R., Santos Fleischmann, A., Ruhoff, A., Bastiaanssen, W., Erickson, T. A., and Melton, F.: Long-term
1260 monitoring of evapotranspiration using the SEBAL algorithm and Google Earth Engine cloud computing, ISPRS Journal of Photogrammetry and Remote Sensing, 178, 81–96, https://doi.org/10.1016/j.isprsjprs.2021.05.018, https://doi.org/10.1016/j.isprsjprs.2021.05.018, 2021.

Lawrence, D. M., Fisher, R. A., Koven, C. D., Oleson, K. W., Swenson, S. C., Bonan, G., Collier, N., Ghimire, B., van Kampenhout, L., Kennedy, D., Kluzek, E., Lawrence, P. J., Li, F., Li, H., Lombardozzi, D., Riley, W. J., Sacks, W. J., Shi, M., Vertenstein, M., Wieder,
1265 W. R., Xu, C., Ali, A. A., Badger, A. M., Bisht, G., van den Broeke, M., Brunke, M. A., Burns, S. P., Buzan, J., Clark, M., Craig, A., Dahlin, K., Drewniak, B., Fisher, J. B., Flanner, M., Fox, A. M., Gentine, P., Hoffman, F., Keppel-Aleks, G., Knox, R., Kumar, S., Lenaerts, J., Leung, L. R., Lipscomb, W. H., Lu, Y., Pandey, A., Pelletier, J. D., Perket, J., Randerson, J. T., Ricciuto, D. M., Sanderson, B. M.,

Slater, A., Subin, Z. M., Tang, J., Thomas, R. Q., Val Martin, M., and Zeng, X.: The Community Land Model Version 5: Description of New Features, Benchmarking, and Impact of Forcing Uncertainty, Journal of Advances in Modeling Earth Systems, 11, 4245–4287, https://doi.org/10.1029/2018MS001583, 2019.

Leij, F., Alves, W., van Genuchten, M. T., and Williams, J.: Unsaturated Soil Hydraulic Database, UNSODA 1.0 User's Manual. Report EPA/600/R-96/095, Tech. rep., US Environmental Protection Agency, Ada, Oklahoma, 1996.

Leuning, R., Cleugh, H. A., Zegelin, S. J., and Hughes, D.: Carbon and water fluxes over a temperate Eucalyptus forest and a tropical wet/dry savanna in {A}ustralia: measurements and comparison with {MODIS} remote sensing estimates, Agricultural and Forest Meteorology, 129, 151–173, https://doi.org/10.1016/j.agrformet.2004.12.004, https://doi.org/10.1016{%}2Fj.agrformet.2004.12.004, 2005.

Liang, X. and Xie, Z.: A new surface runoff parameterization with subgrid-scale soil heterogeneity for land surface models, Advances in Water Resources, 24, 1173–1193, https://doi.org/10.1016/S0309-1708(01)00032-X, http://linkinghub.elsevier.com/retrieve/pii/S030917080100032X, 2001.

Liang, X., Wood, E. F., and Lettenmaier, D. P.: Surface Soil Moisture Parameterization of the VIC-2L Model: Evaluation and Modifications, Journal of Global and Planetary Change, 13, 195–206, https://doi.org/10.1016/0921-8181(95)00046-1, http://www.hydro.washington.edu/Lettenmaier/Models/VIC/VIChome.html, 1996.

Linacre, E. T.: Estimating the net-radiation flux, Agricultural Meteorology, 5, 49–63, https://doi.org/10.1016/0002-1571(68)90022-8, 1968.

Lindauer, M., Schmid, H., Grote, R., Mauder, M., Steinbrecher, R., and Wolpert, B.: Net ecosystem exchange over a non-cleared wind-throw-disturbed upland spruce forest—Measurements and simulations, Agricultural and Forest Meteorology, 197, 219–234, https://doi.org/10.1016/j.agrformet.2014.07.005, https://doi.org/10.1016{%}2Fj.agrformet.2014.07.005https://linkinghub.elsevier.com/retrieve/pii/S0168192314001725, 2014.

Livneh, B., Xia, Y., Mitchell, K. E., Ek, M. B., and Lettenmaier, D. P.: Noah LSM Snow Model Diagnostics and Enhancements, Journal of Hydrometeorology, 11, 721–738, https://doi.org/10.1175/2009JHM1174.1, http://journals.ametsoc.org/doi/10.1175/2009JHM1174.1, 2010.

López-Blanco, E., Lund, M., Williams, M., Tamstorf, M. P., Westergaard-Nielsen, A., Exbrayat, J. F., Hansen, B. U., and Christensen, T. R.: Exchange of CO2 in Arctic tundra: Impacts of meteorological variations and biological disturbance, Biogeosciences, 14, 4467–4483, https://doi.org/10.5194/bg-14-4467-2017, https://bg.copernicus.org/articles/14/4467/2017/, 2017.

M. B. Kirkham: Field Capacity, Wilting Point, Available Water, and the Non-Limiting Water Range, Principles of Soil and Plant Water Relations, pp. 101–115, 2005.

Marcolla, B., Pitacco, A., and Cescatti, A.: Canopy architecture and turbulence structure in a coniferous forest, Boundary-Layer Meteorology, 108, 39–59, https://doi.org/10.1023/A:1023027709805, https://doi.org/10.1023, 2003.

Marcolla, B., Cescatti, A., Manca, G., Zorer, R., Cavagna, M., Fiora, A., Gianelle, D., Rodeghiero, M., Sottocornola, M., and Zampedri, R.: Climatic controls and ecosystem responses drive the inter-annual variability of the net ecosystem exchange of an alpine meadow, Agricultural and Forest Meteorology, 151, 1233–1243, https://doi.org/10.1016/j.agrformet.2011.04.015, https://doi.org/10.1016, 2011.

Marks, D., Domingo, J., Susong, D., Link, T., and Garen, D.: A spatially distributed energy balance snowmelt model for application in mountain basins, Hydrological Processes, 13, 1935–1959, https://doi.org/10.1002/(SICI)1099-1085(199909)13:12/13<1935::AID-HYP868>3.0.CO;2-C, 1999.

Mega, T., Ushio, T., Kubota, T., Kachi, M., Aonashi, K., and Shige, S.: Gauge adjusted global satellite mapping of precipitation (GSMaP_Gauge), in: 2014 XXXIth URSI General Assembly and Scientific Symposium (URSI GASS), IEEE, https://doi.org/10.1109/URSIGASS.2014.6929683, http://ieeexplore.ieee.org/document/6929683/, 2014.

Merbold, L., Eugster, W., Stieger, J., Zahniser, M., Nelson, D., and Buchmann, N.: Greenhouse gas budget (CO_2, CH_4 and N_2O) of intensively managed grassland following restoration, Global Change Biology, 20, 1913–1928, https://doi.org/10.1111/gcb.12518, https://doi.org/10.1111{%}2Fgcb.12518, 2014.

Metselaar, K. and de Jong van Lier, Q.: The Shape of the Transpiration Reduction Function under Plant Water Stress, Vadose Zone Journal, 6, 124–139, https://doi.org/10.2136/vzj2006.0086, http://doi.wiley.com/10.2136/vzj2006.0086, 2007.

Meyers, T. N.: AmeriFlux US-CaV Canaan Valley, https://doi.org/10.17190/AMF/1246042, https://www.osti.gov/biblio/1246042https://www.osti.gov/servlets/purl/1246042, 2016.

Molina-Sanchis, I., Lázaro, R., Arnau-Rosalén, E., and Calvo-Cases, A.: Rainfall timing and runoff: The influence of the criterion for rain event separation, Journal of Hydrology and Hydromechanics, 64, 226–236, https://doi.org/10.1515/johh-2016-0024, http://content.sciendo.com/view/journals/johh/64/3/article-p226.xml, 2016.

Monson, R. K., Turnipseed, A. A., Sparks, J. P., Harley, P. C., Scott-Denton, L. E., Sparks, K., and Huxman, T. E.: Carbon sequestration in a high-elevation, subalpine forest, Global Change Biology, 8, 459–478, https://doi.org/10.1046/j.1365-2486.2002.00480.x, https://doi.org/10.1046, 2002.

Montagnani, L., Manca, G., Canepa, E., Georgieva, E., Acosta, M., Feigenwinter, C., Janous, D., Kerschbaumer, G., Lindroth, A., Minach, L., Minerbi, S., Mölder, M., Pavelka, M., Seufert, G., Zeri, M., and Ziegler, W.: A new mass conservation approach to the study of CO2 advection in an alpine forest, Journal of Geophysical Research Atmospheres, 114, https://doi.org/10.1029/2008JD010650, https://doi.org/10.1029, 2009.

Monteith, J. L. and Unsworth, M.: Principles of Environmental Physics, Elsevier, 4th edn., https://doi.org/10.1016/C2010-0-66393-0, http://linkinghub.elsevier.com/retrieve/pii/C20100663930, 1990.

Morbidelli, R., Saltalippi, C., Flammini, A., and Govindaraju, R. S.: Role of slope on infiltration: A review, Journal of Hydrology, 557, 878–886, https://doi.org/10.1016/j.jhydrol.2018.01.019, 2018.

Nash, J. and Sutcliffe, J.: River flow forecasting through conceptual models part I — A discussion of principles, Journal of Hydrology, 10, 282–290, https://doi.org/10.1016/0022-1694(70)90255-6, https://linkinghub.elsevier.com/retrieve/pii/0022169470902556, 1970.

Niu, G. Y. and Yang, Z. L.: An observation-based formulation of snow cover fraction and its evaluation over large North American river basins, Journal of Geophysical Research: Atmospheres, 112, 1–14, https://doi.org/10.1029/2007JD008674, 2007.

Nobel, P. S.: Biophysical Plant Physiology and Ecology, p. 608, 1983.

Novick, K. A., Ficklin, D. L., Stoy, P. C., Williams, C. A., Bohrer, G., Oishi, A. C., Papuga, S. A., Blanken, P. D., Noormets, A., Sulman, B. N., Scott, R. L., Wang, L., and Phillips, R. P.: The increasing importance of atmospheric demand for ecosystem water and carbon fluxes, Nature Climate Change, 6, 1023–1027, https://doi.org/10.1038/nclimate3114, http://www.nature.com/articles/nclimate3114, 2016.

Ochoa-Tocachi, B. F., Buytaert, W., Antiporta, J., Acosta, L., Bardales, J. D., Célleri, R., Crespo, P., Fuentes, P., Gil-Ríos, J., Guallpa, M., Llerena, C., Olaya, D., Pardo, P., Rojas, G., Villacís, M., Villazón, M., Viñas, P., and De Bièvre, B.: High-resolution hydrometeorological data from a network of headwater catchments in the tropical Andes, Scientific Data, 5, 180 080, https://doi.org/10.1038/sdata.2018.80, http://www.nature.com/articles/sdata201880, 2018.

Ottoni, M. V., Ottoni Filho, T. B., Schaap, M. G., Lopes-Assad, M. L. R., and Rotunno Filho, O. C.: Hydrophysical Database for Brazilian Soils (HYBRAS) and Pedotransfer Functions for Water Retention, Vadose Zone Journal, 17, 0, https://doi.org/10.2136/vzj2017.05.0095, https://dl.sciencesocieties.org/publications/vzj/abstracts/17/1/170095, 2018.

Pachepsky, Y. A., Rajkai, K., and Tóth, B.: Pedotransfer in soil physics: trends and outlook — A review, Agrokémia és Talajtan, 64, 339–360, https://doi.org/10.1063/1.1434987, http://www.akademiai.com/doi/abs/10.1556/0088.2015.64.2.3, 2015.

Paschalis, A., Bonetti, S., Guo, Y., and Fatichi, S.: On the Uncertainty Induced by Pedotransfer Functions in Terrestrial Biosphere Modeling, Water Resources Research, 58, 1–18, https://doi.org/10.1029/2021WR031871, https://onlinelibrary.wiley.com/doi/10.1029/2021WR031871, 2022.

Pastorello, G., Trotta, C., Canfora, E., Chu, H., Christianson, D., Cheah, Y.-W., Poindexter, C., Chen, J., Elbashandy, A., Humphrey, M., Isaac, P., Polidori, D., Reichstein, M., Ribeca, A., van Ingen, C., Vuichard, N., Zhang, L., Amiro, B., Ammann, C., Arain, M. A., Ardö, J., Arkebauer, T., Arndt, S. K., Arriga, N., Aubinet, M., Aurela, M., Baldocchi, D., Barr, A., Beamesderfer, E., Marchesini, L. B., Bergeron, O., Beringer, J., Bernhofer, C., Berveiller, D., Billesbach, D., Black, T. A., Blanken, P. D., Bohrer, G., Boike, J., Bolstad, P. V., Bonal, D., Bonnefond, J.-M., Bowling, D. R., Bracho, R., Brodeur, J., Brümmer, C., Buchmann, N., Burban, B., Burns, S. P., Buysse, P., Cale, P., Cavagna, M., Cellier, P., Chen, S., Chini, I., Christensen, T. R., Cleverly, J., Collalti, A., Consalvo, C., Cook, B. D., Cook, D., Coursolle, C., Cremonese, E., Curtis, P. S., D'Andrea, E., da Rocha, H., Dai, X., Davis, K. J., Cinti, B. D., de Grandcourt, A., Ligne, A. D., De Oliveira, R. C., Delpierre, N., Desai, A. R., Di Bella, C. M., di Tommasi, P., Dolman, H., Domingo, F., Dong, G., Dore, S., Duce, P., Dufrêne, E., Dunn, A., Dušek, J., Eamus, D., Eichelmann, U., ElKhidir, H. A. M., Eugster, W., Ewenz, C. M., Ewers, B., Famulari, D., Fares, S., Feigenwinter, I., Feitz, A., Fensholt, R., Filippa, G., Fischer, M., Frank, J., Galvagno, M., Gharun, M., Gianelle, D., Gielen, B., Gioli, B., Gitelson, A., Goded, I., Goeckede, M., Goldstein, A. H., Gough, C. M., Goulden, M. L., Graf, A., Griebel, A., Gruening, C., Grünwald, T., Hammerle, A., Han, S., Han, X., Hansen, B. U., Hanson, C., Hatakka, J., He, Y., Hehn, M., Heinesch, B., Hinko-Najera, N., Hörtnagl, L., Hutley, L., Ibrom, A., Ikawa, H., Jackowicz-Korczynski, M., Janouš, D., Jans, W., Jassal, R., Jiang, S., Kato, T., Khomik, M., Klatt, J., Knohl, A., Knox, S., Kobayashi, H., Koerber, G., Kolle, O., Kosugi, Y., Kotani, A., Kowalski, A., Kruijt, B., Kurbatova, J., Kutsch, W. L., Kwon, H., Launiainen, S., Laurila, T., Law, B., Leuning, R., Li, Y., Liddell, M., Limousin, J., Lion, M., Liska, A. J., Lohila, A., López-Ballesteros, A., López-Blanco, E., Loubet, B., Loustau, D., Lucas-Moffat, A., Lüers, J., Ma, S., Macfarlane, C., Magliulo, V., Maier, R., Mammarella, I., Manca, G., Marcolla, B., Margolis, H. A., Marras, S., Massman, W., Mastepanov, M., Matamala, R., Matthes, J. H., Mazzenga, F., McCaughey, H., McHugh, I., McMillan, A. M. S., Merbold, L., Meyer, W., Meyers, T., Miller, S. D., Minerbi, S., Moderow, U., Monson, R. K., Montagnani, L., Moore, C. E., Moors, E., Moreaux, V., Moureaux, C., Munger, J. W., Nakai, T., Neirynck, J., Nesic, Z., Nicolini, G., Noormets, A., Northwood, M., Nosetto, M., Nouvellon, Y., Novick, K., Oechel, W., Olesen, J. E., Ourcival, J.-M., Papuga, S. A., Parmentier, F.-J., Paul-Limoges, E., Pavelka, M., Peichl, M., Pendall, E., Phillips, R. P., Pilegaard, K., Pirk, N., Posse, G., Powell, T., Prasse, H., Prober, S. M., Rambal, S., Rannik, Ü., Raz-Yaseef, N., Rebmann, C., Reed, D., de Dios, V. R., Restrepo-Coupe, N., Reverter, B. R., Roland, M., Sabbatini, S., Sachs, T., Saleska, S. R., Sánchez-Cañete, E. P., Sanchez-Mejia, Z. M., Schmid, H. P., Schmidt, M., Schneider, K., Schrader, F., Schroder, I., Scott, R. L., Sedlák, P., Serrano-Ortíz, P., Shao, C., Shi, P., Shironya, I., Siebicke, L., Šigut, L., Silberstein, R., Sirca, C., Spano, D., Steinbrecher, R., Stevens, R. M., Sturtevant, C., Suyker, A., Tagesson, T., Takanashi, S., Tang, Y., Tapper, N., Thom, J., Tomassucci, M., Tuovinen, J.-P., Urbanski, S., Valentini, R., van der Molen, M., van Gorsel, E., van Huissteden, K., Varlagin, A., Verfaillie, J., Vesala, T., Vincke, C., Vitale, D., Vygodskaya, N., Walker, J. P., Walter-Shea, E., Wang, H., Weber, R., Westermann, S., Wille, C., Wofsy, S., Wohlfahrt, G., Wolf, S., Woodgate, W., Li, Y., Zampedri, R., Zhang, J., Zhou, G., Zona, D., Agarwal, D., Biraud, S., Torn, M., and Papale, D.: The FLUXNET2015 dataset and the ONEFlux processing pipeline for eddy covariance data, Scientific Data, 7, 225, https://doi.org/10.1038/s41597-020-0534-3, http://www.nature.com/articles/s41597-020-0534-3, 2020.

Pelletier, J. D., Broxton, P. D., Hazenberg, P., Zeng, X., Troch, P. A., Niu, G., Williams, Z., Brunke, M. A., and Gochis, D.: A gridded global data set of soil, intact regolith, and sedimentary deposit thicknesses for regional and global land surface modeling, Journal of Advances in Modeling Earth Systems, 8, 41–65, https://doi.org/10.1002/2015MS000526, https://onlinelibrary.wiley.com/doi/10.1002/2015MS000526, 2016.

Pomeroy, J. W. and Brun, E.: Physical Properties of Snow, in: Snow Ecology: An Interdisciplinary Examination of Snow-covered Ecosystems, edited by Jones, H. G., Pomeroy, J. W., Walker, D. A., and Hoham, R. W., pp. 45–126, Cambridge University Press, 2001.

Prentice, I. C., Dong, N., Gleason, S. M., Maire, V., and Wright, I. J.: Balancing the costs of carbon gain and water transport: Testing a new theoretical framework for plant functional ecology, Ecology Letters, 17, 82–91, https://doi.org/10.1111/ele.12211, 2014.

Prentice, I. C., Liang, X., Medlyn, B. E., and Wang, Y.-P.: Reliable, robust and realistic: the three R's of next-generation land-surface modelling, Atmospheric Chemistry and Physics, 15, 5987–6005, https://doi.org/10.5194/acp-15-5987-2015, http://www.atmos-chem-phys.net/15/5987/2015/, 2015.

Priestley, C. H. B. and Taylor, R. J.: On the Assessment of Surface Heat Flux and Evaporation Using Large-Scale Parameters, Monthly Weather Review, 100, 81–92, https://doi.org/10.1175/1520-0493(1972)100<0081:OTAOSH>2.3.CO;2, http://journals.ametsoc.org/doi/abs/10.1175/1520-0493{%}281972{%}29100{%}3C0081{%}3AOTAOSH{%}3E2.3.CO{%}3B2, 1972.

Rahmati, M., Weihermüller, L., Vanderborght, J., Pachepsky, Y. A., Mao, L., Sadeghi, S. H., Moosavi, N., Kheirfam, H., Montzka, C., Van Looy, K., Toth, B., Hazbavi, Z., Al Yamani, W., Albalasmeh, A. A., Alghzawi, M. Z., Angulo-Jaramillo, R., Antonino, A. C. D., Arampatzis, G., Armindo, R. A., Asadi, H., Bamutaze, Y., Batlle-Aguilar, J., Béchet, B., Becker, F., Blöschl, G., Bohne, K., Braud, I., Castellano, C., Cerdà, A., Chalhoub, M., Cichota, R., Císlerová, M., Clothier, B., Coquet, Y., Cornelis, W., Corradini, C., Coutinho, A. P., de Oliveira, M. B., de Macedo, J. R., Durães, M. F., Emami, H., Eskandari, I., Farajnia, A., Flammini, A., Fodor, N., Gharaibeh, M., Ghavimipanah, M. H., Ghezzehei, T. A., Giertz, S., Hatzigiannakis, E. G., Horn, R., Jiménez, J. J., Jacques, D., Keesstra, S. D., Kelishadi, H., Kiani-Harchegani, M., Kouselou, M., Kumar Jha, M., Lassabatere, L., Li, X., Liebig, M. A., Lichner, L., López, M. V., Machiwal, D., Mallants, D., Mallmann, M. S., de Oliveira Marques, J. D., Marshall, M. R., Mertens, J., Meunier, F., Mohammadi, M. H., Mohanty, B. P., Pulido-Moncada, M., Montenegro, S., Morbidelli, R., Moret-Fernández, D., Moosavi, A. A., Mosaddeghi, M. R., Mousavi, S. B., Mozaffari, H., Nabiollahi, K., Neyshabouri, M. R., Ottoni, M. V., Ottoni Filho, T. B., Pahlavan-Rad, M. R., Panagopoulos, A., Peth, S., Peyneau, P.-E., Picciafuoco, T., Poesen, J., Pulido, M., Reinert, D. J., Reinsch, S., Rezaei, M., Roberts, F. P., Robinson, D., Rodrigo-Comino, J., Rotunno Filho, O. C., Saito, T., Suganuma, H., Saltalippi, C., Sándor, R., Schütt, B., Seeger, M., Sepehrnia, N., Sharifi Moghaddam, E., Shukla, M., Shutaro, S., Sorando, R., Stanley, A. A., Strauss, P., Su, Z., Taghizadeh-Mehrjardi, R., Taguas, E., Teixeira, W. G., Vaezi, A. R., Vafakhah, M., Vogel, T., Vogeler, I., Votrubova, J., Werner, S., Winarski, T., Yilmaz, D., Young, M. H., Zacharias, S., Zeng, Y., Zhao, Y., Zhao, H., and Vereecken, H.: Development and analysis of the Soil Water Infiltration Global database, Earth System Science Data, 10, 1237–1263, https://doi.org/10.5194/essd-10-1237-2018, https://essd.copernicus.org/articles/10/1237/2018/, 2018.

Remson, I. and Randolph, J. R.: Review of some elements of soil-moisture theory. Professional paper 411-D., USGS, Washington, http://pubs.er.usgs.gov/thumbnails/pp{_}411{_}d.jpg{%}5Cnhttp://pubs.usgs.gov/pp/0411d/report.pdf, 1962.

Remy, C. C., Krofcheck, D. J., Keyser, A. R., Litvak, M. E., Collins, S. L., and Hurteau, M. D.: Integrating Species-Specific Information in Models Improves Regional Projections Under Climate Change, Geophysical Research Letters, 46, 6554–6562, https://doi.org/10.1029/2019GL082762, https://onlinelibrary.wiley.com/doi/abs/10.1029/2019GL082762, 2019.

Rene Orth and Seneviratne, S. I.: Introduction of a simple-model-based land surface dataset for Europe, Environmental Research Letters, 10, 044 012, https://doi.org/10.1088/1748-9326/10/4/044012, http://stacks.iop.org/1748-9326/10/i=4/a=044012?key=crossref.58936444b970135f9309cbcaf985e69fhttps://iopscience.iop.org/article/10.1088/1748-9326/10/4/044012, 2015.

Reverter, B. R., Sánchez-Cañete, E. P., Resco, V., Serrano-Ortiz, P., Oyonarte, C., and Kowalski, A. S.: Analyzing the major drivers of NEE in a Mediterranean alpine shrubland, Biogeosciences, 7, 2601–2611, https://doi.org/10.5194/bg-7-2601-2010, https://doi.org/10.5194{%}2Fbg-7-2601-2010, 2010.

Rodell, M., Houser, P. R., Jambor, U., Gottschalck, J., Mitchell, K., Meng, C.-j., Arsenault, K., Cosgrove, B., Radakovich, J., Bosilovich, M.,
Entin, J. K., Walker, J. P., Lohmann, D., and Toll, D.: The Global Land Data Assimilation System, Bulletin of the American Meteorological Society, 85, 381–394, https://doi.org/10.1175/BAMS-85-3-381, https://journals.ametsoc.org/doi/pdf/10.1175/BAMS-85-3-381http://journals.ametsoc.org/doi/10.1175/BAMS-85-3-381, 2004.

Roesch, A. and Roeckner, E.: Assessment of snow cover and surface albedo in the ECHAM5 general circulation model, Journal of Climate, 19, 3828–3843, https://doi.org/10.1175/JCLI3825.1, 2006.

Romanov, P.: Mapping and monitoring of the snow cover fraction over North America, Journal of Geophysical Research, 108, 8619, https://doi.org/10.1029/2002JD003142, http://doi.wiley.com/10.1029/2002JD003142, 2003.

Ruehr, N. K., Martin, J. G., and Law, B. E.: Effects of water availability on carbon and water exchange in a young ponderosa pine forest: Above- and belowground responses, Agricultural and Forest Meteorology, 164, 136–148, https://doi.org/10.1016/j.agrformet.2012.05.015, https://doi.org/10.1016{%}2Fj.agrformet.2012.05.015, 2012.

Ryu, Y., Jiang, C., Kobayashi, H., and Detto, M.: MODIS-derived global land products of shortwave radiation and diffuse and total photosynthetically active radiation at 5 km resolution from 2000, Remote Sensing of Environment, 204, 812–825, https://doi.org/10.1016/j.rse.2017.09.021, https://doi.org/10.1016/j.rse.2017.09.021, 2018.

Sarmiento, G.: Ecological features of climate in high tropical mountains, in: High Altitude Tropical Biogeography, edited by Vuilleumier, F. and Monasterio, M., pp. 11–45, Oxford University Press, 1986.

Saxton, K. E. and Rawls, W. J.: Soil Water Characteristic Estimates by Texture and Organic Matter for Hydrologic Solutions, Soil Science Society of America Journal, 70, 1569, https://doi.org/10.2136/sssaj2005.0117, https://www.soils.org/publications/sssaj/abstracts/70/5/1569, 2006.

Schaperow, J. and Li, D.: VICGlobal: soil and vegetation parameters for the Variable Infiltration Capacity hydrological model (Version 1.6c) [Data set], https://doi.org/10.5281/zenodo.4059993, 2020.

Scott, R. L., Biederman, J. A., Hamerlynck, E. P., and Barron-Gafford, G. A.: The carbon balance pivot point of southwestern U.S. semiarid ecosystems: Insights from the 21st century drought, Journal of Geophysical Research: Biogeosciences, 120, 2612–2624, https://doi.org/10.1002/2015JG003181, https://doi.org/10.1002{%}2F2015jg003181, 2015.

Seneviratne, S. I., Lehner, I., Gurtz, J., Teuling, A. J., Lang, H., Moser, U., Grebner, D., Menzel, L., Schroff, K., Vitvar, T., and Zappa, M.: Swiss prealpine Rietholzbach research catchment and lysimeter: 32 year time series and 2003 drought event, Water Resources Research, 48, 1–20, https://doi.org/10.1029/2011WR011749, http://doi.wiley.com/10.1029/2011WR011749, 2012.

Serrano-Ortiz, P., Marañón-Jiménez, S., Reverter, B. R., Sánchez-Cañete, E. P., Castro, J., Zamora, R., and Kowalski, A. S.: Post-fire salvage logging reduces carbon sequestration in Mediterranean coniferous forest, Forest Ecology and Management, 262, 2287–2296, https://doi.org/10.1016/j.foreco.2011.08.023, http://linkinghub.elsevier.com/retrieve/pii/S0378112711005159, 2011.

Serreze, M. C., Clark, M. P., Armstrong, R. L., McGinnis, D. A., and Pulwarty, R. S.: Characteristics of the western United States snowpack from snowpack telemetry (SNOTEL) data, Water Resources Research, 35, 2145–2160, https://doi.org/10.1029/1999WR900090, http://doi.wiley.com/10.1029/1999WR900090, 1999.

Shi, P., Sun, X., Xu, L., Zhang, X., He, Y., Zhang, D., and Yu, G.: Net ecosystem CO_2 exchange and controlling factors in a steppe—Kobresia meadow on the Tibetan Plateau, Science in China Series D: Earth Sciences, 49, 207–218, https://doi.org/10.1007/s11430-006-8207-4, https://doi.org/10.1007{%}2Fs11430-006-8207-4http://link.springer.com/10.1007/s11430-006-8207-4, 2006.

Sigut, L., Havrankova, K., Jocher, G., Pavelka, M., Janouš, D., Czerny, R., Stanik, K., and Trusina, J.: FLUXNET2015 CZ-BK2 Bily Kriz grassland., https://doi.org/10.18140/FLX/1440144.

Skovlin, J. and Roecker, S.: soilDB: Soil Database Interface. R package version 2.3., https://cran.r-project.org/package=soilDB, 2018.

Smith, R. E. and Parlange, J. Y.: A parameter-efficient hydrologic infiltration model, Water Resources Research, 14, 533–538, https://doi.org/10.1029/WR014i003p00533, 1978.

1460   Stocker, B. D., Zscheischler, J., Keenan, T. F., Prentice, I. C., Peñuelas, J., and Seneviratne, S. I.: Quantifying soil moisture impacts on light use efficiency across biomes, New Phytologist, 218, 1430–1449, https://doi.org/10.1111/nph.15123, 2018.

Suehrcke, H., Bowden, R. S., and Hollands, K. G.: Relationship between sunshine duration and solar radiation, Solar Energy, 92, 160–171, https://doi.org/10.1016/j.solener.2013.02.026, http://dx.doi.org/10.1016/j.solener.2013.02.026, 2013.

Tague, C. L. and Band, L. E.: Evaluating explicit and implicit routing for watersdhed hydro-ecological models of forest hydrology at the
1465   small catchment scale, Hydrological Processes, 15, 1415–1439, https://doi.org/10.1002/hyp.171, 2001.

Tarboton, D. G.: Terrain analysis using digital elevation models in hydrology (TauDEM), http://nrac.wvu.edu/classes/resm575/readings/tarboton.pdf, 2016.

Teuling, A. J., Lehner, I., Kirchner, J. W., and Seneviratne, S. I.: Catchments as simple dynamical systems: Experience from a Swiss prealpine catchment, Water Resources Research, 46, https://doi.org/10.1029/2009WR008777, 2010.

1470   Thornton, M., Shrestha, R., Wei, Y., Thornton, P., Kao, S., and Wilson, B.: Daymet: Daily Surface Weather Data on a 1-km Grid for North America. Version 4., ORNL DAAC, Oak Ridge, Tennessee, USA., https://doi.org/10.3334/ORNLDAAC/1840, 2020.

Thornton, P., Thornton, M., Mayer, B., Wei, Y., Devarakonda, R., Vose, R., and Cook., R.: Daymet: Daily Surface Weather Data on a 1-km Grid for North America, Version 3, https://doi.org/10.3334/ORNLDAAC/1328, 2018.

Tindall, J. A., Kunkel, J. R., and Anderson, D. E.: Unsaturated zone hydrology for scientist and engineers, Prentice Hall, 1999.

1475   Tóth, B., Weynants, M., Nemes, A., Makó, A., Bilas, G., and Tóth, G.: New generation of hydraulic pedotransfer functions for Europe, European Journal of Soil Science, 66, 226–238, https://doi.org/10.1111/ejss.12192, 2015.

Tromp-van Meerveld, H. J. and McDonnell, J. J.: On the interrelations between topography, soil depth, soil moisture, transpiration rates and species distribution at the hillslope scale, Advances in Water Resources, 29, 293–310, https://doi.org/10.1016/j.advwatres.2005.02.016, 2006.

1480   Ukkola, A. M., Prentice, I. C., Keenan, T. F., van Dijk, A. I. J. M., Viney, N. R., Myneni, R. B., and Bi, J.: Reduced streamflow in water-stressed climates consistent with CO2 effects on vegetation, Nature Climate Change, 6, 75–78, https://doi.org/10.1038/nclimate2831, http://www.nature.com/doifinder/10.1038/nclimate2831, 2015.

Valentini, R., De Angelis, P., Matteucci, G., Monaco, R., Dore, S., and Scarascia Mugnozza, G. E.: Seasonal net carbon dioxide exchange of a beech forest with the atmosphere, Global Change Biology, 2, 199–207, https://doi.org/10.1111/j.1365-2486.1996.tb00072.x, https:
1485   //doi.org/10.1111, 1996.

Van Looy, K., Bouma, J., Herbst, M., Koestel, J., Minasny, B., Mishra, U., Montzka, C., Nemes, A., Pachepsky, Y. A., Padarian, J., Schaap, M. G., Tóth, B., Verhoef, A., Vanderborght, J., van der Ploeg, M. J., Weihermüller, L., Zacharias, S., Zhang, Y., and Vereecken, H.: Pedotransfer Functions in Earth System Science: Challenges and Perspectives, Reviews of Geophysics, 55, 1199–1256, https://doi.org/10.1002/2017RG000581, 2017.

1490   Veihmeyer, F. U. o. C. and Hendrickson, A. U. o. C.: The moisture equivalent as a measure of the field capacity of soils, Soil Science, 32, 181–194, 1931.

Vereecken, H., Weihermüller, L., Assouline, S., Šimůnek, J., Verhoef, A., Herbst, M., Archer, N., Mohanty, B., Montzka, C., Vander-borght, J., Balsamo, G., Bechtold, M., Boone, A., Chadburn, S., Cuntz, M., Decharme, B., Ducharne, A., Ek, M., Garrigues, S., Go-ergen, K., Ingwersen, J., Kollet, S., Lawrence, D. M., Li, Q., Or, D., Swenson, S., Vrese, P., Walko, R., Wu, Y., and Xue, Y.: Infil-

tration from the Pedon to Global Grid Scales: An Overview and Outlook for Land Surface Modeling, Vadose Zone Journal, 18, 1–53, https://doi.org/10.2136/vzj2018.10.0191, https://onlinelibrary.wiley.com/doi/abs/10.2136/vzj2018.10.0191, 2019.

Vogel, R. M. and Kroll, C. N.: Estimation of baseflow recession constants, Water Resources Management, 10, 303–320, https://doi.org/10.1007/BF00508898, http://link.springer.com/10.1007/BF00508898, 1996.

Von Freyberg, J., Radny, D., Gall, H. E., and Schirmer, M.: Implications of hydrologic connectivity between hillslopes and riparian zones on streamflow composition, Journal of Contaminant Hydrology, 169, 62–74, https://doi.org/10.1016/j.jconhyd.2014.07.005, http://dx.doi.org/10.1016/j.jconhyd.2014.07.005, 2014.

Wang, H., Prentice, I. C., and Davis, T. W.: Biophsyical constraints on gross primary production by the terrestrial biosphere, Biogeosciences, 11, 5987–6001, https://doi.org/10.5194/bg-11-5987-2014, https://bg.copernicus.org/articles/11/5987/2014/, 2014.

Wang, Z. and Zeng, X.: Evaluation of snow albedo in land models for weather and climate studies, Journal of Applied Meteorology and Climatology, 49, 363–380, https://doi.org/10.1175/2009JAMC2134.1, 2010.

Weizu, G. and Freer, J.: Patterns of surface and subsurface runoff generation, Tracer Technologies for Hydrological Systems, 229, 265–273, 1995.

Westergaard-Nielsen, A., Lund, M., Hansen, B. U., and Tamstorf, M. P.: Camera derived vegetation greenness index as proxy for gross primary production in a low Arctic wetland area, ISPRS Journal of Photogrammetry and Remote Sensing, 86, 89–99, https://doi.org/10.1016/j.isprsjprs.2013.09.006, https://doi.org/10.1016{%}2Fj.isprsjprs.2013.09.006, 2013.

Wohlfahrt, G., Hammerle, A., Haslwanter, A., Bahn, M., Tappeiner, U., and Cernusca, A.: Seasonal and inter-annual variability of the net ecosystem CO_2 exchange of a temperate mountain grassland: Effects of weather and management, Journal of Geophysical Research, 113, D08 110, https://doi.org/10.1029/2007JD009286, http://doi.wiley.com/10.1029/2007JD009286, 2008.

Wolf, S., Keenan, T. F., Fisher, J. B., Baldocchi, D. D., Desai, A. R., Richardson, A. D., Scott, R. L., Law, B. E., Litvak, M. E., Brunsell, N. A., Peters, W., and van der Laan-Luijkx, I. T.: Warm spring reduced carbon cycle impact of the 2012 US summer drought, Proceedings of the National Academy of Sciences, 113, 5880–5885, https://doi.org/10.1073/pnas.1519620113, http://www.pnas.org/lookup/doi/10.1073/pnas.1519620113, 2016.

Woods, R. a., Sivapalan, M., and Robinson, J. S.: Modeling the spatial variability of subsurface runoff using a topographic index, Water Resources Research, 33, 1061–1073, https://doi.org/10.1029/97WR00232, http://doi.wiley.com/10.1029/97WR00232, 1997.

Xiao, L., Che, T., Chen, L., Xie, H., and Dai, L.: Quantifying snow albedo radiative forcing and its feedback during 2003-2016, Remote Sensing, 9, 1–15, https://doi.org/10.3390/rs9090883, 2017.

Yamamoto, M. K. and Shige, S.: Implementation of an orographic/nonorographic rainfall classification scheme in the GSMaP algorithm for microwave radiometers, Atmospheric Research, 163, 36–47, https://doi.org/10.1016/j.atmosres.2014.07.024, http://dx.doi.org/10.1016/j.atmosres.2014.07.024, 2015.

Yang, H., Choi, H. T., and Lim, H.: Applicability assessment of estimation methods for baseflow recession constants in small forest catchments, Water (Switzerland), 10, https://doi.org/10.3390/w10081074, 2018.

Yang, Y. and Roderick, M. L.: Radiation, surface temperature and evaporation over wet surfaces, Quarterly Journal of the Royal Meteorological Society, 145, 1118–1129, https://doi.org/10.1002/qj.3481, https://onlinelibrary.wiley.com/doi/10.1002/qj.3481, 2019.

Yu, R., Zhang, Z., Lu, X., Chang, I. S., and Liu, T.: Variations in dew moisture regimes in desert ecosystems and their influencing factors, Wiley Interdisciplinary Reviews: Water, 7, https://doi.org/10.1002/wat2.1482, 2020.

Zeller, K. F. and Nikolov, N. T.: Quantifying simultaneous fluxes of ozone, carbon dioxide and water vapor above a subalpine forest ecosystem, Environmental Pollution, 107, 1–20, https://doi.org/10.1016/S0269-7491(99)00156-6, https://doi.org/10.1016, 2000.

Zhang, Y. and Schaap, M. G.: Weighted recalibration of the Rosetta pedotransfer model with improved estimates of hydraulic parameter distributions and summary statistics (Rosetta3), Journal of Hydrology, 547, 39–53, https://doi.org/10.1016/j.jhydrol.2017.01.004, http://dx.doi.org/10.1016/j.jhydrol.2017.01.004, 2017.

Zielis, S., Etzold, S., Zweifel, R., Eugster, W., Haeni, M., and Buchmann, N.: NEP of a Swiss subalpine forest is significantly driven not only by current but also by previous year's weather, Biogeosciences, 11, 1627–1635, https://doi.org/10.5194/bg-11-1627-2014, https://doi.org/10.5194{%}2Fbg-11-1627-2014https://bg.copernicus.org/articles/11/1627/2014/, 2014.